Sensitivity and uncertainty in karst hydrosystem modelling

Naomi Mazzilli

UNIVERSITÉ MONTPELLIER II
SCIENCES ET TECHNIQUES DU LANGUEDOC

THÈSE

pour obtenir le grade de

DOCTEUR DE L'UNIVERSITÉ MONTPELLIER II

Discipline : Eaux continentales et société

École doctorale: Systèmes Intégrés en Biologie, Agronomie, Géosciences, Hydrosciences, Environnement (SIBAGHE)

Laboratoire: HydroSciences Montpellier (UMR 5569, CNRS-IRD-UM1-UM2)

SENSIBILITÉ ET INCERTITUDE DE MODÉLISATION SUR LES BASSINS VERSANTS À FORTE COMPOSANTE KARSTIQUE

soutenue publiquement le 09/11/2011 par

Naomi Mazzilli

JURY

Philippe Ackerer	CNRS	Rapporteur
Martin Sauter	Université de Göttingen	Rapporteur
Bruno Arfib	Université de Provence	Examinateur
Christian Leduc	IRD	Examinateur
Vincent Guinot	Université Montpellier II	Directeur de thèse
Hervé Jourde	Université Montpellier II	Directeur de thèse

Contents

Remerciements

Ce travail de thèse a été réalisé au sein du laboratoire HydroSciences Montpellier (UMR 5569).

J'adresse toute ma reconnaissance à Vincent Guinot et Hervé Jourde, qui ont assuré l'encadrement de cette thèse en parfaite complémentarité.

Je remercie les membres du jury pour l'attention et le temps qu'ils ont consacré à l'évaluation de ce travail. Merci à Philippe Ackerer et Martin Sauter d'avoir accepté d'être les rapporteurs de cette thèse. Merci à Bruno Arfib et Christian Leduc d'avoir accepté le rôle d'examinateur.

Je remercie vivement:

- José Grevellec pour avoir partagé avec moi ses connaissances sur l'hydrodynamique de la zone des garrigues nord-montpelliéraines, et pour la relecture d'une partie de ce travail de thèse.
- Véronique Léonardi pour son aide précieuse sur le travail lié au monitorat (relecture critique d'énoncés...) et pour sa relecture partielle de ce travail de thèse.
- Yvan Rossier pour son aide sur l'utilisation de FEFLOW.
- Romuald Barré pour ses informations sur les circulations souterraines sous le causse de Pompignan et le massif du Coutach.
- Sébastien Tritz pour avoir pris le temps de discuter de son travail sur le bassin du Durzon.
- Hubert Camus pour son aide à la pose d'une sonde piézométrique à l'aven de la baraque.
- les membres du comité de thèse: Roger Moussa, Bruno Arfib, José Grevellec, Frank Vasseur, pour l'attention portée à ce travail et pour m'avoir fait une place dans leurs emplois du temps parfois lourdement chargés.

Pour m'avoir fourni les données nécessaires à ce travail, je remercie également:

- Mahmoud Jazayeri et Antoine Lafare pour les données de piézométrie du Terrieu.
- Thomas Jacob pour les données de gravimétrie issues de son travail de thèse et acquises dans le cadre de l'ANR HydroKarst.
- le bureau d'étude Bergasud (et son directeur Jean-Marc François) pour m'avoir permis de consulter leurs dossiers relatifs à la recherche d'eau sur le bassin du Lez.
- la DREAL Languedoc-Roussillon (en la personne de Julien Renzoni) pour les données de débit et la courbe de tarage du seuil aval de la source du Lez.
- Météo-France pour les données météorologiques extraites de la climathèque dans le cadre du contrat UM2-Météo-France. Merci à Claire Rodier pour l'extraction de ces données.
- l'OHM-CV pour l'accès à la banque de données SevNOL. Merci à Brice Boudevillain pour l'extraction de ces données.
- le Parc naturel régional des Grands Causses pour les données de débit à la source du Durzon.
- le SPC Grand Delta (en la personne de Yann Laborda) pour les données pluviométrie et débit.
- Véolia pour les données de piézométries sur le bassin d'alimentation Lez. Merci Bernard Dejean pour la tournée de reconnaissance de ces piézomètres.

Dans un registre plus informel: merci à tous les collègues qui par leur sourire ont contribué à rendre agréable le quotidien de ces années de thèse. Une bise aux amis qui auraient la drôle d'idée d'ouvrir ce manuscrit. Et un coucou et grand merci à mes parents, dont je sais qu'ils ne manqueront pas de passer par ici.

Résumé étendu

Problématique

Les aquifères karstiques sont associés à des enjeux forts de gestion du risque inondation [Avias, 1995 ; Jourde et al., 2007 ; Mijatovic, 1988], mais aussi de gestion de la ressource en eau [El-Hakim et Bakalowicz, 2007]. En effet, les karsts participent à l'alimentation en eau potable d'environ 20% de la population mondiale. Les formations calcaires karstifiées affleurent sur environ 13% des surfaces continentales libres de glace [Ford et Williams, 2007] (voir Figure 1), et des karsts étendus se retrouvent également sous couverture.

Le karst est un réservoir aquifère original à plusieurs titres :

- d'abord du point de vue de la génèse : c'est le seul type d'aquifère qui a la propriété d'auto-organisation (la circulation de l'eau façonne les vides),
- ensuite par ses caractéristiques physiques : il s'agit d'un milieu avec de très forts contrastes de porosité et perméabilité.

Ces caractéristiques génèrent une dualité des processus d'infiltration et de l'écoulement, ainsi qu'une forte non-linéarité du fonctionnement hydrodynamique.

L'étude et la gestion du milieu karstique requiert une approche pluri-disciplinaire combinant les approches structurale, géomorphologique, hydrodynamique et géochimique. La modélisation numérique fait partie des outils d'étude du karst. Elle permet de tester différentes hypothèses relatives au comportement du système (dans une optique d'amélioration des connaissances), ou de prévoir la réponse du bassin à une sollicitation de nature anthropique ou climatique (dans une optique plus opérationnelle). Cependant, des erreurs sont faites à tous les stades du processus de modélisation : elles proviennent en particulier des données utilisées en forçage ou pour la calibration du modèle, de la conceptualisation du système et de la traduction des processus en équations, ainsi que de l'étape de sélection des paramètres. Ces erreurs se répercutent sur les variables de sortie du modèle. L'étude de la propagation des erreurs constitue une étape essentielle du processus de modélisation : elle est l'objet des analyses de sensibilité et d'incertitude.

L'objectif de cette thèse est de déterminer des caractéristiques générales du comportement de la sensibilité dans la modélisation hydrodynamique des écoulements en milieu karstique. Il s'agit notamment d'étudier l'influence des spécificités du milieu karstique sur la propagation de la sensibilité, en vue de répondre aux questions suivantes :

- est-il possible de calibrer le modèle ?
- la calibration est-elle robuste ?
- peut-on réduire l'incertitude associée à l'estimation des paramètres par un choix adapté des variables de calibration, de la fonction objectif, ou par l'acquisition de données supplémentaires ?

L'analyse est menée de façon systématique pour différents types de modèle (modèles conceptuels globaux et modèles hybrides distribués) et différents sites-test.

Organisation du mémoire et principaux résultats

Ce manuscrit est organisé en un chapitre d'introduction, suivi de deux parties.

Le chapitre 1 présente les spécificités liées au fonctionnement des systèmes karstiques ainsi que les principales approches utilisées pour la modélisation numérique de leur fonctionnement hydrodynamique. Il introduit également les différentes techniques d'analyse de sensibilité et d'incertitude, et présente les principales problématiques associées. Les applications les plus connues de l'analyse de sensibilité et d'incertitude sont probablement le calage et la quantification de l'incertitude associée à une prédiction. Cependant le champ d'étude des analyses de sensibilité et d'incertitude est bien plus vaste ; il comprend notamment les problématiques

- de réduction de l'incertitude,
- de définition ou de sélection des fonctions objectif utilisées pour le calage,
- de recueil des données expérimentales contenant un maximum d'information utile.

La première partie de ce manuscrit est consacrée à l'analyse des propriétés de la sensibilité de modèles conceptuels globaux.

Le chapitre 2 étudie les propriétés analytiques de la sensibilité au biais d'initialisation de deux modèles globaux à réservoirs utilisés pour simuler la relation pluie-débit de sources karstiques : le modèle Vensim proposé par Fleury, 2005 et le modèle à hystérésis proposé par Tritz et al., 2011 (Sections 2.1 à 2.8). L'analyse de sensibilité est menée à partir d'une méthode locale par perturbation.
L'état de remplissage initial des réservoirs d'un modèle global ne peut être déterminé expérimentalement. Par conséquent, une erreur est nécessairement faite lors de la spécification de la condition initiale, et cette erreur se répercute sur l'ensemble des variables du modèle. Ce biais d'initialisation peut perturber le processus de calage, et les résultats de la simulation. Ce problème est classiquement résolu par le calage de la condition initiale, ou la troncature d'une partie de la chronique simulée par le modèle. Dans les deux cas il est important de connaître le comportement de la sensibilité des variables du modèle aux condition initiales : la période où la sensibilité est maximale sera, selon le cas, sélectionnée pour le calage de la condition initiale, ou au contraire éliminée. L'objectif de ce travail est de déterminer des caractéristiques générales de la propagation du biais d'initialisation dans un modèle global. En particulier, nous avons essayé de répondre aux questions suivantes :

- la propagation du biais d'initialisation est-elle fonction de la structure du modèle ? Si oui, peut-on prévoir certaines caractéristiques du biais d'initialisation associées à une structure de modèle donnée ?
- quel est l'effet des fonctions de transfert non-linéaire couramment employées pour la modélisation pluie-débit des sources karstiques sur la propagation du biais d'initialisation ?

L'étude analytique montre que les caractéristiques de la propagation de la sensibilité à la condition initiale sont fonction à la fois de la structure du modèle, de la série climatique (conditions hydrologiques) et de la valeur prise par la condition initiale (état de remplissage des réservoirs). En particulier, les fonctions de transfert à seuil qui sont couramment utilisées afin d'introduire une non-linéarité dans le fonctionnement du modèle peuvent accélérer la propagation (et donc la dissipation) du biais d'initialisation. Cependant, cette accélération de la propagation du biais d'initialisation s'accompagne d'une augmentation de la valeur du biais sur la variable de sortie du modèle. Le cas pour lequel le déclenchement de la fonction de transfert à seuil est conditionné par le niveau de remplissage d'un réservoir à dynamique lente est particulièrement défavorable. En effet, cette configuration provoque un transfert de sensibilité depuis le réservoir à dynamique lente vers

le reste du modèle. Ceci induit des pics de sensibilités sur la variable de sortie du modèle jusqu'à plusieurs années après le début de la simulation. Ce mécanisme peut compromettre le processus de calibration (le phénomène est illustré en Figure 8 en page xiv).

Par ailleurs, l'analyse théorique réalisée pour les deux modèles considérés (modèles Vensim et Hystérésis) permet de déduire des règles générales de comportement du biais d'initialisation en fonction de la structure du modèle, et en particulier d'identifier les cas problématiques ou favorables à la dissipation de la sensibilité. En règle générale, la dissipation du biais d'initialisation est accélérée :

- lors des périodes très sèches, du fait de la vidange totale du réservoir supérieur qui a pour résultat de stopper complètement la propagation de la sensibilité au niveau initial dans ce réservoir,
- lors des périodes très humides, du fait de l'activation des fonctions de transfert rapide qui accélère la propagation de la sensibilité au niveau de remplissage initial.

Ces résultats analytiques sont confirmés par des applications numériques ayant pour objet la simulation des débits à l'exutoire du bassin karstique du Durzon (Larzac, France). En complément à ce travail, la Section 2.9 étend l'analyse aux propriétés analytiques de la sensibilité aux paramètres des modèles.

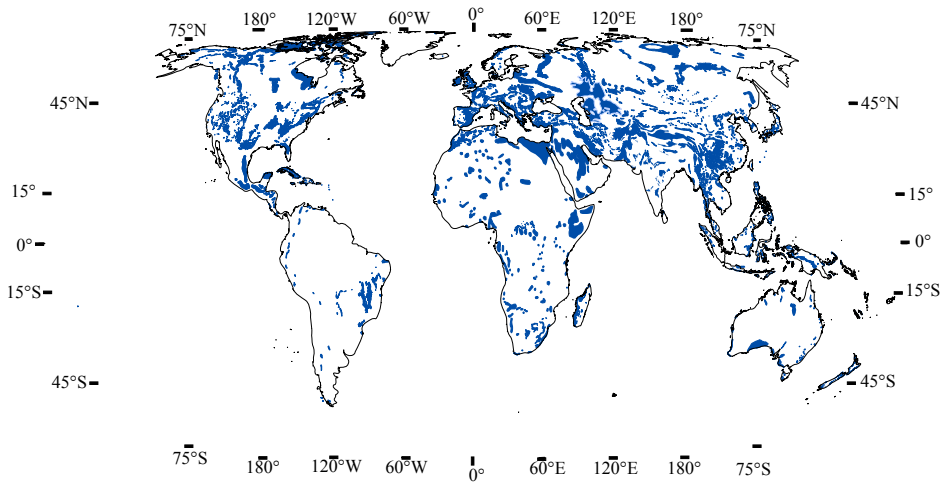

Figure 1 – Cartographie mondiale des formations calcaires karstifiées affleurantes, d'après Ford et Williams, 2007

Le chapitre 3 examine la pertinence de l'utilisation de mesures gravimétriques au sol pour la calibration d'un modèle pluie-débit de type conceptuel, à l'échelle d'un petit bassin karstique. L'analyse est réalisée sur le système du Durzon (Larzac, France - voir Figure 2).

Les données gravimétriques disponibles sur le bassin du Durzon sont de deux types (mesures acquises dans le cadre de l'ANR HydroGéodésie) :

- des mesures de variation absolue de la pesanteur ont été réalisées à fréquence mensuelle ou pluri-mensuelle sur trois sites. La précision de ces mesures est de l'ordre de 1 à 2 μGals, soit l'équivalent d'une variation de stock d'eau de l'ordre de 25 à 50mm,
- des mesures de variation relative de la pesanteur ont été réalisées sur une quarantaine de sites au cours de 4 campagnes de mesures réparties sur deux années. La précision de ces mesures est de l'ordre de 2.5 à 5 μGals, permettant la détection de variations de stock d'eau de l'ordre de 65 à 125mm.

La première partie de l'étude traite de l'interprétation hydrogéologique des mesures gravimétriques in-situ. Les mesures gravimétriques ne sont pas résolues dans le plan vertical, et sont à comparer au stock d'eau total du modèle conceptuel. Par rapport aux mesures de débit, la mesure des variations temporelles du stock d'eau total contient davantage d'informations sur les flux sortants (évapotranspiration et pertes extérieures).

Dans un second temps, nous tentons de quantifier le contenu informatif des données gravimétriques pour la modélisation hydrodynamique à l'échelle du bassin. L'analyse de sensibilité globale indique que l'utilisation des données gravimétriques comme variable de calibration auxiliaire ne permet pas de réduire l'équifinalité. Il y a redondance entre les informations issues des relevés gravimétriques et celles issues des relevés de débit. La faible valeur ajoutée des données gravimétriques peut être liée : (i) à la valeur élevée de l'incertitude expérimentale sur les mesures de variation temporelle du stock d'eau par rapport aux variations saisonnières observées, (ii) à l'inadéquation du modèle proposé ou des fonctions de transfert ou d'évaporation utilisées.

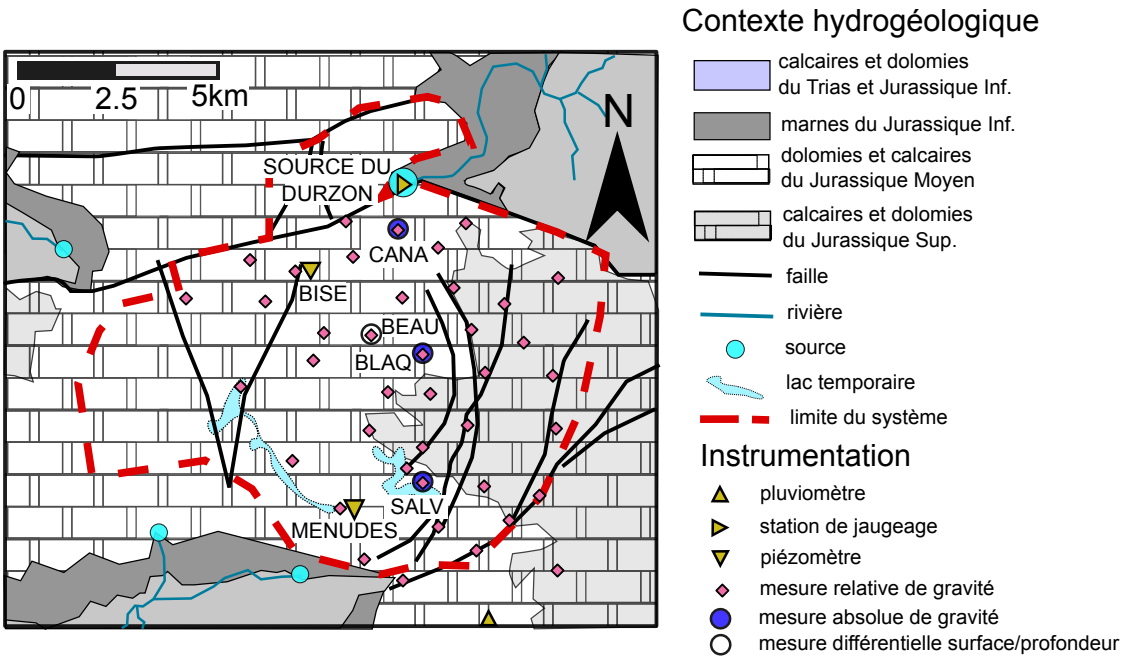

Figure 2 – Contexte hydrogéologique et instrumentation du système karstique du Durzon. Modifié d'après Bruxelles, 2001 ; Jacob, 2009 ; Ricard et Bakalowicz, 1996. Voir chapitre 3.

Le chapitre 4 discute du niveau de complexité optimal pour une modélisation pluie-débit globale, à partir de l'analyse de sensibilité globale de trois modèles de structures différentes et en prenant pour cas d'étude la source du Lez (Hérault, France) :

- un modèle à 10 paramètres et 4 réservoirs précédemment proposé par Fleury et al., 2009 et validé sur le cas de la source du Lez (Hérault, France),
- un modèle à 4 paramètres et 1 réservoir proposé par Fleury, 2011 (comm. perso),
- un modèle de complexité intermédiaire à 5 paramètres et 3 réservoirs, proposé dans le cadre de cette thèse.

Le site d'étude choisi (source du Lez) a pour particularité d'être l'objet d'une gestion active de la ressource. La gestion active consiste à affranchir les prélèvements des variations saisonnières du débit naturel de la source. Dans le cas d'une source karstique vauclusienne (cas de la source du Lez), la mise en œuvre de la gestion active peut être résumée comme suit [Avias, 1995] : (i) l'eau est prélevée sous la cote de débordement, directement dans le conduit karstique, ce qui permet de maintenir un taux de prélèvement supérieur au débit naturel de la source lors des périodes sèches, sans risquer de dénoyer les pompes ; (ii) la surexploitation estivale est compensée dès les premières crues d'automne, ce qui permet le renouvellement intégral de la ressource à l'échelle annuelle. La modélisation du débit de ces sources durant les périodes de hautes eaux est liée aux enjeux de prévision et gestion des crues. La modélisation des hauteurs piézométriques dans le conduit karstique est particulièrement intéressante du point de vue de l'exploitation de la ressource.

Le modèle proposé est structuré en 3 réservoirs (Figure 3), pour un total de 5 paramètres :

- le réservoir supérieur (réservoir E) représente le sol et le compartiment épikarstique. Ce compartiment reçoit les apports des précipitations et est soumis à l'évapotranspiration. Il se vidange dans les deux réservoirs inférieurs M et C,
- le réservoir inférieur M représente le stockage matriciel (blocs fracturés et microfracturés), intégrant l'eau comprise dans la zone saturée et la zone non saturée,
- le second réservoir inférieur C représente le conduit karstique. Les prélèvements en eau potable sont réalisés directement dans ce réservoir. Le débordement de ce réservoir correspond au débit de débordement de l'exutoire de l'hydrosystème.

Le volume échangé entre les conduits karstiques (réservoir C) et la matrice fissurée (réservoir M) est proportionnel au gradient piézométrique entre ces deux volumes.

Par rapport au modèle à dix paramètres, le modèle proposé présente de meilleures performances en calibration et validation pour la simulation des débits et des niveaux piézométriques, avec une incertitude paramétrique réduite. Par rapport au modèle à un réservoir et pour la période de calibration, le modèle proposé présente de meilleures performances pour la simulation des débits, et des performances équivalentes pour la simulation des niveaux piézométriques.

La seconde partie de ce travail est consacrée à l'analyse des propriétés de la sensibilité de modèles hybrides. Les modèles hybrides sont des modèles distribués dans lesquels le système de drainage est représenté par des éléments uni-dimensionnels discrets couplés à un système matrice tri-dimensionnelle représentant les blocs fracturés et micro-fissurés. Les questions posées sont les suivantes :

- est-ce que les paramètres hydrodynamiques, la géométrie du modèle et les conditions aux limites ont la même influence sur la réponse du modèle ?
- les aquifères confinés et non-confinés se comportent-ils de façon similaire vis-à-vis de la propagation de la sensibilité ?
- quelle est l'influence des conduits karstiques discrets sur la propagation de la sensibilité ?
- où faut-il faire porter l'effort d'instrumentation de façon à contraindre au mieux les résultats d'une simulation ?
- peut-on définir des règles générales pour la mise en place d'un réseau d'instrumentation ?

Les chapitres 5 et 6 présentent la mise en place d'un modèle hybride distribué du système karstique du Lez (Hérault, France). Les propriétés analytiques et empiriques de la sensibilité de ce modèle sont étudiées dans le chapitre 7.

Le chapitre 5 présente le système karstique du Lez (Hérault, France), qui fait l'objet de la modélisation hybride distribuée dans les chapitres suivants. Le système aquifère du Lez se développe dans des calcaires karstifiés du Jurassique Supérieur au Crétacé Inférieur. Son principal exutoire est la source du Lez qui alimente la ville de Montpellier en eau potable (voir Figure 5). La source du Lez a servi de cas-test pour l'évaluation des modèles pluie-piézométrie-débit proposés pour la modélisation des sources karstiques en gestion active dans le Chapitre 4 et le système aquifère du Lez y a été brièvement présenté. Le Chapitre 5 offre une présentation du contexte géologique et du comportement hydrodynamique du système plus détaillée, en vue de la modélisation hybride distribuée.

Les premiers travaux sur la source du Lez sont entrepris en 1959 (J. Avias, université de Montpellier II) et les caractéristiques essentielles du régime de la source et l'importance des réserves potentiellement exploitables sont mis en évidence dès 1964 [Drogue, 1964]. Cependant des points d'interrogation subsistent sur les mécanismes de fonctionnement et d'alimentation de l'aquifère qui alimente la source du Lez. En particulier, les relations entre le système du Lez et plusieurs systèmes annexes (plaine de Pompignan, zone Nord du causse de Viols) restent à caractériser de façon qualitative et quantitative. La possibilité d'un drainage du système du Lez à travers le pli de Montpellier fait partie des questions ouvertes.

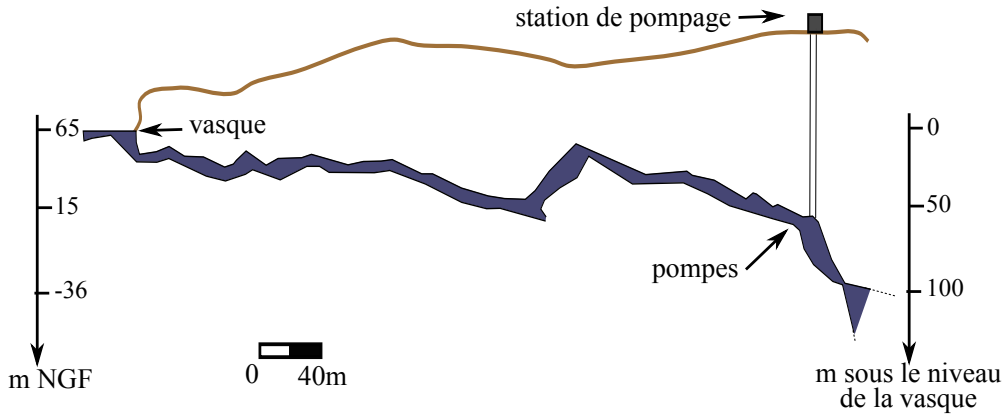

Figure 5 – Coupe du conduit d'amenée des eaux à la source du Lez. Topographie : P. Rousset (GEPS). Voir chapitre 5.

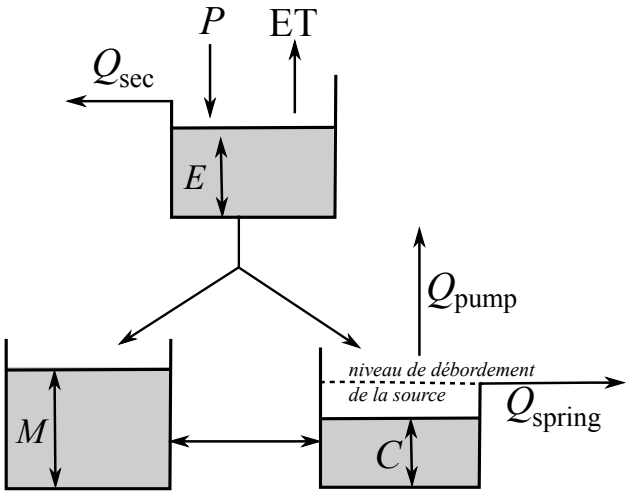

Figure 3 – Structure proposée pour la modélisation des exurgences karstiques en gestion active. P : pluie, ET : évapotranspiration, Q_{sec} : débit alimentant les sources temporaires Q_{pump} : débit prélevé à la source, Q_{spring} : débit simulé. Voir chapitre 4.

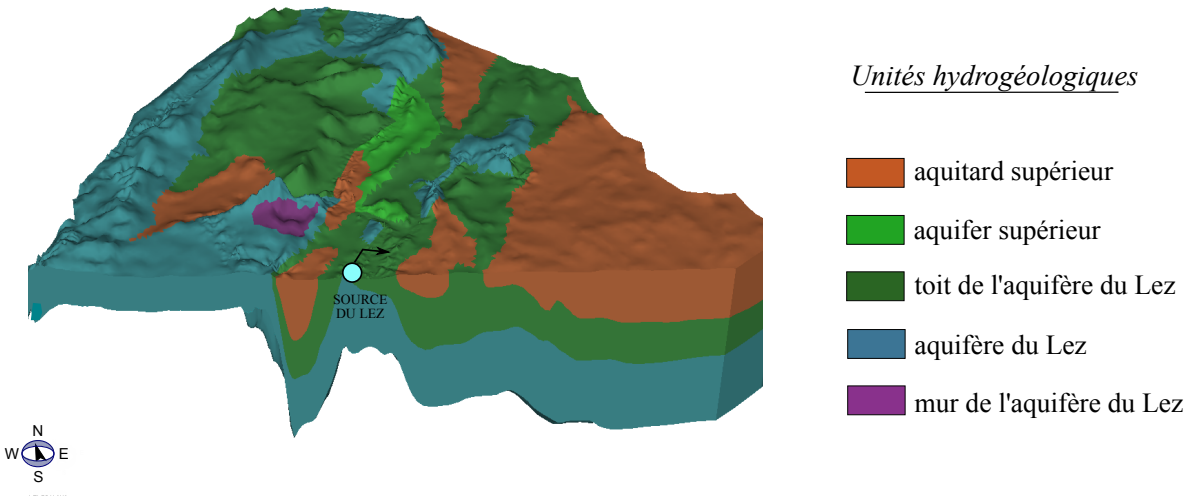

Figure 4 – Modélisation distribuée du système karstique du Lez. Vue en perspective du modèle hydrogéologique. Voir chapitre 6.

Le chapitre 6 présente le modèle hydrodynamique distribué du vaste ensemble karstique situé entre Hérault et Vidourle et englobant le système karstique du Lez. La modélisation proposée est de type hybride : les conduits karstiques sont représentés par des éléments discrets unidimensionnels enchâssés dans une matrice poreuse tridimensionnelle représentative des blocs fracturés et microfracturés. Le couplage entre les drains et la matrice est réalisé en supposant la continuité des potentiels hydrauliques entre les deux systèmes. Le modèle est implanté dans le code commercial FEFLOW (Finite Element subsurface FLOW system) [Diersch, 1998*a*]. Une vue du modèle géologique 3-D de la zone étudiée est présentée en Figure 4.

Les principales simplifications utilisées lors du développement du modèle sont :

- la non-prise en compte des apports d'infiltration concentrée par le ruissellement (par exemple, apports au niveau des pertes situées le long de la faille de Corconne), avec pour conséquence attendue des flux sortants moins importants que dans la réalité, et une dynamique des débits à l'exutoire sensiblement distincte en période de crue,
- la prise en compte d'un nombre réduit d'exsurgences karstiques : seuls les réseaux principaux ont été implantés. Cette simplification est particulièrement critique en période de hautes eaux, où les observations de terrains indiquent la mise en fonctionnement d'un nombre élevé d'exsurgences temporaires,
- l'hétérogénéité limitée des propriétés hydrodynamiques du modèle proposé rend difficile l'utilisation des chroniques piézométriques comme variables de calibration.

Le chapitre 7 analyse la propagation de la sensibilité dans le modèle hybride distribué développé précédemment.

La première partie de ce chapitre (Section 7.1) aborde les propriétés analytiques de la sensibilité de l'équation de diffusivité (utilisée pour décrire l'écoulement dans la matrice) aux paramètres hydrodynamiques et aux conditions aux limites dans le cas d'un régime permanent, et pour un milieu bi-dimensionnel. Nous montrons que le comportement de la sensibilité dépend à la fois du paramètre perturbé et de la variable considérée (Figure 6). En particulier :

- la sensibilité de la charge hydraulique à une perturbation de la conductivité hydraulique se propage principalement dans la direction de l'écoulement, tandis que la sensibilité de la recharge se propage radialement,
- la sensibilité de la vitesse d'écoulement longitudinale à une perturbation de la conductivité hydraulique se propage dans les directions transversales et longitudinales, tandis que la sensibilité de la vitesse d'écoulement transversale se propage dans les directions diagonales à l'écoulement.

Ces résultats analytiques sont confirmés par des applications numériques dans des cas théoriques et des cas de géométrie réelle, en régime permanent mais également en régime transitoire. Ces propriétés analytiques permettent de proposer quelques règles pour le développement et la calibration des modèles, ainsi que pour la mise en place de réseaux d'instrumentation. En particulier, la position optimale des points de mesures dépend de la nature de la variable étudiée. La géométrie optimale d'un réseau d'instrumentation dépend donc du problème étudié. De plus, l'analyse des écarts entre valeurs simulées et observées peut permettre de discriminer entre les sources d'erreur pouvant être à l'origine de ces écarts, à condition que le réseau d'instrumentation soit suffisamment dense et que sa géométrie soit adaptée.

La seconde partie de ce chapitre (Section 7.2) étudie la sensibilité du modèle hybride développé au chapitre 6, par une approche empirique. Les paramètres considérés sont les conditions initiales, les propriétés hydrodynamiques et les paramètres des conduits karstiques. En régime permanent, la condition à la limite imposée à l'exutoire du drain karstique se propage le long du drain. De ce fait, la modification de la propagation de la sensibilité de la piézométrie à une perturbation locale des propriétés hydrodynamiques du fait de la présence des drains karstiques se rapproche

de la modification de la propagation de la sensibilité induite par la présence d'une condition à la limite (voir Figure 7). La propagation de la sensibilité est conditionnée par le caractère limitant ou non-limitant de la débitance du drain karstique par rapport à l'écoulement. Au cours d'une simulation en régime transitoire, la condition à la limite imposée à l'exutoire du drain varie, selon que la cote de débordement soit atteinte ou non. De même, le caractère limitant ou non-limitant de la débitance du drain karstique par rapport à l'écoulement varie également. En conséquence, le régime transitoire est associé à des variations brutales du comportement de la sensibilité.

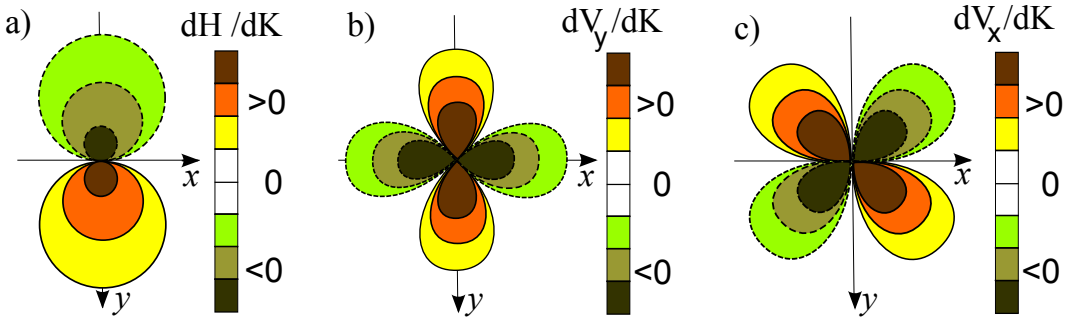

Figure 6 – Étude analytique de la sensibilité de l'équation de diffusivité. Allure théorique de la sensibilité à une perturbation locale de la conductivité hydraulique : a) sensibilité de la charge hydraulique, b) sensibilité de la vitesse longitudinale, c) sensibilité de la vitesse transversale. La zone perturbée est située à l'origine des axes. L'écoulement est supposé parallèle sur cette zone, et dirigé selon l'axe y. On remarque que la sensibilité se propage dans des directions différentes selon la variable considérée. Voir chapitre 7.1.

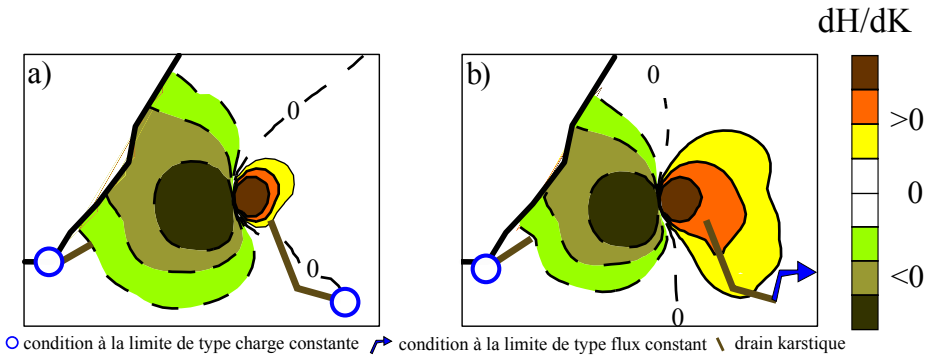

Figure 7 – Étude empirique de la propagation de sensibilité de la charge hydraulique à une perturbation locale de la conductivité hydraulique, en régime permanent et au voisinage d'un drain. Remarquer la modification de la propagation de la sensibilité au voisinage des drains karstiques, par rapport au cas théorique présenté en Figure 6. Voir chapitre 7.2.

Conclusions

Les principales conclusions de ce travail sont les suivantes :

- Cette contribution souligne le potentiel de l'analyse de sensibilité locale. Les méthodes d'analyse globale sont devenues largement répandues dans la modélisation environnementale. Cette étude montre qu'en dépit des limitations inhérentes à l'approximation locale et un-facteur-à-la-fois, l'approche de sensibilité locale permet une compréhension fine du fonctionnement du modèle, pour un coût de calcul réduit.
- Ce travail souligne également l'intérêt, dans un objectif de réduction de l'équifinalité, d'une calibration multi-variable par comparaison à une calibration multi-objectif. Des fonctions objectif différentes correspondent à des mises en valeur différentes d'une même information. La calibration multi-objectif a donc pour but d'utiliser de la façon la plus complète possible l'information disponible, en faisant ressortir au mieux les différentes caractéristiques du signal. L'utilisation de variables différentes (par exemple : la charge hydraulique et son gradient) peut en revanche amener une véritable augmentation du contenu informatif, comme illustré par les résultats des Chapitres 2 et 7.

Les principales pistes de recherche portent sur :

- La détermination du champ d'applicabilité de l'analyse de sensibilité locale pour l'estimation de l'incertitude associée à une simulation, dans le cas de modèles globaux fortement non-linéaires.
- La poursuite de l'intégration de mesures géophysiques dans le processus de calibration, dans le but de réduire l'équifinalité.
- L'intégration de mesures de type hydrochimique dans le processus de calibration, dans le but de réduire l'équifinalité.

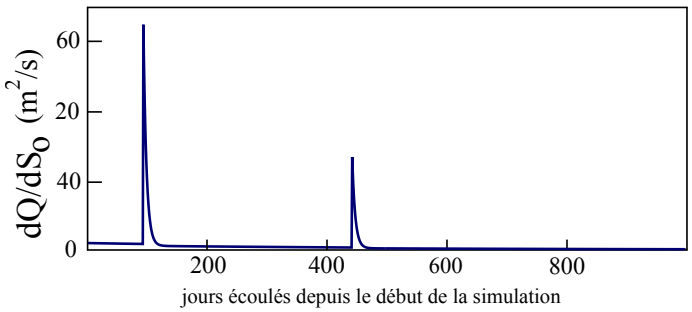

Figure 8 – Étude analytique de la sensibilité du débit simulé en sortie d'un modèle global à réservoir au niveau initial de remplissage du modèle. Exemple de la sensibilité du débit au niveau initial de remplissage du réservoir inférieur du modèle Vensim proposé par Fleury, 2005. Les pics de sensibilité observés 100 et 450 jours après le début de la simulation sont déclenchés par l'activation d'une fonction de transfert à seuil gouvernée par le niveau de remplissage d'un réservoir à dynamique lente. Une erreur de 10cm sur l'estimation du remplissage initial engendre une erreur sur le débit simulé supérieure à $6m^3/s$ 100 jours après le début de la simulation et de $4m^3/s$ environ 450 jours après le début de la simulation. Ces chiffres sont à rapporter au débit de pointe de l'exsurgence considérée ($18m^3/s$). Voir chapitre 2.

References

Avias, J. (1995). « Gestion active de l'exsurgence karstique de la source du Lez ». Dans : *Hydrogéologie* 1, p. 113–127. Cf. p. v, ix, xvii, 90, 93, 134.

Bruxelles, L. (2001). « Dépots et altérites des plateaux du Larzac central : Causses de l'Hospitalet et de Campestre (Aveyron, Gard, Hérault). Évolution morphogénique, consequences géologiques et implications pour l'amenagement ». Thèse de doct. Université de Provence. Cf. p. viii, 39, 40, 72, 73.

Diersch, H. (1998*a*). *Feflow : Reference Manual*. Institute for Water Resources Planning et Systems Research, WASY. Berlin. URL : http://www.feflow.info/manuals.html. Cf. p. xii, 9, 151, 180.

Drogue, C. (1964). « Sur l'étude hydrogéologique des principales résurgences de la région nord-montpelliéraine ». Dans : *Extrait des Mémoires du CERH*. T. 1. Université de Montpellier II. Cf. p. x.

El-Hakim, M. et M. Bakalowicz (2007). « Significance and origin of very large regulating power of some karst aquifers in the Middle East. Implication on karst aquifer classification ». Dans : *Journal of Hydrology* 333.2-4, p. 329–339. DOI : 10.1016/j.jhydrol.2006.09.003. Cf. p. v.

Fleury, P., B. Ladouche, Y. Conroux, H. Jourde et N. Dörfliger (2009). « Modelling the hydrologic functions of a karst aquifer under active water management - The Lez spring ». Dans : *Journal of Hydrology* 365.3-4, p. 235–243. DOI : 10.1016/j.jhydrol.2008.11.037. Cf. p. ix, xviii, 7, 90, 93, 94, 102, 104.

Fleury, P. (2005). « Sources sous-marines et aquifères karstiques côtiers méditerranéens. Fonctionnement et caractérisation ». Thèse de doct. Université Paris VI - Pierre et Marie Curie. URL : http://hydrologie.org/THE/FLEURY.pdf. Cf. p. vi, xiv, xvii, 39, 42, 44, 52, 59, 72.

Ford, D. et P. Williams (2007). *Karst Geomorphology and Hydrology*. [Revised Edition]. Unwin Hyman (London et Boston), p. 601. ISBN : 0045511055. URL : http://eu.wiley.com/WileyCDA/WileyTitle/productCd-0470849967.html. Cf. p. v, vii, xvii, 128.

Jacob, T. (2009). « Apport de la gravimétrie et de l'inclinométrie à l'hydrologie karstique ». Thèse de doct. Université Montpellier II. URL : http://tel.archives-ouvertes.fr/tel-00404851/fr/. Cf. p. viii, 40, 73–75.

Jourde, H., A. Roesch, V. Guinot et V. Bailly-Comte (2007). « Dynamics and contribution of karst groundwater to surface flow during mediterranean flood ». Dans : *Environmental Geology* 51, p. 725–730. DOI : 10.1007/s00254-006-0386-y. Cf. p. v, xvii.

Mijatovic, B. (1988). « Catastrophic flood in the polje of Cetinje in February 1986, a typical example of the environmental impact of karst ». Dans : *Environmental Geology and Water Sciences* 12.2, p. 117–121. DOI : 10.1007/BF02574797. Cf. p. v, xvii.

Ricard, J. et M. Bakalowicz (1996). *Connaissance, aménagement et protection des ressources en eau du Larzac septentrional, Aveyron (France)*. Rap. tech. R38953. BRGM. URL : http://www.brgm.fr/Rapport?code=RR-38953-FR. Cf. p. viii, 39, 40, 72, 73.

Tritz, S., V. Guinot et H. Jourde (2011). « Modelling the behaviour of a karst system catchment using non linear hysteretic conceptual model ». Dans : *Journal of Hydrology* 397.3-4, p. 250–262. DOI : 10.1016/j.jhydrol.2010.12.001. Cf. p. vi, xvii, 7, 38–41, 44, 46, 52, 59, 72, 73, 76, 77, 80, 93, 94.

Introduction

Scientific context

Karstified carbonate formations outcrop over roughly 13% of the Earth's ice-free continental area [Ford and Williams, 2007], and extensive karstified carbonate rock also exists in subcrop. Karst aquifers are associated with key issues for water resource management (they supply approximately 20% of the world population with freshwater [Ford and Williams, 2007]) and also for flood risk mitigation [Avias, 1995; Jourde et al., 2007; Mijatovic, 1988]. These systems are characterized by a highly heterogeneous and organized structure. These specificities of karst structure are associated with specificities in the hydrodynamic behaviour of karst aquifers, the main of which being the duality of flow and a highly non-linear behaviour.

Aim of this work

Numerical modelling provides a valuable tool for answering both operational and fundamental issues on karst functioning. However the strong non-linearity of karst aquifers render their numerical simulation rather tricky.

The present thesis is motivated by the requirement of an improved understanding and insight in the behaviour of numerical models of groundwater flow within karst systems. We aim to work out general characteristics of the sensitivity associated with the numerical modelling of karst systems, with the final purpose of answering the following questions:

(i) is it possible to calibrate the model ?

(ii) is the calibration robust ?

(iii) is it possible to reduce equifinality, through multi-objective calibration or through multi-variable calibration ?

Structure of this thesis

This document is structured as follows.

Chapter 1 provides a brief overview of the karst systems functioning and specificities. The main modelling approaches are summarized. The sensitivity and uncertainty concepts are presented and an overview of the sensitivity and uncertainty assessment techniques is given. The interest of sensitivity and uncertainty analysis for the modelling is illustrated based on a short litterature review.

The first Part of this work is dedicated to the analysis of global reservoir models.

Chapter 2 uses the perturbation approach to investigate the analytical properties of the sensitivity to the initial conditions on the calibration and the simulation results of two karst spring discharge reservoir models: the Vensim model [Fleury, 2005] and the hysteresis-based model [Tritz et al., 2011]. These analytical findings are used to provide general rules for the initialisation bias behaviour depending on model structure.

Chapter 3 examines the relevance of including ground-based gravity data in the calibration process of a global rainfall-discharge reservoir model. The analysis is performed for the Durzon karst system (Larzac, France). The first part of the study aims at analyzing the relevance of available point measurements with respect to the modelling of aquifer-scale water storage dynamics. The second part of the study further investigates the information content of the gravity data with respect to water storage dynamics modelling.

Chapter 4 presents a 5-parameter, 3-reservoir conceptual model for the hydrological modelling of karst springs under active groundwater management. The model accounts for both the spring discharge and the water level within the spring conduit, which makes it suitable for both flood prediction and groundwater management. The model performance is assessed against the 10-parameter, 4-reservoir model proposed by Fleury et al. [Fleury et al., 2009]. The model consistency is further assessed by comparison to the calibration results of a simple 5-parameters, 1-reservoir conceptual model.

The second Part presents the work related to a distributed, hybrid flow model for the Lez karst aquifer system.

Chapter 5 presents the hydrogeologic and hydrodynamic settings for the Lez karst aquifer system, in view of the hybrid flow modelling. The Lez spring is the main outlet of a large karst aquifer system (referred to as the "Lez aquifer") made of Late Jurassic to early Cretaceous limestones. The aquifer is compartimentalized by a network of NE-SW normal faults into a raised, north-western compartment where the aquifer limestone outcrops and a lowered, south-eastern compartment where most of the aquifer is covered by impervious formations.

Chapter 6 presents the distributed, hybrid flow model setup and the calibration results for the steady and transient states.

Chapter 7 investigates the sensitivity behaviour of hybrid flow models, using both analytical and empirical means. As a preliminary step, the analytical properties of the sensitivity of the two-dimensional, steady-state groundwater flow equation to the flow parameters and to the boundary conditions are derived based on the perturbation approach. The sensitivity patterns are shown to depend on the nature of both the perturbed parameter and the variable investigated. The analytical results are confirmed by application examples on idealized and real-world simulations. These analytical properties are used to provide guidelines for model design, model calibration and monitoring network design.
Secondly, we investigate the impact of discrete karst conduits modelling on the sensitivity propagation, based on an empirical approach using the hybrid flow model set up in Chapter 6. The sensitivity of the hybrid flow model to the initial condition, the hydrodynamic properties and the karst conduit properties are assessed for both steady and transient state.

References

Avias, J. (1995). « Gestion active de l'exsurgence karstique de la source du Lez ». In: *Hydrogéologie* 1, pp. 113–127. See pp. v, ix, xvii, 90, 93, 134.

Fleury, P., B. Ladouche, Y. Conroux, H. Jourde and N. Dörfliger (2009). « Modelling the hydrologic functions of a karst aquifer under active water management - The Lez spring ». In: *Journal of Hydrology* 365.3-4, pp. 235–243. DOI: 10.1016/j.jhydrol.2008.11.037. See pp. ix, xviii, 7, 90, 93, 94, 102, 104.

Fleury, P. (2005). « Sources sous-marines et aquifères karstiques côtiers méditerranéens. Fonctionnement et caractérisation ». PhD thesis. Université Paris VI - Pierre et Marie Curie. URL: http://hydrologie.org/THE/FLEURY.pdf. See pp. vi, xiv, xvii, 39, 42, 44, 52, 59, 72.

Ford, D. and P. Williams (2007). *Karst Geomorphology and Hydrology*. [Revised Edition]. Unwin Hyman (London and Boston), p. 601. ISBN: 0045511055. URL: http://eu.wiley.com/WileyCDA/WileyTitle/productCd-0470849967.html. See pp. v, vii, xvii, 128.

Jourde, H., A. Roesch, V. Guinot and V. Bailly-Comte (2007). « Dynamics and contribution of karst groundwater to surface flow during mediterranean flood ». In: *Environmental Geology* 51, pp. 725–730. DOI: 10.1007/s00254-006-0386-y. See pp. v, xvii.

Mijatovic, B. (1988). « Catastrophic flood in the polje of Cetinje in February 1986, a typical example of the environmental impact of karst ». In: *Environmental Geology and Water Sciences* 12.2, pp. 117–121. DOI: 10.1007/BF02574797. See pp. v, xvii.

Tritz, S., V. Guinot and H. Jourde (2011). « Modelling the behaviour of a karst system catchment using non linear hysteretic conceptual model ». In: *Journal of Hydrology* 397.3-4, pp. 250–262. DOI: 10.1016/j.jhydrol.2010.12.001. See pp. vi, xvii, 7, 38–41, 44, 46, 52, 59, 72, 73, 76, 77, 80, 93, 94.

Chapter 1

Scientific context

This chapter provides the scientific context for this thesis. Section 1.1 gives an overview of karst systems functioning and specificities. Section 1.2 summarizes the main approaches for karst aquifer flow modelling. Section 1.3 presents the sensitivity and uncertainty concepts and the sensitivity and uncertainty assessment techniques. The interest of sensitivity and uncertainty analysis for the modelisation is illustrated based on a short litterature review. Section 1.4 states the objectives and structure of the thesis.

Contents

1.1 Introduction to karst aquifers

The word "karst" designates "limestone and dolomite areas that possess a topography peculiar to and dependent upon underground solution and the diversion of surface waters to underground routes"[1]. Karstic features may also develop in evaporite rocks such as gypsum and anhydrite and sometimes in quartzite [White, 1988]. This section provides a brief introduction to karst aquifers.

1.1.1 Karst aquifers specificity

The effective porosity of karstified rocks is a combination of primary (intergranular, "matrix"), secondary (arising from folding and faulting) and tertiary (arising from dissolution) porosities. The relative importance of these three porosities may differ from one karst aquifer system to another, depending on the rock texture and structure as well as on the karst aquifer genesis history [Bakalowicz, 2005; Goldscheider et al., 2008]. High porosity and **high permeability contrasts** are typical of karst aquifers, which is the reason why karst has been termed as "the medium where heterogeneity reaches its paroxysm" [Marsily, 1984]. High permeability contrasts result in a duality of the infiltration, that may be either diffuse (through the soil and fissured matrix) or concentrated (through swallow holes) (see Figure 1.1).

The karstification process is dependent on both chemical conditions and groundwater flow conditions [Kiraly, 2003]. The fact that groundwater flow partly controls the karstification process sparks off an important characteristics of karst aquifers: their **self-organization** ability [Worthington and Ford, 2009].

The time scale of karst development may be shorter than that associated with tectonic uplift and sea level fluctuation. Indeed, the characteristic time scale for the development of a conduit ranges from 10^4 to 10^5 years [Bosák, 2003] but significant modifications of flowpaths may occur within thousands of years [White, 2002]. At the geologic time scale, karst systems may therefore act as **highly dynamic structures**. Water base level downgrade results in a downwards and horizontal development of karst networks. Some parts of the karstic network may then become non-functional. These non-functional conduits may come into use again later, when a water level upgrade happens. Karst aquifer networks thus most often result from a polyphased genesis, which adds to the complexity of their structure and functioning.

1.1.2 Conceptual models of flow within karst aquifers

As a whole, conceptual models of karst aquifer systems (such as those proposed by e.g. Drogue, 1974; Dörfliger et al., 1999; Kiraly, 1975; Mangin, 1975) agree on a main karst system structure, which may be decomposed into [Perrin, 2003; Sauter et al., 2008]:

- the soil and epikarst sub-system, which may store part of the infiltrated water,
- the unsaturated (or vadose) sub-system, that connects the epikarst to the phreatic zone by drainage through a vertical network of fissures and conduits,
- the saturated (or phreatic) sub-system, which is split into a network of high permeability conduits and low permeability volumes with a high storage capacity.

The relative importance of these compartments in the hydrological functioning of the karst system depends on the rock texture and structure as well as on the karst aquifer genesis history. The variety of conceptual models also reflects the diversity of karst systems.

The epikarstic zone is "the uppermost zone of exposed karstified rocks, in which permeability due to fissuring and diffuse karstification is substantially greater as compared to the underlying

1. *International Glossary of Hydrology [UNESCO, 1992]*

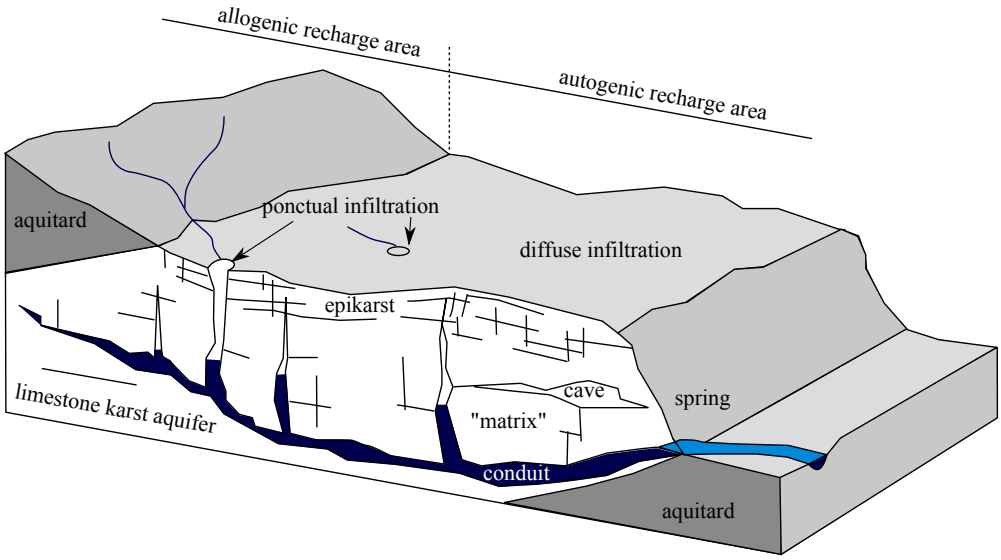

Figure 1.1: Schematic illustration of a heterogeneous karst aquifer system characterised by a duality of recharge (allogenic vs. autogenic), infiltration (point vs. diffuse) and porosity/flow (conduits vs. matrix). After Goldscheider and Drew, 2007.

main vadose zone“ [2]. The thickness of the epikarst depends on the lithology and geomorphological history of the rock [Klimchouk, 2004]. The overall epikarst porosity may reach 10 to 30 percent [Williams, 2008]. These values may vary widely depending on the rock type, climate and other environmental factors. This high porosity is the result of rock decompression and biochemical processes [Williams, 2008]. As the efficiency of these processes diminishes with depth, the hydraulic conductivity also decreases with depth [Perrin, 2003]: epikarst porosity is thought to be at least one order of magnitude higher than that of the underlying infiltration zone [Klimchouk, 2004; Williams, 2008]. Based on [Perrin, 2003] and [Williams, 2008], the hydrodynamic behaviour of the epikarst may be summarised as follows:

- the epikarst is fed by diffuse infiltration (that may be influenced by the soil and vegetation characteristics),
- epikarst drainage is controlled by the vertical hydraulic conductivity of the underlying vadose zone. In most cases, the vadose zone has a low bulk permeability and most of the drainage occurs through vertical high-transmissivity features (fractures, faults, karst conduits). The low permeability of the vadose zone combined with the irregular pattern of the vertical conduits may result in water storage within the epikarst system. The resulting perched epikarst aquifer can be permanent enough to sustain aquatic biota [Williams, 2008]. Fields studies showed that water storage in the epikarst could amount to close to half the total water stored in the karst aquifer [Smart and Friederich, 1986].High fracture density and good interconnection of openings within the vadose zone may also result in a rapid draining of the epikarst [Petrella et al., 2007; Williams, 2008].

The epikarst separates the infiltrated water flow into base flow and quick flow. When the infiltration rate exceeds a certain threshold, part of the water may by-pass the epikarst sub-system [Aquilina et al., 2006; Perrin et al., 2003*b*]. The non-linearity of the percolation response is evidenced by field observations (sprinkling experiments above cave systems [Puech and Jeannin, 1997], cited by [Perrin, 2003]) and isotopic data analysis [Perrin et al., 2003*b*]. The pulses of percolation through the vadose zone during storm events result in a pulse in pressure that stimulates the transfer of water (pulse-through or piston effect) [Williams, 2008].

2. Glossary of Karst and Caves terms (http://network.speleogenesis.info/directory/glossary/).

Flow within the saturated zone splits between diffuse and concentrated flow. Concentrated, fast (frequently $> 100\,\mathrm{m\,h^{-1}}$ [Goldscheider et al., 2008]) and often turbulent flow occurs within the karst conduit network, that acts as a drainage pipe network. Diffuse, slow water flow occurs within the fissured-porous matrix. Storage conditions within the saturated zone have not met general consensus yet [Bakalowicz, 2005]. Groundwater storage within the conduits is often limited. Non-transmissive karstic voids connected to the conduits by high head loss zones ("annex drainage system") and the low-transmissivity porous and fractured rock matrix are considered as being the main saturated zone storage compartment. The relationship between the matrix (and annex drainage system) and the conduit compartments depends on the relative hydraulic head between both. The matrix (and annex drainage system) volumes are recharged by the flow in the karst conduit during flood events and high water level periods, whereas during low water periods an inverse hydraulic head gradient causes the drainage of the matrix volumes by the karst conduits. Numerical modelling [Kiraly, 1998] indicates that water storage within the epikarst layer acts as a "Faraday cage" with respect to water storage within the low permeability volumes. Indeed, in concentrating infiltration, the epikarst layer reduces the recharge of the low permeability volumes by diffuse infiltration through the unsaturated zone.

1.1.3 Methods for the study of karst aquifers

The above-mentionned karst specificities imply that the tools classically used for the study of porous aquifers may turn out to be inadequate for the study of karst aquifers. This section briefly reviews some of the tools used for the hydrogeological investigation of karst aquifer systems. The different methods are complementary rather than competitive. Note that the response recorded at the karst springs (outlet of the karst drainage network) is deemed especially informative, because it is assumed to integrate the processes occuring in the whole aquifer.

Interpretation of piezometric data. A consequence of the drastic permeability contrasts observed within the karstic reservoirs is the very high spatial variability of the hydraulic potential. As a whole, during low water periods the hydraulic head is higher in low permeability volumes than in the karst network. The difference in the potentials between the core of low permeability volumes and the karst network may reach tens of meters [Jeannin, 1996]. As a borehole may intersect volumes of diverse permeabilities, the water level measured in an uncased borehole may be very difficult to interpret. As a consequence, groundwater flow direction and velocity determination based on piezometric maps should be considered with caution [Jeannin, 1996]. Hydraulic head measurements from a large number of wells are required to perform any interpolation [Goldscheider and Drew, 2007] and should be completed with hydraulic conductivities indications [Kiraly, 1998].

Pumping test analysis. In addition to an estimation of the hydrodynamic properties of the matrix and conduits reservoirs, pumping tests may settle the uncertainty as to the connectivity between boreholes, or between a borehole and a spring. However, the interpretation of pumping tests in fractured or karstic aquifers is a challenging task because of the intricate responses of high and low permeability volumes. The degree of karstification partly conditions the choice of the methods used for the interpretation. Tests performed within poorly developed karst systems may be interpreded using the uniform porous continuum hypothesis. Most tests performed in mixed flow karst systems may be interpreted based on the approaches developed for fractured aquifers (e.g. fractal single-medium approach [Audouin and Bodin, 2008; Barker, 1988; Delay et al., 2004; Lods and Gouze, 2008] or dual-medium approach [Bai et al., 1993; Barenblatt et al., 1960; Delay et al., 2007; Kaczmaryk and Delay, 2007; Warren and Root, 1963]). Specific tools have also been proposed for the case when the pumping well intersects the drainage system [Maréchal et al., 2008].

The hydrodynamic response to a pumping test at the local or regional scale strongly depends on the boreholes connectivity to the main flow-path network (up to three orders of magnitude at local scale), as evidenced by [Jazayeri Noushabadi et al., 2011; Jazayeri Noushabadi, 2009]. Moreover, there may be no direct relationship between the hydrodynamic responses obtained at the local and the regional scales for a given borehole. Lastly, as the water table level variations may induce a change in the borehole connectivity to the main flow-path network, pumping tests performed at distinct periods of the year may yield very different results [Jazayeri Noushabadi et al., 2011; Jazayeri Noushabadi, 2009].

Geophysical surveys. Geophysical monitoring provides non-invasive insights into physical properties such as lithology, porosity and the water content. Geophysical techniques have also been successfully applied to the localization of structural features and to a lesser extent to the localization of karst conduits (e.g. [Alfares et al., 2002; Jazayeri Noushabadi, 2009; Quinn et al., 2006; Stevanovic and Dragisic, 1998], see [Chalikakis et al., 2011] for a review). However, these methods are still restricted to the study of near-surface features at a local scale and they require extensive field work.

Geomorphological analysis of karst networks and karst infillings. The geomorphological analysis of karst networks and karst infillings may allow the reconstruction of the surrection, karstification and erosion history at regional scale [Camus, 2003].

Natural and artificial tracer experiments. Artificial tracer tests are originally intended to investigate the relationship between sinkholes and karst springs, and to determine the catchment area of karst springs [Käss, 1998]. These tests may also inform on the conduit network structure [Perrin and Luetscher, 2008; Smart and Friederich, 1986] as well as on reactive transport parameters [Geyer et al., 2007]. The natural tracing approach consists in the analysis of the temporal variations observed in groundwater chemistry (including: physicochemical parameters, isotopic data, bacteriologic concentrations...). While artificial tracer tests perform best in the characterisation of the conduit-dominated karst aquifers, natural tracers also collect informations on low-permeability volumes. Advanced interpretation techniques of natural tracers yield informations on e.g. the storage and transit times within the aquifer subsystems, the relative contributions of the different subsystems to the spring flow, and the interactions between surface water and ground water [Musgrove et al., 2010; Wu et al., 2004].

Systemic / functional analysis. The purpose of the systemic analysis approach [Mangin, 1984] is to infer the structure of the karst system based on its functioning, by means of signal processing or statistical methods. The karst aquifer is considered as a black box system that transforms an input signal (e.g. rainfall) into an output signal (e.g. spring discharge). Note that the systemic approach may be applied to hydrodynamic, hydrothermical or chemical signals. In particular, correlation and spectral analyses are used to characterize the system inertia (regulation time) [Mangin, 1975], water storage or release processes [Mangin, 1975] and karst-river interactions [Bailly-Comte et al., 2008]. Cross-correlations between the discharge rates of neighbouring springs may indicate whether these springs belong to the same hydrological system. Sorted spring discharges analysis provides information on the existence of overflow springs [Marsaud, 1996; Novel et al., 2007].

Mathematical modelling. Mathematical models are abstract and inherently simplified representations, in a mathematical formalism, of chosen aspects of the reality. Models are intrinsically

limited by the representation (understanding) of reality they are based upon. Models are also powerful tools that may be used to improve the knowledge about the functioning of a given system.

The numerical modelling of karst aquifers is particularly challenging. Indeed, porous and fractured aquifers show statistical homogeneity of their physical and hydraulic characteristics on a scale ranging from tens to several hundred of meters. The aquifer geometry and the local hydraulic properties can be defined based on geological data and pumping tests respectively. Local data can then be generalized to the whole aquifer through regionalizing techniques [Monnin and Bakalowicz, 2003]. By constrast, karst systems are capable of self-development and self-organization [Klimchouk et al., 2000]. The "support scale" (as defined by Neuman, 2005) and the REV (Representative Elementary Volume [Bear, 1972]) concepts are no longer appropriate as the flow parameters vary with the scale of observation [Neuman, 2005].

Moreover, the characterics of the conduit network are usually unknown to a large extent. Pumping tests performed close to a karst conduit allow the determination of the conduit hydrodynamic properties but no general method exists for locating the main karst conduits.

Last, karst systems are likely to have a turbulent flow component, which means that the linear Darcy's relationship between the hydraulic head gradient and the flow velocity may not be valid anymore.

1.2 Karst aquifer modelling

The present section focuses on the modelling approach. Models are commonly classified into three main groups based on the amount of physics they incorporate: black-box, conceptual and physically-based [Wheater et al., 1993].

1.2.1 Black-box approaches

Black-box models are empirical models based on the analysis of input and output time series and developed without any consideration of the physical processes at stake nor of the system geometry [Abbott and Refsgaard, 1996]. Linear [Debieche et al., 2002; Labat et al., 1999; Long and Derickson, 1999] and non-linear [Denic-Jukic and Jukic, 2003; Labat et al., 1999] transfer functions and artificial neural network models [Hu et al., 2008; Kong A Siou et al., 2011; Kurtulus and Razack, 2007] belong to the black-box category and have been successfully applied to karst spring discharge modelling. The major limitation of the black-box approach lies in the weakness of physical concepts which implies a lack of predictive power with respect to a modification of the system (climate change or anthropic sollicitation), or to the prediction of extreme events that are not represented in the input series used for model calibration.

1.2.2 Global, conceptual approaches

Global conceptual models are based on physically sound structures and equations that are selected by the modeler as being representative of the main processes at stake, together with semi-empirical ones [Abbott and Refsgaard, 1996]. The structure of conceptual models is a trade-off between adaptability (the model must be able to represent a large variety of hydrological conditions) and parsimony (parameters must be identificable and over-fitting must be prevented) [Perrin et al., 2001]. Because they are based on physically sound structures, conceptual models may offer some insights on the internal behaviour of the system modeled. However, due to the global scale approximation, providing a physical interpretation of the model parameters may prove difficult.

Conceptual models perform well in the prediction of time-series data (provided that the system structure does not change). In particular, conceptual reservoir models have been applied to predict

the rainfall-discharge relationship of karst aquifers in a variety of studies [Bailly-Comte, 2008; Barrett and Charbeneau, 1997; Fleury et al., 2007; Halihan and Wicks, 1998; Le Moine et al., 2008; Tritz et al., 2011], including the Lez aquifer system [Fleury et al., 2009]. The heterogeneity of the karst aquifer is ususally accounted for by the use of distinct reservoirs with different characteristics, each of which stands for a distinct karst sub-system. Changes in the epikarst connectivity with time may be taken into account through the use of an hysteretic function in the shallow reservoir [Tritz et al., 2011]. These models may also account for the activation of temporary outlets [Jukic and Denic-Jukic, 2009; Tritz et al., 2011] and for groundwater-surface water interactions [Bailly-Comte, 2008].

1.2.3 Distributed, physically-based approaches

Distributed, physically-based models try to represent the hydrologic processes based on the fundamental laws of physics (mass, momentum and energy conservation) [Makropoulos et al., 2008]. Such models have important applications to the interpretation and prediction of the effects of a change in the model characteristics, whether it be from anthropic origin or not. As they are distributed, they also offer insights in the internal model behaviour and may allow for spatial flow field assessment.

The main limitation associated with physically-based approach is due to the fact that such models require a good knowledge of the system geometry, which may prove especially problematic in the case of karst aquifers. Setting up a physically-based model also require to make the right assumptions on the nature of the main processes and law of flow at the scale considered. It must also be noted that even "physically-based" models involve a high degree of conceptualisation.

The development of distributed models involves challenges related to the validation of the parameters. Indeed, most parameter values cannot be assessed from direct measurements because the scales involved in field measurement and in the modelling processes are not the same. Depending on the set of observations available, there may be no way to find a unique solution to the calibration problem: most often, several sets of parameters may lead to the same fit. This equifinality [Beven, 1993] issue is not restricted to distributed, physically-based models yet distributed models are especially prone to it because of the large number of parameters involved.

The next section briefly presents the major conceptual approaches for distributed flow modelling in karst aquifers. The choice of the approach depends in particular on the model aims, as well as on the balance between the scale length of the flow domain and the dominating flow type (channelled or diffuse) [Sauter, 1992] (see Figure 1.2).

1.2.3.a Single and dual porosity models

The **single porosity equivalent porous medium** approach is based on the assumption that at the scale relevant to the hydrogeologic analysis, flow and transport do not have to be described individually at the fracture or conduit scale and that they could instead be lumped into effective model parameters. Flow within the fractures and conduits is thus approximated as Darcian and the karst conduits are modeled as high-permeability areas (smeared conduit approach). Such a treatment is often acceptable for the simulation of flow within moderately [Scanlon et al., 2003; Teutsch and Sauter, 1997] karstified aquifers. The parameters fields may be inferred based on the system knowledge (deterministic approach) or they may be treated as a correlated random function of space (stochastic-continuum approach). Because single-continuum models have limited potential for representing heterogeneities such as the karstic conduits, Teutsch and Sauter, 1997 suggest that the continuum approach may be appropriate to deal with water budget issues but not to simulate hydraulic responses of karst aquifers to recharge events. However, the deterministic approach has

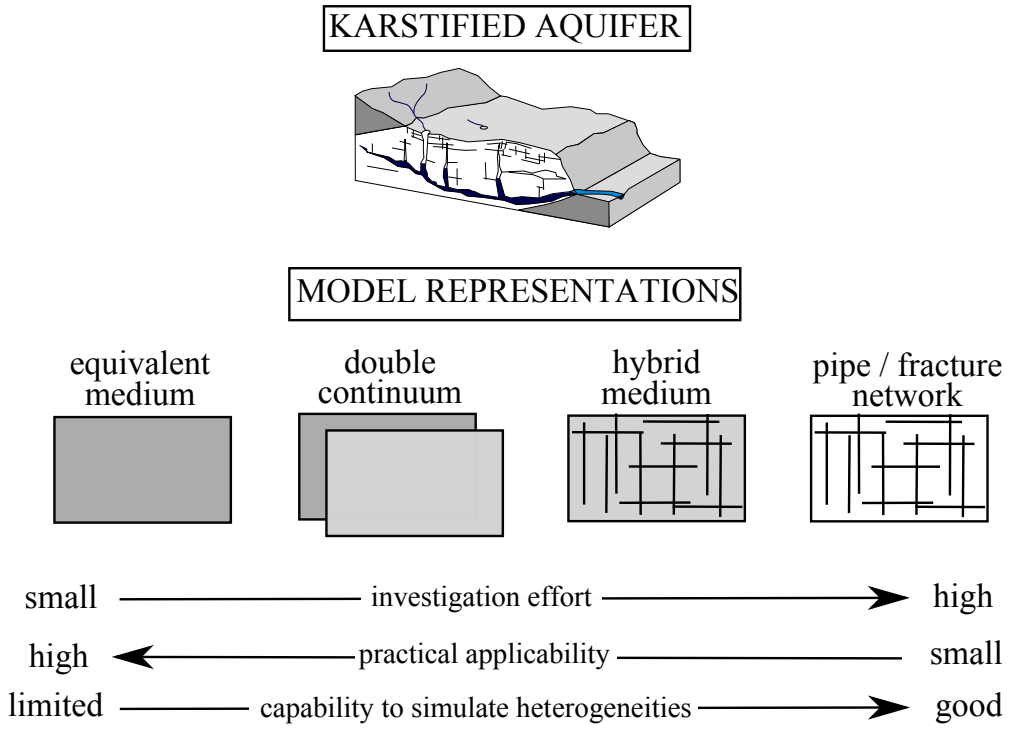

Figure 1.2: Schematic classification of distributive methods applied to modelling karst hydrodynamics. Adapted after Sauter, 1992.

been reported to succeed reasonably well in reproducing spring flow rates at the regional scale [Angelini and Dragoni, 1997; Gonzalez-Herrera et al., 2002; Larocque et al., 1999; Scanlon et al., 2003].

The **dual continuum approach** [Barenblatt et al., 1960; Warren and Root, 1963] represents both the conduit and the matrix systems as distinct yet hydrologically connected continua. One continuum has low conductivity and high storativity, and stands for the diffuse system. The other continuum has opposite characteristics (high conductivity, low storativity) and stands for the conduit system. Flow within both continua is assumed to be laminar. Exchange flow between the two continua is typically controlled by the local difference in potentials and by a lumped parameter which relates to the fractured rock geometry and its hydraulic properties [Cornaton and Perrochet, 2002]. The double continuum approach yields an improved representation of the karst heterogenity without requiring detailed geometrical information on the fracture/conduit system [Teutsch and Sauter, 1991]. It also account for the karst/matrix interaction (low permeability volumes recharge during flood events and quantification of base flow...). Double continuum models have been used successfully to simulate spring discharge, groundwater level fluctuations and tracer breakthrough curves on a regional scale [Najib, 2007; Sauter, 1992; Teutsch, 1993]. Note that the traditional dual approach is based on the main assumption of an uniform distribution of the fracture (conduit) network pattern [Jazayeri Noushabadi, 2009], which makes it relevant at scales smaller than the aquifer scale. Multiple continuum approaches have been proposed by e.g. Bai et al., 1993.

1.2.3.b Discrete features models

Discrete features models (discrete fracture and pipe network models) reduce the karst aquifer system to the only fracture and conduit network. In this approach, the geometry and the hydraulic properties of the fractures and conduits must be specified in either a deterministic [Jeannin, 2001; Peterson and Wicks, 2006; Thraikill, 1974] or a stochastic [Josnin et al., 2002; Jourde, 1998; Jourde

et al., 2002] framework, or a mix of both. The deterministic approach (pipe network model) relies on the assumption that only a small fraction of the karst and fracture network has an impact on the flow path structure (that fraction depends on the scale considered). Based on this assumption, the modelling process focuses on the karst conduit or the fracture intersections that govern the flow path at the scale considered [Jourde et al., 2002; Mohrlok and Sauter, 1997]. In contrast, the stochastic approach (discrete fracture model) is based upon the assumption that the flow field is governed by the statistical properties of the fracture and conduits network (length, connectivity ...). Plausible karst networks may also be generated by the modelling of the karst aquifer genesis [Jaquet et al., 2004]. Both the discrete and the statistical characterisation of the fracture and conduit network require a good knowledge of the site geometry. Such a detailed description of the fracture and conduit geometries and hydraulic properties is only possible at a local scale on well-instrumented sites [Jeannin, 1996, 2001; Josnin et al., 2002].

Flow within the conduits may be described either by the Darcy law or taking into account turbulent head losses by using e.g. the empirical Darcy-Weisbach equation [Thrailkill, 1968], the Louis model [Jeannin, 2001], or an approximation of the Saint-Venant equations [Diersch, 1998*a*].

1.2.3.c Hybrid models

Hybrid models couple a slow, laminar flow component which is related to the fractured porous matrix with a rapid, often turbulent flow component that occurs within the karst conduits. The karst system is modeled as a 1-D (one-dimensional) or 2-D (two-dimensional) discrete pipe network, which is embedded within the 3-D (three-dimensional) matrix continuum. The coupling of the conduit and the matrix systems may be established by assuming continuous heads [Kiraly et al., 1995] or by considering an exchange flow [Clemens et al., 1999]. Hybrid models may take into account variably saturated conditions within the conduit system (free surface flows and pressurized conduit flow) [Reimann et al., 2011; Rooij, 2008] and within the matrix [Rooij, 2008].

1.2.4 Short conclusion

Each model family has his own strenghts and limitations. The nature of the model must be adapted to its intended purposes. In many practical cases, simple models may perform better than complex ones, whithin their range of applicability. In any case, it is important that a clear statement of the assumptions and their implications be made [Risbey et al., 1996]. Some authors advocate a multi-model approach [Makropoulos et al., 2008] for a more thorough understanding of complex systems. Sensitivity analysis and uncertainty analysis provide a means for a better understanding of both models behaviour and models results.

1.3 Sensitivity and uncertainty analysis

This section provides an introduction to the sensitivity and uncertainty analysis (Section 1.3.1). An overview of the main approaches used to perform the sensitivity and uncertainty analysis is given in Sections 1.3.2 to 1.3.4. Section 1.3.5 presents some related issues.

1.3.1 Introduction to sensitivity and uncertainty analysis

Models are not perfect. Indeed, models are abstract, approximate representations of reality. The discrepancy between models and reality is inevitable because of the errors that are made at all stages of the modelling process [Beven and Freer, 2001; Hall, 2003]:

- Errors in the conceptual model structure. As models are simplified views of the reality, no model can be considered as being an entirely true image of the "real world" physical processes.

The modeller task is to work out which physical processes are dominant at the model scale, and to take them into account in a correct way. For example, the scale of the geological discontinuities to be considered in a groundwater flow model depends on the model scale.

- Errors in the input data. These errors may arise from the spatial and temporal variability of the environmental variables, from sampling procedures (observational data are not error-free) or sampling analysis [Dubus et al., 2003] (e.g. spatial and temporal errors in rainfall sampling).
- Errors in the parameters estimation. Because the measurement and the modelling scales are usually not the same, the parameters of hydrogeological models can often not be measured. As a consequence, most parameter values have to be calibrated. Errors in the parameters estimation may stem from error in the calibration process. Errors in the input data may also pass on the calibrated parameters values. Lastly, the objective function used for calibration also influes on the resulting parameter set.
- Errors in the numerical solution of the model equations. Numerical approximations in code (discretization errors, computer round-off errors) lead to errors in the model solution [Dubus et al., 2003]. The magnitude of the error depends on the temporal and spatial resolution of the model setup, on the relative differences in size of adjacent spatial cells or time steps, and on the resolution scheme [Kavetski et al., 2006*a*].

Sensitivity, uncertainty and related concepts.

Difference between uncertainty and sensitivity. Sensitivity and uncertainty analyses are closely related: sensitivity analysis is "the study of how the variation in the output of a model (numerical or otherwise) can be apportioned, qualitatively or quantitatively, to different sources of variation" [Saltelli et al., 2000]. Uncertainty analysis is "the practice of determining the reliability of model outputs by addressing potential sources of uncertainty, including uncertainty associated model structure, forcing, parameters and observations" [Cacuci, 2003; He et al., 2010].

Difference between uncertainty and error. Uncertainty is a "potential deficiency in any phase or activity of modelling and simulation process that is due to a lack of knowledge", whereas error is defined as "a recognizable deficiency in any phase or activity of modelling and simulation that is not due to a lack of knowledge" [Oberkampf and Blottner, 1998].

Equifinality. In a broad sense, equifinality refers to the case "where different conditions lead to similar effects" [Beven, 2006; Beven and Binley, 1992; Ebel and Loague, 2006]. As regards hydrologic modelling, the equifinality concept refers to the fact that given the errors in e.g. input data knowledge, there are "many acceptable representations" of the modelled system, and that these alternative representations "should be considered in assessing the uncertainty associated with predictions". In other words, the equifinality concept traduces the fact that most environmental problems are ill-posed (issues about the unicity, identifiability and stability of the problems solution [Ebel and Loague, 2006]). Equifinality may stem from e.g. the use of a global performance measure for the calibration (reduction of the problem dimension), or from the compensation for the calibrated parameter values for different types of error [Beven, 2006]. A similar concept is that of ambiguity, which has been proposed to denote models "for which predictions made with different stochastic realisations of the input data cannot be distinguished statistically" [Beven, 2006; Zin, 2002].

Sensitivity and uncertainty: what for ? Sensitivity and uncertainty analyses aim at understanding and quantifying the changes in a models outputs that would result from a change in the

model inputs. The scope of these analyses includes all stages of the modelling process [McCuen, 1973]:

- model development through a better understanding of the model behaviour,
- quantification of the uncertainty in model prediction,
- leads for the reduction of the uncertainty,
- definition or selection of the objective function,
- leads for data collection.

1.3.2 Local v.s. global methods

Both qualitative and quantitative methods may be used for sensitivity analysis. Qualitative methods aim at screening the most influential factors within a system with many non-influential ones and will not be described here. Quantitative methods may be categorized according to several criteria [Campolongo et al., 2007; Frey and Patil, 2002; Zin, 2002]. In what follows, we adopt the classification into local and global analysis.

Local analyses examine the model behaviour in the vicinity of a central value, based on a linear approximation of the model dynamics in the vicinity of this central (nominal) value. The main shortcomings of the local approach are related to the first-order approximation. As for non-linear models, the range of validity of local analyses is restricted to "small" changes in the values of the parameters, the meaning of "small" being dependent upon the degree of non-linearity of the model and possibly the nominal value used for the analysis. Local analyses may therefore only adress a small portion of the possible space of input values and they do not give insights into to the equifinality problem.

These shortcomings may be partially overcome. For example:

- second-order derivatives may be included in the analysis to increase the accuracy of the local sensitivity and uncertainty estimates [e.g. Maskey and Guinot, 2003],
- specific procedures may be implemented for the sensitivity calculation in the case of models with discontinous solutions [Bao and Kuo, 1995; Guinot et al., 2007; Zou et al., 1993],
- model implementation may be selected to avoid numerical artefacts due to model thresholds and poorly selected time stepping schemes [Kavetski et al., 2006*a*,*b*; Kitanidis and Bras, 1980].

Global analyses characterize the model behaviour (averaged over the variation of all the parameters) over a finite region in the parameter space. Most global sensitivity methods are based on Monte-Carlo sampling. Both the parameters and the output variables are considered as random variables. The sensitivity analysis is based on a sampling exploration of the input space. The distribution of the output variables is used as a measure of the uncertainty. Global analyses may therefore adress the effect of orders-of-magnitude parameter changes. They are also well suited to the analysis of interactions between the parameters, and to that of equifinality. The global framekwork also allows the study of the model structure uncertainty.

The main drawback of the global analysis is its computational cost, which may turn out to be prohibitive for distributed models. Efficient sampling schemes may lessen the computational cost. Global procedures are not error-free either. The analysis results may be influenced by the discretization of the input sample: choice of the probability distribution functions attributed to the input parameters [Brattin et al., 1996], sampling scheme, absence or presence of correlation between the variables [Dubus and Brown, 2003; Saltelli et al., 2000]. Error estimates may be difficult to obtain [Yeong-Weisse, 2009]. Last, the high computational cost of the global methods implies that most sensitivity and uncertainty measures are integrated over the whole simulation period, which

means that the very informative temporal dynamics of the sensitivity and uncertainty measures is missed. This last limit may be partially overcome by performing the global procedure over a sliding temporal window [e.g. Wagener et al., 2003].

Complementarity of the local and global approaches. The classification into local and global methods is convenient yet the limits between both may be blurred. Indeed, global and local methods may favourably be combined:

- local techniques may be used as a screeening analysis to identify the most important inputs to propagate through a model in a probabilistic framework [Cullen and Frey, 1999],
- global analysis may be used to spot the critical points of functioning of the system, before performing local analyses on these points [Cacuci, 1990],
- local sensitivity derivatives may be used to improve the efficiency of a Monte-Carlo sampling technique (variance reduction technique) [Cao et al., 2006],
- local sensitivity derivatives may be used to improve the efficiency of the stochastic response model method [Isukapalli et al., 2000],
- local sensitivity derivatives may be used to improve the efficiency of global, variance-based methods [Kucherenko et al., 2009; Sobol and Kucherenko, 2009].

1.3.3 Local analysis

This section presents the most widely used local sensitivity and uncertainty measures and the associated methods.

1.3.3.a Local sensitivity and uncertainty measures

Let f be a model defined by

$$f : \begin{cases} \mathbb{R}^p & \longrightarrow \mathbb{R}^n \\ \mathbf{X} & \longrightarrow \mathbf{Y} = f(\mathbf{X}) \end{cases} \tag{1.1}$$

where $\mathbf{X}$ is the vector of the p model input variables and $\mathbf{Y}$ is the vector of the n model output variables.

Sensitivity measures. The effect of a parameter change $\Delta\mathbf{X}$ around the nominal value $\mathbf{X_0}$ over the model response $\mathbf{Y}$ may be expressed by a Taylor series expansion as

$$\mathbf{Y}(\mathbf{X_0}+\Delta\mathbf{X}) = \mathbf{Y}(\mathbf{X_0}) + \sum_j \frac{\partial Y_i}{\partial X_j}\Delta X_j + \frac{1}{2}\sum_j\sum_k \frac{\partial^2 Y_i}{\partial X_j \partial X_k}\Delta X_j \Delta X_k + \dots \tag{1.2}$$

The first-order sensitivity s_{ij} of the variable Y_i to the parameter X_j is defined as

$$s_{ij} = \partial Y_i / \partial X_j \tag{1.3}$$

The sensitivity matrix $[s_{ij}]$ is a first-order approximation of the dependence of the solution on parameter changes. Similarly, the second-order sensitivity s'_{ij} of the variable Y_i to the parameters X_j and X_k is defined as

$$s'_{ijk} = \partial^2 Y_i / \partial X_j \partial X_k \tag{1.4}$$

The second-order sensitivity matrix account for the effects of local interactions among the variables.

Uncertainty measures. The variance of an output variable may be estimated based on the variance of the parameters and on the first-order sensitivity of the output variable [Dettinger and Wilson, 1981]. The variance (second moment) of the variable Y_i is approximated to the first order by

$$\mathrm{var}(Y_i) \simeq \sum_{j=1}^{p} \frac{\partial f}{\partial X_j} \mathrm{var}(X_j) + 2 \sum_{j=1}^{p} \sum_{k=1}^{p-1} \frac{\partial Y_i}{\partial X_j} \frac{\partial Y_i}{\partial X_k} \mathrm{cov}(X_j, X_k) \tag{1.5a}$$

$$\simeq \sum_{j=1}^{p} s_{ij} \mathrm{var}(X_j) + 2 \sum_{j=1}^{p} \sum_{k=1}^{p-1} s_{ij} s_{ik} \mathrm{cov}(X_j, X_k) \tag{1.5b}$$

where $\mathrm{var}(Y_i)$ is the total variance of the output variable Y_i, $\mathrm{var}(X_i)$ is the variance of the input variable X_i and $\mathrm{cov}(X_j, X_k)$ is the covariance between the input variables X_j and X_k. The term $s_{ij}\mathrm{var}(X_j)$ represents the contribution of the variances of the input variable X_j to the total variance of the output Y_i. The term $s_{ij}s_{ik}\mathrm{cov}(X_j, X_k)$ represents the contribution of the (possible) correlation between the input variables X_j and X_k to the total variance of the output Y_i. Note that equation (1.5b) does not require an exact formulation of the input probability distribution function. For non-correlated input variables, equation (1.5b) reduces to

$$\mathrm{var}(Y_i) \simeq \sum_{j=1}^{p} s_{ij} \mathrm{var}(X_j) \tag{1.6}$$

1.3.3.b Numerical Methods

Numerical methods do not require neither knowledge of the model equations, nor any additional computer code writing. However, their computational cost is heavy.

The empirical method. The empirical method consists in approximating the sensitivity coefficients by the finite difference of the perturbed solution:

$$\frac{\partial Y_i}{\partial X_j} \approx \frac{Y_i(X_j + \delta X_j) - Y_i(X_j)}{\delta X_j} \quad \text{(upstream scheme)} \tag{1.7a}$$

$$\frac{\partial Y_i}{\partial X_j} \approx \frac{Y_i(X_j) - Y_i(X_j - \delta X_j)}{\delta X_j} \quad \text{(downstream scheme)} \tag{1.7b}$$

$$\frac{\partial Y_i}{\partial X_j} \approx \frac{Y_i(X_j + \delta X_j) - Y_i(X_j - \delta X_j)}{2\delta X_j} \quad \text{(centred scheme)} \tag{1.7c}$$

The offset difference schemes are first-order accurate whereas the central difference scheme is theoretically second-order accurate. The actual accuracy of the method depends on the perturbation size:

- substractive cancellation errors rise due to the finite precision of the numerical solution (round-off errors), which means that the perturbation size should not be too small,
- perturbations tending to zero may result in infinite empirical sensitivities if the model solution is discontinuous. Note that specific approaches can be used to tackle the problem of direct sensitivity calculation across shocks [Guinot et al., 2008].

The optimal perturbation size is a trade-off between the above-mentionned constraints. As the optimal perturbation size depends on both the parameter and variable investigated, the finite difference approach may require significant tuning of the perturbation factors [Pauw, 2003]. Denote by p the number of parameters involved in the sensitivity analysis. Computing the sensitivity for n variables requires $p+1$ model runs for offset schemes and $2p$ model runs for the centred scheme.

The complex differentiation method The complex differentiation method [Lyness and Moler, 1967] is based on a first-order expansion of the analytic output function f using a complex parameter perturbation ih:

$$f(X+ih) = f(X) + ih\frac{\partial f}{\partial X} - \frac{h^2}{2!}\frac{\partial^2 f}{\partial X^2} - \frac{ih^3}{3!}\frac{\partial^3 f}{\partial X^3} + \dots \tag{1.8}$$

Setting aside the imaginary part of equation (1.8) leads to

$$Im\left[f(X+ih)\right] \approx ih\frac{\partial f}{\partial X} - \frac{ih^3}{3!}\frac{\partial^3 f}{\partial X^3} + \dots \tag{1.9}$$

For infinitesimal perturbations, the sensitivity may therefore be approximated by

$$\frac{\partial f}{\partial X} \approx \frac{Im[f(X+ih)]}{h} + O(h^2) \tag{1.10}$$

In other words, if a complex perturbation is applied to the parameter of interest, then the sensitivity of a model variable to this parameter can be obtained by evaluating the imaginary part of the computed complex variable. Since no subtraction of terms is involved in the sensitivity calculation, the method allows true second-order accuracy to be achieved [Perez et al., 2008].

Computing the sensitivities to p parameters requires p model runs. Computational costs are increased by the complex formulation to up to three times the cost of the original solver [Perez et al., 2008].

1.3.3.c Semi-analytical methods

Semi-analytical methods are cost-effective. However, they require knowledge of the model equations and additional code writing.

Starting point. The first-order approximation of a model f takes the form

$$\begin{cases} \dot{\mathbf{Y}} = g(\mathbf{Y}, \mathbf{X}, t) \\ \mathbf{Y}(t_0) = \mathbf{Y_0} \end{cases} \tag{1.11}$$

where $\mathbf{Y}$ is the vector of output variables, $\mathbf{X}$ is the vector of input variables and $\mathbf{Y_0}$ is the value of $\mathbf{Y}$ at time $t = t_0$. Differentiating equation (1.11) with respect to the vector of parameters $\mathbf{X}$ leads to

$$\begin{cases} \dot{\mathbf{S}} = \mathbf{J}.\mathbf{S} + \mathbf{F} \\ \mathbf{S}(t_0) = \mathbf{S_0} \end{cases} \tag{1.12}$$

where $\mathbf{S}$ is the sensitivity matrix, $\dot{\mathbf{S}}$ is the first-order approximation of $\mathbf{S}$ and $\mathbf{J}$ and $\mathbf{F}$ are termed the jacobian matrix and the parametric jacobian matrix respectively. $\mathbf{S}$, $\mathbf{J}$ and $\mathbf{F}$ are defined as

$$\mathbf{J} = \frac{\partial g}{\partial \mathbf{Y}} = \begin{bmatrix} \partial g_1/\partial Y_1 & \cdots & \partial g_1/\partial Y_p \\ \vdots & \ddots & \vdots \\ \partial g_n/\partial Y_1 & \cdots & \partial g_n/\partial Y_p \end{bmatrix} \tag{1.13a}$$

$$\mathbf{F} = \frac{\partial g}{\partial \mathbf{X}} = \begin{bmatrix} \partial g_1/\partial X_1 & \cdots & \partial g_1/\partial X_p \\ \vdots & \ddots & \vdots \\ \partial g_n/\partial X_1 & \cdots & \partial g_n/\partial X_p \end{bmatrix} \tag{1.13b}$$

$$\mathbf{S} = \frac{\partial \mathbf{Y}}{\partial \mathbf{X}} = \begin{bmatrix} \partial Y_1/\partial X_1 & \cdots & \partial Y_1/\partial X_p \\ \vdots & \ddots & \vdots \\ \partial Y_n/\partial X_1 & \cdots & \partial Y_n/\partial X_p \end{bmatrix} \tag{1.13c}$$

.

Continuous and discrete approaches to sensitivity computation. Semi-analytical methods are based on the numerical resolution of the sensitivity equation (1.12). The differentiation of the model equations and the discretization of the sensitivity equation are non-commutative operations. As a consequence, the sensitivity analysis may yield different results depending on whether the model equations are differentiated first, and then discretized (continuous approach) or discretized first, and then differentiated (discrete approach) [Castaings, 2007]. The sensitivities computed by the discrete approach are dependent on the numerical solution of the model equations. Consequently, it provides no theoretical insights into the general behaviour of the model. Instead, the sensitivity analysis must be repeated for any new situation [Guinot et al., 2007]. On the other hand, the continuous approach does provide general guidelines for the sensitivity behaviour. However, the perturbation approach may yield inaccurate sensitivity estimates when strongly nonlinear model equations are to be solved.

The direct / forward method consists in discretizing and solving the sensitivity equations (1.12) along with the model equations (1.11). Note that a different set of sensitivity equations must be solved in order to obtain the sensitivity to each parameter. As a consequence, the direct method is most efficient for the computation of the sensitivity of several output variables to one given parameter.

The adjoint / backward method [Sykes et al., 1985; Wilson and Metcalfe, 1985] allows the calculation of the sensitivity of a given cost function to the entire parameter set in one model run. The principle of the adjoint method is detailed hereafter. Let V be a cost function defined as

$$V = \int_{t_0}^{t_f} \Phi(t, \mathbf{X}, \mathbf{Y}) dt \tag{1.14}$$

The sensitivity of V with respect to the input variables $\mathbf{X}$ may be written as

$$\begin{aligned} \nabla_X V &= \left(\frac{\partial V}{\partial X_1} \cdots \frac{\partial V}{\partial X_n} \right) \\ &= \int_{t_0}^{t_f} \left(\frac{\partial \Phi}{\partial \mathbf{Y}} \frac{\partial \mathbf{Y}}{\partial \mathbf{X}} + \frac{\partial \Phi}{\partial \mathbf{X}} \right) dt \\ &= \int_{t_0}^{t_f} \left(\frac{\partial \Phi}{\partial \mathbf{Y}} \mathbf{S} + \frac{\partial \Phi}{\partial \mathbf{X}} \right) dt \end{aligned} \tag{1.15}$$

Define the Lagrange multiplier $\boldsymbol{\lambda}$ as $\boldsymbol{\lambda} = [\lambda_1 \cdots \lambda_n]^T$. Equation (1.12) implies that

$$\boldsymbol{\lambda}^T \left(\dot{\mathbf{S}} - \frac{\partial g}{\partial \mathbf{Y}} \mathbf{S} - \frac{\partial g}{\partial \mathbf{X}} \right) = 0 \tag{1.16}$$

Combining equations (1.16) and (1.16) leads to

$$\nabla_X V = \int_{t_0}^{t_f} \left(\frac{\partial \Phi}{\partial \mathbf{Y}} \mathbf{S} + \frac{\partial \Phi}{\partial \mathbf{X}} \right) dt + \int_{t_0}^{t_f} \boldsymbol{\lambda}^T \left(\dot{\mathbf{S}} - \frac{\partial g}{\partial \mathbf{Y}} \mathbf{S} - \frac{\partial g}{\partial \mathbf{X}} \right) dt \tag{1.17}$$

Rearranging equation (1.17) gives

$$\nabla_X V = \int_{t_0}^{t_f} \left(\boldsymbol{\lambda}^T \dot{\mathbf{S}} + \frac{\partial \Phi}{\partial \mathbf{Y}} \mathbf{S} - \boldsymbol{\lambda}^T \frac{\partial g}{\partial \mathbf{Y}} \mathbf{S} \right) dt + \int_{t_0}^{t_f} \left(\frac{\partial \Phi}{\partial \mathbf{X}} + \boldsymbol{\lambda}^T \frac{\partial g}{\partial \mathbf{X}} \right) dt \tag{1.18}$$

Define $\mathbf{P}$ as

$$\mathbf{P} \equiv \boldsymbol{\lambda}^T \dot{\mathbf{S}} + \frac{\partial \Phi}{\partial \mathbf{Y}} \mathbf{S} - \boldsymbol{\lambda}^T \frac{\partial g}{\partial \mathbf{Y}} \mathbf{S} \tag{1.19}$$

Then equation (1.18) becomes

$$\nabla_X V = \int_{t_0}^{t_f} \mathbf{P} dt + \int_{t_0}^{t_f} \left(\frac{\partial \Phi}{\partial \mathbf{X}} + \boldsymbol{\lambda}^T \frac{\partial g}{\partial \mathbf{X}} \right) dt \tag{1.20}$$

Note that $\boldsymbol{\lambda}$ may take any value. Let's take $\boldsymbol{\lambda}$ such that $\mathbf{P}$ be equal to zero. Then the sensitivity of the optimisation criterion is independent on the variable sensitivities. The problem therefore is to find the value of $\boldsymbol{\lambda}$ such that $\int_{t_0}^{t_f} \mathbf{P} dt$ be equal to zero. An integration by parts gives

$$\int_{t_0}^{t_f} \mathbf{P} dt = \int_{t_0}^{t_f} \left[\boldsymbol{\lambda}^T \dot{S} + \left(\frac{\partial \Phi}{\partial \mathbf{Y}} - \boldsymbol{\lambda}^T \frac{\partial g}{\partial \mathbf{Y}} \right) \mathbf{S} \right] dt \tag{1.21a}$$

$$= [\boldsymbol{\lambda}^T \mathbf{S}]_{t_0}^{t_f} \tag{1.21b}$$

provided that

$$\frac{\partial \boldsymbol{\lambda}^T}{\partial t} = \frac{\partial \Phi}{\partial \mathbf{Y}} - \boldsymbol{\lambda}^T \frac{\partial g}{\partial \mathbf{Y}} \tag{1.22}$$

Equation (1.22) is equivalent to

$$\dot{\boldsymbol{\lambda}}^T - \frac{\partial \Phi}{\partial \mathbf{Y}} - \boldsymbol{\lambda}^T \frac{\partial g}{\partial \mathbf{Y}} = 0 \tag{1.23a}$$

$$\dot{\boldsymbol{\lambda}} - \frac{\partial \Phi}{\partial \mathbf{Y}}^T - \frac{\partial g}{\partial \mathbf{Y}} \boldsymbol{\lambda} = 0 \tag{1.23b}$$

As a consequence, if $\boldsymbol{\lambda}$ verifies equation (1.23b) then

$$\int_{t_0}^{t_f} \mathbf{P} dt = [\boldsymbol{\lambda}^T \mathbf{S}]_{t_0}^{t_f} \tag{1.24a}$$

$$= (\boldsymbol{\lambda}^T \mathbf{S})(t_f) - (\boldsymbol{\lambda}^T \mathbf{S})(t_0) \tag{1.24b}$$

Remember that $\mathbf{S}(t_0) = 0$. Then the condition $\int_{t_0}^{t_f} \mathbf{P} dt = 0$ is verified if $\boldsymbol{\lambda}(t_f) = 0$. As a consequence, if $\boldsymbol{\lambda}$ verifies the adjoint equation

$$\lambda : \begin{cases} \dot{\boldsymbol{\lambda}} - \frac{\partial \Phi}{\partial \mathbf{Y}}^T - \frac{\partial g}{\partial \mathbf{Y}} \boldsymbol{\lambda} = 0 \\ \boldsymbol{\lambda}(t_f) = 0 \end{cases} \tag{1.25}$$

then the gradient of the objective function is given by

$$\nabla_X V = \int_{t_0}^{t_f} \left(\frac{\partial \Phi}{\partial \mathbf{X}} + \boldsymbol{\lambda}^T \frac{\partial g}{\partial \mathbf{X}} \right) dt \tag{1.26}$$

Note that the adjoint equation is independent on the parameter investigated. However, the calculation of $\nabla_X V$ requires the storage of the entire unsteady solution.

1.3.4 Global analysis

As a rule, global analyses are dedicated to uncertainty estimation rather than sensitivity estimation. The sensitivity measures are qualitative measures that are derived from the uncertainty analysis.

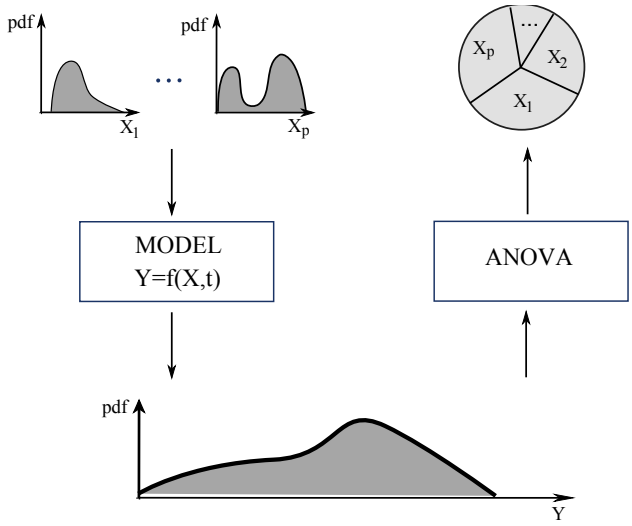

Figure 1.3: General scheme of ANOVA methods. The total variance of the output is apportioned to each of the inputs, as schematized by the pie diagram. Adapted from Saltelli et al., 1999. See discussion in Section 1.3.4.b.

1.3.4.a Reminder: Basic Monte-Carlo method

Monte-Carlo methods (particular cases of sampling-based methods) are probabilistic methods based on the sampling of the output variable space. The input variables are considered as random variables, whose probability distribution traduces the uncertainty in the estimation of the parameter. A probability distribution function is assigned to these input variables and a representative set of inputs is sampled randomly based on the distribution functions. Note that the probability distribution may take parameter correlation into account. The deterministic output of the model is computed for the set of sampled inputs. The model output uncertainty is described by statistics indicators (variance, moments...) which are computed based on the deterministic set of output.

The major drawback of the Monte-Carlo method is its computational cost, which may be prohibitive for fully distributed models. The convergence rate of the standard error is $1/\sqrt{n}$ where n is the number of model runs, and proportional to the variance σ of the parameter distribution. Computational efficiency may be gained through the use of efficient sampling scheme, in particular through variance reduction techniques (latin hypercube e.g.) or through the use of alternative sampling algorithms with higher convergence rate (Monte-Carlo Markov Chains (MCMC) - e.g. Metropolis algorithms [Kuczera and Parent, 1998]). Lower computational cost may also be achieved by running the analysis over a simplified version of the model, termed the response surface [Box and Wilson, 1951].

1.3.4.b Variance-based methods

ANOVA (ANalysis Of VAriance [Archer et al., 1997]) methods are used to determine which proportion of the output variability may be apportioned to each of the input variables (taken separately or in combination with one another - see Figure 1.3). The analysis is based on a variance decomposition of the uncertainty associated with the output variable Y (or with a performance measure) into conditional variance indices:

$$V(Y) = \sum_{i=1}^{n} V_i + \sum_{1 \le i \le j \le n}^{n} V_{i,j} + \cdots + V_{1,\cdots,n} \tag{1.27}$$

where $V(Y)$ is the total variance of the output variable and the conditional variances are defined as

$$V_i = \mathrm{Var}[E(Y|X_i)] \tag{1.28a}$$
$$V_{i,j} = \mathrm{Var}[E(Y|X_i, X_j)] - V_i - V_j \tag{1.28b}$$
$$\vdots \tag{1.28c}$$
$$V_{1,\cdots,n} = \mathrm{Var}[E(Y|X_1, \cdots, X_n)] - \sum_{i=1}^{n} V_i \tag{1.28d}$$

V_i is the expected amount by which the uncertainty over Y is to be reduced, knowing the error-free value of X_i. $V_{i,j}$ is the amount of variance of the output variable which is due to the uncertainty in the interaction between the input variables X_i and X_j.

The evaluation of the conditional variances typically involves Monte-Carlo techniques (Sobol's method [Sobol, 2001]) and/or spectral analysis (fast and extended FAST methods [Cukier et al., 1973; Cukier et al., 1978; Saltelli et al., 1999]).

Although ANOVA can theoretically capture 1st order (main effects from single parameters) to total order effects (i.e., all parameter impacts including all interactions), computational limitations limit its use to 1st and 2nd order interactions. The exact nature of the relationship is not determined by the ANOVA. The convergence of the Monte-Carlo integrations used in Sobol's method may be increased to $1/n$ if Sobol's quasi-random sequence is used [Tang et al., 2007].

Classical ANOVA method uses the F-test to determine "whether a significant difference exist among mean responses for main effects of interactions between factors. The relative magnitude of F values can be used to rank the factors in sensitivity analysis". In addition to the F-test, first-order sensitivity measures are defined as

$$S_i = \frac{V(E[Y|X_i])}{V} = \frac{V_i}{V(Y)} \tag{1.29}$$

where S_i is the fraction of V which is solely due to X_i. Similarly, higher-order sensitivities may be defined as

$$S_{1\ldots n} = \frac{V_{1\ldots n}}{V} \tag{1.30}$$

where $V_{1\ldots n}$ is the partial variance in the model output associated with simultaneous changes in parameters $1\ldots n$ and S_{ij} is the fraction of V which is due to the interaction between $X_1 \ldots$ to X_n.

1.3.4.c Informal Bayesian approaches

The Regionalized sensitivity analysis (RSA) (also termed the Hornberger-Spear-Young method or the generalized sensitivity analysis) [Hornberger and Spear, 1981; Spear and Hornberger, 1980] has been developped with the ambition to tackle the problem of equifinality of the parameters. Instead of selecting a unique parameter set during the calibration process, the RSA divides the parameters set into two groups according to the value of the resulting simulation performance. Parameter sets that yield satisfactory results form the "behavioural" set, as opposed to the complementary "non-behavioural" set. The sensitivity to a given parameter is estimated based on the distance between the probability distributions of the parameter for the behavioural and non-behavioural sets (e.g. F statistics, see Figure 1.5).

Note that in multi-objective frameworks the definition of the behavioural set is not unique. Classical definitions of the behavioural set include (see Figure 1.4):

- Pareto-optimality. A parameter set is Pareto-optimal (non-dominated solution) if no other parameter set is at least equal in all objectives and superior in at least one [Gupta et al., 1998].

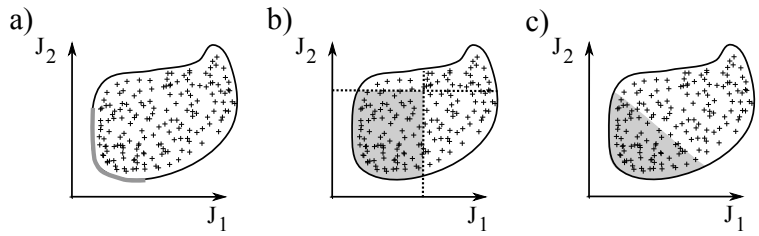

Figure 1.4: How to decide on behavioural simulations: selection of the a) Pareto optimal, b) threshold or c) weighted optimal parameter set. The selected (behavioural) parameter set is greyed out. See discussion in Section 1.3.4.c. After Wagener, 2004.

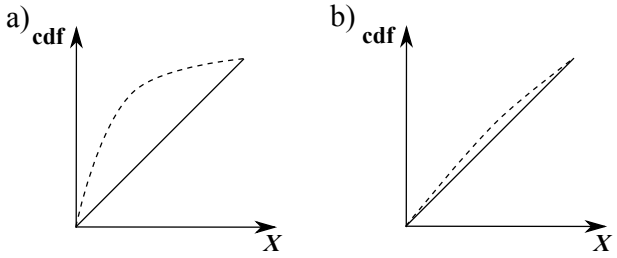

Figure 1.5: RSA method. Parameters deemed a) sensitive and b) insensitive. Dotted line: a posteriori cumulative distribution of the parameter X. Continuous line: a priori (uniform) cumulative distribution of the parameter X. Adapted after Zin, 2002. See discussion in Section 1.3.4.c.

- the thresholding approach. In that method the behavioural set is defined as the set of solutions such that the solution performance is superior to a threshold value with respect to all performance metrics.
- the weighted objective approach. That method aims at reducing the original, multi-objective problem to a scalarized one. An agregated objective function is defined as the linear combination of the set of objectives functions. The behavioural set is defined as the set of solutions such that the solution performance is higher than a given, threshold value on the agregated objective.

The Generalized Likelihood Uncertainty Estimation (GLUE) method [Beven and Binley, 1992] is based on the RSA with the difference that not all behavioural parameter sets are supposed equally acceptable. Instead, each parameter set is associated with a likelihood measure, which is derived based on the goodness-of-fit to the available observation data. The likelihood of non-behavioural parameter sets is set equal to zero. The predictions of the set of behavioural parameters are weighted based on their likelihood and the weighted cumulative distribution of the predicted variable over all behavioural sets is used for uncertainty analysis. The method allows updating of likelihood weights as new data become available. It also allows multiple model structures to be considered. The GLUE method is especially adapted to cope with model non-linearity. Parameters interactions are handled implicitely. What is more, the method is easy to understand and implement.

The RSA and the GLUE methods share the same weaknesses:

- the subjective nature of the criteria used for the selection of the behavioural and non-behavioural sets, of the distance measure used, and of the acceptability threshold. The acceptability threshold value may e.g. be chosen such that the uncertainty in the predicted variables matches that of the measured variables [Kumar et al., 2010],

– the computational efficiency. Efficient sampling schemes (such as variance reduction techniques) exist but they imply making hypotheses upon the a posteriori distribution (distribution conditioned by the observations) of the parameters. The computational efficiency of GLUE has been improved through the use of adaptive MCMC schemes [Blasone et al., 2008; Kuczera and Parent, 1998].

1.3.4.d Formal Bayesian approaches

The RSA and GLUE approaches use an informal likelihood measure to avoid over-conditioning. By contrast, formal Bayesian methods make strong assumptions about the nature of modelling errors [Zin, 2002]. The assumptions about the modelling errors allows the use of efficient algorithms for the estimation of the posterior probability density function of parameters. Markov chain schemes represent a general method for sampling from the posterior distribution. Unlike importance sampling, Markov chain sampling generates samples from a random walk which adapts to the true posterior distribution [Kuczera and Parent, 1998; Vrugt et al., 2002]. The difficulty of Markov chain sampling is the choice of a proposal probability density function, which "determines the explorative capabilities and efficiency of the sampler and therefore the statistical properties of the Markov Chain and its rate of convergence" [Vrugt et al., 2003].

1.3.5 Some issues related to sensitivity and uncertainty analysis

Gain of insights into model behaviour. Most sensitivity studies aim at parameter sensitivity assessment / ranking, based on simulation runs with incremental variations of the parameter values. For example, pipe flow models have been found to be highly sensitive to the Manning coefficient and to the length and width of the pipe conduit, whereas the conduit slope was found to have little impact on the model results [Peterson and Wicks, 2006]. Multiple scenarios have been used to investigate the impact of turbulence on the simulated hydraulic heads and parameter sensitivities of a finite difference groundwater flow model. It appeared that turbulence either increased or decreased simulated heads from their laminar elevations, and also affected the sensitivities of the model parameters [Shoemaker et al., 2008].

Monitoring network design and protection zones spotting. An under-appreciated utility of sensitivity analysis is to assess the reduction in the prediction uncertainty resulting from different actions such as data collection [Hunt and Welter, 2010]. For example, Monte-Carlo based sensitivity analysis has been used to determine the optimal location of monitoring wells for detection of groundwater contamination in three-dimensional heterogenous aquifers [Meyer et al., 1994; Storck et al., 1997]. Kalman filtering has been used to minimize groundwater monitoring network density under the constraint of given threshold values for the standard deviations of the estimation error [Zhou et al., 1991]. Adjoint sensitivity analysis allowed the identification of land use areas that should be protected first in order to maintain a given production rate at a pumping well [Jyrkama and Sykes, 2006]. A Bayesian data worth framework has been used to work out the monitoring network design that would minimize the cost of remediation and sampling in case of groundwater contamination [James and Gorelick, 1994]. Note that the reduction in the prediction uncertainty may be dependent on the nature of the predicted variable, as evidenced by e.g. Barros et al., 2011 for stochastic flow and transport models.

Data worth and parameter identifiability assessment. Data worth and parameter identiability are both related to the calibration process. The identifiability of a given model refers to the capability of model calibration to generate correct and unambiguous parameter estimates [Doherty

and Hunt, 2009; Kleissen et al., 1990]. The worth of observational data is determined by its ability to reduce predictive uncertainty [Dausman et al., 2010].

The identifiability is dependent upon the parameter considered and also the objective function used in the calibration process and the data set used for the calibration [Doherty and Hunt, 2009; Guinot et al., 2011]. Sensitivity-based identifiability measures have been proposed by various authors [Brun et al., 2001; Doherty and Hunt, 2009]. Multi-objective [Efstratiadis and Koutsoyiannis, 2010] or multi-variable [Castro and Goblet, 2003; Hooper et al., 1988; Son and Sivapalan, 2007; Winsemius et al., 2006] calibration approaches are in general better suited than traditional single-objective, single-variable approaches to identify overparameterization issues or deficiencies in the model structure.

The temporal dynamics of the sensitivity may provide a mean to detect the failure of a given model structure to correctly reproduce the observations [Boyle et al., 2000; Gupta et al., 1998; Sun et al., 2001; Wagener et al., 2003; Zhou et al., 1991].

The temporal variability of the model sensitivity may also be used to increase the efficiency of the calibration method [Vrugt et al., 2001; Wagener et al., 2003], e.g. by discarding data sets that contain little information from the calibration period of a given parameter [Vrugt et al., 2001].

1.4 Conclusion

Sensitivity analysis methods can be grouped in two families: local and global methods. Local methods consist in analysing the sensitivity behaviour in the vicinity of a central value, whereas global methods are based on an exploration of the space of the input parameters. Global and local methods are complementary rather than competitive:

- the global approach adresses the effect of orders-of-magnitude parameter changes, but it requires a large number of simulations,
- the local approach allows to gain analytical insights into the model functioning, but caution is required in determining the range of validity.

1.5 References for Chapter 1

Abbott, M. B. and J. C. Refsgaard (1996). *Distributed hydrological modelling*. Ed. by M. B. Abbott and J. C. Refsgaard. Kluwer Academic Publishers, p. 321. See p. 6.

Alfares, W., M. Bakalowicz, R. Guerin and M. Dukhan (2002). « Analysis of the karst aquifer structure of the Lamalou area (Hérault, France) with ground penetrating radar ». In: *Journal of Applied Geophysics* 51, pp. 97–106. DOI: 10.1016/S0926-9851(02)00215-X. See pp. 5, 136.

Angelini, P. and W. Dragoni (1997). « The problem of modeling limestone springs: The case of Bagnara (North Apennines, Italy) ». In: *Ground Water* 35.4, pp. 612–618. DOI: 10.1111/j.1745-6584.1997.tb00126.x. See p. 8.

Aquilina, L., B. Ladouche and N. Dörfliger (2006). « Water storage and transfer in the epikarst of karstic systems during high flow periods ». In: *Journal of Hydrology* 327, pp. 472–485. DOI: 10.1016/j.jhydrol.2005.11.054. See p. 3.

Archer, G. E. B., A. Saltelli and I. M. Sobol (1997). « Sensitivity measures, ANOVA-like techniques and the use of bootstrap ». In: *Journal of Statistical Computation and Simulation* 58.2, pp. 99–120. DOI: 10.1080/00949659708811825. See p. 17.

Audouin, O. and J. Bodin (2008). « Cross-borehole slug test analysis in a fractured limestone aquifer ». In: *Journal of Hydrology* 348, pp. 510–523. DOI: 10.1016/j.jhydrol.2007.10.021. See p. 4.

Bai, M., D. Elsworth and J.-C. Roegiers (1993). « Multiporosity/multipermeability approach to the simulation of naturally fractured reservoirs ». In: *Water Resources Research* 29.6, pp. 1621–1633. DOI: 10.1029/92WR02746. See pp. 4, 8.

Bailly-Comte, V. (2008). « Interactions hydrodynamiques surface/souterrain en milieu karstique - Approche descriptive, analyse fonctionnelle et modélisation hydrologique appliquées au bassin versant expérimental du Coulazou, Causse d'Aumelas, France. » PhD thesis. Université Montpellier II. URL: http://tel.archives-ouvertes.fr/tel-00319965/fr/. See p. 7.

Bailly-Comte, V., H. Jourde, A. Roesch, S. Pistre and C. Batiot-Guilhe (2008). « Time series analyses for karst/river interactions assessment: Case of the Coulazou river (southern France) ». In: *Journal of Hydrology* 349, pp. 98–114. DOI: 10.1016/j.jhydrol.2007.10.028. See p. 5.

Bakalowicz, M. (2005). « Karst groundwater: A challenge for new resources ». In: *Hydrogeology Journal* 13.1, pp. 148–160. DOI: 10.1007/s10040-004-0402-9. See pp. 2, 4.

Bao, J.-W. and Y.-H. Kuo (1995). « On-off switches in the adjoint method: Step functions ». In: *Monthly Weather Review* 123.5, pp. 1589–1594. DOI: doi:10.1175/1520-0493(1995)123<1589:OSITAM>2.0.CO;2. See p. 11.

Barenblatt, G., I. Zheltov and I. Kochina (1960). « Basic concepts in the theory of seepage of homogeneous liquids in fissured rocks ». In: *Journal of Applied Mathematical Methods* 24, pp. 1286–1303. See pp. 4, 8.

Barker, J. A. (1988). « A generalized radial flow model for hydraulic tests in fractured rock ». In: *Water Resources Research* 24.10, pp. 1796–1804. DOI: 10.1029/WR024i010p01796. See p. 4.

Barrett, M. E. and R. J. Charbeneau (1997). « A parsimonious model for simulating flow in a karst aquifer ». In: *Journal of Hydrology* 196.1-4, pp. 47–65. DOI: 10.1016/S0022-1694(96)03339-2. See p. 7.

Barros, F. P. de, S. Ezzedine and Y. Rubin (2011). « Impact of hydrogeological data on measures of uncertainty, site characterization and environmental performance metrics ». In: *Advances in Water Resources* In Press, Accepted Manuscript, pp. –. DOI: 10.1016/j.advwatres.2011.05.004. See p. 20.

Bear, J. (1972). *Dynamics of Fluids in Porous Media*. New York: American Elsevier, p. 764. See pp. 6, 168.

Beven, K. (1993). « Prophecy, reality and uncertainty in distributed hydrological modelling ». In: *Advances in Water Resources* 16.1, pp. 41–51. See p. 7.

— (2006). « A manifesto for the equifinality thesis ». In: *Journal of Hydrology* 320.1-2, pp. 18–36. DOI: 10.1016/j.jhydrol.2005.07.007. See p. 10.

Beven, K. and A. Binley (1992). « The future of distributed models: Model calibration and uncertainty prediction ». In: *Hydrological Processes* 6.3, pp. 279–298. DOI: 10.1002/hyp.3360060305. See pp. 10, 19, 83.

Beven, K. and J. Freer (2001). « Equifinality, data assimilation, and uncertainty estimation in mechanistic modelling of complex environmental systems using the GLUE methodology ». In: *Journal of Hydrology* 249.19, pp. 11–29. DOI: 10.1016/S0022-1694(01)00421-8. See p. 9.

Blasone, R.-S., H. Madsen and D. Rosbjerg (2008). « Uncertainty assessment of integrated distributed hydrological models using GLUE with Markov chain Monte Carlo sampling ». In: *Journal of Hydrology* 353.1-2, pp. 18–32. DOI: 10.1016/j.jhydrol.2007.12.026. See p. 20.

Bosák, P. (2003). « Karst processes from the beginning to the end: How can they be dated ? » In: *Speleogenesis and Evolution of Karst Aquifers* 1.3, pp. 1–24. See pp. 2, 128.

Box, G. and K. Wilson (1951). « On the experimental attainment of optimum conditions ». In: *Journal of the Royal Statistical Society - Series B* 13.1, pp. 1–45. URL: http://www.jstor.org/stable/2983966. See p. 17.

Boyle, D. P., H. V. Gupta and S. Sorooshian (2000). « Toward improved calibration of hydrologic models: Combining the strengths of manual and automatic methods ». In: *Water Resources Research* 36.12, pp. 3663–3674. See p. 21.

Brattin, W. J., T. M. Barry and N. Chiu (1996). « Monte Carlo modeling with uncertain probability density functions ». In: *Human and Ecological Risk Assessment* 2.4, pp. 820–840. DOI: 10.1080/10807039609383652. See p. 11.

Brun, R., P. Reichert and H. R. Kunsch (2001). « Practical identifiability analysis of large environmental simulation models ». In: *Water Resources Research* 37.4, pp. 1015–1030. DOI: 10.1029/2000WR900350. See p. 21.

Cacuci, D. (1990). « Global optimization and sensitivity analysis ». In: *Nuclear Science and Engineering* 104.1, pp. 78–88. See p. 12.

— (2003). *Sensitivity and Uncertainty Analysis: Theory*. Ed. by Chapman and Hall/CRC. Sensitivity and Uncertainty Analysis. CRC Press. ISBN: 9781584881155. See pp. 10, 44, 52.

Campolongo, F., J. Cariboni and A. Saltelli (2007). « An effective screening design for sensitivity analysis of large models ». In: *Environmental Modelling and Software* 22, pp. 1509–1518. DOI: 10.1016/j.envsoft.2006.10.004. See p. 11.

Camus, H. (2003). « Vallées et réseaux karstiques de la bordure carbonatée sud-cévenole : Relations avec la surrection, le volcanisme et les paléoclimats ». PhD thesis. Université Bordeaux III. See pp. 5, 124.

Cao, Y., M. Hussaini, T. Zang and A. Zatezalo (2006). « A variance reduction method based on sensitivity derivatives ». In: *Applied Numerical Mathematics* 56.6, pp. 800–813. DOI: 10.1016/j.apnum.2005.06.010. See p. 12.

Castaings, W. (2007). « Analyse de sensibilité et estimation de paramètres pour la modélisation hydrologique : Potentiel et limitations des méthodes variationnelles ». PhD thesis. Université Joseph Fourier - Grenoble I. URL: http://tel.archives-ouvertes.fr/tel-00264807/fr/. See p. 15.

Castro, M. C. and P. Goblet (2003). « Calibration of regional groundwater flow models: Working toward a better understanding of site-specific systems ». In: *Water Resources Research* 39.6, p. 1172. DOI: 10.1029/2002WR001653. See p. 21.

Chalikakis, K., V. Plagnes, R. Guerin, R. Valois and F. Bosch (2011). « Contribution of geophysical methods to karst-system exploration: An overview ». In: *Hydrogeology Journal* 19, pp. 1–12. DOI: 10.1007/s10040-011-0746-x. See p. 5.

Clemens, T., D. Hückinghaus, R. Liedl and M. Sauter (1999). « Simulation of the development of karst aquifers: Role of the epikarst ». In: *International Journal of Earth Sciences* 88, pp. 157–162. See p. 9.

Cornaton, F. and P. Perrochet (2002). « Analytical 1D dual-porosity equivalent solutions to 3D discrete single-continuum models. Application to karstic spring hydrograph modelling ». In: *Journal of Hydrology* 262.1-4, pp. 165–176. DOI: 10.1016/S0022-1694(02)00033-1. See p. 8.

Cukier, R., C. Fortuin, K. Shuler, A. Petschek and J. Schaibly (1973). « Study of the sensitivity of coupled reaction systems to uncertainties in rate coefficients. I. Theory ». In: *Journal of Chemical Physics* 59, pp. 3873–3878. See p. 18.

Cukier, R., H. Levine and K. Shuler (1978). « Nonlinear sensitivity analysis of multiparameter model systems ». In: *Journal of Computational Physics* 26, pp. 1–42. See p. 18.

Cullen, A. and H. Frey (1999). *Probabilistic techniques in exposure assessment: A handbook for dealing with variability and uncertainty in models and inputs*. New York: Plenum Press. See p. 12.

Dausman, A. M., J. Doherty, C. D. Langevin and M. C. Sukop (2010). « Quantifying data worth toward reducing predictive uncertainty ». In: *Ground Water*. DOI: 10.1111/j.1745-6584.2010.00679.x. See p. 21.

Debieche, T. H., Y. Guglielmi and J. Mudry (2002). « Modeling the hydraulical behavior of a fissured-karstic aquifer in exploitation conditions ». In: *Journal of Hydrology* 257.1-4, pp. 247–255. DOI: 10.1016/S0022-1694(01)00539-X. See p. 6.

Delay, F., G. Porel and S. Bernard (2004). « Analytical 2D model to invert hydraulic pumping tests in fractured rocks with fractal behavior ». In: *Geophysical Research Letters* 31.16, p. L16501. DOI: 10.1029/2004GL020500. See p. 4.

Delay, F., A. Kaczmaryk and P. Ackerer (2007). « Inversion of interference hydraulic pumping tests in both homogeneous and fractal dual media ». In: *Advances in Water Resources* 30.3, pp. 314–334. DOI: 10.1016/j.advwatres.2006.06.008. See pp. 4, 167.

Denic-Jukic, V. and D. Jukic (2003). « Composite transfer functions for karst aquifers ». In: *Journal of Hydrology* 274.1-4, pp. 80–94. DOI: 10.1016/S0022-1694(02)00393-1. See p. 6.

Dettinger, M. D. and J. L. Wilson (1981). « First order analysis of uncertainty in numerical models of groundwater flow: Part 1. Mathematical development ». In: *Water Resources Research* 17.1, pp. 149–161. DOI: 10.1029/WR017i001p00149. See p. 13.

Diersch, H. (1998*a*). *Feflow : Reference Manual*. Institute for Water Resources Planning and Systems Research, WASY. Berlin. URL: http://www.feflow.info/manuals.html. See pp. xii, 9, 151, 180.

Doherty, J. and R. J. Hunt (2009). « Two statistics for evaluating parameter identifiability and error reduction ». In: *Journal of Hydrology* 366.1-4, pp. 119–127. DOI: 10.1016/j.jhydrol.2008.12.018. See pp. 20, 21.

Drogue, C. (1974). « Structure de certains aquifères karstiques d'après les résultats de travaux de forage ». In: *Comptes Rendus de l'Académie des Sciences - Série III* 278, pp. 2621–2624. See p. 2.

Dubus, I. G. and C. D. Brown (2003). « How much confidence should we assign to results obtained through Monte Carlo modelling ? » In: *Pesticide in Air, Plant, Soil & Water System. Proceedings of the XII international Symposium Pesticide Chemistry held in Piacenza, Italy (June 4-6, 2003)*. Ed. by A. Del Re, E Capri, L Padovani and M Trevisan. La Goliardica Pavese, pp. 409–415. See p. 11.

Dubus, I. G., C. D. Brown and S. Beulke (2003). « Sources of uncertainty in pesticide fate modelling ». In: *The Science of the Total Environment* 317.1-3, pp. 53–72. DOI: 10.1016/S0048-9697(03)00362-0. See p. 10.

Dörfliger, N., P.-Y. Jeannin and F. Zwahlen (1999). « Water vulnerability assessment in karst environments: A new method of defining protection areas using a multi-attribute approach and GIS tools (EPIK method) ». In: *Environmental Geology* 39.2, pp. 165–176. DOI: 10.1007/s002540050446. See p. 2.

Ebel, B. A. and K. Loague (2006). « Physics-based hydrologic-response simulation: Seeing through the fog of equifinality ». In: *Hydrological Processes* 20.13, pp. 2887–2900. DOI: 10.1002/hyp.6388. See p. 10.

Efstratiadis, A. and D. Koutsoyiannis (2010). « One decade of multi-objective calibration approaches in hydrological modelling: A review ». In: *Hydrological Sciences Journal* 55.1, pp. 58–78. DOI: 10.1080/02626660903526292. See pp. 21, 96.

Fleury, P., B. Ladouche, Y. Conroux, H. Jourde and N. Dörfliger (2009). « Modelling the hydrologic functions of a karst aquifer under active water management - The Lez spring ». In: *Journal of Hydrology* 365.3-4, pp. 235–243. DOI: 10.1016/j.jhydrol.2008.11.037. See pp. ix, xviii, 7, 90, 93, 94, 102, 104.

Fleury, P., V. Plagnes and M. Bakalowicz (2007). « Modelling of the functioning of karst aquifers with a reservoir model: Application to Fontaine de Vaucluse (South of France) ». In: *Journal of Hydrology* 345.1-2, pp. 38–49. DOI: 10.1016/j.jhydrol.2007.07.014. See p. 7.

Frey, H. C. and S. R. Patil (2002). « Identification and review of sensitivity analysis methods ». In: *Risk Analysis* 22.3, pp. 553–578. DOI: 10.1111/0272-4332.00039. See p. 11.

Geyer, T., S. Birk, T. Licha, R. Liedl and M. Sauter (2007). « Multitracer test approach to characterize reactive transport in karst aquifers ». In: *Ground Water* 45.1, pp. 36–45. DOI: 10.1111/j.1745-6584.2006.00261.x. See p. 5.

Goldscheider, N. and D. Drew (2007). *Methods in Karst Hydrogeology*. International Contributions to Hydrogeology. Taylor & Francis. See pp. 3, 4.

Goldscheider, N., J. Meiman, M. Pronk and C. Smart (2008). « Tracer tests in karst hydrogeology and speleology ». In: *International Journal of Speleology* 37.1, pp. 27–40. See pp. 2, 4.

Gonzalez-Herrera, R., I. Sanchez-y Pinto and J. Gamboa-Vargas (2002). « Groundwater-flow modeling in the Yucatan karstic aquifer, Mexico ». In: *Hydrogeology Journal* 10.5, pp. 539–552. DOI: 10.1007/s10040-002-0216-6. See p. 8.

Guinot, V., B. Cappelaere, C. Delenne and D. Ruelland (2011). « Objective functions for conceptual hydrological model calibration: Theoretical analysis of distance- and weak form-based functions ». In: *Journal of Hydrology* 401.1-2, pp. 1–13. DOI: 10.1016/j.jhydrol.2011.02.004. See pp. 21, 72, 114.

Guinot, V., M. Leménager and B. Cappelaere (2007). « Sensitivity equations for hyperbolic conservation law-based flow models ». In: *Advances in Water Resources* 30.9, pp. 1943–1961. DOI: 10.1016/j.advwatres.2007.03.004. See pp. 11, 15.

Guinot, V., C. Delenne and B. Cappelaere (2008). « An approximate Riemann solver for sensitivity equations with discontinuous solutions ». In: *Advances in Water Resources* 32.1, pp. 61–77. DOI: 10.1016/j.advwatres.2008.10.002. See p. 13.

Gupta, H. V., S. Sorooshian and P. O. Yapo (1998). « Toward improved calibration of hydrologic models: Multiple and noncommensurable measures of information ». In: *Water Resources Research* 34.4, pp. 751–763. DOI: 10.1029/97WR03495. See pp. 18, 21, 96.

Halihan, T. and C. M. Wicks (1998). « Modeling of storm responses in conduit flow aquifers with reservoirs ». In: *Journal of Hydrology* 208.1-2, pp. 82–91. DOI: 10.1016/S0022-1694(98)00149-8. See p. 7.

Hall, J. W. (2003). « Handling uncertainty in the hydroinformatic process ». In: *Journal of Hydroinformatics* 5.4, pp. 215–232. See p. 9.

He, M., T. S. Hogue, K. J. Franz, S. A. Margulis and J. A. Vrugt (2010). « Characterizing parameter sensitivity and uncertainty for a snow model across hydroclimatic regimes ». In: *Advances in Water Resources* 34.1, pp. 114–127. DOI: 10.1016/j.advwatres.2010.10.002. See p. 10.

Hooper, R. P., A. Stone, N. Christophersen, E. de Grosbois and H. M. Seip (1988). « Assessing the Birkenes model of stream acidification using a multisignal calibration methodology ». In: *Water Resources Research* 24.8, pp. 1308–1316. DOI: 10.1029/WR024i008p01308. See p. 21.

Hornberger, G. and R. Spear (1981). « An approach to the preliminary analysis of environmental systems ». In: *Journal of Environmental Management* 12.1, pp. 7–18. See p. 18.

Hu, C. H., Y. H. Hao, T. C. J. Yeh, B. Pang and Z. Wu (2008). « Simulation of spring flows from a karst aquifer with an artificial neural network ». In: *Hydrological Processes* 22.5, pp. 596–604. DOI: 10.1002/hyp.6625. See p. 6.

Hunt, R. J. and D. E. Welter (2010). « Taking account of unknown unknowns ». In: *Ground Water* 48.4, pp. 477–477. DOI: 10.1111/j.1745-6584.2010.00681.x. See p. 20.

Isukapalli, S. S., A. Roy and P. G. Georgopoulos (2000). « Efficient sensitivity/uncertainty analysis using the combined stochastic response surface method and automated differentiation: Application to environmental and biological systems ». In: *Risk Analysis* 20.5, pp. 591–602. DOI: 10.1111/0272-4332.205054. See p. 12.

James, B. R. and S. M. Gorelick (1994). « When enough is enough: The worth of monitoring data in aquifer remediation design ». In: *Water Resources Research* 30.12, pp. 3499–3513. DOI: 10.1029/94WR01972. See p. 20.

Jaquet, O., P. Siegel, G. Klubertanz and H. Benabderrhamane (2004). « Stochastic discrete model of karstic networks ». In: *Advances In Water Resources* 27.7, pp. 751–760. DOI: 10.1016/j.advwatres.2004.03.007. See p. 9.

Jazayeri Noushabadi, M., H. Jourde and G. Massonnat (2011). « Influence of the observation scale on permeability estimation at local and regional scales through well tests in a fractured and karstic aquifer (Lez aquifer, Southern France) ». In: *Journal of Hydrology* 403.1-3, pp. 321–336. DOI: 10.1016/j.jhydrol.2011.04.013. See p. 5.

Jazayeri Noushabadi, M. R. (2009). « Characterisation of relationships between fracture network and flow-path network in fractured and karstic reservoirs numerical modelling and field investigation (Lez aquifer, Southern France) ». PhD thesis. Université Montpellier II. URL: http://www.hydrosciences.org/IMG/pdf/PHD_2009_M_Reza_Jazayeri.pdf. See pp. 5, 8, 59.

Jeannin, P.-Y. (1996). « Structure et comportement hydraulique des aquifères karstiques ». PhD thesis. Université de Neuchâtel. URL: http://91.121.162.160/THE/JEANNIN.pdf. See pp. 4, 9, 91.

— (2001). « Modeling flow in phreatic and epiphreatic karst conduits in the Höffloch cave (Muotatal, Switzerland) ». In: *Water Resources Research* 37.2, pp. 191–200. DOI: 10.1029/2000WR900257. See pp. 8, 9.

Josnin, J.-Y., H. Jourde, P. Fenart and P. Bidaux (2002). « A three-dimensional model to simulate joint networks in layered rocks ». In: *Canadian Journal of Earth Sciences* 39, pp. 1443–1455. See pp. 8, 9.

Jourde, H. (1998). « Simulation d'essais de puits en milieu fracturé à partir d'un modèle discret basé sur des lois mécaniques de fracturation. Validation sur suites expérimentaux ». PhD thesis. Université Montpellier II. See p. 8.

Jourde, H., F. Cornaton, S. Pistre and P. Bidaux (2002). « Flow behavior in a dual fracture network ». In: *Journal of Hydrology* 266.1-2, pp. 99–119. DOI: 10.1016/S0022-1694(02)00120-8. See pp. 8, 9.

Jukic, D. and V. Denic-Jukic (2009). « Groundwater balance estimation in karst by using a conceptual rainfall-runoff model ». In: *Journal of Hydrology* 373.3-4, pp. 302–315. DOI: 10.1016/j.jhydrol.2009.04.035. See p. 7.

Jyrkama, M. and J. Sykes (2006). « Sensitivity and uncertainty analysis of the recharge boundary condition ». In: *Water Resources Research* 42.W01404, pp. 1–11. DOI: 10.1029/2005WR004408. See pp. 20, 168.

Kaczmaryk, A. and F. Delay (2007). « Interference pumping tests in a fractured limestone (Poitiers-France): Inversion of data by means of dual-medium approaches ». In: *Journal of Hydrology* 337.1-2, pp. 133–146. DOI: 10.1016/j.jhydrol.2007.01.025. See p. 4.

Kavetski, D., G. Kuczera and S. W. Franks (2006*a*). « Calibration of conceptual hydrological models revisited: 1. Overcoming numerical artefacts ». In: *Journal of Hydrology* 320.1-2, pp. 173–186. DOI: 10.1016/j.jhydrol.2005.07.012. See pp. 10, 11.

— (2006*b*). « Calibration of conceptual hydrological models revisited: 2. Improving optimisation and analysis ». In: *Journal of Hydrology* 320.1-2, pp. 187–201. DOI: 10.1016/j.jhydrol.2005.07.013. See p. 11.

Kiraly, L. (1975). « Hydrogeology of Karstic Terrains ». In: ed. by A. Burger and L. Dubertet. B 3. IUGS. Chap. Rapport sur l'état actuel des connaissances dans le domaine des caractères physique des roches karstiques, pp. 53–67. See p. 2.

— (1998). « Modeling karst aquifers by the combined discrete channel and continuum approach ». In: *Bulletin du Centre d'Hydrogéologie de Neuchâtel* 16, pp. 77–98. See pp. 4, 154.

— (2003). « Karstification and groundwater flow ». In: *Speleogenesis and Evolution of Karst Aquifers* 1.3, 26 pp. URL: http://www.speleogenesis.info/archive/publication.php?PubID=3244. See p. 2.

Kiraly, L., P. Perrochet and Y. Rossier (1995). « Effect of the epikarst on the hydrograph of karst springs: A numerical approach. » In: *Bulletin du Centre d'Hydrogéologie de Neuchâtel* 14, pp. 199–220. See p. 9.

Kitanidis, P. K. and R. L. Bras (1980). « Real-time forecasting with a conceptual hydrologic model: 1. Analysis of uncertainty ». In: *Water Resources Research* 16.6, pp. 1025–1033. DOI: 10.1029/WR016i006p01025. See p. 11.

Kleissen, F. M., M. B. Beck and H. S. Wheater (1990). « The identifiability of conceptual hydrochemical models ». In: *Water Resources Research* 26.12, pp. 2979–2992. DOI: 10.1029/WR026i012p02979. See p. 21.

Klimchouk, A., D. Ford, A. Palmer, W. Dreybrodt and members of the Commission on Karst Hydrogeology & Speleogenesis (IUS) (2000). *Speleogenesis Evolution of Karst Aquifers*. Ed. by N. S. Society. Huntsville, Alabama, p. 527. See p. 6.

Klimchouk, A. (2004). « Towards defining, delimiting and classifying epikarst: Its origin, processes and variants of geomorphic evolution ». In: *Speleogenesis and Evolution of Karst Aquifers* 2.1, pp. 1–13. See p. 3.

Kong A Siou, L., A. Johannet, V. Borrell and S. Pistre (2011). « Complexity selection of a neural network model for karst flood forecasting: The case of the Lez Basin (southern France) ». In: *Journal of Hydrology* 403.3-4, pp. 367–380. DOI: 10.1016/j.jhydrol.2011.04.015. See p. 6.

Kucherenko, S., M. Rodriguez-Fernandez, C. Pantelides and N. Shah (2009). « Monte Carlo evaluation of derivative-based global sensitivity measures ». In: *Reliability Engineering and System Safety* 94.7, pp. 1135–1148. DOI: 10.1016/j.ress.2008.05.006. See p. 12.

Kuczera, G. and E. Parent (1998). « Monte Carlo assessment of parameter uncertainty in conceptual catchment models: The Metropolis algorithm ». In: *Journal of Hydrology* 211.1-4, pp. 69–85. DOI: 10.1016/S0022-1694(98)00198-X. See pp. 17, 20.

Kumar, S., M. Sekhar, D. V. Reddy and M. S. Mohan Kumar (2010). « Estimation of soil hydraulic properties and their uncertainty: Comparison between laboratory and field experiment ». In: *Hydrological Processes* 24.23, pp. 3426–3435. DOI: 10.1002/hyp.7775. See p. 19.

Kurtulus, B. and M. Razack (2007). « Evaluation of the ability of an artificial neural network model to simulate the input-output responses of a large karstic aquifer: The La Rochefoucauld aquifer (Charente, France) ». In: *Hydrogeology Journal* 15.2, pp. 241–254. DOI: 10.1007/s10040-006-0077-5. See p. 6.

Käss, W. (1998). *Tracing Technique in Geohydrology*. Ed. by G. Matthess. Balkema. See p. 5.

Labat, D., R. Ababou and A. Mangin (1999). « Linear and nonlinear input/output models for karstic springflow and flood prediction at different time scales ». In: *Stochastic Environmental Research and Risk Assessment* 13.5, pp. 337–364. DOI: 10.1007/s004770050055. See p. 6.

Larocque, M., O. Banton, P. Ackerer and M. Razack (1999). « Determining karst transmissivities with inverse modeling and an equivalent porous media ». In: *Ground Water* 37.6, pp. 897–903. DOI: 10.1111/j.1745-6584.1999.tb01189.x. See p. 8.

Le Moine, N., V. Andreassian and T. Mathevet (2008). « Confronting surface- and groundwater balances on the La Rochefoucauld-Touvre karstic system (Charente, France) ». In: *Water Resources Research* 44.3, W03403. DOI: 10.1029/2007WR005984. See p. 7.

Lods, G. and P. Gouze (2008). « A generalized solution for transient radial flow in hierarchical multifractal fractured aquifers ». In: *Water Resources Research* 44.12, W12405–. DOI: 10.1029/2008WR007125. See p. 4.

Long, A. J. and R. G. Derickson (1999). « Linear systems analysis in a karst aquifer ». In: *Journal of Hydrology* 219.3-4, pp. 206–217. DOI: 10.1016/S0022-1694(99)00058-X. See p. 6.

Lyness, J. and C. Moler (1967). « Numerical differentiation of analytic functions ». In: *SIAM Journal on Numerical Analysis* 4, pp. 202–210. See p. 14.

Makropoulos, C., D. Koutsoyiannis, M. Stanic, S. Djordjevic, D. Prodanovic, T. Dasic, S. Prohaska, C. Maksimovic and H. Wheater (2008). « A multi-model approach to the simulation of large scale karst flows ». In: *Journal of Hydrology* 348.3-4, pp. 412–424. DOI: 10.1016/j.jhydrol.2007.10.011. See pp. 7, 9.

Mangin, A. (1975). « Contribution à l'étude hydrodynamique des aquifères karstiques ». PhD thesis. Institut des Sciences de la Terre de Dijon. See pp. 2, 5.

— (1984). « L'approche systémique du karst. Conséquences conceptuelles et méthodologiques ». In: *Bulletin de la Société Méridionale de Spéléologie et de Préhistoire* 24, pp. 131–145. See p. 5.

Marsaud, B. (1996). « Structure et fonctionnement de la zone noyée des karsts à partir des résultats expérimentaux ». PhD thesis. Université Paris XI Orsay. See p. 5.

Marsily, G. de (1984). « Méthodes et domaines d'application de la mécanique des fluides en milieux poreux et fissurés ». In: *Annales des Mines* 5-6, pp. 5–10. See p. 2.

Maréchal, J.-C., B. Ladouche, N. Dörfliger and P. Lachassagne (2008). « Interpretation of pumping tests in a mixed flow karst system ». In: *Water Resources Research* 44, pp. –. DOI: 10.1029/2007WR006288. See pp. 4, 91.

Maskey, S. and V. Guinot (2003). « Improved first-order second moment method for uncertainty estimation in flood forecasting ». In: *Hydrological Sciences Journal* 48.2, pp. 183–196. DOI: 10.1623/hysj.48.2.183.44692. See p. 11.

McCuen, R. H. (1973). « The role of sensitivity analysis in hydrologic modeling ». In: *Journal of Hydrology* 18.1, pp. 37–53. DOI: 10.1016/0022-1694(73)90024-3. See p. 11.

Meyer, P. D., A. J. Valocchi and J. Wayland Eheart (1994). « Monitoring network design to provide initial detection of groundwater contamination ». In: *Water Resources Research.* 30.9, pp. 2647–2659. DOI: 10.1029/94WR00872. See pp. 20, 167.

Mohrlok, U. and M. Sauter (1997). « Modelling groundwater flow in a karst terrane using discrete and double-continuum approaches: Importance of spatial and temporal distribution of recharge ». In: *Modelling in Karst Systems, Proceedings of the 6th Conf. on Limestone Hydrology and Fissured Media held in La Chaux-de-Fonds, Switzerland (August 10-17, 1997).* Ed. by P.-Y. Jeannin and M. Sauter. Vol. 2, pp. 167–170. See p. 9.

Monnin, M. and M. Bakalowicz (2003). « Land and Marine Hydrogeology ». In: ed. by M. Taniguchi, K. Wang and T. Gamo. Elsevier. Chap. 6. Natural tracing in karst aquifers, pp. 93–114. See p. 6.

Musgrove, M., L. Stern and J. Banner (2010). « Springwater geochemistry at Honey Creek State Natural Area, central Texas: Implications for surface water and groundwater interaction in a karst aquifer ». In: *Journal of Hydrology* 388.1-2, pp. 144–156. DOI: 10.1016/j.jhydrol.2010.04.036. See p. 5.

Najib, K. (2007). « Phénomènes de remontées de nappe extrêmes en terrain carbonaté fracturé et karstifié: Évaluation de l'aléa et prévention du risque dans le cadre de la protection de bâtiments ». PhD thesis. Université Montpellier II. See p. 8.

Neuman, S. P. (2005). « Trends, prospects and challenges in quantifying flow and transport through fractured rocks ». In: *Hydrogeology Journal* 13.1, pp. 124–147. DOI: 10.1007/s10040-004-0397-2. See p. 6.

Novel, J. P., A. Dimadi, A. Zervopoulou and M. Bakalowicz (2007). « The Aggitis karst system, Eastern Macedonia, Greece: Hydrologic functioning and development of the karst structure ». In: *Journal of Hydrology* 334.3-4, pp. 477–492. DOI: 10.1016/j.jhydrol.2006.10.029. See p. 5.

Oberkampf, W. L. and F. G. Blottner (1998). « Issues in computational fluid dynamics code verification and validation ». In: 36, pp. 687–695. DOI: 10.2514/2.456. See p. 10.

Pauw, D. de (2003). « Practical aspects of sensitivity analysis for dynamic models ». In: *Proceedings of the 4th MATHMOD Conference held in Vienna, Austria (February 5-7, 2003)*. Ed. by I. Troch and F. Breitenecker. See p. 13.

Perez, P., F. Castellvi and A. Martinez-Cob (2008). « A simple model for estimating the Bowen ratio from climatic factors for determining latent and sensible heat flux ». In: *Agricultural and Forest meteorology* 148, pp. 25–37. DOI: 10.1016/j.agrformet.2007.08.015. See p. 14.

Perrin, C., C. Michel and V. Andreassian (2001). « Does a large number of parameters enhance model performance? Comparative assessment of common catchment model structures on 429 catchments ». In: *Journal of Hydrology* 242.3-4, pp. 275–301. DOI: 10.1016/S0022-1694(00)00393-0. See pp. 6, 38, 77, 100.

Perrin, J. (2003). « A conceptual model of flow and transport in a karst aquifer based on spatial and temporal variations of natural tracers ». PhD thesis. University of Neuchâtel. URL: http://www1.unine.ch/chyn/pdf/publi_cyberthesis_full/these_PerrinJ.pdf. See pp. 2, 3.

Perrin, J. and M. Luetscher (2008). « Inference of the structure of karst conduits using quantitative tracer tests and geological information: Example of the Swiss Jura ». In: *Hydrogeology Journal* 16.5, pp. 951–967. DOI: 10.1007/s10040-008-0281-6. See p. 5.

Perrin, J., P.-Y. Jeannin and F. Zwahlen (2003*b*). « Epikarst storage in a karst aquifer: A conceptual model based on isotopic data, Milandre test site, Switzerland ». In: *Journal of Hydrology* 279, pp. 106–124. DOI: 10.1016/S0022-1694(03)00171-9. See p. 3.

Peterson, E. W. and C. M. Wicks (2006). « Assessing the importance of conduit geometry and physical parameters in karst systems using the storm water management model (SWMM) ». In: *Journal of Hydrology* 329.1-2, pp. 294–305. DOI: 10.1016/j.jhydrol.2006.02.017. See pp. 8, 20.

Petrella, E., P. Capuano and F. Celico (2007). « Unusual behaviour of epikarst in the Acqua dei Faggi carbonate aquifer (Southern Italy) ». In: *Terra Nova* 19.1, pp. 82–88. DOI: 10.1111/j.1365-3121.2006.00720.x. See p. 3.

Puech, V. and P.-Y. Jeannin (1997). « Contribution à la compréhension du fonctionnement hydraulique de l'épikarst; expériences d'arrosage sur le site de Bure ». In: *Modelling in Karst Systems, Proceedings of the 6th Conf. on Limestone Hydrology and Fissured Media held in La Chaux-de-Fonds, Switzerland (August 10-17, 1997)*. Ed. by P.-Y. Jeannin and M. Sauter. Vol. 1, pp. 293–296. See p. 3.

Quinn, J. J., D. Tomasko and J. A. Kuiper (2006). « Modeling complex flow in a karst aquifer ». In: *Sedimentary Geology* 184, pp. 343–351. DOI: 10.1016/j.sedgeo.2005.11.009. See p. 5.

Reimann, T., R. Liedl, T. Geyer, M. Sauter, N. Doerfliger and J.-C. Maréchal (2011). « A non-steady and non-uniform hybrid model for karst aquifer characterization ». In: *Geophysical Research Abstracts* 13.EGU2011-8648. See p. 9.

Risbey, J., M. Kandlikar and A. Patwardhan (1996). « Assessing integrated assessments ». In: *Climatic Change* 34.3, pp. 369–395. DOI: 10.1007/BF00139298. See p. 9.

Rooij, R. de (2008). « Towards improved numerical modeling of karst aquifers: coupling turbulent conduit flow and laminar matrix flow under variably saturated conditions ». PhD thesis. University of Neuchâtel. URL: http://www1.unine.ch/chyn/pdf/publi_cyberthesis_full/these_deRooijR.pdf. See p. 9.

Saltelli, A., S. Tarantola and K. P.-S. Chan (1999). « A quantitative model-independent method for global sensitivity analysis of model output ». In: *Technometrics* 41.1, pp. 39–56. See pp. 17, 18.

Saltelli, A., S. Tarantola, and F. Campolongo (2000). « Sensitivity anaysis as an ingredient of modeling ». In: *Statistical Science* 15.4, pp. 377–395. URL: http://projecteuclid.org/euclid.ss/1009213004. See pp. 10, 11.

Sauter, M. (1992). « Quantification and forecasting of regional groundwater flow and transport in a karst aquifer (Gallusquelle, Malm, SW. Germany) ». PhD thesis. Eberhard Kärls Universität Tübingen. URL: http://w210.ub.uni-tuebingen.de/dbt/volltexte/2005/2039/. See pp. 7, 8.

Sauter, M., L. J. Florea, M. Covington, F. Goabrovsek, Y. Gao, R. Green, J. Gulley, R. Harmon, E. Herman, P.-Y. Jeannin, W. K. Jones, T. Kincaid, P. Moore, J. Mylroie, I. D. Sasowsky, E. Screaton and C. M. Wicks (2008). « Focus group on karst hydrology - conceptual models, aquifer characterization, and numerical modeling ». In: *Proceedings of the Frontiers of Karst Research workshop held in San Antonio, Texas (May 3-5, 2007)*. Ed. by I. Sasowsky, W. White and J. Martin. Special publication 13. Karst Waters Institute. Leesburg, pp. 77–81. URL: http://works.bepress.com/lee_florea/32. See p. 2.

Scanlon, B. R., R. E. Mace, M. E. Barrett and B. Smith (2003). « Can we simulate regional groundwater flow in a karst system using equivalent porous media models? Case study, Barton Springs Edwards aquifer, USA ». In: *Journal of Hydrology* 276.1-4, pp. 137–158. DOI: 10.1016/S0022-1694(03)00064-7. See pp. 7, 8.

Shoemaker, W. B., K. J. Cunningham, E. L. Kuniansky and J. Dixon (2008). « Effects of turbulence on hydraulic heads and parameter sensitivities in preferential groundwater flow layers ». In: *Water Resources Research* 44.3, W03501. DOI: 10.1029/2007WR006601. See p. 20.

Smart, P. and H. Friederich (1986). « Water movement and storage in the unsaturated zone of a maturely karstified carbonate aquifer, Mendip Hills, England ». In: *Proceedings of the 1st Conference on Environmental Problems of Karst Terrains and their Solutions held in Bowling Green, Kentucky (October 28-30, 1986)*. Ed. by O. D. National Water Well Association, pp. 59–87. See pp. 3, 5.

Sobol, I. M. (2001). « Global sensitivity indices for nonlinear mathematical models and their Monte Carlo estimates ». In: *Mathematics and Computers in Simulation* 55.1-3, pp. 271–280. DOI: 10.1016/S0378-4754(00)00270-6. See p. 18.

Sobol, I. M. and S. Kucherenko (2009). « Derivative based global sensitivity measures and their link with global sensitivity indices ». In: *Mathematics and Computers In Simulation* 79.10, pp. 3009–3017. DOI: 10.1016/j.matcom.2009.01.023. See p. 12.

Son, K. and M. Sivapalan (2007). « Improving model structure and reducing parameter uncertainty in conceptual water balance models through the use of auxiliary data ». In: *Water Resources Research* 43.1, W01415–. DOI: http://dx.doi.org/10.1029/2006WR005032. See p. 21.

Spear, R. C. and G. M. Hornberger (1980). « Eutrophication in peel inlet - II. Identification of critical uncertainties via generalized sensitivity analysis ». In: *Water Research* 14.1, pp. 43–49. DOI: 10.1016/0043-1354(80)90040-8. See p. 18.

Stevanovic, Z. and V. Dragisic (1998). « An example of identifying karst groundwater flow ». In: *Environmental Geology* 35.4, pp. 241–244. DOI: 10.1007/s002540050309. See p. 5.

Storck, P., J. W. Eheart and A. J. Valocchi (1997). « A method for the optimal location of monitoring wells for detection of groundwater contamination in three-dimensional heterogenous aquifers ». In: *Water Resources Research* 33.9, pp. 2081–2088. DOI: 10.1029/97WR01704. See p. 20.

Sun, N., N. Z. Sun, M. Elimelech and J. N. Ryan (2001). « Sensitivity analysis and parameter identifiability for colloid transport in geochemically heterogeneous porous media ». In: *Water Resources Research* 37.2, pp. 209–222. DOI: 10.1029/2000WR900291. See p. 21.

Sykes, J., J. Wilson and R. Andrews (1985). « Sensitivity analysis for steady state groundwater flow using adjoint operators ». In: *Water Resources Research* 21.3, pp. 359–371. DOI: 10.1029/WR021i003p00359. See pp. 15, 167.

Tang, Y., P. Reed, T. Wagener and K. van Werkhoven (2007). « Comparing sensitivity analysis methods to advance lumped watershed model identification and evaluation ». In: *Hydrology and*

Earth System Sciences 11, pp. 793–817. URL: http://www.hydrol-earth-syst-sci.net/11/793/2007/. See p. 18.

Teutsch, G. and M. Sauter (1991). « Groundwater modelling in karst terranes: Scale effects, data acquisition and field validation ». In: *Proceedings of the 3rd Conference on Hydrogeology, Ecology, Monitoring and Management of Ground Water in Karst Terranes held in Nashville, Tennessee, USA (Dec. 4-6, 1991)*. Ed. by J. Quinlan and A. Stanley. Nashville, pp. 17–38. See p. 8.

Teutsch, G. (1993). « An extended double-porosity concept as a practical modelling approach for a karstified terrain ». In: *Hydrogeological Processes in Karst Terranes. Proceedings of the Antalya Symposium and Field Seminar held in Antalya, Turkey (October 7-17, 1990)*. Ed. by G. Giinay. Vol. 207. IAHS. See p. 8.

Teutsch, G. and M. Sauter (1997). « Distributed parameter modelling approaches in karst-hydrological investigation ». In: *Modelling in Karst Systems, Proceedings of the 6th Conf. on Limestone Hydrology and Fissured Media held in La Chaux-de-Fonds, Switzerland (August 10-17, 1997)*. Ed. by P.-Y. Jeannin and M. Sauter, pp. 19–23. See p. 7.

Thraikill, J. (1974). « Pipe flow models of a Kentuky limestone aquifer ». In: *Ground Water* 12.4, pp. 202–205. See p. 8.

Thrailkill, J. (1968). « Chemical and hydrologic factors in the excavation of limestone caves ». In: *Geological Society of America Bulletin* 79.1, pp. 19–46. DOI: 10.1130/0016-7606. See p. 9.

Tritz, S., V. Guinot and H. Jourde (2011). « Modelling the behaviour of a karst system catchment using non linear hysteretic conceptual model ». In: *Journal of Hydrology* 397.3-4, pp. 250–262. DOI: 10.1016/j.jhydrol.2010.12.001. See pp. vi, xvii, 7, 38–41, 44, 46, 52, 59, 72, 73, 76, 77, 80, 93, 94.

UNESCO (1992). *International Glossary of Hydrology*. Ed. by U. N. E. Scientific and Cultural. 385. Collection WMO/OMM/VMO, p. 413. URL: http://webworld.unesco.org/water/ihp/db/glossary/glu/aglo.htm. See p. 2.

Vrugt, J., W. Bouten and A. Weerts (2001). « Information content of data for identifying soil hydraulic parameters from outflow experiments ». In: *Soil Science Society of America Journal* 65.1, pp. 19–27. DOI: 10.2136/sssaj2001.65119x. See p. 21.

Vrugt, J. A., W. Bouten, H. V. Gupta and S. Sorooshian (2002). « Toward improved identifiability of hydrologic model parameters : The information content of experimental data ». In: *Water Resources Research* 12, p. 1312. DOI: 10.1029/2001WR001118. See p. 20.

Vrugt, J. A., H. V. Gupta, W. Bouten and S. Sorooshian (2003). « A Shuffled Complex Evolution Metropolis algorithm for optimization and uncertainty assessment of hydrologic model parameters ». In: *Water Resources Research* 8.8, p. 1201. DOI: 10.1029/2002WR001642. See p. 20.

Wagener, T., N. McIntyre, M. J. Lees, H. S. Wheater and H. V. Gupta (2003). « Towards reduced uncertainty in conceptual rainfall-runoff modelling: Dynamic identifiability analysis ». In: *Hydrological Processes* 17.2, pp. 455–476. DOI: 10.1002/hyp.1135. See pp. 12, 21.

Wagener, T. (2004). « Model identification and evaluation using multiple-objectives and recursive methods ». In: *Uncertainty Analysis in Environmental Modeling workshop held in Lugano, Italy (July 6-8, 2004)*. See p. 19.

Warren, J. and P. Root (1963). « The behavior of naturally fractured reservoirs ». In: *SPE Journal* 3.3, pp. 245–255. DOI: 10.2118/426-PA. See pp. 4, 8.

Wheater, H., A. Jakeman and K. Beven (1993). « Modelling Change in Environmental Systems ». In: ed. by A. Jakeman, M. Beck and M. McAleer. Wiley-Blackwell Publishing, Inc. Chap. Progress and directions in rainfall-runoff modelling, pp. 101–132. See p. 6.

White, W. B. (1988). *Geomorphology and Hydrology of Karst Terrains*. Oxford: Oxford University Press, 464pp. See p. 2.

— (2002). « Karst hydrology: Recent developments and open questions ». In: *Engineering Geology* 65.2-3, pp. 85–105. DOI: 10.1016/S0013-7952(01)00116-8. See p. 2.

Williams, P. W. (2008). « The role of the epikarst in karst and cave hydrogeology: A review ». In: *International Journal of Speleology* 37.1, pp. 1–10. DOI: 10.2307/2423146. See p. 3.

Wilson, J. L. and D. E. Metcalfe (1985). « Illustration and verification of adjoint sensitivity theory for steady state groundwater flow ». In: *Advances in Water Resources* 21.11, pp. 1602–1610. DOI: 10.1029/WR021i011p01602. See p. 15.

Winsemius, H., H. Savenije, A. Gerrits, E. Zapreeva and R. Klees (2006). « Comparison of two model approaches in the Zambezi river basin with regard to model reliability and identifiability ». In: *Hydrology and Earth System Sciences* 10, pp. 339–352. URL: http://www.hydrol-earth-syst-sci.net/10/339/2006/. See p. 21.

Worthington, S. and D. Ford (2009). « Self-organized permeability in carbonate aquifers ». In: *Ground Water* 47.3, pp. 326–336. DOI: 10.1111/j.1745-6584.2009.00551.x. See p. 2.

Wu, Y., X. Wen and Y. Zhang (2004). « Analysis of the exchange of groundwater and river water by using Radon-222 in the middle Heihe basin of northwestern China ». In: *Environmental Geology* 45.5, pp. 647–653. DOI: 10.1007/s00254-003-0914-y. See p. 5.

Yeong-Weisse, A. (2009). « Global sensitivity analysis of ordinary differential equations. Adaptive density propagation using approximate approximations ». PhD thesis. Freie Universität Berlin. URL: http://citeseerx.ist.psu.edu/viewdoc/download?doi=10.1.1.153.8981&rep=rep1&type=pdf. See p. 11.

Zhou, Y. X., C. B. M. Testroet and F. C. Vangeer (1991). « Using Kalman filtering to improve and quantify the uncertainty of numerical groundwater simulations. 2. Application to monitoring network design ». In: *Water Resources Research* 27.8, pp. 1995–2006. DOI: 10.1029/91WR0051. See pp. 20, 21.

Zin, I. (2002). « Incertitudes et ambiguïté dans la modélisation hydrologique ». PhD thesis. INPG. URL: http://hydrologie.org/THE/ZIN.pdf. See pp. 10, 11, 19, 20.

Zou, X., I. Navon and J. Sela (1993). « Variational data assimilation with moist threshold processes using the NMC spectral model ». In: *Tellus A* 45.5, pp. 370–387. DOI: 10.1034/j.1600-0870.1993.t01-4-00004.x. See p. 11.

Part 1. Analysis of global rainfall-discharge models

Introduction to Part 1

This part is devoted to the analysis of the sensitivity properties for global modelling approaches. The main issues addressed are:

(i) is it possible to calibrate the model ?

(ii) is the calibration robust ?

(iii) is it possible to reduce equifinality through multi-variable calibration ?

(iv) is it possible to reduce equifinality through multi-objective calibration ?

(v) what is the optimal degree of complexity associated with global, conceptual rainfall-discharge modelling ?

These questions are addressed using both analytical and empirical sensitivity approaches.

Chapter 2 adresses items (i) and (ii). The perturbation approach is used to investigate the analytical properties of the initialisation bias, depending on the hydrodynamic conditions and the model structure, with the aim to:

- check whether the rules classically adopted for model initialisation can be justified on analytical grounds. Most studies assume that one hydrological year is long enough to ensure the dissipation of the initialisation bias, but the validity of this practice is not assessed,
- assess the influence of model structure on the initialisation bias behaviour,
- assess the influence of the threshold transfer functions on the initialisation bias behaviour. These transfer functions are classically used to account for the pressurized flow connection, which is responsible for the fast component of the catchment response to rainfall events. The threshold functioning is used to account for the influence of karst connectivity on the connectivity of the hydrosystem,
- derive general rules for the choice of the warm-up period based on model structure and hydrological conditions.

Chapter 3 adresses item (iii). It aims to assess the added value of ground-based gravity data to the discharge-based calibration of a global, rainfall-discharge model.

Chapter 4 adresses items (iv) and (v). A conceptual model is proposed for the rainfall-discharge-water level modelling of karst springs under active groundwater management. The model performance is assessed against that of alternative model structures.

Chapter 2

Use of local sensitivity analysis for model structure selection

In this chapter the perturbation approach is used to investigate the analytical properties of the sensitivity to the initial conditions on the calibration and the simulation results of two karst spring discharge reservoir models (Sections 2.1 to 2.8). The propagation of the uncertainty in the initial conditions is shown to depend on both the model structure and the initial values of the state variables. In particular, depending on model structure, non-linearity may either hasten or delay the dissipation of the initialisation bias. The analytical results are confirmed by application examples of real-world simulations. These analytical findings are used to provide general rules for the initialisation bias behaviour depending on model structure. Complementary comments on the analytical properties of the sensitivity to the models parameters are given in Section 2.9. This work is currently in revision for Advances in Water Resources [Mazzilli et al., 2011*c*]. It has also been presented at the ModelCare 2011 Conference held in Leipzig, Germany (Sept. 18-22, 2011) [Mazzilli et al., 2011*d*].

Contents

2.1 Introduction

Numerical models are important tools for groundwater management. Good model development practices include the assessment of model performance but also of model uncertainty and physical realism [Wagener et al., 2004]. This paper focuses on the influence of initial conditions on the calibration and simulation results of two reservoir models for karst spring discharge.

Specifying the initial state of a given model inevitably leads to an initialisation bias in model output, because an experimental assessment of the internal state of lumped models is not possible. If the error on the initial values assigned to the internal variables is too important, the initialisation bias may affect the calibration or the simulation result significantly. Two main approaches are adopted to address the issue of initialisation bias in conceptual hydrological modelling: (i) the calibration of the initial state estimate (by Kalman filter-based [Delft et al., 2009; Refsgaard, 1997; Weerts and El Serafy, 2006] or e.g. variational methods [Seo et al., 2009]), and (ii) the truncation of the model output [Perrin et al., 2001; Tritz et al., 2011]. The calibration method is generally used in an operational flood forecasting context, whereas the output truncation method is usually preferred for continous time modelling for example in groundwater resource management. The output truncation method consists in running the model for a sufficiently long time to make the initialisation bias negligible before retaining data for analysis. The period after which the model output variables become independent from the initialisation bias is called the warm-up period.

A good a priori estimate of the model initial state is required for both the calibration of the initial state [Refsgaard, 1997] and the truncation of the model output. The availability of realistic initial state estimates is all the more challenging as the modelling time scale is short. At the monthly or annual time scale, relevant initial state estimates can be obtained by running the model with mean meteorological inputs until a steady state is reached [Mouelhi, 2003], but such a procedure may turn out to be irrelevant for strongly non-linear models. At the daily time step, the computational cost of the steady state method becomes important and the definition of a mean meteorological time serie is problematic [Le Moine, 2010]. Under certain conditions, the steady state can be estimated by analytical procedures [Le Moine, 2010].

The choice of the calibration or warm-up period is strongly linked to the sensitivity of the model output to the initial conditions. Indeed, calibration should be performed over periods when the model output is sensitive to the calibration parameter. Conversely, the warm-up period should stop as soon as the model output becomes insensitive to the initial state, in order to preserve as

much data as possible for the analysis. The issue of an optimal determination of the warm-up period for reservoir-based models has been little addressed in the literature. So has been the issue of the consequence of an improperly chosen warm-up period on calibration results. This paper investigates the influence of model non-linearity on the sensitivity behaviour based on the local perturbation approach. The perturbation technique provides theoretical insights into the general behaviour of the sensitivity to the initial conditions. The analysis is carried out for two reservoir models that have both been validated on the application site selected for this study by previous authors [Fleury, 2005; Tritz et al., 2011]. The main issues addressed are: (i) does model structure have consequences on the length of the warm-up period, (ii) can guidelines be defined for the choice of the warm-up period, so as to minimize the impact of the initialisation bias on model calibration ?

The present work is structured in the following way. The application site is presented in Section 2.2. Sections 2.2.3 and 2.2.2 details the structure and governing equations for the Vensim and the hysteresis-based models respectively. Section 2.3 briefly presents the perturbation approach used for the derivation of the sensitivity equations and the sensitivity for two rainfall-discharge models specifically designed for karst system modelling. The sensitivity properties are and exemplified by real-world applications in Section 2.4. Section 2.5 focuses on the estimation of the uncertainty on the calibration results. Section 2.6 is devoted to a discussion and Section 2.7 is devoted to the conclusion and to practical recommandations.

2.2 Application site and models

2.2.1 Site and data

The Durzon karst system is located in the Grands Causses area in the Southern Massif Central (France). This Vauclusian karst system is embedded in a 400m thick formation of middle to upper Jurassic limestones and dolomites, deposited on top of a 200m thick formation of upper-Liassic marls [Bruxelles, 2001]. This latter formation constitutes the aquifer bedrock. The North Eastern and Southern boundaries of the system are delimited by thrust faults. The other boundaries are delimited by the topography. The main outlet of the catchment is the Durzon spring, which is located in the Northern part of the catchment (see Figure 2.1). The recharge area estimates range from 100 to 120km^2 based on geomorphological characteristics, mass balance and tracing experiments [Bruxelles, 2001; Ricard and Bakalowicz, 1996]. Following Fleury, 2005 and Tritz et al., 2011, a recharge area of 116.8km^2 is used in the present study.

Discharge data is available for the catchment main outlet only. The Durzon spring discharges measured over the 2001-2008 period range from 0.5 to 18m^3/s, with an average 1.4m^3/s. Note that since the measured variable is the water level at the spring pool, discharge values must be derived by application of a stage-discharge relationship [Tritz et al., 2011]. The stage-discharge relationship is fitted on in situ measurements. Various fitting criteria may yield equally acceptable stage-discharge relationships. For a given water level, the comparison of discharge values obtained using different fitting criteria yields an uncertainty of about 3% on the discharge value [Tritz et al., 2011].

Meteorological data are measured at the “Le Caylar” Meteo-France meteorological station, some 10km S-SE of the Durzon spring. The average annual rainfall for the 2001-2008 period is 1069mm. The average daily temperatures range from -8 to +28°C. The average annual temperature is 10°C. The daily potential evapotranspiration is estimated from the monthly potential evapotranspiration (computed using Thornthwaite’s formula [Thornthwaite, 1948]) using a sine function-based

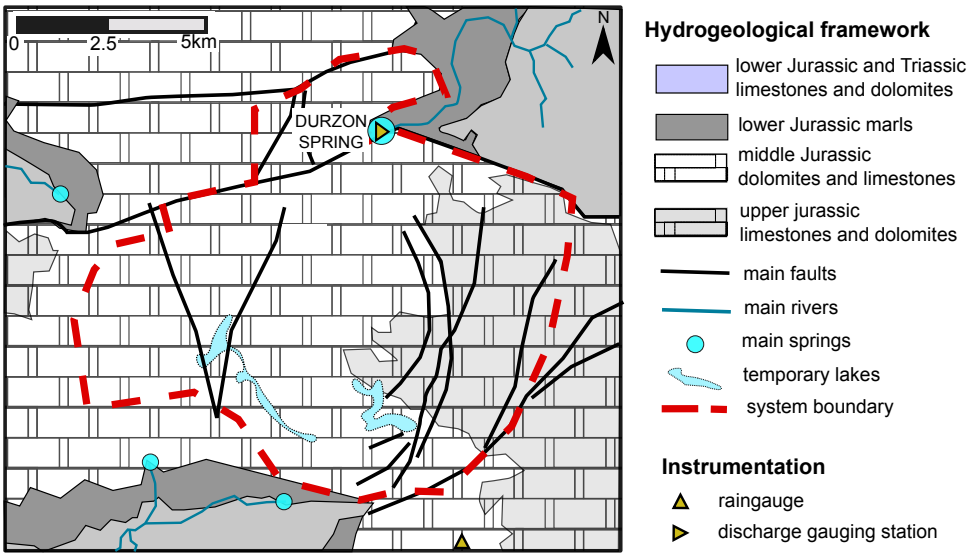

Figure 2.1: Hydrogeological framework and instrumentation of the Durzon area. Modified after Bruxelles, 2001; Jacob, 2009; Ricard and Bakalowicz, 1996.

interpolation, as proposed in Tritz et al., 2011

$$\mathrm{PET}(t) = \left[1 - a\,cos\left(2\pi\frac{t - t_{\min}}{T}\right)\right]\overline{\mathrm{PET}} \tag{2.1}$$

where t is the time where the PET is to be interpolated, $\overline{\mathrm{PET}}$ is the average value of the PET series computed from Thornthwaite's formula, T is the period of the PET signal (one year), $t_{\min}$ is the time at which the PET is minimum and a is the dimensionless amplitude of the signal. The parameters $t_{\min}$ and a have been estimated by means of a classical least-squares optimization procedure by Tritz et al., 2011 (see parameter values in Table 2.1 and see PET time series in Figure 2.2).

2.2.2 Hysteresis-based model

The hysteresis-based model (Figure 2.3a) has been proposed in Tritz et al., 2011 and validated for the simulation of the Durzon karst spring discharge. The hysteresis-based model is made of two reservoirs. The upper reservoir H represents the epikarst and soil zones. The lower reservoir L represents the saturated and vadose zones. The model functioning may be described as follows.

1. The epikarst reservoir H receives the incoming precipitations and is affected by evapotranspiration. Note that the epikarst reservoir may fall dry.
2. Part of the water contained in the reservoir H leaks to the lower reservoir L (discharge Q_{HL}) via a linear discharge relationship. This flux accounts for the classical recharge process to the saturated zone.

Symbol	Meaning	Value
a	Dimensionless amplitude of the sine wave	0.8
$t_{\min}$	Time of minimum PET	15 January
T	Period of the interpolation function	1yr
$\overline{\mathrm{PET}}$	Average potential evapotranspiration rate	1.95mm/d

Table 2.1: Parameters for the potential evapotranspiration model.

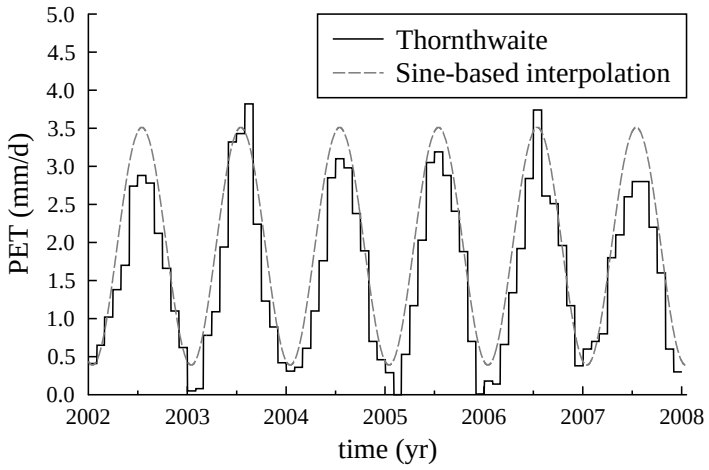

Figure 2.2: Potential evapotranspiration rate. Black line: monthly values computed using Thornthwaite's formula. Grey line: daily values interpolated based on equation (2.1) [Tritz et al., 2011].

3. Part of the water contained in H may flow outside of the catchment (discharge Q_{sec}), provided that the water level in H exceeds a given threshold H_{sec}. This flux accounts for the activation of temporary, secondary springs when the connectivity of the epikarst zone is sufficient.
4. Part of the water contained in H may flow directly to the outlet of the catchment (discharge Q_{HY}). Physically, such a connection is allowed by a network of fractures and karst conduits. It is responsible for the fast component of the catchment response to rainfall events.
5. The water in the lower reservoir L leaks to the outlet of the catchment (discharge Q_L) via a classical, linear discharge relationship.

The nonlinear, hysteretic transfer function used to model the discharge Q_{HY} constitutes the main originality of the model. As in most models, the water level in the epikarst reservoir H must reach a given threshold H_2 before the connectivity of the karst system becomes nonzero and the fast response flow Q_{HY} is initiated. However, karst connectivity is preserved until the water level in H drops below a lower threshold $H_1 < H_2$ (hysteretic transfer). This behaviour can be compared to that of a siphon. It traduces the fact that, for a given matric potential, the water content (and thus the connectivity of the medium) is higher during the drying cycle than during the wetting cycle. The nonlinear function used to model Q_{HY} accounts for the influence of the amount of water stored in the soil and epikarst reservoir on the conveyance area of the flow.

The mass balance equations of the hysteresis-based model are the following:

$$\frac{\mathrm{d}H}{dt} = \begin{cases} P - \mathrm{ET} - Q_{\text{sec}} - Q_{\text{HY}} - Q_{\text{HL}} & \text{if } H > 0 \\ \max(P - \mathrm{ET}, 0) & \text{if } H = 0 \end{cases} \tag{2.2a}$$

$$\frac{\mathrm{d}L}{dt} = Q_{\text{HL}} - Q_{\text{L}} \tag{2.2b}$$

where H and L are the water levels in the reservoirs H and L respectively, P is the precipitation rate, ET is the evapotranspiration rate, Q_{sec} is the secondary springs discharge, Q_{HY} is the fast flow component through the epikarst zone to the outlet of the catchment, Q_{HL} is the infiltration rate to the lower reservoir and Q_{L} is the baseflow discharge from the lower reservoir L to the outlet of the catchment. Note that discharges are expressed as specific discharge. Both the evapotranspiration and the infiltration stop when the water level reaches the minimum value $H = 0$ (see equation (2.2a)), which prevents the reservoir from becoming too seriously under-saturated.

The internal fluxes are assumed to obey the following relationships

$$Q_{\text{sec}} = \varepsilon_{\text{sec}} k_{\text{sec}} (H - H_{\text{sec}}) \tag{2.3a}$$

$$Q_{\text{HY}} = \varepsilon_{\text{HY}} k_{\text{HY}} \left(\frac{H - H_1}{H_2 - H_1} \right)^{\alpha} \tag{2.3b}$$

$$Q_{\text{HL}} = k_{\text{HL}} H \tag{2.3c}$$

$$Q_{\text{L}} = k_{\text{L}} L \tag{2.3d}$$

where k_{sec}, k_{HY}, k_{HL} and k_L are specific discharge coefficients, α is a positive exponent, H_{sec} is the threshold level in reservoir H above which the secondary springs are activated, H_1 and H_2 are the lower and upper threshold levels for the hysteretic discharge function respectively, and ε_{sec} and ε_{HY} are indicators of the secondary springs activation and of the karst system connectivity respectively. The fact that the baseflow discharge Q_{L} is modeled by a linear discharge relationship (see equation (2.3d)) means that the reservoir L cannot fall dry. The indicator of the secondary springs activation ε_{sec} is defined as

$$\varepsilon_{\text{sec}} = \begin{cases} 1 & \text{if } H > H_{\text{sec}} \\ 0 & \text{if } H \leq H_{\text{sec}} \end{cases} \tag{2.4}$$

The indicator of the karst system connectivity is switched to 1 if H rises above H_2 and it is switched to 0 if H falls below H_1

$$\left.\begin{array}{ll} \varepsilon_{\text{HY}} & = 0 \\ H & = H_2 \end{array}\right\} \Rightarrow \varepsilon_{\text{HY}} = 1 \tag{2.5a}$$

$$\left.\begin{array}{ll} \varepsilon_{\text{HY}} & = 1 \\ H & = H_1 \end{array}\right\} \Rightarrow \varepsilon_{\text{HY}} = 0 \tag{2.5b}$$

The actual evapotranspiration rate is assumed to be equal to the potential evapotranspiration rate as long as the soil-epikarst reservoir H is not empty

$$\text{ET} = \begin{cases} \text{PET} & \text{if } H > 0 \\ 0 & \text{if } H = 0 \end{cases} \tag{2.6}$$

The discharge at the outlet of the catchment Q is defined as the sum of the epikarstic Q_{HY} and baseflow Q_L discharges, multiplied by the total area of the catchement A.

$$Q = A(Q_{\text{HY}} + Q_L) \tag{2.7}$$

2.2.3 Vensim model

The Vensim model has been proposed in Fleury, 2005. It is based on the Bemer [Bézès, 1976] and Medor [Hreiche, 2003] models. The model has been validated over four karst springs located on the Larzac plateau [Fleury, 2005]. In the following, this model will be termed the Vensim model from the modelling platform used for its implementation by Fleury, 2005.

The Vensim model is made of three reservoirs (see model structure in Figure 2.3b). The upper reservoir H represents the soil zone. The lower reservoir S accounts for the long-time storage that occurs mainly within the saturated zone. The lower reservoir R accounts for the rapid infiltration towards the outlet through fractures and karst conduits. Possible secondary springs are neglected. The model functioning may be described as follows.

1. The epikarst reservoir H receives the incoming precipitations and is affected by evapotranspiration. Evapotranspiration stops when the water level reaches a minimum value H_{min}.

2. Part of the water contained in the reservoir H leaks to the lower reservoirs S and R, provided that the water level in H is larger than zero. Note that the infiltration from the reservoir H to the reservoirs H and S is modeled as an all-or-nothing process.
3. The distribution of Q_{H} between the S and R reservoirs depends on the water level in the reservoir S. When the water level in S rises above a threshold value S_{sill}, the proportion of water routed to the reservoir R increases. This accounts for the influence of the karst connectivity on the catchment response.
4. The water in the lower reservoirs S and R leaks to the outlet of the catchment via classical, linear discharge relationships.

The use of threshold transfer functions in both the Vensim and the hysteresis-based models is justified by the consideration of the threshold transfer process within the karst system [Blavoux et al., 1992; Bonacci, 2007; Pulido-Bosch et al., 1995]. However, the models differ in the conceptualization of the threshold transfer. In particular, in the Vensim model the switch in the distribution coefficient is associated with the water level in the long-term storage, saturated zone reservoir. In the hysteresis-based model, all threshold transfer functions are associated with the water level in the soil-epikarst reservoir. Note that the time constants associated with the saturated zone and the soil-epikarst reservoirs are expected to differ by at least one order of magnitude. The implications of this on the sensitivity behaviour are discussed in Section 2.3.

The mass balance equations of the Vensim model are the following:

$$\frac{\mathrm{d}H}{dt} = \begin{cases} P - \mathrm{ET} - Q_{\mathrm{H}} & \text{if } H_{\min} < H \leq 0 \\ \max(P - \mathrm{ET}, 0) & \text{if } H = H_{\min} \end{cases} \tag{2.8a}$$

$$\frac{\mathrm{d}S}{dt} = XQ_{\mathrm{H}} - Q_{\mathrm{S}} \tag{2.8b}$$

$$\frac{\mathrm{d}R}{dt} = (1 - X)Q_{\mathrm{H}} - Q_{\mathrm{R}} \tag{2.8c}$$

with

$$X = \begin{cases} X_{\mathrm{D}} & \text{if } S \leq S_{\mathrm{sill}} \\ X_{\mathrm{W}} & \text{if } S > S_{\mathrm{sill}} \end{cases} \tag{2.9}$$

H, R and S are the water levels in the reservoir H, R and S respectively, P is the precipitation rate, ET is the evapotranspiration rate, $H_{\min}$ is the minimum water level admissible in the reservoir H, Q_{H} is the total discharge rate from the reservoir H towards the rapid and slow drainage reservoirs, Q_{R} and Q_{S} are the discharge rates from the reservoirs R and S respectively, X_{W} and X_{D} are the distribution coefficients for Q_{H} in high and low water level periods respectively ($X_{\mathrm{D}} > X_{\mathrm{W}}$) and S_{sill} is the threshold level that triggers the switch in the distribution coefficient. The internal fluxes are assumed to obey the following relationships

$$Q_{\mathrm{H}} = \varepsilon_{\mathrm{H}} \max(P - \mathrm{ET}, 0) \tag{2.10a}$$

$$Q_{\mathrm{S}} = k_{\mathrm{S}} S \tag{2.10b}$$

$$Q_{\mathrm{R}} = k_{\mathrm{R}} R \tag{2.10c}$$

where k_{R} and k_{S} are specific discharge coefficients and ε_{H} is defined by the following relation

$$\varepsilon_{\mathrm{H}} = \begin{cases} 1 & \text{if } H = 0 \\ 0 & \text{if } H < 0 \end{cases} \tag{2.11}$$

The discharge at the outlet of the catchment Q is defined as the sum of the specific discharges Q_{R} and Q_{S}, multiplied by the total area of the catchement A.

$$Q = A(Q_{\mathrm{R}} + Q_{\mathrm{S}}) \tag{2.12}$$

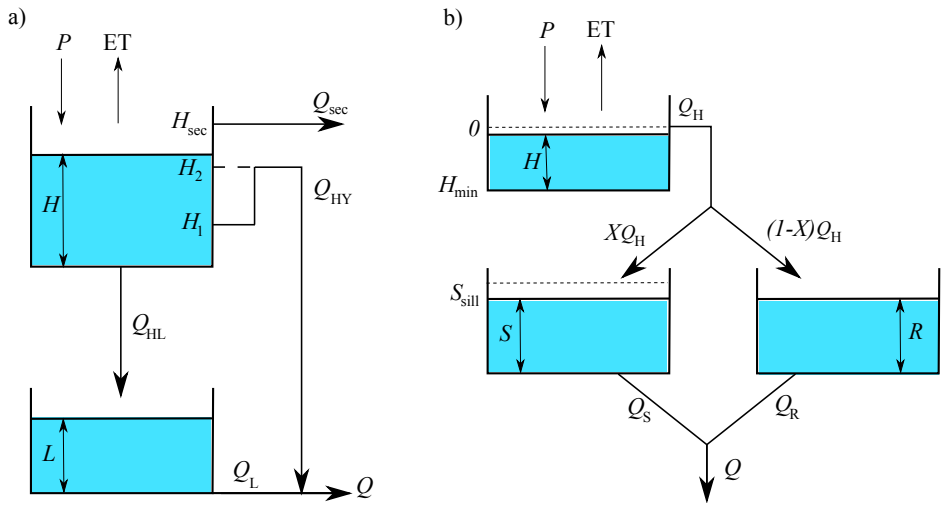

Figure 2.3: Structure and notations for: a) the hysteresis-based model [Tritz et al., 2011], b) the Vensim model [Fleury, 2005].

2.3 Sensitivity analysis

2.3.1 Presentation of the perturbation approach

The perturbation approach is based upon a linear approximation of the model equations in the vicinity of a central value. The approach provides an in-depth insight into the model behaviour, at little computational cost. A short presentation of the perturbation method is given hereafter. More details on sensitivity calculation can be found in e.g. Cacuci, 2003.

The sensitivity equations are derived by carrying out a perturbation analysis of the model equations. Let ϕ be the parameter with respect to which the sensitivity analysis is carried out. The model balance equations (2a-b) and (8a-c)can be rewritten in a more general manner as

$$\frac{\partial U}{\partial t} = f(U, \phi, t) \tag{2.13}$$

where U is the variable vector and ϕ is the parameter vector. Differentiating equation (2.13) with respect to ϕ leads to

$$\frac{\partial}{\partial t}\left(\frac{\partial U}{\partial \phi}\right) = \frac{\partial f}{\partial U}\frac{\partial U}{\partial \phi} + \frac{\partial f}{\partial \phi} \tag{2.14}$$

The sensitivity of the variable U to the parameter ϕ is defined as $\mathcal{U}_\phi \equiv \partial U/\partial\phi$. Then equation (2.14) may be rewritten as

$$\frac{\partial \mathcal{U}_\phi}{\partial t} = \frac{\partial f}{\partial U}\mathcal{U}_\phi + \frac{\partial f}{\partial \phi} \tag{2.15}$$

Similarly, the discharge Q at the outlet can be expressed as

$$Q = Q(U, \phi, t) \tag{2.16}$$

The sensitivity of the discharge Q to the parameter ϕ is defined as $\mathcal{Q}_\phi \equiv \partial Q/\partial\phi$. Differentiating equation (2.16) with respect to parameter ϕ leads to

$$\mathcal{Q}_\phi = \frac{\partial Q}{\partial U}\mathcal{U}_\phi + \frac{\partial Q}{\partial \phi} \tag{2.17}$$

2.3.2 General sensitivity properties for the hysteresis-based model

The sensitivity equations are derived using the perturbation approach presented in Section 2.3.1. The sensitivity equations are detailed in 2.8.1.

2.3.2.a Sensitivity to L_0

The impact of the initial level L_0 on the simulated spring discharge decreases exponentially with a time constant $T = 1/k_{\mathrm{R}}$. Note that neither the activation of the hysteretic transfer nor the activation of the secondary springs nor the drying of the reservoir H have an impact on the sensitivities to the initial level L_0.

2.3.2.b Sensitivity to H_0

Assume that neither the hysteretic transfert nor the secondary springs are activated. Also assume that the reservoir H does not dry out ($H > 0$). Then the governing equations for the sensitivity of H, L and Q to the initial water level H_0 in the reservoir H may be solved analytically, leading to

$$\mathcal{H}_{H_0} = \exp(-k_{\mathrm{HL}} t) \tag{2.18a}$$

$$\mathcal{L}_{H_0} = \frac{k_{\mathrm{HL}}}{k_L - k_{\mathrm{HL}}} \left(\exp(-k_{\mathrm{HL}} t) - \exp(-k_L t)\right) \tag{2.18b}$$

$$\mathcal{Q}_{H_0} = A \frac{k_{\mathrm{HL}} k_L}{k_L - k_{\mathrm{HL}}} \left(\exp(-k_{\mathrm{HL}} t) - \exp(-k_L t)\right) \tag{2.18c}$$

The sensitivity of the spring discharge to H_0 reaches its maximum at time $t_{\max} = \ln(k_L/k_{\mathrm{HL}})/(k_L - k_{\mathrm{HL}})$.

The activation of the rapid transfer functions (hysteretic transfer or of the secondary springs) result in a faster decrease in $\mathcal{H}_{H_0}$ (see equation (2.26a)). It is also associated with an increase in the sensitivity $\mathcal{Q}_{H_0}$ (see equation (2.26d)). Heavy rainfall events therefore help erasing the influence of the initial water level H_0. In other words, heavy rainfall events make the minimal warm-up period shorter. However, since the influence of H_0 on the spring discharge Q is increased during these rainfall events, care should be taken not to include these events within the calibration period.

The drying of the reservoir H results in the cancellation of $\mathcal{H}_{H_0}$ (see equation (2.27a)). After the emptying of the reservoir H, the sensitivities $\mathcal{L}_{H_0}$ and $\mathcal{Q}_{H_0}$ decrease exponentially. Also note that subsequent filling of the reservoir H and the possible activation of the rapid transfert function will have no impact on the discharge sensitivity $\mathcal{Q}_{H_0}$. A complete emptying of the reservoir H therefore prevents the simulated discharge from subsequent artefacts due to a burst in $\mathcal{H}_{H_0}$ during the activation of the hysteretic transfer function.

2.3.3 General sensitivity properties for the Vensim model

The sensitivity equations are derived using the perturbation approach presented in Section 2.3.1. The sensitivities of the water levels in the reservoirs H, S and R to the parameter ϕ are denoted by $\mathcal{H}_\phi$, $\mathcal{S}_\phi$ and $\mathcal{R}_\phi$ respectively. The sensitivity equations are given in 2.8.2.

2.3.3.a Sensitivity to R_0

The impact of the initial level R_0 on the simulated spring discharge decreases exponentially with a time constant $T = 1/k_{\mathrm{R}}$. Note that neither the activation of the hysteretic transfer nor the activation of the secondary springs nor the drying of the reservoir H have an impact on the sensitivities to the initial level R_0.

2.3.3.b Sensitivity to S_0

The particularity of the Vensim model lies in the fact that the value of the distribution coefficient X depends on the water level in the reservoir S. This means that that the sensitivity of the level R to the initial water level in S is non-zero (see equation (2.29c)).

Assume that the threshold S_{sill} is not activated. Then the behaviour of the sensitivity to S_0 is similar to that of the sensitivity to R_0. The impact of the initial level S_0 on the simulated spring discharge decreases exponentially with a time constant $T = 1/k_{\text{S}}$.

The activation of the threshold S_{sill} results in a decrease in $\mathcal{S}_{S_0}$ and in an increase in $\mathcal{R}_{S_0}$, based on equations (2.29b) and (2.29c) (see Figure 2.4b). The activation of the threshold S_{sill} thus hastens the disappearance of the influence of the initial condition S_0. On the other hand, an activation of S_{sill} results in a pulse for the sensitivity $\mathcal{R}_{S_0}$ of the water level in the reservoir R and therefore in a pulse for the sensitivity $\mathcal{Q}_{S_0}$ of the spring discharge.

The de-activation of the threshold S_{sill} has no impact on the behaviour of the sensivities to S_0 (see Figure 2.4b and see proof in Appendix 2.8.2).

2.3.3.c Sensitivity to H_0

The reservoir H differs from the reservoirs S and R in that its response is all-or-nothing. The sensitivity $\mathcal{H}_{H_0}$ is piecewise constant (see Figure 2.5). It is equal to one at the beginning of the simulation and it cancels when the reservoir H overflows for the first time ($\varepsilon_H = 1$ at time $t = t_H$) or when it dries out ($H = H_{\min}$) (see Figure 2.5). Consider the case where H has not dried out. Then the first activation of the overflow triggers a pulse in the sensitivities $\mathcal{S}_{H_0}$ and $\mathcal{R}_{H_0}$ (see terms $X\partial Q_{\text{H}}/\partial H_0$ and $(1-X)\partial Q_{\text{H}}/\partial H_0$ in equations (2.28c) and (2.28d) respectively, and see Figure 2.4c). On the contrary, a complete emptying of the reservoir H before the first overflow completely stops the propagation of the sensitivity to H_0 towards the reservoirs S and R. Also note that a simulation that begins with a low water period with no complete emptying of the reservoir H only delays the propagation of the sensitivity to H_0 within the model (see Figure 2.5b). Last, a complete emptying of the reservoir H after the first overflow has no impact on the propagation of the sensitivity to H_0.

Consider the case where the first activation of the overflow happens before the reservoir H dries out. If the threshold S_{sill} is not activated, then for $t \geq t_H$ the sensitivities $\mathcal{S}_{H_0}$ and $\mathcal{R}_{H_0}$ decrease exponentially. The activation of the threshold S_{sill} results in a decrease in $\mathcal{S}_{H_0}$ and in an increase in $\mathcal{R}_{H_0}$ (see Figure 2.4c).

2.4 Computational examples

The analysis of the sensitivity behaviour undertaken in Section 2.3 is valid regardless of the particular values assigned to the parameters. The following computational examples aim at illustrating some features of the sensitivity behaviour as a function of model structure. The sensitivity equations are solved numerically using an explicit Euler scheme. The parameter set used for the simulations is the one proposed by Tritz et al., 2011 (see parameters in Tables 2.4 and 2.2). For each example the simulation starts from a different time. The initial conditions are modified accordingly (see values in Tables 2.5 and 2.3).

2.4.1 Computational example 1

The first case tested is that of the time series used in Tritz et al., 2011. The simulation starts on 1 January 2002. The internal water levels are presented in Figure 2.6.1.

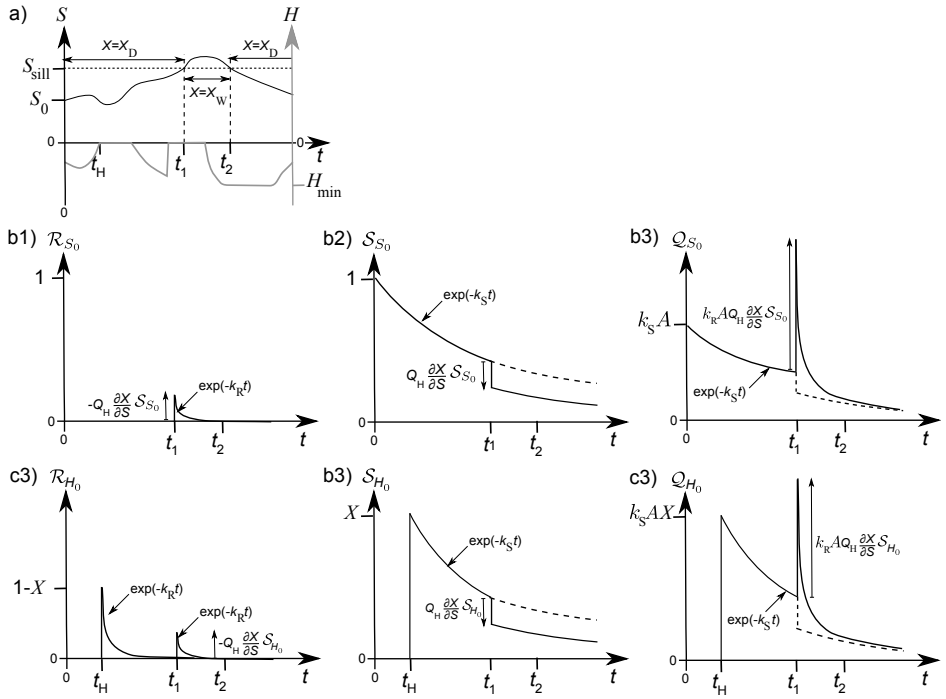

Figure 2.4: Vensim model. Typical behaviour of the sensitivities to H_0 and S_0 contingent on the reservoir H overflow and on the activation of the switch in the distribution coefficient. The reservoir H overflows for the first time at time t_H. The threshold S_{sill} is activated at time t_1 and desactivated at time t_2. Graph a): water level in the reservoirs S (dark line) and H (bold, grey line), Graphs b): sensitivity of R (graph b1), S (graph b2) and Q (graph b3) to the initial condition S_0, Graphs c): sensitivity of R (graph c1), S (graph c2) and Q (graph c3) to the initial condition H_0. Note that the value of $\mathcal{Q}_{H_0}$ by the time of the first overflow is independent from the magnitude of the rainfall event that triggers the overflow.

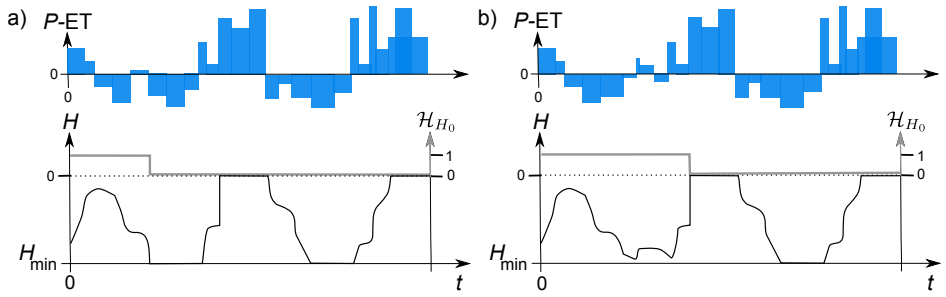

Figure 2.5: Vensim model. Typical behaviour of the sensitivities to the initial water level H_0 contingent on the activation or de-activation of the rapid tranfer function: a) complete emptying of the reservoir H before the first overflow, b) no emptying of the reservoir H before the first overflow.

Symbol	Meaning	Value
H_{sec}	threshold level for secondary spring activation	145mm
k_{sec}	specific discharge coefficient for the secondary springs discharge function	2.9×10^{-2}/d
H_1	lower threshold level for the hysteretic discharge function	100mm
H_2	upper threshold level for the hysteretic discharge function	119mm
k_{HY}	specific discharge coefficient for the hysteretic discharge function	2×10^{-2}mm/d
α	exponent for the hysteretic discharge function	2.4
k_{HL}	specific discharge coefficient for the infiltration to the lower reservoir	7×10^{-3}/d
k_{L}	specific discharge coefficient for the baseflow discharge	4×10^{-3}/d

Table 2.2: Hysteresis-based model. Parameter set used in Section 2.4, 2.5.2 and 2.5.4.

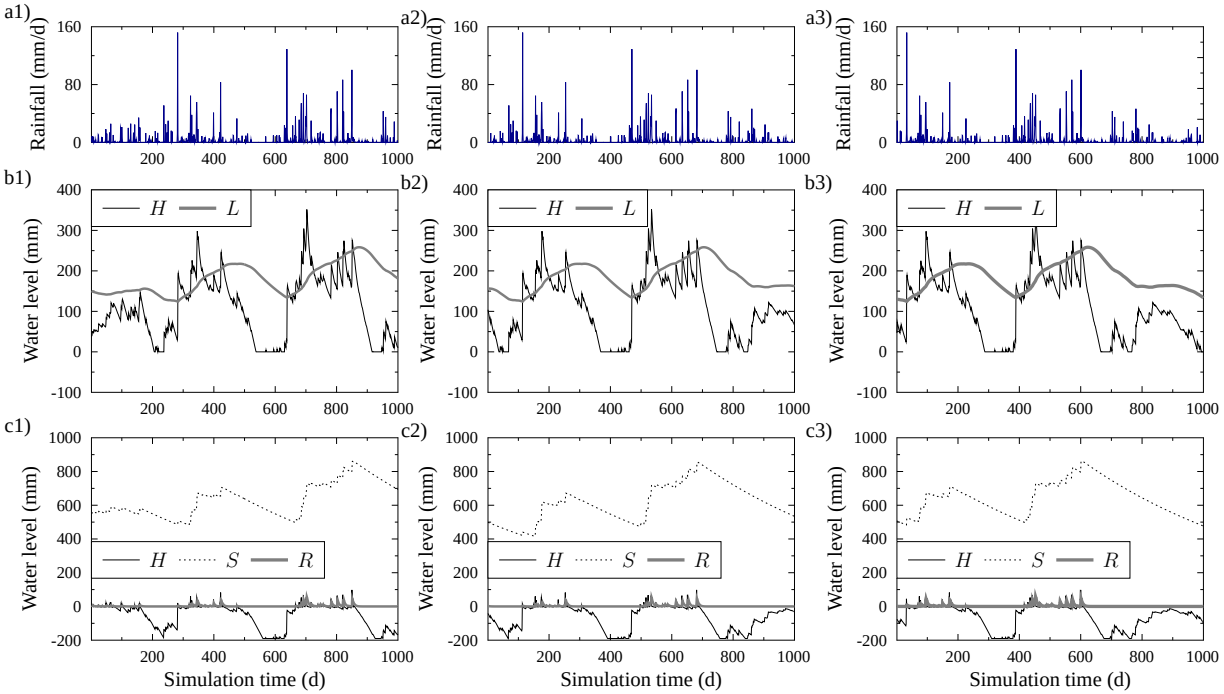

Figure 2.6: Daily rainfall (graphs a) and simulated water levels for the hysteresis-based (graphs b) and Vensim (graphs c) models for: the computational example 1 (graphs 1), the computational example 2 (graphs 2), the computational example 3 (graphs 3).

Example	Symbol	Meaning	Value
1	H_0	initial water level in the reservoir H	40mm
	L_0	initial water level in the reservoir L	150mm
2	H_0	initial water level in the reservoir H	108mm
	L_0	initial water level in the reservoir L	156mm
3	H_0	initial water level in the reservoir H	50mm
	L_0	initial water level in the reservoir L	130mm

Table 2.3: Hysteresis-based model. Initial conditions used in Section 2.4, 2.5.2 and 2.5.4.

Symbol	Meaning	Value
$H_{\min}$	minimum water level admissible in the reservoir H	-190mm
X_{D}	distribution coefficient in low water level	0.81
X_{W}	distribution coefficient in high water level	0.24
S_{sill}	threshold level for the switch in the distribution coefficient	600mm
k_{S}	specific discharge coefficient for the reservoir S discharge function	1.5×10^{-3}/d
k_{R}	specific discharge coefficient for the reservoir R discharge function	1.8×10^{-1}/d

Table 2.4: Vensim model. Parameter set used in Sections 2.4, 2.5.3 and 2.5.4.

Example	Symbol	Meaning	Value
1	H_0	initial water level in the reservoir H	5mm
	S_0	initial water level in the reservoir S	550mm
	R_0	initial water level in the reservoir R	50mm
2	H_0	initial water level in the reservoir H	-35mm
	S_0	initial water level in the reservoir S	500mm
	R_0	initial water level in the reservoir R	0mm
3	H_0	initial water level in the reservoir H	-100mm
	S_0	initial water level in the reservoir S	508mm
	R_0	initial water level in the reservoir R	1mm

Table 2.5: Vensim model. Initial conditions used in Sections 2.4, 2.5.3 and 2.5.4.

Consider the hysteresis-based model model. Figure 2.7a shows the sensitivities to the initial water levels in the reservoirs H and L. The sensitivities $\mathcal{L}_{Lo}$ and $\mathcal{Q}_{Lo}$ decrease exponentially as stated in Section 2.3.2.a. The activation of the hysteretic transfer on days 70, 110 and 160 results in a decrease of $\mathcal{H}_{H_0}$ and in an increase of $\mathcal{Q}_{H_0}$ as predicted in Section 2.3.2.b. Note that the magnitude of both the decrease in $\mathcal{H}_{H_0}$ and the increase in $\mathcal{Q}_{H_0}$ remains limited, which must be related to the fact that the rainfall remains low. The drying of reservoir H at day 205 results in a sudden drop of $\mathcal{H}_{H_0}$ and in a change in the derivatives of $\mathcal{L}_{H_0}$ and $\mathcal{Q}_{H_0}$.

Consider now the Vensim model. Figure 2.7b shows the sensitivities to the initial water level in the reservoir S. Up to day 375, the sensitivity of the water level in R to S_0 is equal to zero and the sensitivity of the water level in S to S_0 decreases exponentially. The activation of the switch in the distribution coefficient (activation of the threshold S_{sill}) at days 375 and 700 results in a sudden decrease in $\mathcal{S}_{S_0}$, and in a sudden increase in $\mathcal{R}_{S_0}$ as stated in Section 2.3.3. The increase in $\mathcal{R}_{S_0}$ triggers an increase in the discharge sensitivity $\mathcal{Q}_{S_0}$. Note that the de-activation of the threshold S_{sill} at day 550 has no impact on the sensitivities behaviour, which confirms the analysis of Section 2.3.3.b. Figure 2.7c shows the sensitivities to the initial water level in the reservoir H. The reservoir H is overflowing at the beginning of the simulation ($t_H = t_0$). The sensitivities $\mathcal{S}_{H_0}$ and $\mathcal{R}_{H_0}$ decrease exponentially until the threshold S_{sill} is activated. The activation of S_{sill} results in a decrease in $\mathcal{S}_{H_0}$ and in an increase in $\mathcal{R}_{H_0}$ and $\mathcal{Q}_{H_0}$, as predicted in Section 2.3.3.c.

For both models, the maximum discharge sensitivity values are reached during the activation of the threshold transfer functions. As for the hysteresis-based model, the drying of the reservoir H during the warm-up year prevents the simulated discharge from any subsequent sensitivity burst. On the contrary , discharge sensitivity bursts for the Vensim model are triggered by any activation of the S_{sill} threshold. Also note that the maximum discharge sensitivity values for the Vensim model are approximately one order of magnitude higher than those of the hysteresis-based model.

2.4.2 Computational example 2

The second computational example starts on 19 June 2002. The rainfall time serie starts with a low water period, followed by a heavy rainfall event. The internal water levels are presented in Figure 2.6.2.

Consider the hysteresis-based model. Figure 2.8a shows the sensitivities to the initial water levels in the reservoirs H and L as a function of the simulation time. The sensitivities $\mathcal{L}_{Lo}$ and $\mathcal{Q}_{Lo}$ decrease exponentially. The complete emptying of the reservoir H at day 45 results in a brutal drop in the sensitivities to H_0.

Consider the Vensim model. Figure 2.8b shows the sensitivities to the initial water level in the reservoir S. The successive activations of the threshold S_{sill} from day 190 to day 220 result in a

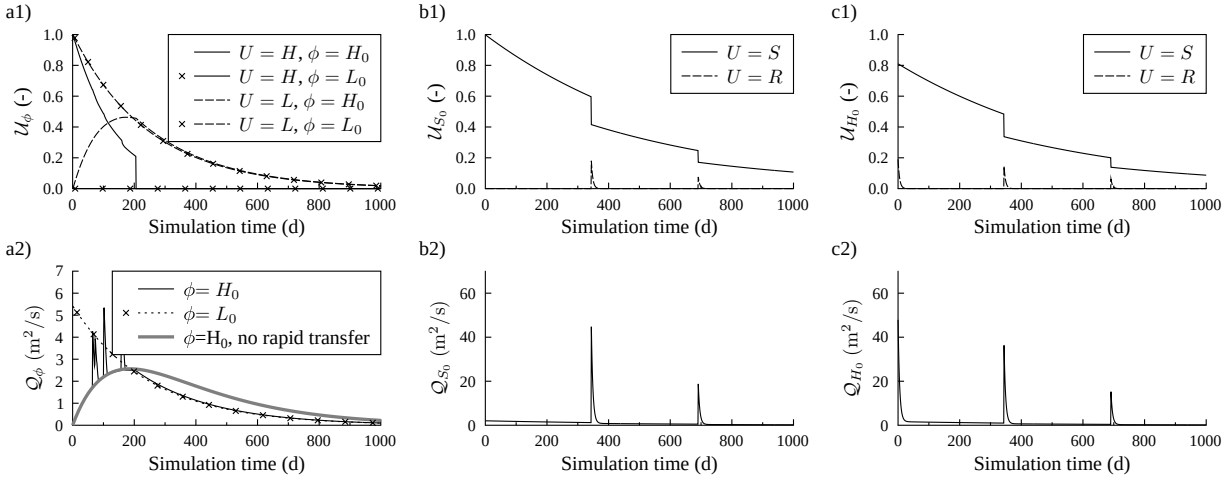

Figure 2.7: Computational example 1. Graphs a): hysteresis-based model. Sensitivity of the simulated water levels (graph 1) and of the simulated discharge (graph 2) to H_0 and L_0. Graphs b): Vensim model. Sensitivity of the simulated water levels (graph 1) and of the simulated discharge (graph 2) to S_0. Graphs c): Vensim model. Sensitivity of the simulated water levels (graph 1) and of the simulated discharge (graph 2) to H_0. The simulation parameters are given in Tables 2.2 and 2.4.

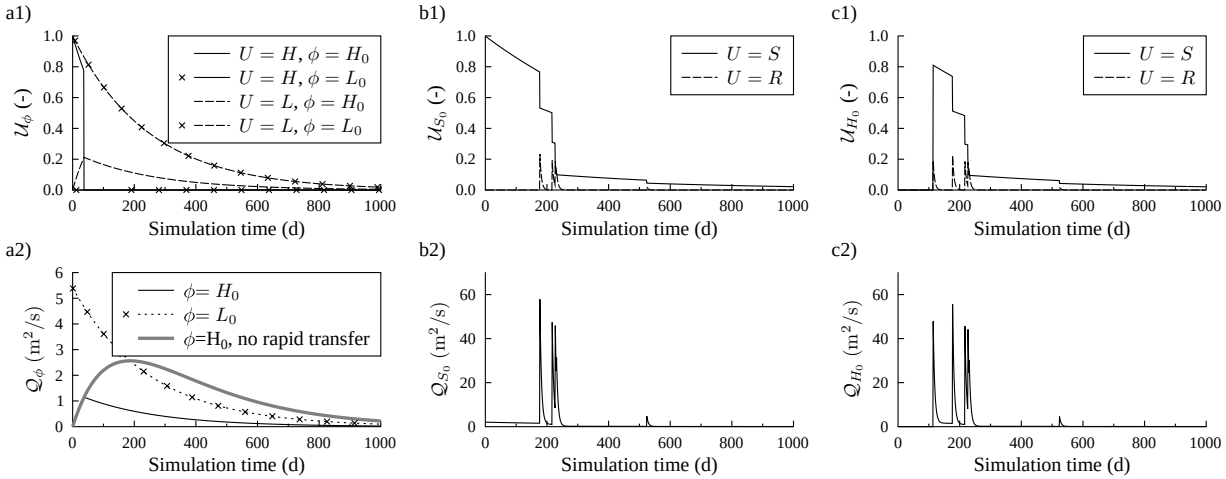

Figure 2.8: Computational example 2. Graphs a): hysteresis-based model. Sensitivity of the simulated water levels (graph 1) and of the simulated discharge (graph 2) to H_0 and L_0. Graphs b): Vensim model. Sensitivity of the simulated water levels (graph 1) and of the simulated discharge (graph 2) to S_0. Graphs c): Vensim model. Sensitivity of the simulated water levels (graph 1) and of the simulated discharge (graph 2) to H_0. The simulation parameters are given in Tables 2.2 and 2.4.

strong decrease in $\mathcal{S}_{S_0}$ as compared to simulation 1, but also in sensitivity bursts for the simulated water level in R and for the spring discharge Q. Figure 2.8c shows the sensitivities of the water levels and of the spring discharge to the initial water level in the reservoir H. The sensitivities to H_0 are equal to zero until the first overflow of the reservoir H (day 110). The behaviour of the sensitivities to H_0 against the activations of the threshold S_{sill} after the first overflow is similar to that of the sensitivities to S_0, as stated in Section 2.3.3.c.

The fact that the simulation begins with a low water period has different consequences for the Vensim and the hysteresis-based models. The low water period delays the propagation of the sensitivity to H_0 for the Vensim model. On the contrary, for the hysteresis-based model the sensitivity to H_0 leaks towards the lower reservoir and the simulated discharge from the beginning of the simulation on.

2.4.3 Computational example 3

The last computational example starts on 8 September 2002. The rainfall time serie starts with a drought period, which is followed by a heavy rainfall event. The internal water levels are presented in Figure 2.6.3.

Consider the hysteresis-based model. Figure 2.9a shows the sensitivities to the initial water levels in the reservoirs H and L as a function of the simulation time. The sensitivities $\mathcal{L}_{Lo}$ and $\mathcal{Q}_{Lo}$ to the initial water level in L decrease exponentially as stated in Section 2.3.2.a. The activation of the hysteretic transfer from day 40 to day 100 results in a decrease of the sensitivity $\mathcal{H}_{H_0}$ and in an increase of the sensitivity $\mathcal{Q}_{H_0}$ as seen in Section 2.3.2.b. Note that the magnitude of both the decrease in $\mathcal{H}_{H_0}$ and the increase in $\mathcal{Q}_{H_0}$ is larger than in the computational example 1, which must be related to the importance of the rainfall events.

Consider the Vensim model. Figures 2.9b and 2.9c show the sensitivities to the initial water level in the reservoirs S and H respectively. The sensitivities behaviour is similar to that observed in the example 1. The sensitivity $\mathcal{S}_{S_0}$ decreases exponentially. The activation of the S_{sill} results in a sudden decrease in $\mathcal{S}_{S_0}$, and in an increase in $\mathcal{R}_{S_0}$ and $\mathcal{Q}_{S_0}$. The sensitivities to H_0 are equal to zero until day 30 when the first overflow of the reservoir H occurs. The first overflow results in a burst in the sensitivities of S, R and Q. After the first overflow, the behaviour of the sensitivities to H_0 is similar to that of the sensitivities to S_0.

This example illustrates the influence of a heavy rainfall period on sensitivity propagation. As for the hysteresis-based model, the activation of the hysteretic transfer due to intense rainfall results in a rapid decrease of the sensitivity to H_0. On the contrary, for the Vensim model the propagation of the sensitivity to H_0 and S_0 is independent from the magnitude of the rainfall event.

2.5 Assessment of the appropriateness of the warm-up period

The theoretical developments presented in Section 2.3 provide a qualitative understanding of the behaviour of the Vensim and hysteresis-based models in relation to their initialisation period. In practice, two questions may arise when working on a given model and meteorological input series:

(i) do the initial conditions have an influence on the calibration results ?

(ii) do the initial conditions have an influence on the simulation results ?

These questions call for quantitative answers. Answering question (i) requires an estimation of the uncertainty on the calibration criterion. Answering question (ii) requires an estimation of the uncertainty on the simulated variable.

The aim of this Section is to assess the suitability of the local approach for answering question (i) for the Vensim and hysteresis-based models, based on the Durzon example. Both the warm-up

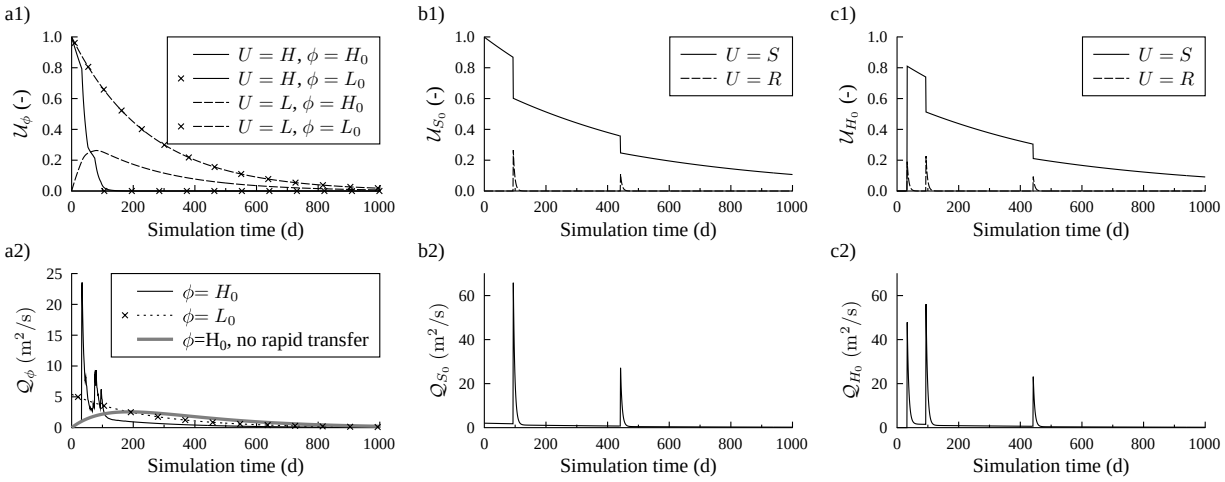

Figure 2.9: Computational example 3. Graphs a): hysteresis-based model. Sensitivity of the simulated water levels (graph 1) and of the simulated discharge (graph 2) to H_0 and L_0. Graphs b): Vensim model. Sensitivity of the simulated water levels (graph 1) and of the simulated discharge (graph 2) to S_0. Graphs c): Vensim model. Sensitivity of the simulated water levels (graph 1) and of the simulated discharge (graph 2) to H_0. The simulation parameters are given in Tables 2.2 and 2.4.

and the calibration periods are assumed to be one-year-long, which is the duration used in Tritz et al., 2011. The calibration is assumed to be based on the Nash criterion only, which is the procedure adopted by Tritz et al., 2011 and Fleury, 2005. The Nash efficiency is the one of the most widely used measure of model performance. It is a normalized variant of the mean squared error criterion. The Nash criterion be interpreted as the sum of three indicators involving the correlation coefficient between the measured and modelled variable as well as a measure of conditional and unconditional bias [Murphy, 1988; Weglarczyk, 1998]. An alternative decomposition involves the correlation, the bias and a measure of relative variability in the measured and modelled signals [Gupta et al., 2009]. Theoretical justifications for its use in model performance assessment include the fact that the Nash optimum corresponds to the maximum likelihood estimator for a homoscedastic, gaussian distribution of model errors [Cacuci, 2003]. In practice, calibration is often based on a set of performance measures [Moussa et al., 2007, e.g.] so that model performance is assessed against different aspect of the system response [Madsen, 2000; Yapo et al., 1998]. Note the main conclusions of the analysis presented below remain valid for others, distance-based measures of model performance.

Section 2.5.1 details the methodology for the estimation of the uncertainty on the performance criterion, based on the local perturbation approach. Numerical applications to the Vensim and hysteresis-based models are given in Sections 2.5.3 and 2.5.2. The validity of the local approach is checked in Section 2.5.4. The available warm-up period may sometimes be too short to allow for a proper elimination of the initialisation bias. In that case, an intuitive solution would consist in replicating the warm-up time series several times, so as to obtain a sufficiently long warm-up period. The suitability of this approach for the studied daily, non-linear models is assessed in Section 2.5.5.

2.5.1 Principle of local uncertainty estimation

Denote by $\Delta\phi$ the uncertainty in the initial water level in the reservoir Φ ($\Phi = \mathrm{H}, \mathrm{S}, \mathrm{L}$ or R). The uncertainty $\Delta\mathcal{Q}_{\phi(t)}$ in the discharge estimate at time t may be approximated to the first order by

$$\Delta\mathcal{Q}_{\phi(t)} \equiv \mathcal{Q}_{\phi(t)}\Delta\phi \tag{2.19}$$

where $\mathcal{Q}_{\phi(t)}$ denotes the sensitivity of the simulated spring discharge to the parameter ϕ at time t. The value of $\mathcal{Q}_{\phi(t)}$ can be obtained by solving numerically the sensitivity equations as done in Section 2.4.

Similarly, the bias $\Delta\mathcal{N}_\phi$ in the Nash efficiency may be approximated to the first order by

$$\Delta\mathcal{N}_\phi \equiv \mathcal{N}_\phi \Delta\phi \tag{2.20}$$

where $\mathcal{N}_\phi$ denotes the sensitivity of the Nash criterion to the initial water level ϕ in the reservoir Φ. The Nash criterion may be expressed as

$$N = 1 - \frac{\int_{t_1}^{t_2}(Q - Q_{\text{obs}})^2\,dt}{\int_{t_1}^{t_2}(Q_{\text{obs}} - \overline{Q_{\text{obs}}})^2\,dt} \tag{2.21}$$

where t_1 and t_2 are the initial and final times for the calibration period, Q_{obs} is the spring discharge measured at time t and $\overline{Q_{\text{obs}}}$ is the mean measured spring discharge during the calibration period. Differentiating equation (2.21) with respect to parameter ϕ leads to

$$\mathcal{N}_\phi = -2\int_{t_1}^{t_2} Q^*\mathcal{Q}_\phi\,dt \tag{2.22a}$$

where

$$Q^* = \frac{Q - Q_{\text{obs}}}{\int_{t_1}^{t_2}(Q_{\text{obs}} - \overline{Q_{\text{obs}}})^2\,dt} \tag{2.23}$$

Equation (2.19) can therefore be recast into

$$\Delta\mathcal{N}_\phi \equiv \int_{t_1}^{t_2} J_\phi\,dt \tag{2.24}$$

where

$$J_\phi = -2Q^*\Delta\mathcal{Q}_\phi \tag{2.25a}$$

2.5.2 Case of the hysteresis-based model

Similarly, the uncertainty on the simulated spring discharge can be estimated for a 25% variation in H_0 or L_0 (see Figure 2.10a). The uncertainty in the discharge estimate is larger for a perturbation in S_0 than for a perturbation in H_0, which is due to the difference in the sensitivities ($|\mathcal{Q}_{S_0}| > |\mathcal{Q}_{H_0}|$ based on Section 2.4). Note that unlike the case of the Vensim model, the maximum uncertainty in the discharge estimate during the calibration period (days 366 to 731) is reached at the beginning of the calibration period (no sensitivity burst). Indeed, for the three computational examples the reservoir H dried out before day 366. The consequence of the complete emptying of the reservoir H is that subsequent activations of the rapid transfert function have no impact on the sensitivity value (see Section 2.3.2). The maximum uncertainty in the discharge estimate is approximately $\Delta\mathcal{Q}_{S_0} = 0.05\text{m}^3/\text{s}$, to be compared to the average low water spring discharge $Q \simeq 0.6\text{m}^3/\text{s}$.

The efficiency bias over the calibration period can be estimated based on equation (2.25) (see numerical estimates in Table 2.6). Note that $\Delta\mathcal{N}$ is a function of both the discharge sensitivity and the discharge error (see equation (2.22a)).The maximum efficiency bias is $\Delta\mathcal{N} = 2\times10^{-3}$ regardless of the parameter considered, which makes an influence of the initial condition on calibration unlikely.

Model	Example n°	Parameter	$\Delta\mathcal{Q}_{\phi\ (t=366)}$ (m^3/s)	$\Delta\mathcal{N}_\phi$ (%)
Hysteresis	1	H_0	1.3×10^{-2}	4.8×10^{-2}
		L_0	4.7×10^{-2}	1.7×10^{-1}
	2	H_0	8.3×10^{-3}	6.0×10^{-3}
		L_0	4.9×10^{-2}	3.5×10^{-2}
	3	H_0	6.0×10^{-3}	1.9×10^{-2}
		L_0	4.1×10^{-2}	1.3×10^{-1}
Vensim	1	H_0	1.5×10^{-3}	4.3×10^{-2}
		S_0	2.1×10^{-1}	5.9
	2	H_0	1.4×10^{-3}	2.3×10^{-2}
		S_0	2.0×10^{-2}	3.4×10^{-1}
	3	H_0	1.7×10^{-2}	7.8×10^{-1}
		S_0	1.0×10^{-1}	4.6

Table 2.6: Hysteresis-based and Vensim models. Local estimates of the uncertainty in the simulated spring discharge at day 366 and of the bias in the Nash coefficient over the calibration period (days 366 to 731), assuming a 25% uncertainty in the initial water level ϕ.

2.5.3 Case of the Vensim model

Assume that a relative uncertainty of 25% on the estimation of H_0 (resp. S_0). The uncertainty on the simulated spring discharge can be estimated based on equation (2.19) (see Figure 2.10b). The uncertainty in the discharge estimate is one to two orders of magnitude higher for a perturbation in S_0 than for a perturbation in H_0, which is due to the difference in the order of magnitude of the absolute value of the perturbation ($|S_0| > |H_0|$). The uncertainty in the discharge estimate at the begining of the calibration period (day 366) is the largest for example 3 (see Table 2.6), which must be related to the magnitude of the absolute value of the perturbation and also to the relatively low number of activations of the threshold S_{sill} in the corresponding simulation. Note that for computational examples 1 and 3, the maximum uncertainty in the discharge estimate during the calibration period (days 366 to 731) is reached at days 700 and 450 respectively, by the time of the activation of the switch in the distribution coefficient. The maximum uncertainty in the discharge estimate is approximately $\Delta\mathcal{Q}_{S_0} = 2.5\text{m}^3/\text{s}$, to be compared to the corresponding spring discharge $Q \simeq 18\text{m}^3/\text{s}$. The activation of the switch in the distribution coefficient may hence hinder the estimation of the flood peaks discharges.

Similarly, the efficiency bias $\Delta\mathcal{N}$ over the calibration period can be estimated from equation (2.25) (see numerical estimates in Table 2.6). Note that $\Delta\mathcal{N}$ is a function of both the discharge sensitivity and the discharge error (see equation (2.22a)).The maximum bias in the Nash efficiency is $\Delta\mathcal{N}_{H_0} = 8 \times 10^{-3}$ for a perturbation in H_0 (computational example 3) and $\Delta\mathcal{N}_{S_0} = 6 \times 10^{-2}$ for a perturbation in S_0 (computational example 1). An inaccurate estimate of the initial water level in the reservoir S may therefore have an impact on the calibration results.

Equation (2.22a) suggests that two options can be considered in order to reduce the efficiency bias

1. extend the calibration period. Indeed, at large time the discharge sensitivity $\mathcal{Q}_\phi$ tends to zero, which means that the numerator of equation (2.22a) tends to a finite value. On the other hand, the denominator of (2.22a) is approximately proportional to the length $t_2 - t_1$ of the calibration period. As a consequence, for very large calibration periods the efficiency bias tends to zero.
2. extend the warm-up period. Indeed, the efficiency bias $\Delta\mathcal{N}_\phi$ is all the more reduced as the discharge sensitivity $\mathcal{Q}_\phi$ is low.

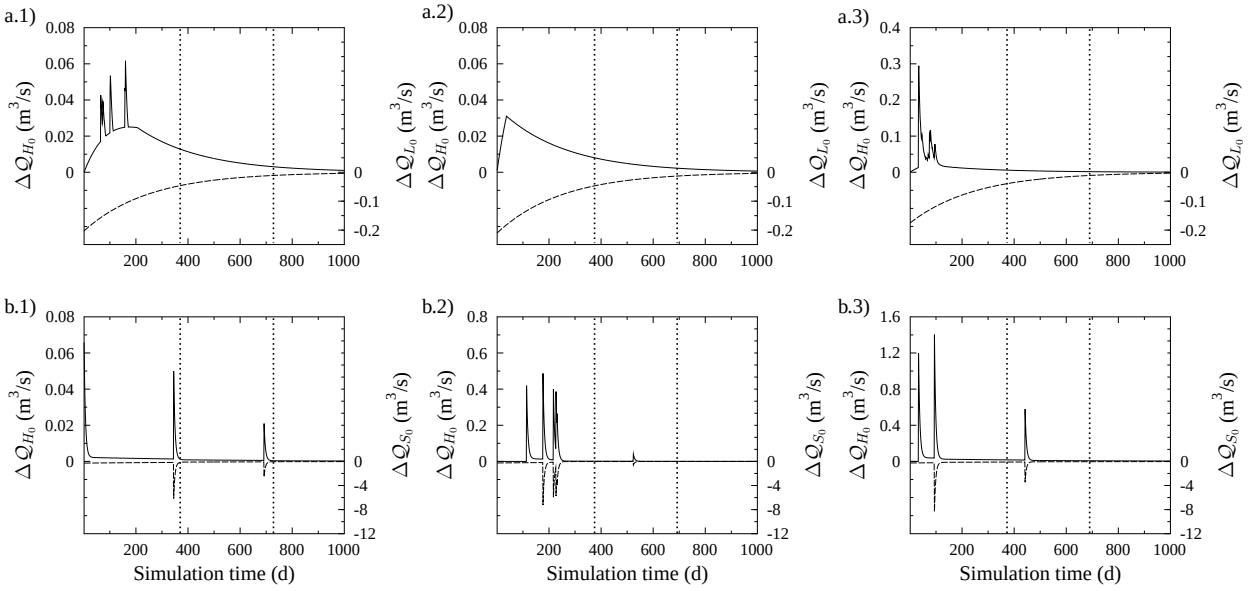

Figure 2.10: Local uncertainty $\Delta\mathcal{Q}$ in the discharge estimate for the hysteresis-based and Vensim models. Hysteresis-based model (graphs a): case of a 25% perturbation in the initial H_0 (left y-axis, solid line) and L_0 (right y-axis, dotted line) estimates. Vensim model (graphs b): case of a 25% perturbation in the initial H_0 (left y-axis, solid line) and S_0 (right y-axis, dotted line) estimates. The uncertainty estimates are calculated for the computational examples 1 (graphs a1 and b1), 2 (graphs a2 and b2) and 3 (graphs a3 and b3). The beginning and the final time for the calibration period are indicated by vertical, dotted lines.

2.5.4 Validity of the local uncertainty estimates

The range of validity of the local sensitivity and uncertainty analyses is restricted to "small" perturbations in the values of the parameters, the meaning of "small" being dependent upon the degree of non-linearity of the model, and possibly the nominal value used for the analysis. The validity of the local sensitivity and uncertainty estimates is checked by comparison against empirical estimates in 2.8.4. The linear approximation is found to be valid for the hysteresis-based model for perturbations up to 50% of the nominal value of the perturbed parameter. On the other hand, for the Vensim model the linear approximation fails for perturbations as small as 10% of the nominal value of the parameter perturbed. The difference in the range of validity of the linear approximation is due to the difference in the degree of nonlinearity in the two models.

2.5.5 Compensating the lack of data with a repetition of available time series

The available warm-up period may sometimes be too short to allow for a proper elimination of the initialisation bias. An intuitive solution would consist in replicating the input time series of the warm-up period several times, so as to obtain a sufficiently long warm-up period. These replicated time series would be inserted before the current warm-up period in the input time series of the model (see Figure 2.11a-b). For this reason, the newly extended time series is termed a "pre-warm-up period". Since this artificially reconstructed pre-warm-up time series is not necessarily representative of the actual forcings that occured over the pre-warm-up period, it is not certain at all that this practice would allow the initialisation bias to be eliminated. The purpose of the present subsection is to investigate whether it is actually the case.

Consider the time series used in the computational example 1 (Section 2.4.1) for the Vensim model. Assume that the available meteorological data record starts on day 731. The data record is extended artificially back to day 1 with the data recorded on days 731 to 1461 (see Figure 2.11a,b). The period day 1 - day 730 is used to produce an initial state estimate for the internal variables

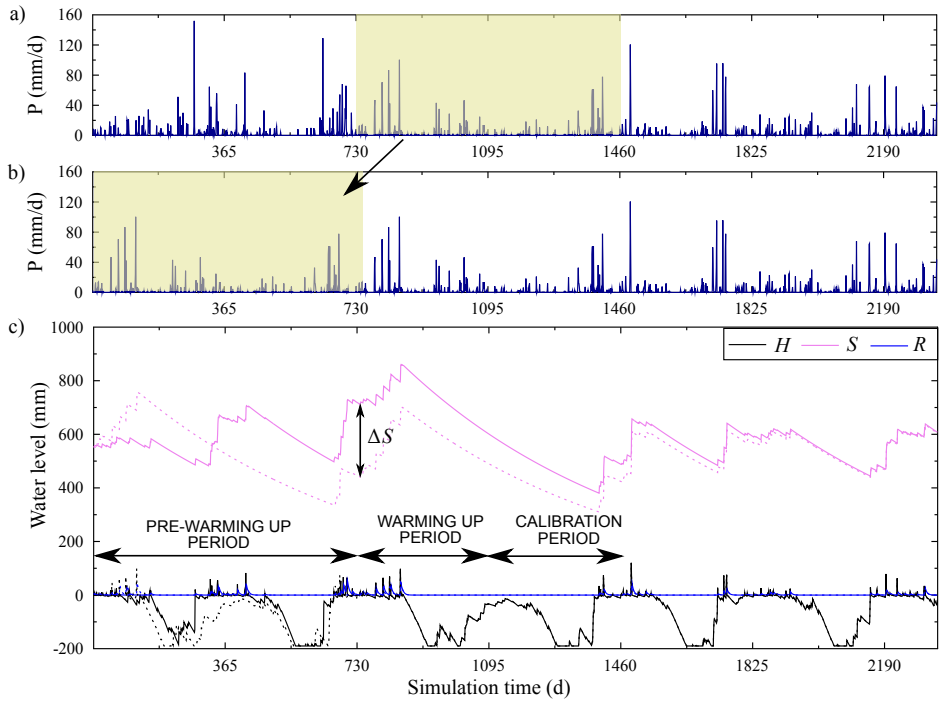

Figure 2.11: Initial estimate of state variables. a) actual meteorological record, b) extended meteorological record, c) water level in the reservoir H, S and R for a simulation using the actual (solid lines) or extended (dotted lines) meteorological record.

of the model which is hoped to be more realistic than the modeller's best guess (pre-warming up period). This initial state estimate can be compared to the state reached by running the model for the true meteorological data record (see Figure 2.11c). The difference in the initial state estimates at day 731 for the actual and extended record data is negligible for the reservoirs H and R. However, the difference in the S estimate is 38% of the S value for the actual record. The repetition of the available data record may thus not suffice to eliminate the bias due to the initialisation uncertainty.

2.6 Discussion

This Section is a summary and interpretation of the results obtained in Sections 2.3 to 2.5.

2.6.1 Sensitivity to the initial water level in the lower reservoirs

The functioning of the reservoir L of the hysteresis-based model and that of the reservoir R of the Vensim model is linear. Indeed, the emptying of these reservoirs is modeled by a linear discharge relationship and the water level in these reservoirs does not trigger any change in the model functioning (no associated threshold transfer function). As a consequence, the sensitivity to the initial water levels (L_0 or R_0) is controlled by the only specific discharge coefficient k_Φ of the reservoir Φ considered ($\Phi = \mathrm{L}, \mathrm{R}$). The sensitivity decreases exponentially, with a time constant $T = 1/k_\Phi$

1. in the case of the hysteresis-based model, the reservoir L accounts for baseflow discharge, which means that the numerical value of the specific discharge coefficient k_L is low. As a consequence, the discharge sensitivity to L_0 is relatively low, but it decreases slowly,
2. in the case of the Vensim model, the reservoir R accounts for rapid infiltration towards the outlet, which means that the numerical value of the specific discharge coefficient k_R is high. As a consequence, the discharge sensitivity to R_0 is high, but it decreases rapidly.

The emptying of the reservoir S of the Vensim model is modelled by a linear discharge relationship. The difference with the reservoirs R and L lies in the fact that the water level in the reservoir S has an influence on model functioning. Indeed, the distribution coefficient X of the upper reservoir overflow discharge Q_{H} is defined as $X = X_{\mathrm{D}}$ if $S \leq S_{\mathrm{sill}}$ and $X = X_{\mathrm{W}}$ if $S > S_{\mathrm{sill}}$ (see Section 2.2.3). The activation of the threshold S_{sill} heavily affects the behaviour of the sensitivity to the initial water level S_0 (see Figure 2.4b)

1. assume that the threshold S_{sill} is not activated. Then the sensitivity to S_0 decreases exponentially, with a time constant $T = 1/k_{\mathrm{S}}$. Since the reservoir S accounts for long-term storage within the karst aquifer, the specific discharge coefficient k_{S} associated with the linear discharge relationship is small. As a consequence, the decrease of the sensitivity to S_0 is slow (large time constant), but the numerical value of the sensitivity of the simulated spring discharge is small.

2. the activation of the threshold S_{sill} triggers the leaks of part of the sensitivity to S_0 towards the reservoir R. The sensitivity of S to S_0 decreases suddenly, while the sensitivity of R to S_0 increases. This sensitivity peak is rapidly drained off the reservoir R (high specific discharge coefficient k_{R}), which results in a sensitivity peak in the simulated discharge (see Figure 2.4b).

3. each activation of the threshold S_{sill} therefore results in a sensitivity peak of the simulated discharge to S_0. The magnitude of the peak is proportional to the overflow discharge Q_{H} and to the remaining sensitivity of S to S_0. Since the decrease of the sensitivity of S to S_0 is slow, discharge sensitivity peaks of significant magnitude may occur years after the begining of the simulation. Also note that the number, magnitude and time of occurence of these sensitivity peaks is difficult to predict since they are linked to internal model variables (water level in the reservoir S and residual sensitivity of S to S_0).

2.6.2 Sensitivity to the initial water level in the upper reservoirs

During low water periods the upper reservoir of the hysteresis-based model leaks towards the lower reservoir. By contrast, the upper reservoir of the Vensim model is disconnected from the lower reservoirs. For both models, a rapid emptying function is activated during high water periods

1. in the case of the hysteresis-based model, the propagation of the sensitivity to H_0 towards the lower reservoir starts at the beginning of the simulation. The activation of the rapid transfer functions results in a sudden decrease of the sensitivity to H_0, since part of the sensitivity to H_0 leaks directly towards the outlet (via the hysteretic transfer function) or is removed from the model (via the secondary springs transfer function). The consequence is a burst in the discharge sensitivity to H_0, the magnitude of which is proportional to the remaining sensitivity of H,

2. in the case of the Vensim model, the propagation of the sensitivity to H_0 into the model only begins with the activation of the overflow discharge (see Figure 2.5). The first activation of the overflow discharge triggers a Dirac peak in the sensitivity of the water level H to H_0, the magnitude of which is independant from the magnitude of the overflow discharge. The sensitivity to H_0 leaks entirely towards the lower reservoirs. Subsequent activations of the overflow discharge have no effect on the propagation of the sensitivity to H_0. The propagation of the sensitivity to H_0 in the reservoirs S and R is similar to that of the sensitivity to S_0 and R_0 respectively (see Figure 2.4c).

As the upper reservoirs are affected by evapotranspiration, a complete emptying of these reservoirs is possible. The complete emptying of the reservoir H causes the sensitivity of H to H_0 to cancel.

1. In the case of the hysteresis-based model, part of the sensitivity to H_0 leaks towards the lower reservoir even during low flow periods. A complete emptying of the reservoir H therefore stops the propagation of the sensitivity towards the lower reservoir,
2. In the case of the Vensim model, the upper and lower reservoirs are disconnected during low water periods. As a consequence, a complete emptying of the reservoir H before the first overflow stops the propagation of the sensitivity to H_0 into the lower reservoirs. On the other hand, a low water period that does not result in a complete emptying of the reservoir only delays the propagation of the sensitivity. Lastly, a complete emptying of the reservoir H after the first overflow has no impact on the sensitivity propagation.

2.7 Conclusion - practical recommandations

2.7.1 General rules for the initialisation bias behaviour

The theoretical considerations and the application examples presented in Sections 2.3 to 2.5 and discussed in Section 2.6 have evidenced the role of model structure in the behaviour of the sensitivity to the initial conditions. As a broad rule, the dissipation of the sensitivity is favoured by

1. very low water periods. Indeed, the drying of the upper reservoir completely stops the propagation of the sensitivity to the initial water level in the upper reservoir,
2. very high water periods. Indeed, the activation of the rapid transfer functions (i.e., threshold functions) in a given reservoir speeds up the propagation of the sensitivity to the initial water level in that reservoir.

The above-mentioned considerations must be adjusted according to the structure of the reservoirs considered.

1. Consider the case where leaks occur from the upper reservoir H towards the lower reservoirs whatever the water level in H (no threshold). Then the sensitivity to the initial water level in H leaks towards the lower reservoirs starting from the beginning of the simulation on. The drying of the upper reservoir therefore leads to the dissipation of a proportion of the sensitivity all the more important as the drying occurs rapidly after the beginning of the simulation. Such a behaviour is illustrated by the computational example 2 for the hysteresis-based model (see Figure 2.4.2b).
2. Consider the case where a rapid transfer function from a given reservoir is activated above a given threshold. Assume that the transfer function is all-or-nothing (e.g. transfer function Q_{H} from the reservoir H of the Vensim model). Then a single activation of that rapid transfer function triggers the propagation of all the sensitivity to the initial water level in that reservoir towards the other reservoirs or towards the outlet of the model (see Figure 2.5 for an illustration of that property for the Vensim model). Now, assume that the rapid transfer functions are not all-or-nothing (e.g. transfer function Q_{HY} from the reservoir H of the hysteresis-based model). Then the propagation of the sensitivity becomes faster as the transfer functions are activated frequently and associated with high discharges. In other words, the propagation of the sensitivity is sped if the meteorological time serie includes numerous heavy rainfall events. Such a behaviour is illustrated by the computational example 3 for the hysteresis-based model (Figure 2.4.3b).

Conversely, the propagation of the sensitivity is impaired in the following situations

1. if the upper reservoir is disconnected from the lower reservoirs during the low water period, and the simulation begins with a low water period that does not results in a complete emptying

of the upper reservoir. Indeed, the propagation of the sensitivity is delayed until the first activation of the transfer functions towards the lower reservoirs. Such a behaviour is illustrated by Figure 2.4c for the Vensim model.

2. if a threshold transfer function is associated to the water level in a reservoir with slow dynamics. Indeed, sensitivity bursts associated with the activation of the threshold transfer function may occur years after the simulation start. Such a behaviour is illustrated by the computational example 1 (Figure 2.7b,c) for the Vensim model.

The sensitivity to the initial water level in a lower, linear reservoir is controlled by the only specific discharge coefficient k associated with the reservoir linear discharge relationship. Indeed, the sensitivity $\mathcal{Q}$ of the simulated discharge to the initial water level in that reservoir is $\mathcal{Q} = kA\exp(-kt)$ where A is the total catchment area and t is the simulation time. The sensitivity decreases exponentially with a time constant $T = 1/k$. The initial water level in a linear reservoir with a low discharge coefficient therefore has a relatively mild influence on the simulated discharge, but its influence decreases slowly (large time constant). On the other hand, the initial water level in a linear reservoir with a high discharge coefficient has a relatively high influence on the simulated discharge but its influence decreases slowly.

2.7.2 Consequences for the modelling practice

As regards the modelling practice, the main results of this study can be summarized as follows.

1. Threshold-based transfer functions generate Dirac sensitivity patterns. When associated with long-term memory reservoir and fast discharge models, they may generate a substantial initialisation bias even after very long periods of inactivity.
2. As a consequence of the above remark, the commonly-used one-year warm-up period may not ensure a proper elimination of the initialisation bias.
3. When the available warm-up period is too short to allow for a proper elimination of the initialisation bias, an intuitive workaround would consist in artificially extending the warm-up time series by replicating it several times. However, the artificially extended warm-up time series may not be representative of the actual forcings. As regards the present study, such a procedure proved inefficient to reduce the initialisation bias.
4. This work stresses the fact that the specification of the initial state may significantly bias the calibration step. This initialisation bias issue is little regarded in most practical applications. A careful examination of the initialisation bias behaviour should be part of the good modelling practices. In particular, the use of elaborate procedures for locating the global optimum of the objective function used for parameter optimization can only be justified in so far as the initialisation bias has been efficiently eliminated.
5. Local sensitivity analysis can be used as a low-computational cost tool to identify the main characteristics of the bias behaviour, even for conceptual models with strongly non-linear transfer functions.
6. The last remark is specific to the modelling of karst spring discharge. Recent studies have emphasized the need to account for the influence of the karst flowpath network connectivity on the system response dynamics [Fleury, 2005; Jazayeri Noushabadi, 2009; Tritz et al., 2011]. The change in connectivity may be accounted for in the model structure by a threshold function, the activation of which depends on the water level in a given reservoir. As for the Vensim model, the threshold function triggers the switch in the distribution coefficient based on the water level in the lower, slow discharge reservoir. As regards the hysteresis-based model, the threshold function triggers the activation of the hysteretic transfer, based on the

water level in the upper reservoir. Our study indicates that whenever possible, the activation of the threshold function should not be associated with the water level in a slow dynamics reservoir.

2.8 Appendix

2.8.1 Sensitivity equations for the hysteresis-based model

Denote by $\mathcal{H}_\phi$ and $\mathcal{L}_\phi$ the sensitivities of the water levels in the reservoirs H and L to the parameter ϕ. Applying the perturbation approach to the model equations (2.2) and (2.7) for a perturbation in $\phi = H_0$ leads to the following set of sensitivity equations

$$\frac{d\mathcal{H}_{H_0}}{dt} = -\mathcal{H}_{H_0}\left[k_{\text{sec}}\left(\varepsilon_{\text{sec}} + \frac{\partial \varepsilon_{\text{sec}}}{\partial H}(H - H_{\text{sec}})\right) + k_{\text{HY}}\left(\frac{\partial \varepsilon_{\text{HY}}}{\partial H} + \varepsilon_{\text{HY}}\frac{\alpha}{H - H_1}\right)\left(\frac{H - H_1}{H_2 - H_1}\right)^{\alpha} + k_{\text{HL}}\right] \quad \text{for } H \tag{2.26a}$$

$$\mathcal{H}_{H_0} = 0 \quad \text{for } H \tag{2.26b}$$

$$\frac{d\mathcal{L}_{H_0}}{dt} = k_{\text{HL}}\mathcal{H}_{H_0} - k_L\mathcal{L}_{H_0} \tag{2.26c}$$

$$\mathcal{Q}_{H_0} = k_{\text{HY}}A\mathcal{H}_{H_0}\left(\frac{\partial \varepsilon_{\text{HY}}}{\partial H} + \varepsilon_{\text{HY}}\frac{\alpha}{H - H_1}\right)\left(\frac{H - H_1}{H_2 - H_1}\right)^{\alpha} + k_L A\mathcal{L}_{H_0} \tag{2.26d}$$

$$\mathcal{H}_{H_0}(t = 0) = 1 \tag{2.26e}$$

$$\mathcal{L}_{H_0}(t = 0) = 0 \tag{2.26f}$$

$$\mathcal{Q}_{H_0}(t = 0) = A\varepsilon_{\text{HY}}k_{\text{HY}}\frac{\alpha}{H_2 - H_1}\left(\frac{H(t = 0) - H_1}{H_2 - H_1}\right)^{\alpha - 1} \tag{2.26g}$$

Similarly, applying equations the perturbation appraoch to the model equations (2.2) and (2.7) for a perturbation in $\phi = L_0$ leads to

$$\frac{d\mathcal{H}_{L_0}}{dt} = 0 \tag{2.27a}$$

$$\frac{d\mathcal{L}_{L_0}}{dt} = -k_L\mathcal{L}_{L_0} \tag{2.27b}$$

$$\mathcal{Q}_{L_0} = A\left[\varepsilon_{\text{HY}}k_{\text{HY}}\frac{\alpha\mathcal{H}_{L_0}}{H_2 - H_1}\left(\frac{H - H_1}{H_2 - H_1}\right)^{\alpha - 1} + k_L\mathcal{L}_{L_0}\right] \tag{2.27c}$$

$$\mathcal{H}_{L_0}(t = 0) = 0 \tag{2.27d}$$

$$\mathcal{L}_{L_0}(t = 0) = 1 \tag{2.27e}$$

$$\mathcal{Q}_{L_0}(t = 0) = k_L A \tag{2.27f}$$

where $\mathcal{H}_\phi$ and $\mathcal{L}_\phi$ denote the sensitivities to the parameter ϕ of the water levels in the reservoirs H and L respectively.

2.8.2 Sensitivity equations for the Vensim model

Consider a perturbation in the parameter $\phi = H_0$. Then the perturbation approach leads to the following set of sensitivity equations

$$\frac{\mathrm{d}\mathcal{H}_{H_0}}{dt} = 0 \qquad \text{for } H_{\min} < H < 0 \tag{2.28a}$$

$$\mathcal{H}_{H_0} = 0 \qquad \text{for } H = H_{\min} \text{ or } H = 0 \tag{2.28b}$$

$$\frac{\mathrm{d}\mathcal{S}_{H_0}}{dt} = \frac{\partial X}{\partial S}\mathcal{S}_{H_0} Q_{\mathrm{H}} + X\frac{\partial Q_{\mathrm{H}}}{\partial H_0} - k_{\mathrm{S}}\mathcal{S}_{H_0} \tag{2.28c}$$

$$\frac{\mathrm{d}\mathcal{R}_{H_0}}{dt} = -\frac{\partial X}{\partial S}\mathcal{S}_{H_0} Q_{\mathrm{H}} + (1-X)\frac{\partial Q_{\mathrm{H}}}{\partial H_0} - k_{\mathrm{R}}\mathcal{R}_{H_0} \tag{2.28d}$$

$$\mathcal{Q}_{H_0} = A\left(k_{\mathrm{R}}\mathcal{R}_{H_0} + k_{\mathrm{S}}\mathcal{S}_{H_0}\right) \tag{2.28e}$$

$$\mathcal{H}_{H_0}(t=0) = 1 \tag{2.28f}$$

$$\mathcal{S}_{H_0}(t=0) = 0 \tag{2.28g}$$

$$\mathcal{R}_{H_0}(t=0) = 0 \tag{2.28h}$$

$$\mathcal{Q}_{H_0}(t=0) = 0 \tag{2.28i}$$

Note that the term $\partial X/\partial S$ is equivalent to a dirac impulse which is turned on whenever $S = S_{\mathrm{sill}}$ (see demonstration in 2.8.3). Also note that the de-activation of the threshold means that the inflow rate XQ_{H} into the reservoir S is lower than the outflow rate $k_{\mathrm{S}}S$ from the reservoir S towards the spring. Since the specific discharge coefficient of the inflow is much greater than that of the outflow, the de-activation of S_{sill} requires that the outflow from the reservoir H be zero ($\varepsilon_{\mathrm{H}} = 0$ and therefore $Q_{\mathrm{H}} = 0$).

Similarly, for a perturbation in $\phi = S_0$

$$\frac{\mathrm{d}\mathcal{H}_{S_0}}{dt} = 0 \tag{2.29a}$$

$$\frac{\mathrm{d}\mathcal{S}_{S_0}}{dt} = \frac{\partial X}{\partial S}\mathcal{S}_{S_0} Q_{\mathrm{H}} - k_{\mathrm{S}}\mathcal{S}_{S_0} \tag{2.29b}$$

$$\frac{\mathrm{d}\mathcal{R}_{S_0}}{dt} = -\frac{\partial X}{\partial S}\mathcal{S}_{S_0} Q_{\mathrm{H}} - k_{\mathrm{R}}\mathcal{R}_{S_0} \tag{2.29c}$$

$$\mathcal{Q}_{S_0} = A\left(k_{\mathrm{R}}\mathcal{R}_{S_0} + k_{\mathrm{S}}\mathcal{S}_{S_0}\right) \tag{2.29d}$$

$$\mathcal{H}_{S_0}(t=0) = 0 \tag{2.29e}$$

$$\mathcal{S}_{S_0}(t=0) = 1 \tag{2.29f}$$

$$\mathcal{R}_{S_0}(t=0) = 0 \tag{2.29g}$$

$$\mathcal{Q}_{S_0}(t=0) = k_{\mathrm{S}}A \tag{2.29h}$$

Lastly, a perturbation in $\phi = R_0$ yields

$$\frac{\mathrm{d}\mathcal{H}_{R_0}}{dt} = 0 \tag{2.30a}$$
$$\frac{\mathrm{d}\mathcal{S}_{R_0}}{dt} = 0 \tag{2.30b}$$
$$\frac{\mathrm{d}\mathcal{R}_{R_0}}{dt} = -k_{\mathrm{R}}\mathcal{R}_{R_0} \tag{2.30c}$$
$$\mathcal{Q}_{R_0} = A\left(k_{\mathrm{R}}\mathcal{R}_{R_0} + k_{\mathrm{S}}\mathcal{S}_{R_0}\right) \tag{2.30d}$$
$$\mathcal{H}_{R_0}(t=0) = 0 \tag{2.30e}$$
$$\mathcal{S}_{R_0}(t=0) = 0 \tag{2.30f}$$
$$\mathcal{R}_{R_0}(t=0) = 1 \tag{2.30g}$$
$$\mathcal{Q}_{R_0}(t=0) = k_{\mathrm{R}}A \tag{2.30h}$$

2.8.3 Sensitivity source term $\partial Q_{\mathrm{H}}/\partial H_0$ (Vensim model)

This Appendix details the calculation of the term $\partial Q_{\mathrm{H}}/\partial H_0$ that appear in equations (2.28c) and (2.28d). Denote by t_H the time of the first overflow of the reservoir H. The overflow discharge is a discontinuous function of time:

$$Q_{\mathrm{H}} = 0 \qquad \text{for } t < t_H \tag{2.31a}$$
$$Q_{\mathrm{H}} = P - \mathrm{ET} \qquad \text{for } t \geq t_H \tag{2.31b}$$

Assume that H_0 is perturbed by an amount $\delta H_0 > 0$. Due to the perturbation in H_0, the time of the overflow t_H is advanced by a time δt (see Figure 2.12). The difference in the outflow between $t_H - \delta t$ and t_H that results from the perturbation δH_0 is

$$\int_{t_H-\delta t}^{t_H} \delta Q_{\mathrm{H}} dt = \int_{t_H-\delta t}^{t_H} (P - \mathrm{ET}) dt \tag{2.32}$$

As δH_0 tends to zero, equation (2.32) can be approximated as

$$\delta Q_{\mathrm{H}} \delta t = (P - \mathrm{ET})\delta t \tag{2.33}$$

Similarly, the difference in the filling of the reservoir H that results from the perturbation δH_0 can be expressed as

$$\delta H_0 = -(P - \mathrm{ET})\delta t \tag{2.34}$$

Combining equations (2.33) and (2.34) leads to

$$\frac{\delta Q_{\mathrm{H}}}{\delta H_0}\delta t = 1 \tag{2.35}$$

The sensitivity of the overflow discharge to the perturbation in H_0 is defined as

$$\frac{\partial Q_{\mathrm{H}}}{\partial H_0} = \lim_{\delta H_0 \to 0} \frac{\delta Q_{\mathrm{H}}}{\delta H_0} \tag{2.36}$$

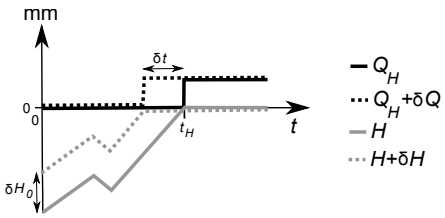

Figure 2.12: Vensim model. Calculation of the term $\partial Q_{\mathrm{H}}/\partial H_0$. Influence of a perturbation in the inital water level H_0 on the water level H and on the overflow discharge Q_{H}.

and verifies

$$\left(\frac{\partial Q_{\mathrm{H}}}{\partial H_0}\right) \xrightarrow[t\to t_H]{} +\infty \tag{2.37a}$$

$$\int_{t_H^-}^{t_H^+} \frac{\partial Q_{\mathrm{H}}}{\partial H_0} = 1 \tag{2.37b}$$

$$\left(\frac{\partial Q_{\mathrm{H}}}{\partial H_0}\right)_{t<t_H} = 0 \tag{2.37c}$$

$$\left(\frac{\partial Q_{\mathrm{H}}}{\partial H_0}\right)_{t>t_H} = 0 \tag{2.37d}$$

The function $\partial Q_{\mathrm{H}}/\partial H_0$ is thus a Dirac function of magnitude $1\mathrm{s}^{-1}$.

2.8.4 Validity of local uncertainty estimates

The aim of this Appendix is to check the validity of the local sensitivity and uncertainty estimates by comparison against empirical estimates.

2.8.5 Case of the hysteresis-based model

Since the hysteresis-based model is linear with respect to a perturbation in the parameter L_0, the validity of the local sensitivity and uncertainty analyses for a perturbation in L_0 need not to be checked.

The validity of the linear approximation for perturbations in H_0 is first checked by a graphic comparison between the local and empirical discharge sensitivities estimates. Figure 2.13 shows the empirical discharge sensitivity $\mathcal{Q}_{H_0}^{\mathrm{emp}}$ computed based on perturbations ΔH_0 ranging from 10 to 50% of the nominal value of H_0. The visual comparison of the empirical (Figure 2.13) and local (Figures 2.7.a2, 2.8.a2 and 2.9.a2 sensitivity estimates shows a good agreement between the empirical and local approaches. The corresponding empirical and local uncertainties on the Nash criterion are given in Table 2.7. The relative error on the Nash uncertainty estimate is at maximum 7% for a 50% perturbation in H_0, which confirms the suitability of the local approach.

2.8.6 Vensim model

Since the Vensim model is linear with respect to a perturbation in the parameter R_0, the validity of the local sensitivity and uncertainty analyses with respect to a perturbation in R_0 need not to be checked.

The validity of the linear approximation with respect to a perturbation in S_0 or H_0 is first checked by a graphic comparison between the local and empirical discharge sensitivity estimates. Experimental sensitivities are computed based on the results of two simulations. In the second simulation, the investigated parameter ϕ_0 is modified by an amount $\Delta\phi_0$ as compared to the first

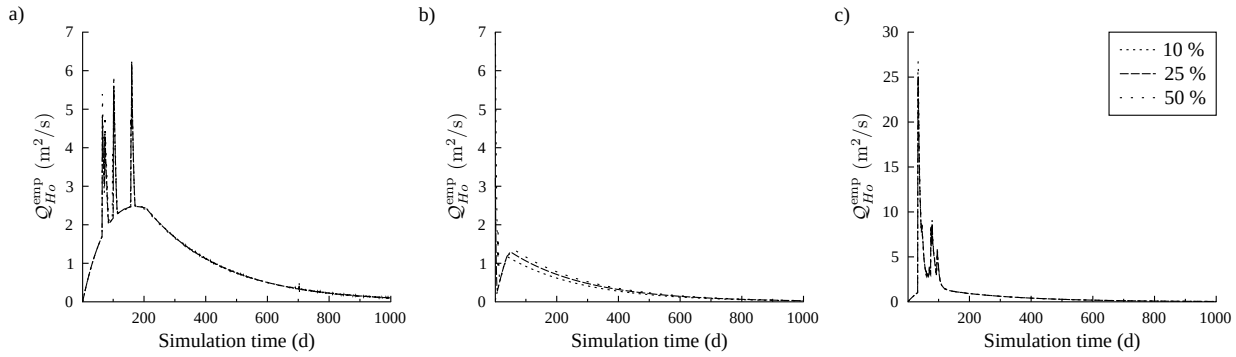

Figure 2.13: Hysteresis-based model. Discharge sensitivity estimates for a perturbation in the initial water level H_0. Empirical estimates for: a) the computational example 1, b) the computational example 2, c) the computational example 3. The simulation parameters are specified in Table 2.2.

Example n°	ΔH_0 (%)	$\Delta\mathcal{N}_\phi^{\text{emp}}$ (%)	$\Delta\mathcal{N}_\phi^{\text{loc}}$ (%)
1	10	1.9×10^{-2}	1.9×10^{-2}
	25	5.0×10^{-2}	4.8×10^{-2}
	50	1.0×10^{-1}	9.6×10^{-2}
2	10	2.4×10^{-3}	2.4×10^{-3}
	25	6.3×10^{-3}	6.0×10^{-3}
	50	1.1×10^{-2}	1.2×10^{-2}
3	10	7.5×10^{-3}	7.6×10^{-3}
	25	1.8×10^{-2}	1.9×10^{-2}
	50	3.6×10^{-2}	3.8×10^{-2}

Table 2.7: Hysteresis-based model. Empirical ($\Delta\mathcal{N}_\phi^{\text{emp}}$) vs local ($\Delta\mathcal{N}_\phi^{\text{loc}}$) uncertainty estimates of the Nash criterion over the calibration period (days 366 to 731).

simulation value. The empirical sensitivity $\mathcal{Q}^{\text{emp}}_{\phi_0}$ of the spring discharge to the parameter ϕ_0 is approximated as the ratio of the difference between the results of the two simulations runs to the perturbation $\Delta\phi_o$

$$\mathcal{Q}^{\text{emp}}_{\phi_0\ (t)} = \frac{Q_{(\phi_0+\Delta\phi_0,t)} - Q_{(\phi_0,t)}}{\Delta\phi_0} \tag{2.38}$$

Figure 2.14a shows the empirical discharge sensitivity estimates $\mathcal{Q}^{\text{emp}}_{S_0}$ for ΔS_0 ranging from 10 to 50% of the nominal value of S_0. The empirical estimates must be compared to the local estimates which are plotted in Figures 2.7.b2, 2.8.b2 and 2.9.b2. The visual comparison of the local and empirical sensitivities shows a strong difference between both, even for a 10% perturbation. The empirical sensitivities do show peaks by the date the threshold S_{sill} is activated. However, empirical sensitivities also exhibit a number of supplementary peaks. Figure 2.14b shows the empirical estimates $\mathcal{Q}^{\text{emp}}_{H_0}$ of the discharge sensitivity computed based on perturbations ΔH_0 ranging from 10 to 50% of the nominal value of H_0. The empirical estimates must be compared to the local sensitivities which are plotted in Figures 2.7.c2, 2.8.c2 and 2.9.c2. A visual comparison of the local and empirical sensitivities shows a strong difference between both. However, the situation is the reverse of that of a perturbation in S_0 as the empirical sensitivities lack a number of additional peaks compared to the local sensitivities.

The comparison of the empirical and local estimates of the uncertainty on the Nash criterion (see values in Table 2.8) confirms the failure of the local approach for the uncertainty estimation.

The poor performance of the local uncertainty analysis may be associated to two factors: (i) the time discretization adopted for the solution of the model equations and (ii) the dynamics of the reservoir. Indeed, the reservoir S is characterized by a high storage and a slow drainage. As a consequence, the perturbation ΔS_0 considered is important as compared to the daily changes in the water level. A perturbation in S_0 is likely to strongly modify the number of activations of the switch in the distribution coefficient and therefore the number of peaks in the sensitivity to S_0. On the other hand, the daily changes in the water level in the reservoir H are large compared to the perturbations ΔH_0 considered. At a daily time step, the result is that the perturbation in S_0 is not likely to trigger a switch in the distribution coefficient. The case of the simulation 2 is somewhat different. The perturbation $\Delta H_0 < 0$ results in a complete emptying of the reservoir H. Since the emptying occurs before the first overflow, the propagation of the sensitivity to H_0 is completely stopped, as explained in Section 2.3.3.c.

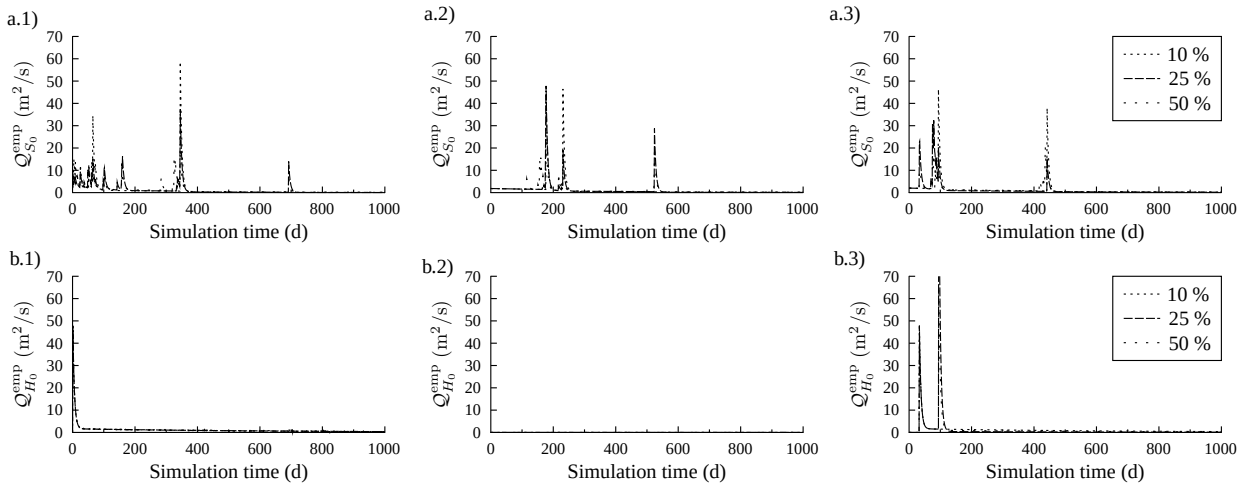

Figure 2.14: Empirical discharge sensitivity estimates for a perturbation in: a) the initial water level in the reservoir S, b) the initial water level in the reservoir H for 1) the computational example 1, 2) the computational example 2, 3) the computational example 3. The simulation parameters are given in Table 2.4.

	Example n°	$\Delta\phi_o$ (%)	$\Delta\mathcal{N}^{\mathrm{emp}}_{\phi}$ (%)	$\Delta\mathcal{N}^{\mathrm{loc}}_{\phi}$ (%)
$\phi = H_0$	1	10	1.9×10^{-2}	1.7×10^{-2}
		25	5.1×10^{-2}	4.3×10^{-2}
		50	1.3×10^{-2}	8.7×10^{-2}
	2	10	0	9.2×10^{-3}
		25	0	4.2×10^{-2}
		50	0	1.2×10^{-2}
	3	10	1.8×10^{-1}	3.4×10^{-1}
		25	1.3×10^{-1}	7.8×10^{-1}
		50	5.7×10^{-1}	1.6
$\phi = S_0$	1	10	2.9×10^{-1}	2.4
		25	4.6	5.9
		50	6.3	12
	2	10	3.2×10^{-1}	1.4×10^{-1}
		25	2.8	3.4×10^{-1}
		50	7.2	6.8×10^{-1}
	3	10	3.5	1.8
		25	4.3	4.6
		50	27	9.2

Table 2.8: Vensim model. Empirical ($\Delta\mathcal{N}^{\mathrm{emp}}_{\phi}$) vs local ($\Delta\mathcal{N}^{\mathrm{loc}}_{\phi}$) uncertainty estimates for the Nash criterion over the calibration period (days 366 to 731).

2.9 Complementary discussion: Sensitivity behaviour for the model parameters

The preceding sections emphasize the role of the threshold transfer functions in the behaviour of the initialisation bias. It must be noted that the analysis remains to a large extend valid as regards the behaviour of the sensitivities of the model parameters.

As an example, consider the Vensim model. Section 2.3.3 demonstrated that threshold functions associated with the water level in a slow dynamics reservoir are related to the occurrence of bursts in the initialisation bias of the simulated discharge. The sensitivities to a perturbation in a given parameter ϕ can be written as

$$\frac{d\mathcal{S}_\phi}{dt} = \frac{\partial X}{\partial S}\mathcal{S}_\phi Q_H + X\frac{\partial Q_H}{\partial \phi} - \frac{\partial k_S}{\partial \phi} - k_S\mathcal{S}_\phi \tag{2.39a}$$

$$\frac{d\mathcal{R}_\phi}{dt} = -\frac{\partial X}{\partial S}\mathcal{S}_\phi Q_H + (1-X)\frac{\partial Q_H}{\partial \phi} - \frac{\partial k_R}{\partial \phi} - k_R\mathcal{R}_\phi \tag{2.39b}$$

$$\mathcal{Q}_\phi = A\left(k_R\mathcal{R}_\phi + k_S\mathcal{S}_\phi\right) \tag{2.39c}$$

The activation of the threshold S_{sill} on the water level triggers in a pulse in the discharge sensitivity $\mathcal{Q}_\phi$ to the parameter ϕ (see term $\partial X/\partial S$ in equations (2.39), also see discussion in Section 2.3.3), provided that $\mathcal{S}_\phi$ is non-zero. Note that $\mathcal{S}_\phi$ is different from zero for any parameter ϕ associated with the reservoir S or with the reservoirs located upstream of the reservoir S.

The association of a threshold transfer function with the water level in a slow dynamics reservoir is thus related to the occurrence of bursts in the sensitivities of the simulated discharge to any parameter that controls the water level in that slow dynamics reservoir.

2.10 References for Chapter 2

Blavoux, B., J. Mudry and J.-M. Puig (1992). « The karst system of the Fontaine de Vaucluse (South-eastern France) ». In: *Environmental Geology* 19.3, pp. 215–225. DOI: 10.1007/BF01704088. See p. 43.

Bonacci, O. (2007). « Analysis of long-term (1878-2004) mean annual discharges of the karst spring Fontaine de Vaucluse (France) ». In: *Acta Carsologica* 36.1, pp. 151–156. See p. 43.

Bruxelles, L. (2001). « Dépots et altérites des plateaux du Larzac central: Causses de l'Hospitalet et de Campestre (Aveyron, Gard, Hérault). Évolution morphogénique, consequences géologiques et implications pour l'amenagement ». PhD thesis. Université de Provence. See pp. viii, 39, 40, 72, 73.

Bézès, C. (1976). « Contribution à la modélisation des systèmes aquifères karstiques; établissement du modèle BEMER; son application à quatre systèmes karstiques du midi de la France ». PhD thesis. Université Montpellier II. See p. 42.

Cacuci, D. (2003). *Sensitivity and Uncertainty Analysis: Theory*. Ed. by Chapman and Hall/CRC. Sensitivity and Uncertainty Analysis. CRC Press. ISBN: 9781584881155. See pp. 10, 44, 52.

Delft, G. van, G. Y. El Serafy and A. W. Heemink (2009). « The ensemble particle filter (EnPF) in rainfall-runoff models ». In: *Stochastic Environmental Research and Risk Assessment* 23.8, pp. 1203–1211. DOI: 10.1007/s00477-008-0301-z. See p. 38.

Fleury, P. (2005). « Sources sous-marines et aquifères karstiques côtiers méditerranéens. Fonctionnement et caractérisation ». PhD thesis. Université Paris VI - Pierre et Marie Curie. URL: http://hydrologie.org/THE/FLEURY.pdf. See pp. vi, xiv, xvii, 39, 42, 44, 52, 59, 72.

Gupta, H. V., H. Kling, K. K. Yilmaz and G. F. Martinez (2009). « Decomposition of the mean squared error and NSE performance criteria: Implications for improving hydrological modelling ». In: *Journal of Hydrology* 377.1-2, pp. 80–91. DOI: 10.1016/j.jhydrol.2009.08.003. See p. 52.

Hreiche, A. (2003). « Modélisation conceptuelle de la transformation pluie-débit dans le contexte méditerranéen ». PhD thesis. Université Montpellier II. URL: http://tel.archives-ouvertes.fr/tel-00004188/fr/. See p. 42.

Jacob, T. (2009). « Apport de la gravimétrie et de l'inclinométrie à l'hydrologie karstique ». PhD thesis. Université Montpellier II. URL: http://tel.archives-ouvertes.fr/tel-00404851/fr/. See pp. viii, 40, 73–75.

Jazayeri Noushabadi, M. R. (2009). « Characterisation of relationships between fracture network and flow-path network in fractured and karstic reservoirs numerical modelling and field investigation (Lez aquifer, Southern France) ». PhD thesis. Université Montpellier II. URL: http://www.hydrosciences.org/IMG/pdf/PHD_2009_M_Reza_Jazayeri.pdf. See pp. 5, 8, 59.

Le Moine, N. (2010). « Le bassin versant de surface vu par le souterrain : Une voie d'amélioration des performances et du réalisme des modèles pluie-débit ? » PhD thesis. Université Pierre et Marie Curie. URL: http://hydrologie.org/THE/LE_MOINE.pdf. See p. 38.

Madsen, H. (2000). « Automatic calibration of a conceptual rainfall-runoff model using multiple objectives ». In: *Journal of Hydrology* 235.3-4, pp. 276–288. DOI: 10.1016/S0022-1694(00)00279-1. See pp. 52, 96, 114.

Mazzilli, N., V. Guinot and H. Jourde (2011*c*). « Sensitivity analysis of conceptual model calibration to initialisation bias. Application to karst spring discharge models. » In: *revision for Advances In Water Resources*. See p. 37.

— (2011*d*). « Sensitivity analysis of conceptual model calibration to initialisation bias. Application to karst spring discharge models. » In: *ModelCare 2011 Conference held in Leipzig, Germany (18-22 Sept. 2011)*. See p. 37.

Mouelhi, S. (2003). « Vers une chaîne cohérente de modèles pluie-débit conceptuels globaux aux pas de temps pluriannuel, annuel, mensuel et journalier ». PhD thesis. Cemagref d'Antony, ENGREF. URL: http://tel.archives-ouvertes.fr/tel-00005696/fr/. See p. 38.

Moussa, R., N. Chahinian and C. Bocquillon (2007). « Distributed hydrological modelling of a Mediterranean mountainous catchment - Model construction and multi-site validation ». In: *Journal of Hydrology* 337, pp. 35–51. DOI: 10.1016/j.jhydrol.2007.01.028. See p. 52.

Murphy, A. (1988). « Skill scores based on the mean square error and their relationships to the correlation coefficient ». In: *Monthly Weather Review* 116.12, pp. 2417–2424. DOI: 10.1175/1520-0493(1988)116<2417:SSBOTM>2.0.CO;2. See p. 52.

Perrin, C., C. Michel and V. Andreassian (2001). « Does a large number of parameters enhance model performance? Comparative assessment of common catchment model structures on 429 catchments ». In: *Journal of Hydrology* 242.3-4, pp. 275–301. DOI: 10.1016/S0022-1694(00)00393-0. See pp. 6, 38, 77, 100.

Pulido-Bosch, A., A. Padilla-Benitez, D. Dimitov, and M. Machkova (1995). « The discharge variability of some karst springs in Bulgaria studied by time series analysis. » In: *Hydrological Sciences Journal* 40.4, p. 517. DOI: 10.1080/02626669509491436. See p. 43.

Refsgaard, J. C. (1997). « Validation and intercomparison of different updating procedures for real-time forecasting ». In: *Nordic Hydrology* 28.2, pp. 65–84. DOI: 10.2166/nh.1997.005. See p. 38.

Ricard, J. and M. Bakalowicz (1996). *Connaissance, aménagement et protection des ressources en eau du Larzac septentrional, Aveyron (France)*. Tech. rep. R38953. BRGM. URL: http://www.brgm.fr/Rapport?code=RR-38953-FR. See pp. viii, 39, 40, 72, 73.

Seo, D.-J., L. Cajina, R. Corby and T. Howieson (2009). « Automatic state updating for operational streamflow forecasting via variational data assimilation ». In: *Journal of Hydrology* 367.3-4, pp. 255–275. DOI: 10.1016/j.jhydrol.2009.01.019. See p. 38.

Thornthwaite, C. (1948). « An approach toward a rational classification of climate ». In: *Geographical Review* 38.1, pp. 55–94. URL: http://www.jstor.org/stable/210739. See pp. 39, 73, 77, 93.

Tritz, S., V. Guinot and H. Jourde (2011). « Modelling the behaviour of a karst system catchment using non linear hysteretic conceptual model ». In: *Journal of Hydrology* 397.3-4, pp. 250–262. DOI: 10.1016/j.jhydrol.2010.12.001. See pp. vi, xvii, 7, 38–41, 44, 46, 52, 59, 72, 73, 76, 77, 80, 93, 94.

Wagener, T., H. S. Wheater and H. V. Gupta (2004). *Rainfall-runoff modelling in gauged and ungauged catchments*. Ed. by T. K. Wei. London: Imperial College Press, p. 332. ISBN: 978-1-86094-466-6. URL: http://www.icpress.co.uk/environsci/p335.html. See p. 38.

Weerts, A. H. and G. Y. H. El Serafy (2006). « Particle filtering and ensemble Kalman filtering for state updating with hydrological conceptual rainfall-runoff models ». In: *Water Resources Research* 42.9, W09403–. DOI: 10.1029/2005WR004093. See p. 38.

Weglarczyk, S. (1998). « The interdependence and applicability of some statistical quality measures for hydrological models ». In: *Journal of Hydrology* 206.1-2, pp. 98–103. DOI: 10.1016/S0022-1694(98)00094-8. See p. 52.

Yapo, P. O., H. V. Gupta and S. Sorooshian (1998). « Multi-objective global optimization for hydrologic models ». In: *Journal of Hydrology* 204.1-4, pp. 83–97. DOI: 10.1016/S0022-1694(97)00107-8. See pp. 52, 114.

Chapter 3

Use of ground-based gravity measurements for the calibration of a global rainfall-discharge reservoir model

This chapter focuses on the relevance of the inclusion of ground-based gravity data in the calibration process of a global rainfall-discharge reservoir model. The analysis is performed for the Durzon karst system (Larzac, France). The first part of the study focuses on the hydrological interpretation of the ground-based gravity measurements. The second part of the study investigates the information content of the gravity data with respect to water storage dynamics modelling. This work is currently in revision for Environmental Earth Sciences [Mazzilli et al., 2011*b*].

Contents

3.1 Problem statement

In most cases, the parameter values for global, rainfall-discharge reservoir models can not be directly derived from field measurements. Instead the model parameters must be estimated based on the goodness-of-fit between observed and modelled variables [Wagener and Gupta, 2005].

Most global reservoir models are calibrated against discharge measurements. In such models, the number of parameters to be calibrated is small (typically 4 to 10). Nevertheless, in many cases the calibration results are plagued with equifinality. Including internal model state variables (i.e., water content) in the calibration procedure may help reduce equifinality [Guinot et al., 2011; Kuczera and Mroczkowski, 1998] but aquifer-scale water storage estimation is challenging.

Space-borne gravitational surveys such as the GRACE (Gravity Recovery and Climate Experiment) satellite mission have the potential to address regional-scale water storage variations [Strassberg et al., 2009; Werth et al., 2009]. Regarding small or intermediate scale aquifers, local observations (such as groundwater level or soil moisture) remain the only option for water storage variations monitoring. In particular, ground-based gravity measurements provide depth-integrated estimates of local water storage variations [Pool and Eychaner, 1995]. The use of ground-based gravity measurements as the only calibration constraint for a field-scale reservoir model has been shown to improve model results substantially as compared to calibration against soil moisture or groundwater head measurements [Creutzfeldt et al., 2010].

Because their representativeness is usually difficult to assess, the integration of local measurements into the calibration process of spatially-integrated reservoir models is not straightforward. Local data may thus be considered as "soft data", i.e., data "that cannot be used directly as exact numbers" with regards to the calibration process of spatially-integrated reservoir models. The inclusion of soft data in the calibration process has been reported to significantly improve both model consistency and model predictive uncertainty [Seibert and McDonnell, 2002; Vache and McDonnell, 2006].

The present paper examines the relevance of the inclusion of auxiliary ground-based gravity data in the calibration process of a daily rainfall-discharge reservoir model. The case under study is that of the Durzon karst system (Larzac plateau, southern France), that has been the subject of extensive geodetic monitoring [Jacob et al., 2009, 2008, 2010*a*,*b*]. The purpose of this work is (i) to discuss the hydrodynamic interpretation of the gravity data, (ii) to investigate the possible use of this data to constrain the calibration of a global reservoir model.

This contribution is structured as follows. The study area and the available field data are presented in Section 3.2.1. The hydrological interpretation of ground-based gravity measurements is discussed in Section 3.2.2. Section 3.2.3 discusses the potential benefits of including the auxiliary gravity data into the calibration process of a global rainfall-discharge reservoir model.

3.2 Study area and field data

3.2.1 Site overview

The Durzon karst system is located in the Grands Causses area in the Southern Massif Central (France). The main outlet of this system is the Durzon vauclusian spring, which is located in the Northern part of the catchment on the Hospitalet fault (see Figure 3.1). The north-eastern and the southern boundaries of the system are delineated by thrust faults. The other boundaries are delineated by the topography. Based on geomorphological characteristics, mass balance and tracing experiments [Bruxelles, 2001; Ricard and Bakalowicz, 1996], recharge area estimates range from 100 to 120 km^2. Following [Fleury, 2005] and [Tritz et al., 2011], a recharge area of 116.8 km^2 is considered in the present study. The karst system is embedded in a 400 m thick formation of

middle to upper Jurassic limestones and dolomites, deposited on top of a 200 m thick formation of upper-Liassic marls [Bruxelles, 2001] (see Figure 3.1). This latter formation constitutes the aquifer bedrock. The thickness of the vadose zone ranges from approximately 50 m upstream of the catchment to approximately 180 m downstream. The morphology of the cavities indicates that karstification is still at an early stage [Bruxelles, 2001]. The karstification is predominantly regressive, i.e., it develops from the Durzon spring towards the upstream of the catchment [Bruxelles, 2001]. The southern, upstream part of the catchment is less affected by karstification dynamics. Inefficient vertical drainage in this part of the catchment is evidenced by the very low number of swallow-holes and the presence of dolomitic sands and clay formations at the surface [Bruxelles, 2001]. During intense and long-lasting rainfall events, the amount of precipitation may exceed the infiltration capacity toward the saturated zone and fill up the soil and epikarst reservoirs and ponding occurs at the surface [Bruxelles and Caubel, 1996].

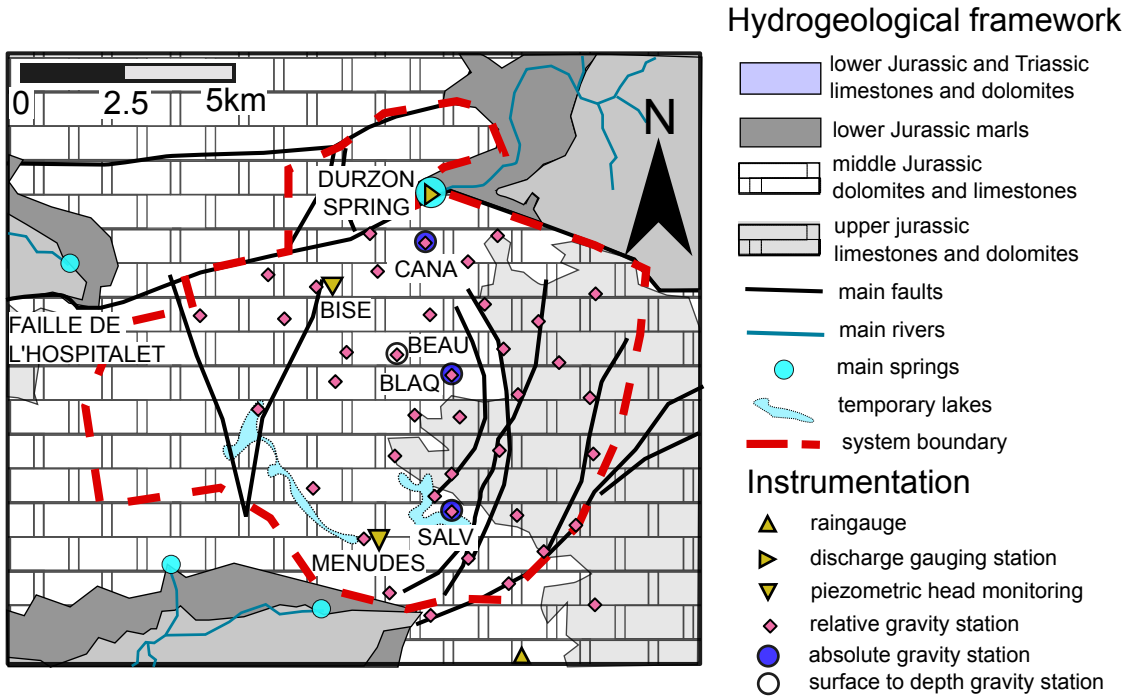

Figure 3.1: Hydrogeological framework and instrumentation of the Durzon area. Modified after Bruxelles, 2001; Jacob, 2009; Ricard and Bakalowicz, 1996.

3.2.2 Meteorological data

Rainfall data are measured at the "Le Caylar" Météo-France meteorological station, some 10 km S-SE of the Durzon spring. The daily potential evapotranspiration (PET) is estimated from the Thornthwaite's [Thornthwaite, 1948] monthly potential evapotranspiration using a sine function-based interpolation as proposed by [Tritz et al., 2011]. For a more thorough description of the meteorological data see Section 2.2.1.

3.2.3 Gravity data

Extensive geodetic monitoring was performed on the Durzon system as part of the ANR research project HydroGéodésie 2006-2009. Water storage variations have been investigated based on several gravimetric techniques [Jacob, 2009]:

1. Absolute gravity measurements have been carried out at three sites (BLAQ, CANA and SALV) on a monthly basis from January 2006 to September 2008 [Jacob et al., 2008] (see Figure 3.2b). These measurements give insights into the temporal dynamics of the water storage,
2. Time-lapse microgravity measurements have been carried out over 40 sites, and complemented by absolute gravity measurements [Jacob et al., 2010*b*] (see Figure 3.2a). In total, four microgravity surveys have been carried out, in both low and high water level periods. These surveys provide insights into the 2D heterogeneity of the water storage at the aquifer scale,
3. Time-lapse surface to depth gravity measurements have been performed six times down a pit cave [Jacob et al., 2010*b*]. These measurements provide vertical resolution for the gravity signal measured by surface instruments. Water storage variations at the surface to depth gravity site are thought to occur within the first 60 m of the karst, plausibly in the epikarst.

The gravity data presented hereafter are corrected for the regional contribution of hydrology calculated from the European Center for Medium range Weather Forecasts model (ECMWF model) [Viterbo and Beljaars, 1995] which quantifies global soil moisture and snow variations. Gravity variations are converted into water height based on the infinite Bouger slab approximation. All gravity data are taken from [Jacob, 2009].

3.3 Interpretation of ground-based gravity measurements in terms of aquifer-scale water storage dynamics indicators

3.3.1 Hydrogeomorphological interpretation of the gravity signal

An intrinsic limitation of surface-based gravity measurements is that they cannot be used to infer the vertical distribution of water storage variations. However, Jacob et al., 2010*b* suggest that the main storage function may be held by the epikarst reservoir. Note that significant water storage within the infiltration zone may occur in areas with low transfer capacity towards the saturated zone. Low vertical transfer capacity is expected in the southern, upstream part of the catchment but also in the middle and downstream parts of the catchment in areas remote from the main drainage system. Also note that predominant water storage within the soil-epikarst reservoir or the infiltration zone has been evidenced in various karst systems [Lastennet and Mudry, 1997; Perrin et al., 2003*a*].

3.3.2 2-D storage heterogeneity within the karst system

Ground-based gravimeters are sensitive to local-scale hydrological signals. Indeed, the radius of the sampling area of ground-based gravity measurements is smaller than 500 m. However, water storage properties are likely to vary laterally within the karst system. Such lateral variations are evidenced by magnetic resonance soudings [Legchenko and Valla, 2002] water content measurements [Boucher et al., 2010].

Microgravity surveys have been conducted in order to characterize the 2D storage heterogeneity. The water storage amplitude within the Durzon system has been shown to range from 100 mm in low water periods to 550 mm in high water level periods [Jacob et al., 2010*b*] (see Figure 3.2a). No simple relationship has been established between the water storage amplitude and known geologic or karstic features [Jacob et al., 2010*b*]. However, some characteristics of the gravity signal may be related to geomorphological considerations. In the western part of the basin, high-amplitude storage areas match depressions filled with poorly permeable, clay soil. By contrast, low-amplitude storage areas in the centre of the basin match hilly surfaces with thin soil cover [Jacob et al., 2010*b*].

3.3.3 Analysis of the gravity-inferred water storage dynamics

Absolute gravity measurements do give insights on the temporal dynamics of water storage (see Figure 3.2b). Water storage variations recorded by the absolute gravimeters at BLAQ, CANA and SALV sites range from 230 to 360 mm. During summer, the water storage variations are mostly driven by evapotranspiration [Jacob, 2009]. Conversely, winter water storage variations are mainly driven by rainfall and by drainage towards the saturated zone and the outlet [Jacob, 2009]. SALV site exhibits a pluri-annual storage trend which may suggest enhanced water storage due to inefficient vertical transfer in the upstream part of the catchment [Jacob et al., 2008].

3.3.4 Relevance of gravity measurements with respect to aquifer-scale water storage dynamics modelling

The contribution of ground-based absolute gravity measurements to the modelling of the Durzon aquifer-scale water storage dynamics may be questioned. Indeed, significant 2D heterogeneity of the aquifer storage has been identified by microgravity surveys (Section 3.3.2). At the same time, due to the heavy time investment required to conduct such surveys, only a few measurement campaigns have been carried out. On the other hand, absolute gravity measurements have been conducted with monthly time step. This is more appropriate to investigate water storage dynamics, but such measurements could only be performed at a few locations. Nevertheless, the following observations hint that absolute gravity measurements at BLAQ site may be considered as a proxy for aquifer scale water storage dynamics:

1. the aquifer-scale water storage variations infered from mass balance calculation are in good agreement with the water storage variations inferred from gravity monitoring at BLAQ site [Jacob et al., 2008],

2. a rough estimate of the seasonal aquifer-scale water storage variations can be obtained by integrating the local water storage variations inferred from microgravity measurements over the whole catchment area. The thus obtained aquifer-scale water storage variations are in good agreement with the water storage variations derived from absolute gravity surveys at BLAQ site (see Figure 3.2).

The good correspondence between the gravity-inferred water storage variations at BLAQ site and the aquifer scale water storage dynamics can be related to the relatively centred location of this site in the catchment, where both the vadose zone thickness and the density of karst features are intermediate, yielding intermediate storage and infiltration processes (see also Jacob et al., 2010*b*). However, note that such correspondence is fortuitous and could not be predicted in advance based on the sole aquifer characteristics.

In the following, we investigate the use the absolute gravity time series at BLAQ site as a proxy for aquifer scale water storage variation. Note that much caution is needed in the interpretation, because the lack of representativeness of ground-based gravity measurements with respect to aquifer scale storage dynamics is difficult to quantify. Furthermore, the associated uncertainty may not be stationary. As an example, the heterogeneity in the water storage variations that results from the heterogeneity in the basin vegetation cover may be enhanced during dry months, when evapotranspiration reaches its maximum, which means that the representativeness of gravity-inferred water storage variations with respect to aquifer scale storage dynamics may be time-dependent.

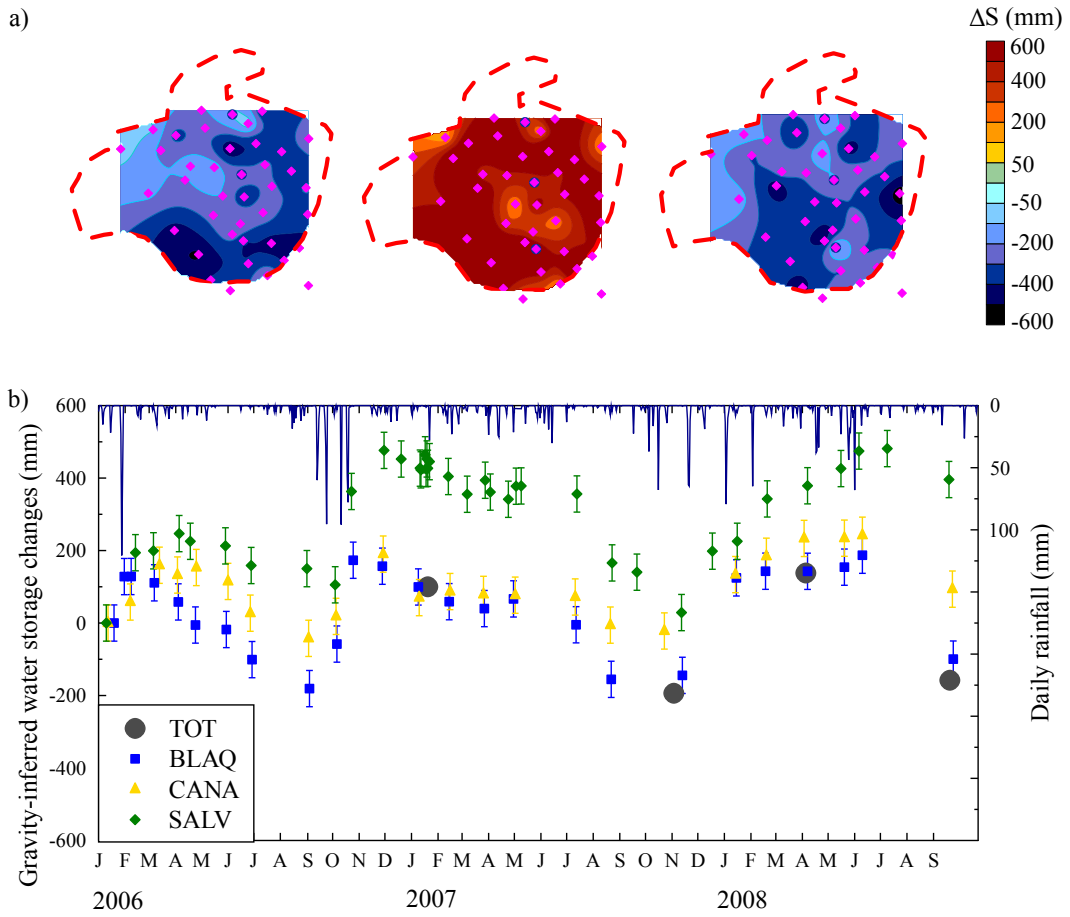

Figure 3.2: Temporal dynamics of the gravity signal. a) Gravity-inferred water stock difference ΔS between: left) mid-January 2007 and early November 2007, middle) early November 2007 and early April 2008, right) early April 2008 and mid-September 2008. Modified after Jacob et al., 2010*b*. b) Squares, triangles and diamonds: gravity changes inferred from absolute gravity measurements at BLAQ, CANA and SALV sites respectively. Circles: mean basin-scale gravity changes based on the integration of microgravity measurements. The first measurement at each site arbitrarily sets the reference gravity value.

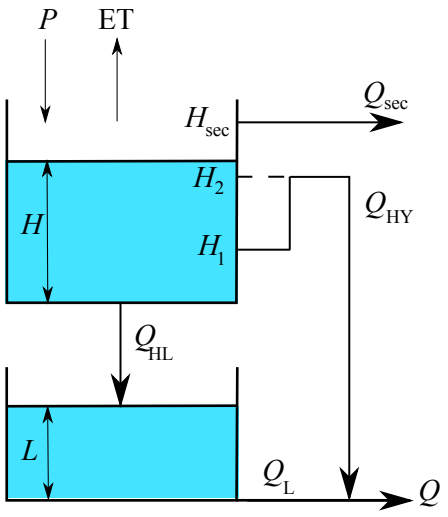

Figure 3.3: Structure and notations for the hysteresis-based model [Tritz et al., 2011].

3.4 Use of ground based gravity measurements for model calibration

3.4.1 Model description and calibration

The model considered in this study is the hysteresis-based model proposed by Tritz et al., 2011. A presentation of the model functioning and governing equations is given in Section 2.2.2 (also see model structure in Figure 3.3). In particular, the evapotranspiration is assumed to be equal to the PET as long as the upper reservoir is not empty. The potential evapotranspiration is calculated based on a the Thornthwaite's formula [Thornthwaite, 1948] (see Section 3.2.2). Note that the Thornthwaite's method is reported to underestimate the PET in arid regions and seasons [e.g. Lu et al., 2005].

The hysteresis-based model has been calibrated against discharge data over the January 2006 - October 2008 period by Monte Carlo sampling of the parameter space (see parameter set in Table 3.1, see sampling range in Table 3.2, and see calibration results in Figure 3.4). Note that an uniform sampling of the parameter space is performed for the parameters H_1, H_2, H_{sec} and α whereas a log-uniform sampling is performed for the parameters k_{HY}, k_{sec}, k_{HL} and k_{L}. The model performance is assessed based on the Nash efficiency N_{sim} [Nash and Sutcliffe, 1970] and a modified balance error BE_{sim} [Perrin et al., 2001]. Both criteria have been modified so as to account for the $\phi = 3\%$ discharge measurement imprecision [Tritz et al., 2011]

$$N_{\text{sim}} = 1 - \frac{\sum \text{Err}(Q)^2}{\sum (Q_{\text{obs}} - \overline{Q_{\text{obs}}})^2} \tag{3.1a}$$

$$\text{BE}_{\text{sim}} = 1 - \left| \frac{\sum \text{Err}(Q)}{\sum Q_{\text{obs}}} \right| \tag{3.1b}$$

where $\text{Err}(Q)$ is the modelling error, defined as

$$\text{Err}(Q) = \begin{cases} Q_{\text{sim}} - (1-\phi)Q_{\text{obs}} & \text{if } Q_{\text{sim}} \leq (1-\phi)Q_{\text{obs}} \\ 0 & \text{if } (1-\phi)Q_{\text{obs}} < Q_{\text{sim}} < (1+\phi)Q_{\text{obs}} \\ Q_{\text{sim}} - (1+\phi)Q_{\text{obs}} & \text{if } Q_{\text{sim}} > (1+\phi)Q_{\text{obs}} \end{cases} \tag{3.2}$$

The calibration yields a Nash efficiency of 0.87 and a balance error of 5.5%.

3.4.2 What to compare ?

The physical meaning of the two reservoirs in the hysteresis-based model has been discussed in Section 2.2.2. Roughly speaking, the upper reservoir is meant to account for soil-epikarst storage whereas the lower reservoir represents the vadose and saturated zones. However, these physical considerations are only indicative. Rather, the upper reservoir accounts for rapid water storage dynamics, whereas the lower reservoir represents slower water storage processes, regardless of the physical reservoirs actually involved. Indeed, geophysical investigations over the Durzon basin have shown that long-term storage processes may occur within the soil-epikarst system (see discussion above). As a consequence, gravity-inferred water storage variations should be compared to the sum of the water storage variations in the upper and lower reservoirs of the hysteresis-based model.

Denote by $\mathcal{H}_\phi$, $\mathcal{L}_\phi$ and $\mathcal{Q}_\phi$ the sensitivity of the variables H, L and Q respectively to the parameter ϕ. Applying the perturbation approach to the model equations leads to the following

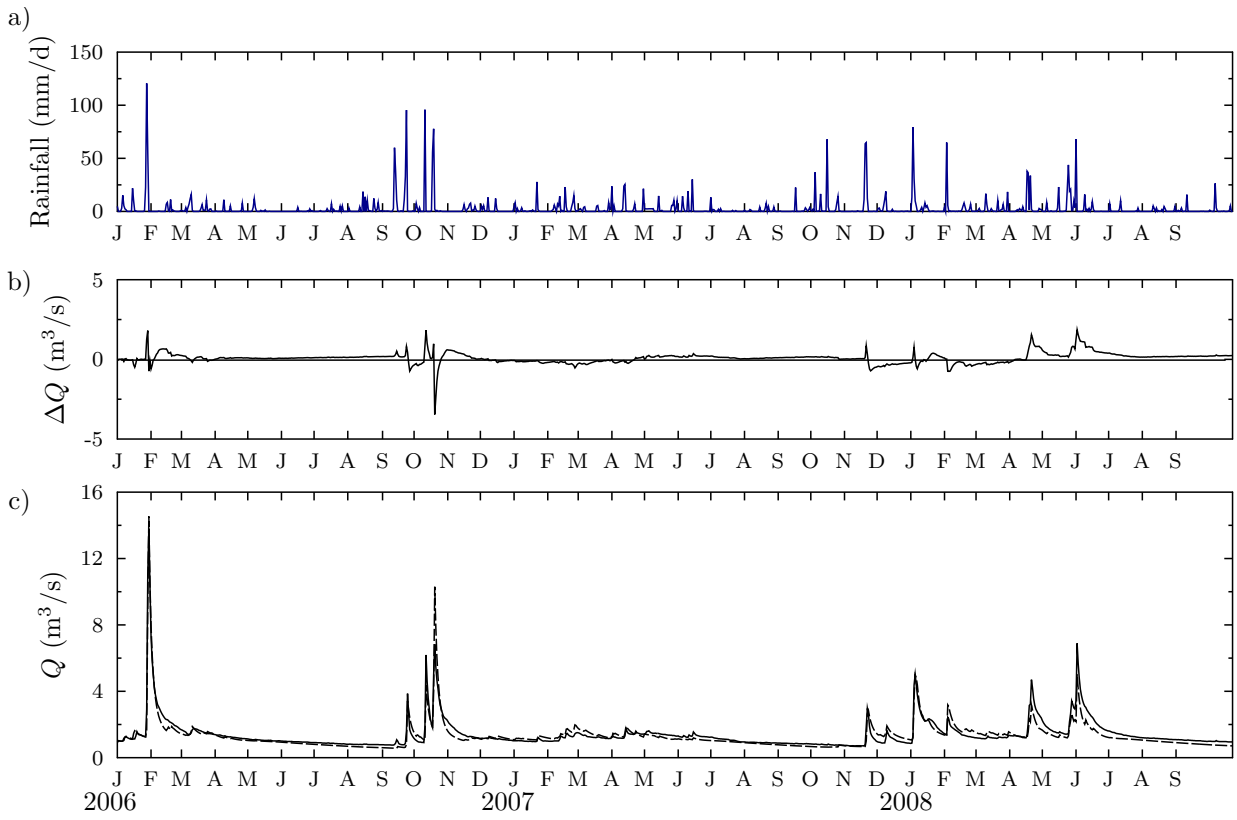

Figure 3.4: Hysteresis-based model. Simulation results over the calibration period: a) difference ΔQ between the measured and the simulated spring discharge, b) measured (Q_{obs}, solid line) vs. simulated (Q_{sim}, dotted line) spring discharge.

Symbol	Meaning	Value
H_{sec}	threshold level for the secondary springs activation	143 mm
k_{sec}	specific discharge coefficient for the secondary springs discharge	$8.0 \times 10^{-2}\,\mathrm{d}^{-1}$
H_1	lower threshold level for the hysteretic discharge	27 mm
H_2	upper threshold level for the hysteretic discharge	99 mm
k_{HY}	specific discharge coefficient for the hysteretic discharge	$7.3 \times 10^{-2}\,\mathrm{mm\,d}^{-1}$
α	exponent for the hysteretic discharge	3 6
k_{HL}	specific discharge coefficient for the infiltration to the reservoir L	$7.3 \times 10^{-3}\,\mathrm{d}^{-1}$
k_{L}	specific discharge coefficient for the baseflow discharge	$5.0 \times 10^{-3}\,\mathrm{d}^{-1}$

Table 3.1: Parameter set for the hysteresis-based model. Parameter set resulting from the calibration over the January 2006 - October 2008 period.

Symbol	Min. Value	Max. Value
H_{sec}	0	400 mm
k_{sec}	$1 \times 10^{-2}\,\mathrm{mm\,d}^{-1}$	$1\,\mathrm{mm\,d}^{-1}$
H_1	0	400 mm
H_2	0	400 mm
k_{HY}	$10^{-2}\,\mathrm{mm\,d}^{-1}$	$1\,\mathrm{mm\,d}^{-1}$
α	1	7
k_{HL}	$10^{-4}\,\mathrm{mm\,d}^{-1}$	$10^{-2}\,\mathrm{mm\,d}^{-1}$
k_{L}	$10^{-4}\,\mathrm{mm\,d}^{-1}$	$10^{-2}\,\mathrm{mm\,d}^{-1}$

Table 3.2: Parameter range for the Monte-Carlo sampling performed in Sections 3.4.1 and 3.4.5.

set of sensitivity equations:

$$\frac{\mathrm{d}}{\mathrm{d}t}(\mathcal{H}_\phi + \mathcal{L}_\phi) = -\frac{\partial \mathrm{ET}}{\partial \phi} - \frac{\partial Q_{\mathrm{sec}}}{\partial \phi} - \mathcal{Q}_\phi \tag{3.3a}$$

$$\mathcal{Q}_\phi = \frac{\partial Q_{\mathrm{HY}}}{\partial \phi} + \frac{\partial Q_{\mathrm{L}}}{\partial \phi} \tag{3.3b}$$

Equation (3.3) indicates that compared to discharge measurements, water storage measurements contain enhanced information on the parameters related to the evapotranspiration and to the secondary springs activation. The information on the secondary springs fluxes is expected to be predominant during flood events, while information on the evapotranspiration fluxes is dominant during low-flow periods. As a consequence:

- the information content of the water storage measurements is the highest during flood events or during low-flow periods,
- due to low-frequency sampling of the gravimetric information, the information content of the available water storage measurements as regards the parameters related to secondary springs activation is likely to be reduced,
- by contrast, the monthly sampling of the gravimetric information may be adapted to the water storage dynamics during low flow periods.

The perspective of gaining information on the evapotranspiration function is all the more interesting that rainfall-discharge models are usually little sensitive to the evapotranspiration signal (low-pass filter behaviour) [Oudin et al., 2006; Oudin et al., 2005].

3.4.3 Comparison between gravity-inferred and modelled water storage variations

The comparison between the total water storage variations inferred from absolute gravity measurements at BLAQ site and the simulated water level variations in the reservoirs of the hysteresis-based model yields the following comments (Figure 3.5).

1. There is a globally good agreement between the water storage variations inferred from gravity measurements and the sum of the simulated water levels in the upper and lower reservoirs of the hysteresis-based model (linear regression coefficient R^2 of 0.7). Note that most of the water storage variations simulated by the hysteresis-based model occur within the upper, rapid-dynamics reservoir. Furthermore, taking into account the contribution of water storage variations within the lower, slow-dynamics reservoir helps better reproduce the seasonal variability of the gravity signal,
2. The upper reservoir of the hysteresis-based model systematically dries out at the beginning of the summer periods, which results in unrealistic zero evapotranspiration-related water storage variations during the summer periods. This unrealistic behaviour does show up by comparison to the gravity-inferred storage variations. Indeed, the simulated summer water storage decrease is lower than the corresponding gravity-inferred water storage decrease. Modifications in either the selected parameter set or the evapotranspiration function or the model structure may be considered in order to improve the simulation of the evapotranspiration-related water storage variations, for the following reasons:
   a) The actual evapotranspiration is taken equal to the potential evapotranspiration when the upper reservoir is not empty is likely to yield overestimated summer evapotranspiration fluxes, until the upper reservoir dries out. Taking into account the fact that the vegetation may limit its transpiration to face drought conditions [Hernandez-Santana et al., 2008; Otieno et al., 2007] could help sustain non-zero evapotranspiration fluxes for a longer period,

b) The limited depth of the upper reservoir ($H \geq 0$) is meant to prevent excessive undersaturation. Increasing the depth of the upper reservoir would delay its drying and thus result in more realistic evapotranspiration fluxes, but it would also probably deteriorate discharge simulations at the beginning of the autumn period. Another option is to stop the infiltration towards the lower reservoir L when H falls below a given value $H_{\min}$. This would delay the drying of the upper reservoir H, but deteriorated simulations of the summer recession discharge are likely. Lastly, it may be questioned whether only the upper reservoir should be submitted to evapotranspiration fluxes. Indeed, the upper and the lower reservoirs can be seen as a decomposition of the water storage between two principal components, with contrasted flow dynamics properties. In that view, the lower, slow dynamics reservoir could also be used to feed the evapotranspiration fluxes.

3. The overall fit between the gravity-inferred and the simulated water storage variations during high flow periods is good. The main discrepancy is observed during winter 2006/2007. The September - November rainy period yields an increase of equivalent magnitude in the simulated and the gravity-inferred water storages. However, the gravity measurements indicate a slower storage decrease than the simulation results. Note that this period is associated with no particular degradation of the quality of the simulation of the discharge time serie. The overestimation of the main flood peak is balanced by the underestimation of the November recession discharge, yielding a 2% balance error on the simulated spring discharge over the October to December period (see Figure 3.4). The fact that the discrepancy between the gravity-inferred and the simulated water storage is not associated with a bad estimation of the output fluxes suggests that the cause of the discrepancy may be lack of representativeness of the gravity signal of the BLAQ station for that particular period. A heterogeneous spatial distribution of rainfall during the October event could be the cause for that lack of representativeness.

The overall good agreement between the gravity signal and the simulation results provides an indication of model consistency. However, it must be noted that the hysteresis-based model proposed by Tritz et al., 2011 is partly "right for the wrong reasons". The relatively good fit of the simulated total water storage variations with the gravity-inferred water storage variations masks the fact that unrealistic summer evapotranspiration fluxes are simulated. This observation illustrates the fact that although physical soundness is recognized as a desirable property for global reservoir models, the physical interpretation of the model structure and laws can not be validated on the sole basis of a good simulation performance on the model output variable.

The above remarks also emphasize the complexity of the interpretation of the discrepancies between the gravity signal and the simulation results, since these discrepancies cannot be systematically charged on bad model calibration or bad model structure. A consequence of that observation is that the inclusion of gravity-inferred water storage variations in the calibration process of a global reservoir model should account for the uncertainty that results from the lack of representativeness of the ground-based gravity measurements with respect to aquifer scale water storage dynamics.

3.4.4 Definition of a criterion of fit between simulated and gravity-inferred water storage variations

The criterion of fit for gravity-inferred water storage variations should account for the uncertainty that results from the lack of representativeness of ground-based gravity measurements with respect to aquifer scale water storage dynamics. Taking into account this uncertainty is of critical importance for the integration of the gravity-inferred information into the calibration process. Indeed, an overestimation of the uncertainty may hinder the ability of the gravimetric information to constrain the parameters. On the contrary, underestimating the uncertainty may constrain

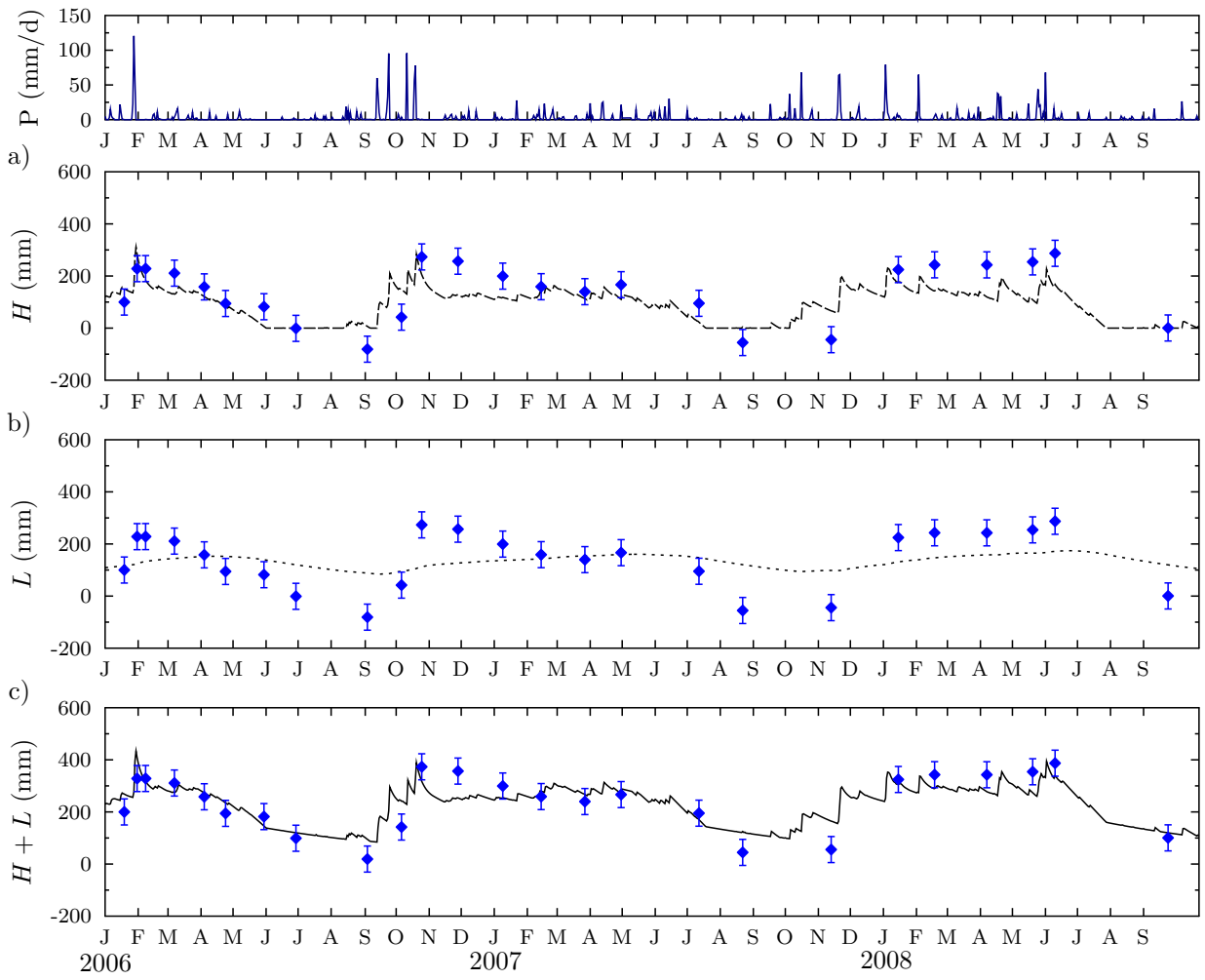

Figure 3.5: Hysteresis-based model. Comparison between water storage variations inferred from absolute gravity measurements at BLAQ site (diamonds) and simulated water level variations (graph a, dashed line: H, graph b, dotted line: L, and graph c, solid line: the sum of the above). The origin of the gravity-inferred water storage is set arbitrarily so as to obtain the best visual fit between the simulated water storage variations and the water storage variations inferred from gravity measurements.

the calibration to reproduce local effects and therefore bias the calibration. Two options may be considered:

1. use an objective function which is based on the sign of the water storage variation (trend indicator). It is then assumed that the uncertainty that stems from the lack of representativeness of the gravity measurements is accounted for indirectly (soft fit criterion),
2. use a classical (i.e., distanced-based or weak-form) objective function and take into account the uncertainty that stems from the lack of representativeness of the gravity measurements.

Two criteria are considered in the present study: a trend indicator and a distance-based function.

The trend indicator TI proposed thereafter aims to characterize the agreement of gravity-inferred and simulated water storage variations trends. Let t_i (i=1...N) be the times of gravity measurements and dWS be the instrumental uncertainty. Denote by $\mathrm{WS}_{\mathrm{gravi}}$ the gravity-inferred water storage by $\mathrm{WS}_{\mathrm{sim}}$ the simulated total water storage

$$\mathrm{WS}_{\mathrm{sim}}(t) = H(t) + L(t) \tag{3.4}$$

and denote by $\Delta_{t_{i-1}}^{t_i}\mathrm{WS}_{\mathrm{gravi}}$ and $\Delta_{t_{i-1}}^{t_i}\mathrm{WS}_{\mathrm{sim}}$ the gravity-inferred and the simulated water storage variations between the times t_{i-1} and t_i

$$\Delta_{t_{i-1}}^{t_i}\mathrm{WS}_{\mathrm{gravi}} = \mathrm{WS}_{\mathrm{gravi}}(t_i) - \mathrm{WS}_{\mathrm{gravi}}(t_{i-1}) \tag{3.5a}$$

$$\Delta_{t_{i-1}}^{t_i}\mathrm{WS}_{\mathrm{sim}} = \mathrm{WS}_{\mathrm{sim}}(t_i) - \mathrm{WS}_{\mathrm{sim}}(t_{i-1}) \tag{3.5b}$$

The indicator TI is defined as:

$$\mathrm{TI} = \frac{\sum_{t_2}^{t_N} p(t_i)}{N-1} \tag{3.6}$$

where $p(t_i)$ is equal to 1 if the signs of the gravity-inferred $\mathrm{WS}_{\mathrm{gravi}}$ and the simulated $\mathrm{WS}_{\mathrm{sim}}$ water storage variations are the same, or if the amplitude of both $\mathrm{WS}_{\mathrm{gravi}}$ and $\mathrm{WS}_{\mathrm{sim}}$ is below the gravity-measurements instrumental uncertainty dWS, and $p(t_i)$ is equal to 0 otherwise:

$$p(t_i) = \begin{cases} 1 & \text{if } \begin{array}{l} \Delta_{t_{i-1}}^{t_i}\mathrm{WS}_{\mathrm{gravi}} \times \Delta_{t_{i-1}}^{t_i}\mathrm{WS}_{\mathrm{sim}} > 0 \\ \left|\Delta_{t_{i-1}}^{t_i}\mathrm{WS}_{\mathrm{gravi}}\right| < \mathrm{dWS} \text{ and } \left|\Delta_{t_{i-1}}^{t_i}\mathrm{WS}_{\mathrm{sim}}\right| < \mathrm{dWS} \end{array} \\ 0 & \text{otherwise} \end{cases} \tag{3.7}$$

Note that the proposed indicator TI takes values between 0 and 1, where higher TI values indicate a better agreement between the gravity-inferred and the simulated water storage variations.

The second performance criterion retained for the analysis is the Nash efficiency. The criterion is modified so as to account for an uncertainty dWS' that stems from both the gravity instrumental uncertainty and the lack of representativeness of the local data with respect to aquifer-scale storage dynamics. Denote by $\overline{\Delta\mathrm{WS}_{\mathrm{gravi}}}$ the mean gravity-inferred water storage variation. The modified Nash criterion N_{WS} is defined as

$$N_{\mathrm{WS}} = 1 - \frac{\sum_{t_2}^{t_N} \left(\mathrm{Err}_{t_i}(\Delta\mathrm{WS})\right)^2}{\sum_{t_2}^{t_N} \left(\Delta_{t_{i-1}}^{t_i}\mathrm{WS}_{\mathrm{gravi}} - \overline{\Delta\mathrm{WS}_{\mathrm{gravi}}}\right)^2} \tag{3.8}$$

where

$$\mathrm{Err}_{t_i}(\Delta\mathrm{WS}) = \left|\Delta_{t_{i-1}}^{t_i}\mathrm{WS}_{\mathrm{gravi}} - \Delta_{t_{i-1}}^{t_i}\mathrm{WS}_{\mathrm{sim}}\right| - \mathrm{dWS}' \quad \text{if } \left|\Delta_{t_{i-1}}^{t_i}\mathrm{WS}_{\mathrm{gravi}} - \Delta_{t_{i-1}}^{t_i}\mathrm{WS}_{\mathrm{sim}}\right| > \mathrm{dWS}' \tag{3.9a}$$

$$\mathrm{Err}_{t_i}(\Delta\mathrm{WS}) = 0 \quad \text{otherwise} \tag{3.9b}$$

3.4.5 Tests of complementarity between simulated and gravity-inferred water storage variations for the proposed model structure and ET function

The first test investigates the capacity of the gravity-inferred water storage variations to better constrain the evapotranspiration signal. The aim of this test is to check whether the gravity-derived informations may help to detect wrong evapotranspiration estimates. The test is structured as follows. The time $t_{\min}$ at which the potential evapotranspiration is minimal (see equation (2.1) on page 40) is varied from the 1st of January to the end of December. The calibration procedure of the hysteresis-based model is repeated for each value of $t_{\min}$. Other PET parameter values are kept constant (see parameter values in Table 2.1). Note that unrealistic $t_{\min}$ values are spanned during the procedure. These unrealistic $t_{\min}$ values are expected to cause unrealistic evapotranspiration fluxes during the corresponding simulations. For each $t_{\min}$ value, the fit between simulated and gravity-inferred water storage variations is estimated based on the two criteria described above. The instrumental uncertainty is equivalent to ±45mm storage variations.

The test results are presented in Figure 3.6. The Nash criterion on the discharge efficiency N_{sim} and the indicators based on the gravity measurements TI and N_{WS} show similar behaviour. Quite expectingly, all criteria reach a minimum around $t_{\min} = 200$ d, that is, when the minimum of the potential evapotranspiration function occurs around mid-July. The optimum of the discharge efficiency N_{sim} is obtained for $t_{\min}$ between mid-January and mid-March. The optimum of the TI and N_{WS} criteria is larger since it is obtained for $t_{\min}$ between January and May.

The fact that the gravity-based performance indicators reach their lower values for unrealistic evapotranspiration functions suggests that the proposed indicators may indeed be used to detect wrong evapotranspiration estimates. However, the gravity-based and the discharge-based efficiencies (TI and N_{sim} criteria) are in phase. This means that the gravity-derived information can not be used to further constrain the evapotranspiration signal and that TI and N_{sim} provide redundant information.

The second test investigates further the information content of the gravity-inferred water storage variations, in comparison to that of the discharge time serie. As a first approximation, the uncertainty dWS' defined above (see Section 3.4.4) is taken equal to the instrumental uncertainty dWS. Indeed, an accurate estimation of the uncertainty associated with the lack of representativeness of the local gravity measurements with respect to aquifer scale storage dynamics would require a finer characterization of the spatial and temporal water storage heterogeneity within the aquifer. A consequence of equaling dWS′ to dWS is that dWS′ is underestimated, which means that the N_{WS} criterion used in the test is more strict.

Multiple simulations of the hysteresis-based model are run based on a Monte-Carlo method from prior distributions (see parameter range in Table 3.2) until a total of 500000 parameter sets achieve a Nash efficiency larger than zero. Uniform prior distributions are assumed for E_{H1}, E_{H2}, E_{sec} and α. Log-uniform prior distributions are assumed for k_{HY}, k_{sec}, k_{EL} and k_{L}. The evapotranspiration signal used for the simulations is kept constant (see parameters value in Table 2.1). For each parameter set we compute both the Nash criterion for the simulated discharge N_{sim} and the modified Nash criterion N_{gravi} for the gravity-inferred water storage variations (see results in Fig. 3.7).

Assume that the purpose of the calibration procedure is to select a single optimal parameter set. Fig. 3.7 shows that low N_{gravi} values also yield a low N_{sim} values. Conversely, the optimal fit for the gravity-inferred water storage variations is obtained for the parameter set that also yields the optimum fit for discharge measurements. As a result, the multicriteria optimization problem can be solved without compromise. It may be concluded that: (i) the proposed model can not be forced into better reproducing the water storage dynamics inferred from the gravity measurements, (ii) the information derived from the gravity measurements is redundant with that derived from the discharge measurements.

Assume now that the calibration procedure aims to select multiple optimal parameter sets using the generalized likelihood uncertainty estimation (GLUE) methodology Beven and Binley, 1992. The GLUE methodology states that, owing to the multiple errors that stem in all stages of the modelling process, the selection of an unique parameter set as the best predictor for the system behaviour may be meaningless. Instead, it proposes to divide the parameter sets into two groups according to the value of the objective function. Parameter sets that yield satisfactory results form the "behavioural" set, as opposed to the "complementary" "non-behavioural" set. Each parameter set is associated with a likelihood measure, which is derived based on the goodness-of-fit to the available observation data. The likelihood of non-behavioural parameter sets is set equal to zero. In what follows, we consider two likelihood measures:

1. the Nash efficiency based on discharge measurements,
2. the arithmetic mean of the Nash efficiency on discharge measurements and the gravity-inferred

water storage variations.

The Monte-Carlo parameter sets are ranked according to the associated likelihood measures and the best 10% are retained as "behavioural". The cumulated GLUE parameter distributions are presented in Fig. 3.8. The conditioned parameter distributions show no significant difference as a function of the likelihood measure (two-sample Kolmogorov-Smirnov nonparametric statistic with 0.05 probability level Siegel, 1956). This result stresses the low discriminatory potential of the gravity-derived information.

Possible reasons for the low information content of the gravity data include:

1. the relatively high value of the instrumental uncertainty (equivalent to ±45 mm storage variations) as compared to the seasonal amplitude of the monitored water storage variations (about 230 mm at BLAQ). Note that even though the instrumental uncertainty may be reduced, the uncertainty stemming from the lack of representativeness of the local measurements with respect to aquifer-scale storage dynamics should still be accounted for,
2. the inadequacy of the model structure or that of the model transfer functions.

3.5 Conclusion

This work focuses on the possible contribution of auxiliary geodetic data to the calibration of a global reservoir model for daily karst spring discharge simulation.

The first part of the study is devoted to the hydrodynamic interpretation of the ground-based gravity measurements. Absolute gravity measurements at one particular site were deemed likely to contain information on aquifer scale storage dynamics. However, the difficulty in quantifying the uncertainty associated with the lack of representativeness of these local measurements with respect to aquifer scale storage dynamics was recognized as a major impediment to the integration of local data into the calibration process.

The second part of the study further investigats the information content of the gravity data with respect to water storage dynamics modelling. The gravity-derived information was found unable to further constrain the single-objective, discharge-based model calibration process. The failure of the inclusion of the local information in the calibration process may be related to: (i) the high value of the experimental uncertainty as compared to the seasonal amplitude of the monitored water storage variations, (ii) the inadequacy of the model structure or that of the model transfer functions.

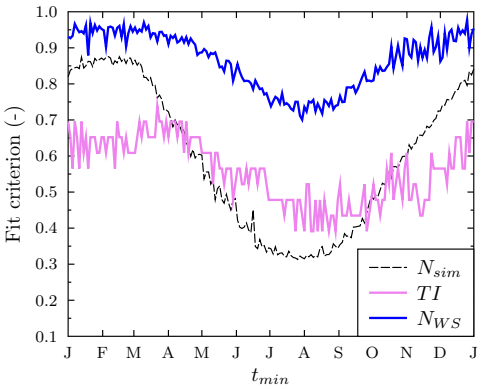

Figure 3.6: Comparison between the Nash criterion on discharge measurements N_{sim}, the trend indicator TI and the modified Nash criterion N_{WS}, for varying t_{min} values in the PET function.

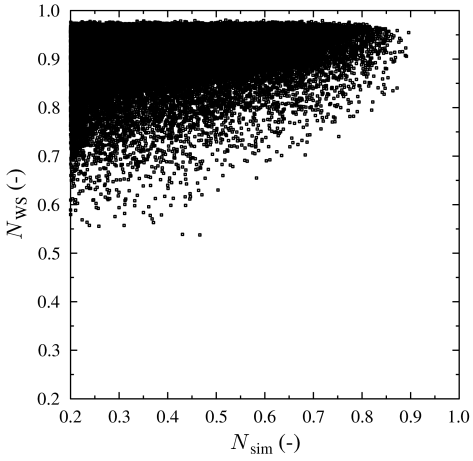

Figure 3.7: Comparison between the Nash criterion on discharge measurements N_{sim} and the Nash criterion on gravity-inferred water storage N_{WS}. Each dot stands for a different parameter set.

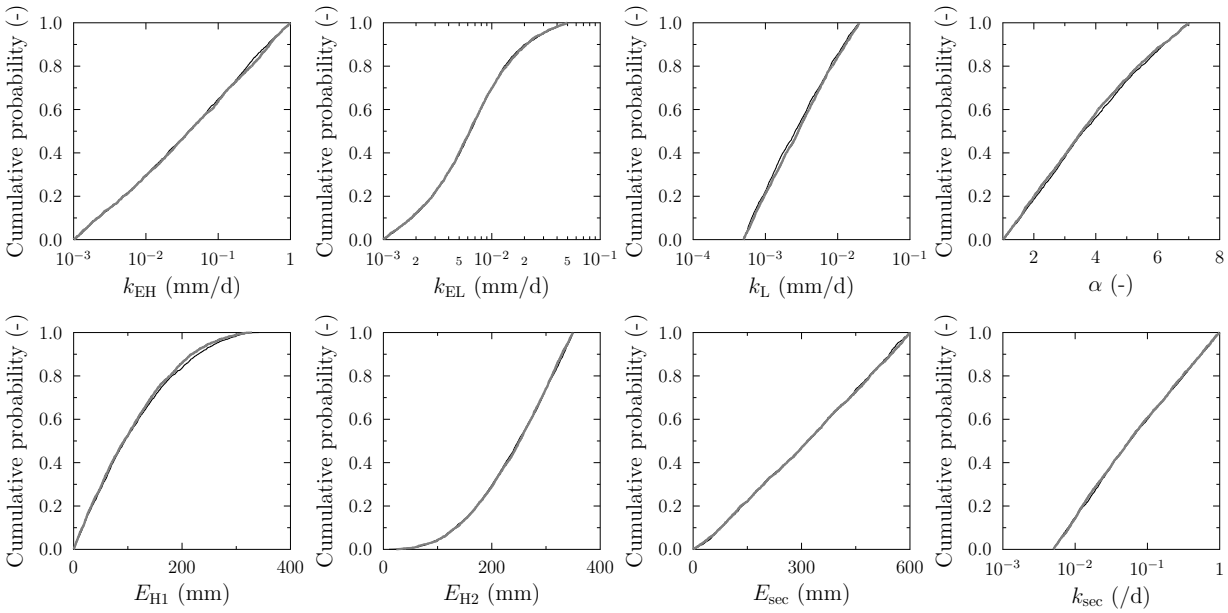

Figure 3.8: GLUE distributions for the parameters of the hysteresis-based model considering: (i) the Nash efficiency based on discharge measurements (black line), (ii) the arithmetic mean of the Nash efficiency on discharge measurements and the gravity-inferred water storage variations (grey line) as a likelihood measure.

3.6 References for Chapter 3

Beven, K. and A. Binley (1992). « The future of distributed models: Model calibration and uncertainty prediction ». In: *Hydrological Processes* 6.3, pp. 279–298. DOI: 10.1002/hyp.3360060305. See pp. 10, 19, 83.

Boucher, M., H. Guyard, K. Chalikakis and A. Legtchenko (2010). *Suivi des variations temporelles du stock d'eau dans la zone non saturée du bassin versant karstique du Durzon (Larzac, Hérault-Aveyron) par la méthode RMP. Synthèse des 3 premières campagnes de mesure (2009-2010).* Tech. rep. ANR HydroGéodésie-2. See p. 74.

Bruxelles, L. (2001). « Dépots et altérites des plateaux du Larzac central: Causses de l'Hospitalet et de Campestre (Aveyron, Gard, Hérault). Évolution morphogénique, consequences géologiques et implications pour l'amenagement ». PhD thesis. Université de Provence. See pp. viii, 39, 40, 72, 73.

Bruxelles, L. and A. Caubel (1996). « Lacs temporaires et circulations de surface sur le causse de l'Hospitalet du Larzac en 1996: Fonctionnement et implications géomorphologiques ». In: *Bulletin de la Société Languedocienne de Géographie* 3-4, pp. 253–288. URL: http://www.karstologie.com/lacs.html. See p. 73.

Creutzfeldt, B., A. Güntner, S. Vorogushyn and B. Merz (2010). « The benefits of gravimeter observations for modelling water storage changes at the field scale ». In: *Hydrology and Earth System Sciences* 7.2, pp. 2221–2260. URL: http://www.hydrol-earth-syst-sci-discuss.net/7/2221/2010/. See p. 72.

Fleury, P. (2005). « Sources sous-marines et aquifères karstiques côtiers méditerranéens. Fonctionnement et caractérisation ». PhD thesis. Université Paris VI - Pierre et Marie Curie. URL: http://hydrologie.org/THE/FLEURY.pdf. See pp. vi, xiv, xvii, 39, 42, 44, 52, 59, 72.

Guinot, V., B. Cappelaere, C. Delenne and D. Ruelland (2011). « Objective functions for conceptual hydrological model calibration: Theoretical analysis of distance- and weak form-based functions ». In: *Journal of Hydrology* 401.1-2, pp. 1–13. DOI: 10.1016/j.jhydrol.2011.02.004. See pp. 21, 72, 114.

Hernandez-Santana, V., J. Martinez-Fernandez, C. Moran and A. Cano (2008). « Response of Quercus pyrenaica (melojo oak) to soil water deficit: A case study in Spain ». In: *European Journal of Forest Research* 127.5, pp. 369–378. DOI: 10.1007/s10342-008-0214-x. See p. 79.

Jacob, T., J. Chery, R. Bayer, N. Le Moigne, J. P. Boy, P. Vernant and F. Boudin (2009). « Time-lapse surface to depth gravity measurements on a karst system reveal the dominant role of the epikarst as a water storage entity ». In: *Geophysical Journal International* 177.2, pp. 347–360. DOI: 10.1111/j.1365-246X.2009.04118.x. See p. 72.

Jacob, T. (2009). « Apport de la gravimétrie et de l'inclinométrie à l'hydrologie karstique ». PhD thesis. Université Montpellier II. URL: http://tel.archives-ouvertes.fr/tel-00404851/fr/. See pp. viii, 40, 73–75.

Jacob, T., R. Bayer, J. Chery, H. Jourde, N. Le Moigne, J.-P. Boy, J. Hinderer, B. Luck and P. Brunet (2008). « Absolute gravity monitoring of water storage variation in a karst aquifer on the Larzac plateau (Southern France) ». In: *Journal of Hydrology* 359, pp. 105–117. DOI: 10.1016/j.jhydrol.2008.06.020. See pp. 72, 74, 75.

Jacob, T., J. Chéry, F. Boudin and R. Bayer (2010*a*). « Monitoring deformation from hydrologic processes in a karst aquifer using long-baseline tiltmeters ». In: *Water Resources Research* 46.9, W09542–. DOI: 10.1029/2009WR008082. See p. 72.

Jacob, T., R. Bayer, J. Chery and N. Le Moigne (2010*b*). « Time-lapse microgravity surveys reveal water storage heterogeneity of a karst aquifer ». In: *Journal of Geophysical Research* 115.B6, B06402–. DOI: 10.1029/2009JB006616. See pp. 72, 74–76.

Kuczera, G. and M. Mroczkowski (1998). « Assessment of hydrologic parameter uncertainty and the worth of multiresponse data ». In: *Water Resources Research* 34.6, pp. 1481–1489. DOI: 10.1029/98WR00496. See p. 72.

Lastennet, R. and J. Mudry (1997). « Role of karstification and rainfall in the behavior of a heterogeneous karst system ». In: *Environmental Geology* 32.2, pp. 114–123. DOI: 10.1007/s002540050200. See p. 74.

Legchenko, A. and P. Valla (2002). « A review of the basic principles for proton magnetic resonance sounding measurements ». In: *Journal of Applied Geophysics* 50.1-2 (May 2002), pp. 3–19. DOI: 10.1016/S0926-9851(02)00127-1. See p. 74.

Lu, J., G. Sun, S. G. Mac Nulty and D. M. Amatya (2005). « A comparison of six potential evapotranspiration methods for regional use in the southeastern United States ». In: *Journal of the American Water Resources Association* 41.3, pp. 621–633. DOI: 10.1111/j.1752-1688.2005.tb03759.x. See p. 77.

Mazzilli, N., H. Jourde, T. Jacob, V. Guinot, M. Boucher, H. Guyard, K. Chalikakis, A. Legtchenko and N. Le Moigne (2011*b*). « On the use of point-based gravity measurements to constrain the calibration of a global rainfall-discharge reservoir model. Case of the Durzon karst system (Larzac, southern France) ». In: in revision for Environmental Earth Sciences. See p. 71.

Nash, J. and J. Sutcliffe (1970). « River flow forecasting through conceptual models. Part I - A discussion of principles ». In: *Journal of Hydrology* 10.3, pp. 282–290. DOI: 10.1016/0022-1694(70)90255-6. See pp. 77, 100.

Otieno, D. O., M. W. T. Schmidt, C. Kurz-Besson, R. L. Do Vale, J. S. Pereira and J. D. Tenhunen (2007). « Regulation of transpirational water loss in Quercus suber trees in a Mediterranean-type ecosystem ». In: *Tree Physiology* 27.8, pp. 1179–1187. DOI: 10.1093/treephys/27.8.1179. See p. 79.

Oudin, L., C. Perrin, T. Mathevet, V. Andreassian and C. Michel (2006). « Impact of biased and randomly corrupted inputs on the efficiency and the parameters of watershed models ». In: *Journal of Hydrology* 320.1-2, pp. 62–83. DOI: 10.1016/j.jhydrol.2005.07.016. See p. 79.

Oudin, L., C. Michel and F. Anctil (2005). « Which potential evapotranspiration input for a lumped rainfall-runoff model ? Part 1 - Can rainfall-runoff models effectively handle detailed potential evapotranspiration inputs ? » In: *Journal of Hydrology* 303.1-4, pp. 275–289. DOI: 10.1016/j.jhydrol.2004.08.025. See p. 79.

Perrin, C., C. Michel and V. Andreassian (2001). « Does a large number of parameters enhance model performance? Comparative assessment of common catchment model structures on 429 catchments ». In: *Journal of Hydrology* 242.3-4, pp. 275–301. DOI: 10.1016/S0022-1694(00)00393-0. See pp. 6, 38, 77, 100.

Perrin, J., P.-Y. Jeannin and F. Zwahlen (2003*a*). « Implications of the spatial variability of infiltration-water chemistry for the investigation of a karst aquifer: A field study at Milandre test site, Swiss Jura ». In: *Hydrogeology Journal* 11.6, pp. 673–686. DOI: 10.1007/s10040-003-0281-5. See p. 74.

Pool, D. R. and J. H. Eychaner (1995). « Measurements of aquifer-storage change and specific yield using gravity surveys ». In: *Ground Water* 33.3, pp. 425–432. DOI: 10.1111/j.1745-6584.1995.tb00299.x. See p. 72.

Ricard, J. and M. Bakalowicz (1996). *Connaissance, aménagement et protection des ressources en eau du Larzac septentrional, Aveyron (France)*. Tech. rep. R38953. BRGM. URL: http://www.brgm.fr/Rapport?code=RR-38953-FR. See pp. viii, 39, 40, 72, 73.

Seibert, J. and J. J. McDonnell (2002). « On the dialog between experimentalist and modeler in catchment hydrology: Use of soft data for multicriteria model calibration ». In: *Water Resources Research* 38.11, p. 1241. DOI: 10.1029/2001WR000978. See p. 72.

Siegel, S. (1956). *Nonparametric statistics for the behavioral sciences*. Ed. by N. Y. McGraw-Hill. See p. 84.

Strassberg, G., B. R. Scanlon and D. Chambers (2009). « Evaluation of groundwater storage monitoring with the GRACE satellite: Case study of the High Plains aquifer, central United States ». In: *Water Resources Research* 45, W05410. DOI: 10.1029/2008WR006892. See p. 72.

Thornthwaite, C. (1948). « An approach toward a rational classification of climate ». In: *Geographical Review* 38.1, pp. 55–94. URL: http://www.jstor.org/stable/210739. See pp. 39, 73, 77, 93.

Tritz, S., V. Guinot and H. Jourde (2011). « Modelling the behaviour of a karst system catchment using non linear hysteretic conceptual model ». In: *Journal of Hydrology* 397.3-4, pp. 250–262. DOI: 10.1016/j.jhydrol.2010.12.001. See pp. vi, xvii, 7, 38–41, 44, 46, 52, 59, 72, 73, 76, 77, 80, 93, 94.

Vache, K. B. and J. J. McDonnell (2006). « Process-based strategies for model structural improvement and reduction of model prediction uncertainty ». In: *Predictions in Ungauged Basins: Promise and Progress. Proceedings of symposium S7 held during the 7th IAHS Scientific Assembly at Foz do Iguaçu, Brazil (April 3-9, 2005)*. Vol. 303. IAHS, pp. 30–37. URL: http://iahs.info/redbooks/a303/303004.htm. See p. 72.

Viterbo, P. and A. C. M. Beljaars (1995). « An improved land surface parameterization scheme in the ECMWF model and its validation ». In: *Journal of Climate* 8, pp. 2716–2748. DOI: 10.1175/1520-0442(1995)008<2716:AILSPS>2.0.CO;2. See p. 74.

Wagener, T. and H. Gupta (2005). « Model identification for hydrological forecasting under uncertainty ». In: *Stochastic Environmental Research and Risk Assessment* 19.6, pp. 378–387. DOI: 10.1007/s00477-005-0006-5. See p. 72.

Werth, S., A. Güntner, S. Petrovic and R. Schmidt (2009). « Integration of GRACE mass variations into a global hydrological model ». In: *Earth and Planetary Science Letters* 277.1-2, pp. 166–173. DOI: 10.1016/j.epsl.2008.10.021. See p. 72.

Chapter 4

Use of global sensitivity analysis for model calibration

This chapter illustrates the use of global sensitivity analysis for model calibration purposes. Sections 4.1 to 4.6 present a conceptual model for the hydrological modelling of karst springs under active groundwater management. The model performance is assessed against that of alternative model structures. Section 4.7 discusses on the influence of the nature of the objective function used for the calibration on the calibration result. Part of these results have been presented at the H_2Karst Conference held in Besançon, France (Sept. 1-3, 2011) [Mazzilli et al., 2011*a*].

Contents

4.1 Problem background: active spring management principle and modelling

The principle of the active management is to make the water withdrawal independent from the seasonal variability of the resource. As regards the management of vauclusian karst springs, this goal may be achieved by pumping below the spring overflow level, directly within the spring karst conduit [Avias, 1995]. Pumping may then be performed at a rate close to the spring annual average even during low water periods, with a limited risk of dewatering the pumps. The overexploitation of the resource during dry months is counterbalanced by the first autumnal floods, so that on a yearly time scale only renewable resources are mobilized.

Modelling the water level and the discharge of the karst springs under active management is an issue for groundwater resource exploitation. Moreover, spring discharge modelling may be associated with flood risk assessment issues. The only conceptual model proposed in the litterature for the rainfall - water level - discharge modelling of karst springs under active management is the 10-parameters, 4-reservoirs model proposed by Fleury et al., 2009. The relatively high number of parameters used in this model is likely to cause equifinality issues. Our aim is to propose a conceptual model that would be more satisfying as regards both model conceptualisation and model equifinality, and with at least equal performance as regards spring water level and spring discharge modelling.

The proposed model and the application site are described in Sections 4.2 and 4.3. The goodness of the model performance during calibration and validation is evaluated in Section 4.4. The model performance is also assessed by comparison to the existing, 10-parameters model (Section 4.5) and against alternative model structures of similar complexity (Section 4.6).

4.2 Model description

4.2.1 Model structure and functioning

The proposed model is made of three reservoirs (see model structure in Figure 4.1) and it comprises a total of 5 parameters. An interpretation of the model structure and functioning in terms of physical storage entities and processes is proposed hereafter.

The upper reservoir E represents the soil and epikarst zone. The lower reservoir, denoted by M hereafter, represents the matrix storage within both the saturated and unsaturated zones. The reservoir C stands for the spring karst conduit. In what follows, the volumes of water stored in reservoirs E, M and C are denoted by E, M and C respectively.

The model functioning may be summarized as follows:

1. the upper reservoir E receives the incoming precipitations and is affected by evapotranspiration,
2. part of the water contained in the reservoir E leaks to the reservoir M, which accounts for the classical recharge processes to the matrix zone (discharge Q_{EM}),
3. when E exceeds a given threshold E_{ext}, part of the water contained in the reservoir E flows outside of the catchment. This flux accounts for the activation of temporary springs (discharge Q_{ext}),
4. part of the water contained in the reservoir E may bypass the matrix compartment and flow directly to the drain (discharge Q_{EC}). Physically, such a connection is allowed via a network of fractures and preferential flowpaths. It is responsible for the fast component of the catchment response to rainfall events,

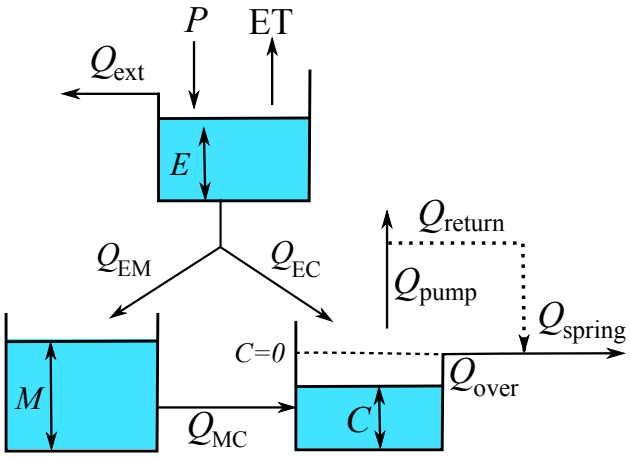

Figure 4.1: Structure and notation for the proposed model. Note that the Q_{MC} transfer function is proportional to the water level difference between both subsystems, which means that inflow from the reservoir C to the reservoir M is possible.

5. water exchange between the spring conduit and the matrix subsystem is accounted for via a discharge Q_{MC}, which is proportional to the storage difference between the reservoirs M and C,
6. part of the water contained in the reservoir C is removed by pumping (rate Q_{pump}),
7. spring overflow occurs when the water level within the reservoir C exceeds zero (rate Q_{over}),
8. when the spring overflow rate is lower than a minimal value Q_{return}, part of the pumped water is released to the river so as to ensure a minimal spring flow rate $Q_{spring} = Q_{return}$.

An effective porosity coefficient ω is used to establish a correspondence between the water level in the reservoir C and the observed piezometric water level within the spring karst conduit at the outlet of the aquifer (Lez spring).

The main characteristic of the proposed model lies in the transfer function between the spring conduit and the matrix subsystems, which is proportional to the water level difference between both subsystems. This conceptualization of conduit - matrix interactions is supported by direct observations on a variety of karst aquifers [e.g. Bailly-Comte et al., 2010; Jeannin, 1996]. Conceptual flow models that account for the matrix-conduit interaction have been proposed by Butscher and Huggenberger, 2007; Maréchal et al., 2008 and Hartmann et al., 2009.

4.2.2 Governing equations

The model has three balance equations:

$$\frac{\mathrm{d}E}{dt} = \begin{cases} P - \mathrm{ET} - Q_{ext} - Q_{EM} - Q_{EC} & \text{if } E > 0 \\ \max(P - \mathrm{ET}, 0) & \text{if } E = 0 \end{cases} \tag{4.1a}$$

$$\frac{\mathrm{d}M}{dt} = Q_{EM} - Q_{MC} \tag{4.1b}$$

$$\frac{\mathrm{d}C}{dt} = Q_{EC} + Q_{MC} - Q_{pump} - Q_{over} \tag{4.1c}$$

where ET is the evapotranspiration rate, P is the precipitation rate, Q_{EC} is the fast flow component through the epikarst zone, Q_{EM} is the infiltration rate to the lower reservoir, Q_{ext} is the discharge to secondary springs, Q_{MC} is the transfer rate from the reservoir M to the reservoir C, Q_{pump} is the discharge pumped from the spring conduit and Q_{over} is the overflow discharge at the spring pool. Note that discharges are expressed as height of water per day. The actual evapotranspiration rate

is assumed to be equal to the potential evapotranspiration rate as long as the soil-epikarst reservoir E is not empty. The discharges Q_{ext}, Q_{EM} and Q_{EC} are assumed to obey classical, linear laws [Maillet, 1906].

$$Q_{\text{ext}} = \begin{cases} \max(P - \text{ET}, 0) & \text{if } E = E_{\text{ext}} \\ 0 & \text{otherwise} \end{cases} \tag{4.2a}$$

$$Q_{\text{EC}} = k_{\text{EC}} E \tag{4.2b}$$

$$Q_{\text{EM}} = k_{\text{EM}} E \tag{4.2c}$$

where k_{EC}, k_{EM} are specific discharge coefficients and E_{ext} is the threshold for the activation of the temporary springs. The discharge Q_{MC} from the reservoir M towards the reservoir C is set proportional to the water level difference between the reservoirs M and C

$$Q_{\text{MC}} = k_{\text{MC}}(M - C) \tag{4.3}$$

where k_{MC} is a specific discharge coefficient. Note that Q_{MC} can take negative values, that is, water flow from the reservoir C to the reservoir M is allowed. The discharge Q_{over} is defined as

$$Q_{\text{over}} = \max(C, 0) \tag{4.4}$$

The spring discharge Q_{spring} is defined as the maximum of the overflow discharge Q_{over} and the return flow Q_{return}, multiplied by the total area of the catchment A.

$$Q_{\text{spring}} = A \max(Q_{\text{over}}, Q_{\text{return}}) \tag{4.5}$$

The water level WL within the spring conduit is defined as

$$\text{WL} = z_0 + C/\omega \tag{4.6}$$

where z_0 is the pool overflow level (65 m ASL) and ω is an equivalent storage coefficient.

The model equations (4.1) to (4.6) are solved numerically using an explicit Euler scheme. The state variables at time $n+1$ are expressed as

$$E_{n+1} = \begin{cases} \max\left[E_n + \Delta t \left(P_{n+1} - \text{ET}_{n+1} - Q_{\text{ext}n} - Q_{\text{EM}n} - Q_{\text{EC}n}\right), 0\right] & \text{if } E_n > 0 \\ E_n + \Delta t \max\left(P_{n+1} - \text{ET}_{n+1}, 0\right) & \text{if } E_n = 0 \end{cases} \tag{4.7a}$$

$$M_{n+1} = M_n + \Delta t \left(Q_{\text{EM}n} - Q_{\text{MC}n}\right) \tag{4.7b}$$

$$C_{n+1} = C_n + \Delta t \left(Q_{\text{EC}n} - Q_{\text{MC}n} - Q_{\text{pump}n} - Q_{\text{over}n}\right) \tag{4.7c}$$

where the subscripts $n+1$ and n denote the values of the variable at the time $n+1$ and n respectively. Note that P_{n+1} and ET_{n+1} are the mean rainfall rate and evapotranspiration rate between the times $n+1$ and $n+2$ respectively. Indeed, the fact that the model operates on a daily time step, together with the model serial structure would result in a one-day delay of the predicted to the observed flood peaks. The one-day time lag in the meteorological data is meant to make up for the one-day time lag between the predicted and observed flood peaks. Note that the application of the model to another basin or its numerical implementation with a different computational time step could make this operation unnecessary.

4.3 Application example

4.3.1 Site overview

The model is applied to the Lez spring (Hérault, southern France), which is a pioneer site in active groundwater management Avias, 1987. The Lez spring is the main outlet of a large karst

aquifer (referred to hereafter as the "Lez aquifer") made of Late Jurassic to early Cretaceous limestones. The aquifer is compartimentalized by a network of NE-SW normal faults into a raised, north-western compartment where the aquifer limestone outcrops and a lowered, south-eastern compartment where most of the aquifer is covered by impermeable formations (see Figure 4.2). The Lez spring is located at a contact between the middle Jurassic to late Creataceous limestones and the impermeable formations. Mass balance calculations yield recharge area estimates ranging around 150 km^2 Marjolet and Salado, 1978. Following Fleury et al., 2009, a recharge area of 130 km^2 is assumed in the present study.

The Lez spring has been used for the water supply of the city of Montpellier since 1854. The methods used for water withdrawal have evolved with the water demand. Gravity-driven water withdrawal was performed until 1965. Pumps were then installed some 6.5 m below the overflow level of the spring. This solution allowed the withdrawal of up to 800 $l s^{-1}$, even during low flow periods when the natural outflow of the spring was lower than 200 $l s^{-1}$ Avias, 1995. Since 1982, pumping is performed directly within the karst conduit, some 48 m below the spring pool overflow level (see Figure 4.3). During low water periods the pumping rate exceeds the natural spring discharge and the spring dries out. Part of the pumped water is then returned to the river in order to sustain aquatic biota (a minimum 160 $l s^{-1}$ discharge is required). The drawdown of the water level within the spring conduit may reach several tens of meters at the end of the low-water period.

4.3.2 Meteorological data

The input rainfall rate is taken as a weighted function of the rainfall rate measured at three Météo-France stations as proposed by Fleury et al., 2009

$$P = p_P P_P + p_M P_M + (1 - p_P - p_M) P_V \tag{4.8}$$

where p_P, p_M and $1 - p_P - p_M$ are the weight coefficients for the rainfall rates P_P, P_M and P_V measured at the Prades, Saint-Martin-de-Londres and Valflaunès rainfall stations respectively (see location in Figure 4.2 and see weigths values in Table 4.1). The weight coefficients are deduced from time series analysis Fleury et al., 2009. The average annual rainfall rate for the 1997/2005 period is 1037 mm.

The daily potential evapotranspiration (PET) is estimated from the Thornthwaite Thornthwaite, 1948 formula (computed at the Montpellier Fréjorgues Meteo-France meteorological station) using a sine function-based interpolation, as proposed by Tritz et al., 2011

$$\mathrm{PET}(t) = \left[1 - a \cos\left(2\pi \frac{t - t_{\min}}{T}\right)\right] \overline{\mathrm{PET}} \tag{4.9}$$

where t is the time where the PET is to be interpolated, $\overline{\mathrm{PET}}$ is the average value of the PET series computed from Thornthwaite's formula, T is the period of the PET signal (one year), $t_{\min}$ is the time at which the PET is minimal and a is the dimensionless amplitude of the signal. The parameter $t_{\min}$ and a have been estimated by means of a classical least-squares optimization procedure (see parameter values in Table 4.1 and see PET time series in Figure 4.4).

The evapotranspiration rate ET is taken equal to the potential evapotranspiration PET as long as the upper soil/epikarst reservoir is not empty.

4.3.3 Discharge and piezometric water level data

Spring discharge measurements are performed some 500 m downstream of the spring pool. The measured spring discharge includes the potential return flow to the river. Note that although spring

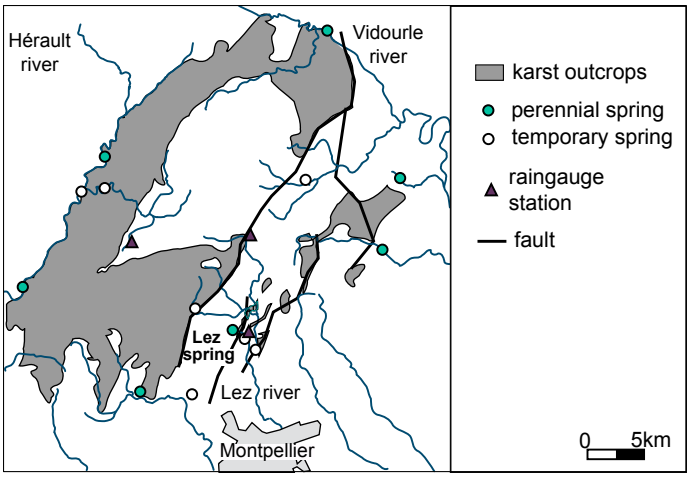

Figure 4.2: Lez aquifer: hydrogeological setting. Only the main springs are featured on the map. Adapted from Fleury et al., 2009.

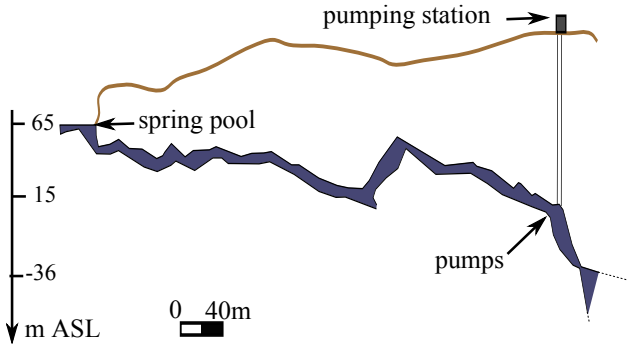

Figure 4.3: Lez aquifer: schematic cross-section of the Lez spring karst conduit and the pumping station.

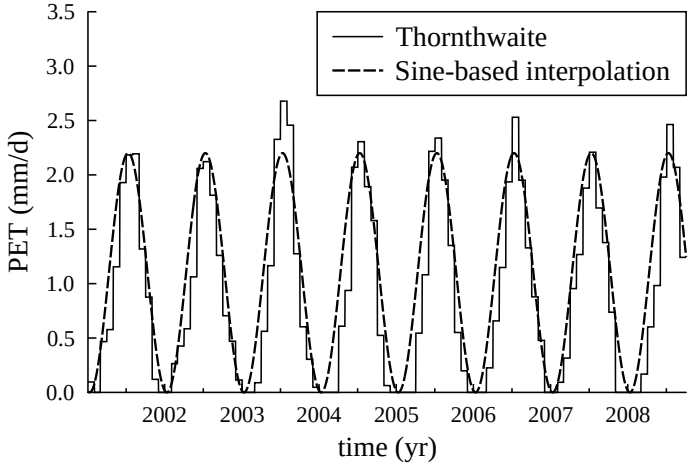

Figure 4.4: Potential evapotranspiration rate. Grey, solid line: monthly PET value computed using Thornthwaite's formula. Black, dotted line: daily values interpolated based on equation (4.9) Tritz et al., 2011.

Symbol	Meaning	Value
p_{P}	rainfall weight coefficient for the Prades station	0.187
p_{M}	rainfall weight coefficient for the Saint-Martin station	0.386
a	Dimensionless amplitude of the sine wave	1
$t_{\min}$	Time of minimum PET	10 January
T	Period of the interpolation function	1 year
$\overline{\mathrm{PET}}$	Average potential evapotranspiration rate	$1.1\,\mathrm{mm\,d^{-1}}$

Table 4.1: Parameters for the rainfall and potential evapotranspiration models.

water level and discharge measurements have been performed since 1946, simultaneously complete time series are only available for the 1997/2005 period.

The mean spring overflow discharge is an average $1.1\,\mathrm{m^3\,s^{-1}}$ for the 1997-2005 period. The minimum spring discharge is $160\,\mathrm{l\,s^{-1}}$ (return flow). The maximum spring discharge is $16\,\mathrm{m^3\,s^{-1}}$ (1997-2005 period). The discharge measurement uncertainty is estimated to be about ±5%. The pumping rate is in average $1.1\,\mathrm{m^3\,s^{-1}}$ over the 1997-2005 period. The pumping rate measurement uncertainty is estimated to be negligible. The minimal piezometric level within the karst conduit is 38 m ASL for the 1997-2005 period, with an average 147 days of overflow per year. The water level measurement uncertainty is estimated to be negligible.

4.4 Calibration performance and predictive capability

Section 4.4.1 evaluates the model's ability to reproduce the spring discharge and water level observations, taken separately. It also investigates the competition between the discharge and water level calibration objectives. Section 4.4.2 presents a Monte-Carlo based analysis of the identifiability of the model parameters. Section 4.4.3 evaluates the model predictive capability.

Note that the spring discharge and the spring water level can not be considered as completely independant variables. Rather, the spring discharge and the spring water level time series may be seen as the time-slice partition of a same signal into a low flow (spring water level) and a high flow (spring discharge) signals.

4.4.1 Calibration performance

The calibration procedure is performed over a eight-year period (1997-2005 data) based on a Monte-Carlo algorithm. Before calibration, the model is run during a three-years initialization period.

Calibration performance for the spring overflow discharge The discharge modelling error Err_Q is defined so as to take into account the $\varepsilon = \pm 5\%$ measurement uncertainty on the spring discharges

$$\mathrm{Err}_Q = \begin{cases} Q_{\mathrm{spring}} - (1-\varepsilon)Q_{\mathrm{obs}} & \text{if } Q_{\mathrm{spring}} < (1-\varepsilon)Q_{\mathrm{obs}} \\ Q_{\mathrm{spring}} - (1+\varepsilon)Q_{\mathrm{obs}} & \text{if } Q_{\mathrm{spring}} > (1+\varepsilon)Q_{\mathrm{obs}} \\ 0 & \text{otherwise} \end{cases} \tag{4.10}$$

where Q_{spring} and Q_{obs} are the simulated and measured spring discharge respectively.

As a first approach, the model performance is assessed based on the Nash-Sutcliffe efficiency (see definition in Table 4.3). The influence of the performance indicator on the calibration results will be investigated further in Section 4.7.1. Note that the values of the performance indicators over the calibration period for the different models are summarized in Table 4.8 (page 116).

The calibration results are shown in Figure 4.5 (Nash efficiency 0.86 - see parameter set in Table 4.2). The overall dynamics of the spring discharge is satisfyingly reproduced by the model. However, the model appears to overreact to some rainfall events and underreact to other events. As an example, the first automn 2004 flood peak is not simulated by the model because the spring overflow level is not reached. This must be related to a delay in the simulated piezometric head rise, which in turn results in a bad estimation of the spring overflow time. On the contrary, the first autumn 2005 rainfall events does trigger a flood peak, whereas measurements indicate no spring overflow.

Calibration performance for the water level within the conduit The model performance is assessed based on the Nash-Sutcliffe efficiency measure. The calibration results are shown in Figure 4.5 (Nash efficiency 0.81 - see parameter set in Table 4.2). The overall dynamics of the spring water table is reproduced satisfyingly by the model. However, large errors (10m of amplitude) occur during summer 1997 and summer 2003. The simulated piezometric head is either overestimated (summer 1997) or underestimated (summer 2003). Note that the calibrated effective porosity value is close to the value proposed by Roesch and Jourde, 2006 based on hydrodynamic considerations.

Calibration performance for the joint discharge and water level variables The competition between the discharge and water level calibration objectives is illustrated using the concept of Pareto optimality. In a multi-objective framework, a solution (parameter set) is Pareto-optimal if no other solution is at least equal in all objectives and superior in at least one [Gupta et al., 1998]. The set of Pareto-optimal solutions is referred to as the Pareto front. In practice, the Pareto front is approximated by means of e.g. evolutionary algorithms (see review in Efstratiadis and Koutsoyiannis, 2010). In what follows, a very rough approximation of the Pareto front is obtained based on a Monte-Carlo approach.

The Pareto front for the two-objective problem is plotted in Figure 4.9. Maximal values of the performance indicator with respect to the discharge variable (Nash efficiency approx. 0.86) may be associated with relatively low values of the performance indicator with respect to the water level simulation (Nash efficiency approx. 0.4). On the other hand, the maximal performance indicator with respect to the water level variable is associated with the maximal performance indicator with respect to the discharge variable. Note that the trade-off between both objectives is small.

The multiobjective calibration problem may be turned into a single-objective calibration problem via the aggregation of the various objective functions. Such aggregate measures include the arithmetic mean or the Euclidian distance to the objectives [Madsen, 2000]. In this study, the discharge and the water level are considered as equally important and the aggregated criteria is chosen so as to maximize the efficiency with respect to both objectives. The criterion retained for the analysis is the normalized, Euclidian distance E in the N_Q, N_{WL} space

$$E = \sqrt{\frac{N_Q^2 + N_{\mathrm{WL}}^2}{2}} \qquad \text{if } N_Q > 0 \text{ and } N_{\mathrm{WL}} > 0 \tag{4.11a}$$

$$E = 0 \qquad \text{otherwise} \tag{4.11b}$$

where N_Q and N_{WL} are the Nash-Sutcliffe efficiencies for the discharge and spring water level data respectively. Note that E varies between 0 and 1. Figure 4.7 shows the simulation results for the "best compromise" parameter set ($N_Q = 0.84$, $N_P = 0.81$ - see parameter set in Table 4.2). Note that the simulated time series are very similar to the ones resulting from calibration against each objective taken separately. Also note that the calibrated value of the k_{EM} parameter is very low. This means that the best calibration result is obtained when the discharge from the reservoir E to the reservoir M is close to zero. This point is discussed with greater details in Section 4.4.2.

4.4.2 Model identifiability

Model identifiability is defined here as the capability of model calibration to constrain the; parameters used by the model. Parameter identifiability is studied as follows. The model is run over the 1997-2005 calibration period for Monte-Carlo parameter sets. Figure 4.8 shows dotty plots resulting from model realisations, with the performance indicator on the y-axis and the parameter values on the x-axis. Calibration against spring discharge data alone (Figure 4.8a) yields well identified optimum values for all parameters. Calibration against spring water level data alone (Figure 4.8b) yields well identified optimum values for the k_{EC}, k_{MC} and ω parameters. By contrast, the k_{EM} and E_{ext} values are poorly defined. Calibration against both spring discharge and water level data (Figure 4.8c) yields well identified parameter optima except for the k_{EM} parameter.

The poor identifiability of the E_{ext} parameter based on water level data alone is not surprising as E_{ext} is mainly associated with spring discharge control during flood events. The poor identifiability and low values of the k_{EM} parameter means that water transfer from the soil/epikarst reservoir to the matrix system is not dominant. The matrix reservoir acts mainly as a buffer for the karst conduit reservoir. This rapid identifiability analysis indicates that for the specific case of the Lez spring, the k_{EM} discharge coefficient can be set equal to zero with no degradation of the model performances. The proposed model therefore behaves as a four-parameters model.

Note that calibration against spring discharge data alone, spring water level data alone and both spring discharge and water level data yield similar optimum values for all parameters except k_{EM} which is an indication for good parameter identifiability.

4.4.3 Predictive capability

The predictive capability of the model is evaluated based on a standard split-sample test scheme [Klemes, 1986]. The available data set is split into three sets of equal length. The model is successively calibrated against one time period and tested against the others. The periods considered hereafter are denoted by P_1 (Jan. 1997 to Oct. 1999), P_2 (Oct. 1999 to Aug. 2002) and P_3 (Aug. 2002 to July 2005). The cumulated rainfall over the P_1 and P_2 periods are similar, but the number of overflow days is sensibly higher for P_2. The P_3 period is notably wetter (see Table 4.4).

Figure 4.10 plots the perfomance measure for the calibration period against the the perfomance measure for the validation period. Calibration against the P_1 and P_3 periods yields almost equal performance during the validation period. The performance indicator is degraded in validation mode when the calibration is performed against the P_2 data set.

4.4.4 Conclusion

The proposed model yields satisfying performances as regards the simulation of the water level and the discharge time series for both the calibration and validation tests. There is no competition between the simulation of the water level time series and that of the discharge time series. A simple, Monte-Carlo based analysis indicates good model identifiability except for the k_{EM} parameter. Indeed, the very low values taken by the k_{EM} parameter indicate that for the specific case of the Lez spring the proposed model structure may be simplified into a 4-parameter structure, by setting the Q_{EM} transfer rate equal to zero.

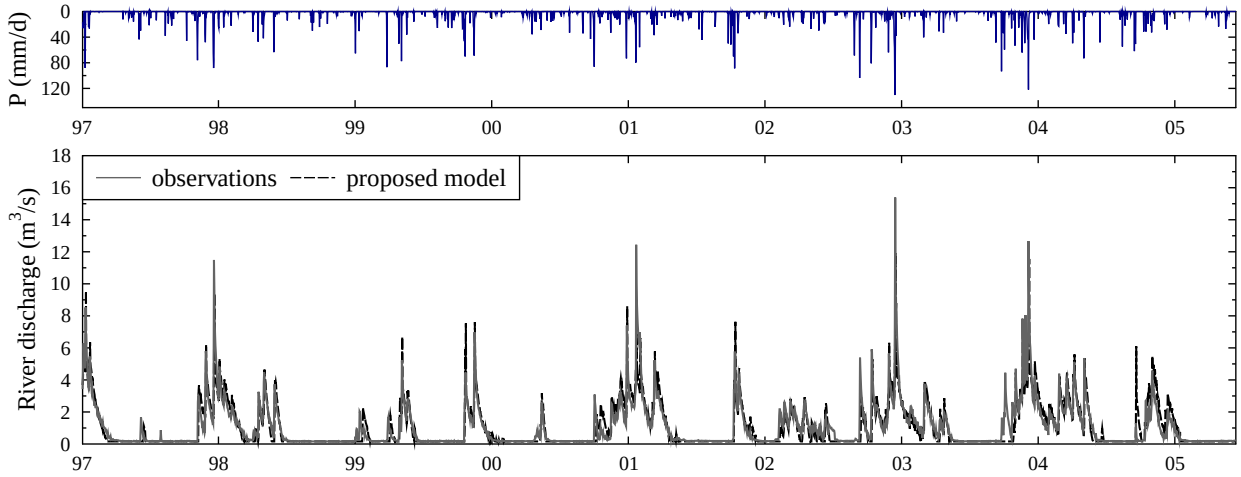

Figure 4.5: Proposed model. Simulation results for the parameter set resulting from a calibration against discharge data alone: top) daily rainfall, bottom) observed and simulated river discharge. See discussion in Section 4.4.1.

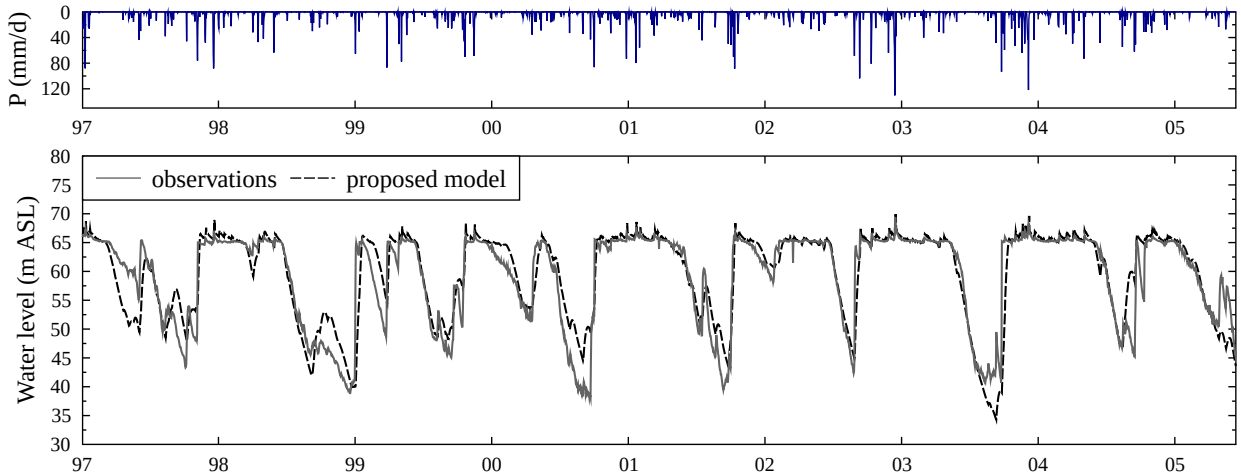

Figure 4.6: Proposed model. Simulation results for the parameter set resulting from a calibration against water level data alone: top) daily rainfall, bottom) observed and simulated water levels. See discussion in Section 4.4.1.

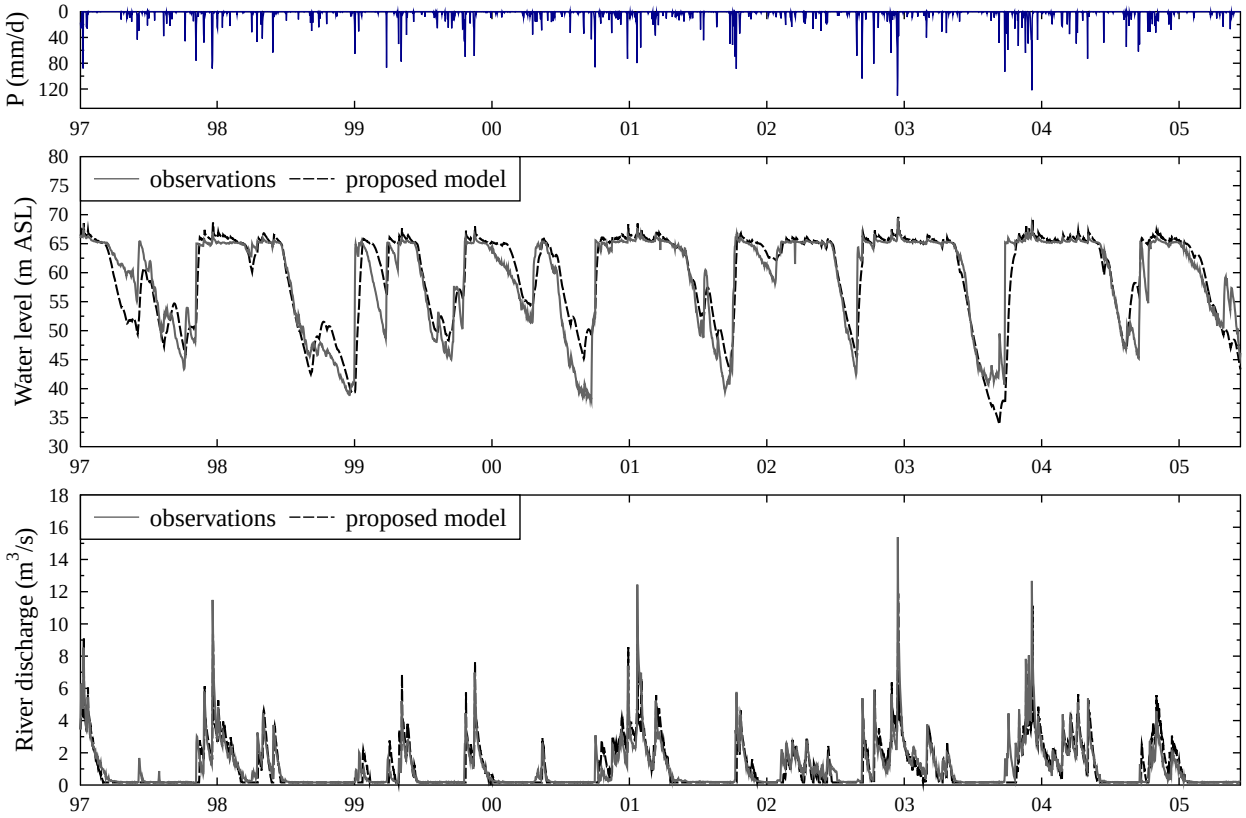

Figure 4.7: Proposed model. Simulation results for the parameter set resulting from a calibration against discharge and water level data: top) daily rainfall, middle) observed and simulated water levels, bottom) observed and simulated river discharge. See discussion in Sections 4.4.1.

Symbol	Meaning	Q-set	P-set	PQ-set
E_{ext}	threshold level for the secondary springs	70 mm	93 mm	96 mm
k_{EC}	specific discharge coefficient from E to C	$4.0\,10^{-2}$ /d	$4.5\,10^{-2}$ /d	$4.0\,10^{-2}$ /d
k_{EM}	specific discharge coefficient from E to M	$2.3\,10^{-2}$ /d	$4.0\,10^{-4}$ /d	$3.8\,10^{-4}$ /d
k_{MC}	specific discharge coefficient from M to C	$2.8\,10^{-2}$ /d	$2.1\,10^{-2}$ /d	$3.2\,10^{-2}$ /d
ω	effective porosity	-	$1.8\,10^{-3}$	$1.8\,10^{-3}$

Table 4.2: Proposed model. Parameter set obtained by calibration to discharge data alone (Q-set), water level data alone (P-set), and joint discharge and water level data (PQ-set).

Name	Symbol	Reference	Formula
Nash and Sutcliffe efficiency	NSE	[Nash and Sutcliffe, 1970]	$\mathrm{NSE}_\phi = 1 - \frac{\sum \mathrm{Err}_\phi{}^2}{\sum \left(\phi_{\mathrm{obs}} - \overline{\phi_{\mathrm{obs}}}\right)^2}$
Volumetric efficiency	VE	-	$\mathrm{VE}_\phi = 1 - \frac{\sum \lvert\mathrm{Err}_\phi\rvert}{\sum \lvert\phi_{\mathrm{obs}} - \overline{\phi_{\mathrm{obs}}}\rvert}$
Modified balance error	MBE	[Perrin et al., 2001]	$\mathrm{MBE}_\phi = 1 - \left\lvert \frac{\sum \mathrm{Err}_\phi}{\sum \phi_{\mathrm{obs}} - \overline{\phi_{\mathrm{obs}}}} \right\rvert$

Table 4.3: Definition of the objective functions used in Section 4.7.1 ϕ_{obs} is measured value of the ϕ variable, $\overline{\phi_{\mathrm{obs}}}$ is the mean of ϕ_{obs} over the modelling period, Err_ϕ is the modelling error for the ϕ variable ($\mathrm{Err}_\phi = \phi - \phi_{\mathrm{obs}}$). Note that the NSE, VE and MBE measures all take values between $-\infty$ and 1, where the highest values indicate better agreement between the simulated and observed variable.

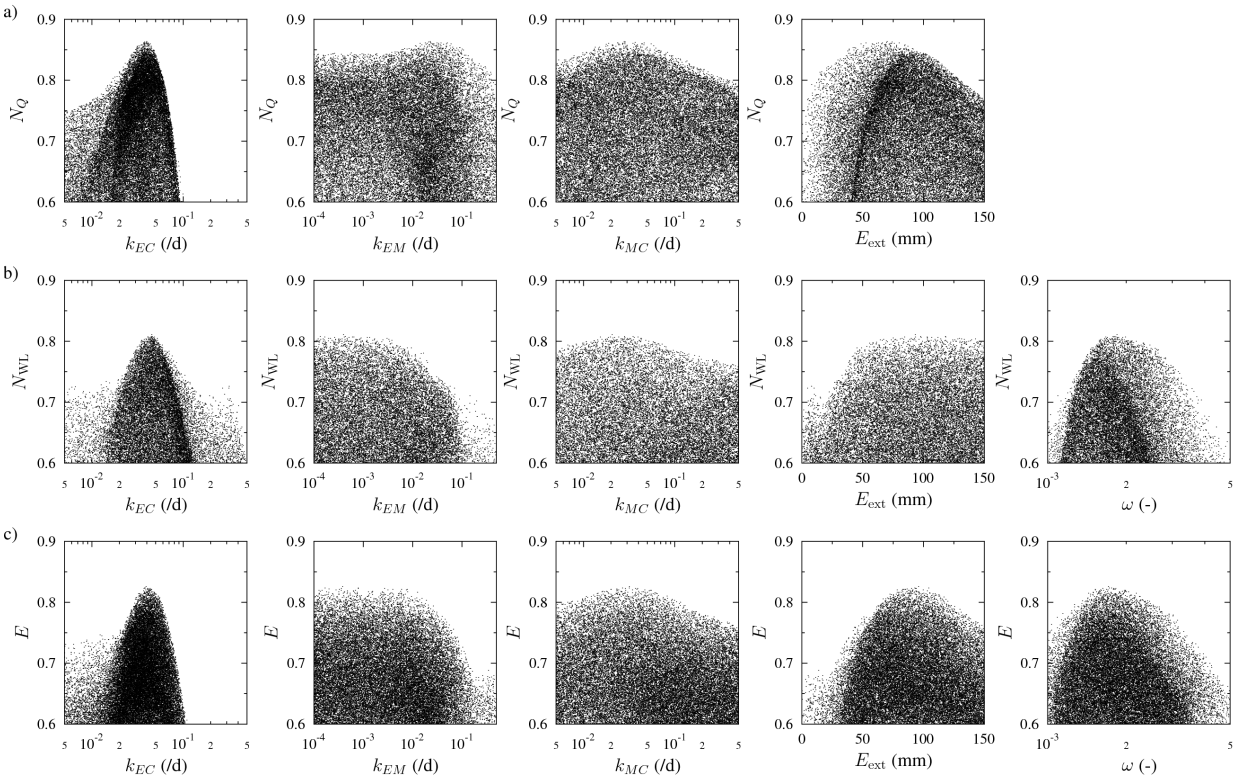

Figure 4.8: Proposed model. Dotty plot resulting from model realisations, with the performance indicator on the y-axis and the parameter values on the x-axis: a) calibration against the spring discharge alone, b) calibration against the spring water level alone, c) calibration against both discharge and water level.

Period	average rainfall	average Q_{pump}	average Q_{spring}	spring overflow
P_1	937 mm/yr	$1.1\,\text{m}^3\,\text{s}^{-1}$	$0.9\,\text{m}^3\,\text{s}^{-1}$	103 d/yr
P_2	891 mm/yr	$1.1\,\text{m}^3\,\text{s}^{-1}$	$1.0\,\text{m}^3\,\text{s}^{-1}$	140 d/yr
P_3	1171 mm/yr	$1.1\,\text{m}^3\,\text{s}^{-1}$	$1.3\,\text{m}^3\,\text{s}^{-1}$	193 d/yr

Table 4.4: Characteristics of the sub-periods used for the split-sample test: average rainfall, average pumping rate, average measured spring discharge and average spring overflow frequency for the Lez spring. Period length: 1027 days.

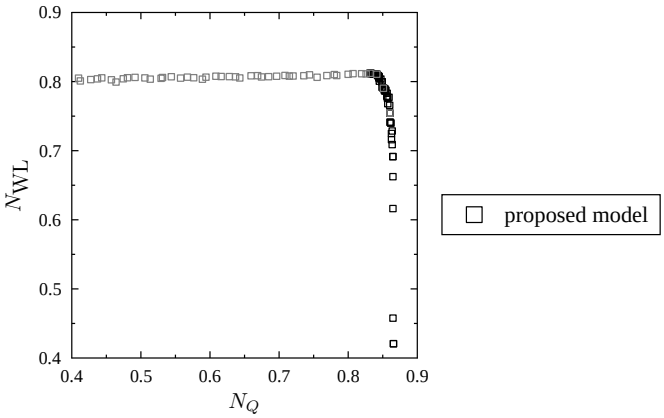

Figure 4.9: Proposed model. Pareto-optimal solutions with respect to the Nash efficiencies for the river discharge (x-axis) and the water level (y-axis) data, for the proposed model. The grey square markers denote non-optimal solutions that yield maximum N_{WL} performance for a given N_Q value. See discussion in Section 4.4.1.

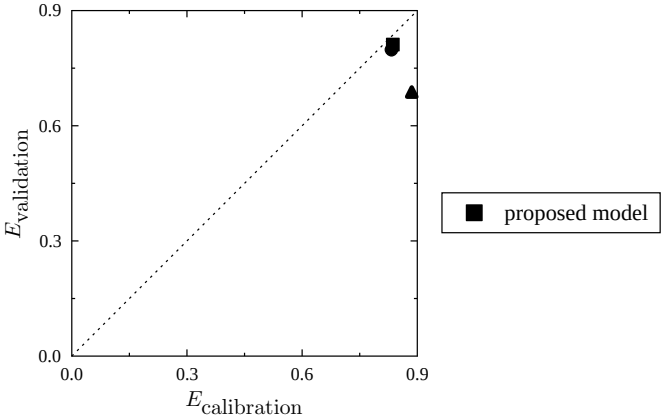

Figure 4.10: Proposed model. Split sample test results. Model performance for the calibration (x-axis) and validation (y-axis) periods for the proposed model. Calibration on the P_1, P_2 and P_3 periods are denoted by square, triangle and circle markers respectively. See discussion in Section 4.4.3.

4.5 Model evaluation against the existing, 10-parameters model

4.5.1 Description of the 10-parameters model

Model structure and functioning The existing model [Fleury et al., 2009] is made of four reservoirs (see model structure in Figure 4.11) and involves a total of 10 parameters. An interpretation of the model structure and functioning in terms of physical storage entities and processes is proposed hereafter, based on [Fleury et al., 2009].

The upper reservoir E represents the soil zone. The reservoirs S and R represent the slow and rapid infiltration zones respectively. The reservoir C represents the saturated zone. In what follows, the volumes of water stored in reservoirs E, S, R and C are denoted by E, S, R and C respectively.

The model functioning may be summarized as follows:

1. the upper reservoir E receives the incoming precipitations and is affected by evapotranspiration. Evapotranspiration stops when the water level reaches a threshold value E_{inf},
2. part of the water contained in the reservoir E leaks to the reservoirs S and R, provided that the water level in E is larger than zero. This accounts for slow and rapid infiltration processes in the unsaturated zone respectively (discharges Q_{ES} and Q_{ER}),
3. part of the water contained in the reservoir E leaks to the reservoir C, provided that the water level in E is larger than zero. This accounts for slow flow towards the saturated zone (discharge Q_{EC}),
4. when C exceeds a given threshold C_{ext}, part of the flow Q_{EC} to the saturated zone is directed outside of the catchment, which accounts for the activation of temporary springs (discharge Q_{ext}),
5. the reservoirs S and R leak towards the outlet of the catchment, which accounts for drainage towards the saturated zone (discharges Q_{S} and Q_{R}),
6. part of the water contained in the reservoir C is removed by pumping (rate Q_{pump}),
7. spring overflow occurs when the water level within the reservoir C exceeds zero (rate Q_{C}),
8. when the spring overflow rate is lower than a minimal value Q_{return}, part of the pumped water is released to the river so as to ensure a minimal spring flow rate $Q_{\text{spring}} = Q_{\text{return}}$.

An equivalent storage coefficient is used to establish a correspondence between the water level in the reservoir C and the observed water level within the spring karst conduit.

Note that the model description given above slightly differs from the model description given by Fleury et al., 2009. Indeed, in [Fleury et al., 2009] the effective infiltration is calculated based on a time-dependant infiltration threshold. If the rainfall intensity is higher than the threshold, then the effective infiltration is taken equal to the rainfall minus the infiltration threshold. If the rainfall is smaller than the threshold, then the effective infiltration is taken equal to zero. The effective rainfall intensity is calculated by means of a third-party software (TEMPO software [Pinault, 2001]) and it is used as an input for the rainfall-discharge model. In the description given above, the effective infiltration calculation has been integrated into the rainfall-discharge model, for the sake of unbiased comparison.

Governing equations. The model has four balance equations:

$$\frac{\mathrm{d}E}{dt} = \begin{cases} P - \mathrm{ET} - Q_\mathrm{H} & \text{if } E_\mathrm{inf} < E \leq 0 \\ \max(P - \mathrm{ET}, 0) & \text{if } E = E_\mathrm{inf} \end{cases} \tag{4.12a}$$

$$\frac{\mathrm{d}S}{dt} = Q_\mathrm{ES} - Q_\mathrm{S} \tag{4.12b}$$

$$\frac{\mathrm{d}R}{dt} = Q_\mathrm{ER} - Q_\mathrm{R} \tag{4.12c}$$

$$\frac{\mathrm{d}C}{dt} = Q_\mathrm{EC} - Q_\mathrm{pump} - Q_\mathrm{over} \tag{4.12d}$$

where ET is the evapotranspiration rate, P is the precipitation rate, Q_H is the total discharge from the reservoir E, Q_ES, Q_ER and Q_EC are the discharges from the reservoir E to the reservoirs S, R and C respectively, Q_ext is the discharge to secondary springs, Q_pump is the discharge pumped within the spring conduit, Q_over is the overflow discharge at the spring pool and E_inf is the lowest permissible water level in the reservoir E. Note that discharges are expressed as height of water per day. The actual evapotranspiration rate is assumed to be equal to the potential evapotranspiration rate as long as the soil-epikarst reservoir E is not empty. The discharges Q_H, Q_ext, Q_ES, Q_ER, Q_S, Q_R and Q_over are assumed to obey classical, linear laws [Maillet, 1906]:

$$Q_\mathrm{H} = \begin{cases} \max(P - \mathrm{ET}, 0) & \text{if } E = 0 \\ 0 & \text{otherwise} \end{cases} \tag{4.13}$$

and

$$Q_\mathrm{ES} = k_\mathrm{ES} Q_\mathrm{H} \tag{4.14a}$$

$$Q_\mathrm{ER} = k_\mathrm{ER} Q_\mathrm{H} \tag{4.14b}$$

$$Q_\mathrm{EC} = k_\mathrm{EC}(1 - \varepsilon_\mathrm{ext} X) Q_\mathrm{H} \tag{4.14c}$$

$$Q_\mathrm{ext} = k_\mathrm{EC} \varepsilon_\mathrm{ext} X Q_\mathrm{H} \tag{4.14d}$$

$$Q_\mathrm{S} = k_\mathrm{S} S \tag{4.14e}$$

$$Q_\mathrm{R} = k_\mathrm{R} R \tag{4.14f}$$

where k_ES, k_ER, k_EC and X are partition coefficients, k_S and k_R are specific discharge coefficients, C_ext is the threshold for the activation of the temporary springs and ε_ext is defined by the following relation:

$$\varepsilon_\mathrm{ext} = \begin{cases} 1 & \text{if } C > C_\mathrm{ext} \\ 0 & \text{if } C \leq C_\mathrm{ext} \end{cases} \tag{4.15}$$

The partition coefficients for the reservoir E are bound by the relation

$$k_\mathrm{ES} + k_\mathrm{ER} + k_\mathrm{EC} = 1 \tag{4.16}$$

The discharge Q_C is defined as

$$Q_\mathrm{C} = \max(k_\mathrm{C} C, 0) \tag{4.17}$$

where k_C is a specific discharge coefficient. The spring overflow discharge Q_over is defined as

$$Q_\mathrm{over} = Q_\mathrm{S} + Q_\mathrm{R} + Q_\mathrm{C} \tag{4.18}$$

The river discharge Q_spring is defined as the maximum of the overflow Q_over and the return flow Q_return, multiplied by the total area of the catchment A:

$$Q_\mathrm{spring} = A \max(Q_\mathrm{over}, Q_\mathrm{return}) \tag{4.19}$$

The water level WL within the spring conduit is defined as

$$\mathrm{WL} = z_0 + C/\omega_H \qquad \text{if } C > 0 \tag{4.20a}$$

$$\mathrm{WL} = z_0 + C/\omega_L \qquad \text{if } C \leq 0 \tag{4.20b}$$

where ω_H and ω_L are equivalent storage coefficients for the high and low water periods respectively and z_0 is the pool overflow level (65 m ASL).

The model equations (4.12) to (4.19) are solved numerically using an explicit Euler scheme. As for the proposed model, a one-day time lag in the meteorological data is used so as to make up for the one-day time lag between the predicted and observed flood peaks.

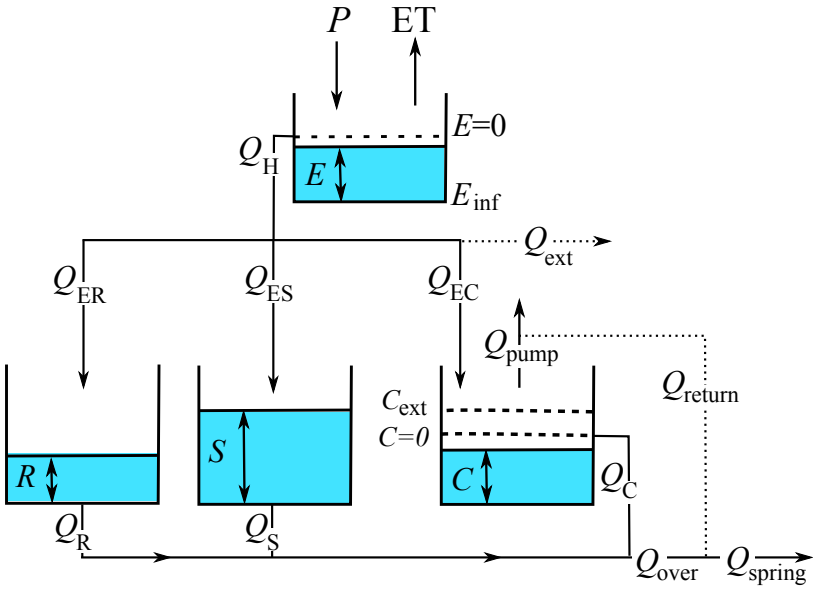

Figure 4.11: Structure and notation for the existing, 10-parameters model [Fleury et al., 2009].

4.5.2 Calibration performance and predictive capability

Calibration performance for the discharge and water level variables, taken separately. Figure 4.13 shows the simulation results for the parameter set resulting from a calibration against discharge data alone (Nash efficiency 0.83). The simulated hydrograph is similar to that obtained by calibration of the proposed, 5-parameters model: over-reaction and under-reaction of the 10-parameters model are triggered by the same rainfall events as the proposed model. However, the 10-parameters model also tends to simulate a number a low-amplitude flood peaks during low-flow periods. The fact that the 10-parameters model may simulate spring overflow even though the simulated spring water level is lower than the pool overflow level is due to the parallel structure of the R, S and C reservoirs. Indeed, the spring overflow discharge is taken as the sum of the discharges from the reservoirs R, S and C. On the other hand, the spring water level is considered based on the water level within the reservoir C only. Rainfall events of moderate magnitude that result in a piezometric rise with no overflow of the reservoir C may therefore be associated with a non-zero spring overflow discharge.

Figure 4.14 shows the simulation results for the parameter set resulting from a calibration against water level data alone. The calibration performance is significantly less than that of the proposed model (Nash efficiency 0.73). Major discrepancies in the simulated water level recessions occur during the summer 1999, 2003 and 2005, with simulated water levels much lower than the observations.

Calibration performance for the joint discharge and water level variables. The Pareto front for the two-objective calibration is shown in Figure 4.16. It is seen that the trade-off between both objectives is very important. Figure 4.15 shows the simulation results for the "best compromise" parameter set ($N_Q = 0.72$, $N_P = 0.59$). The simulation of the spring water level and the spring discharge time series is significantly degraded compared to the single-objective calibration exercise.

Model identifiability. Figure 4.12 shows the dotty plots resulting from the 10-parameters model realisations, with the agregated performance indicator E on the y-axis and the parameter values on the x-axis. Most parameter optimum are poorly defined which is likely to be associated with low predictive capability.

Predictive capability. The predictive capability is assessed by the standard split-sample test procedure described in Section 4.4.3 (see Figure 4.17 for test results). Calibration against the P_1 period yields a relatively similar performance during the validation period. By contrast, calibration against the P_2 or P_3 periods yields very degraded performances during the validation run.

4.5.3 Conclusion

It may be concluded from Section 4.5.2 that the proposed 5-parameters model performs better than the existing 10-parameters model for spring discharge and water level simulation, with reduced parametric uncertainty and enhanced predictive capability.

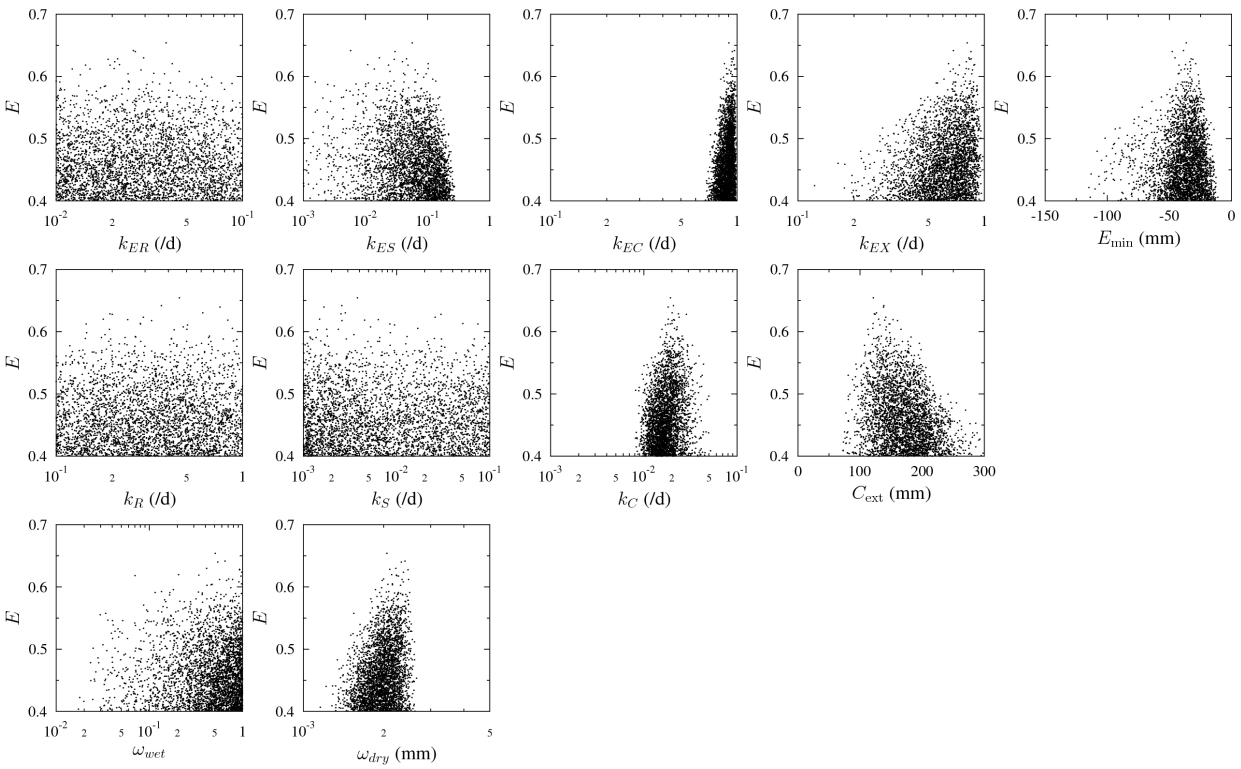

Figure 4.12: Existing model. Dotty plot resulting from model realisations, with the E measure on the y-axis and the parameter values on the x-axis. Calibration against joint discharge and water level data.

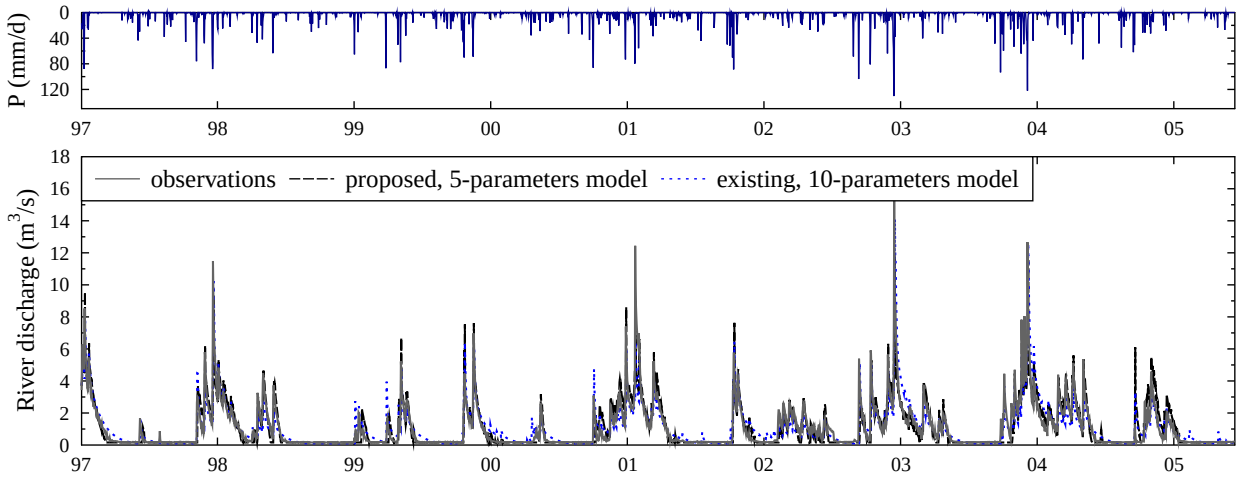

Figure 4.13: Existing model. Simulation results for the parameter set resulting from a calibration against discharge data alone: top) daily rainfall, bottom) observed and simulated spring discharge. See discussion in Sections 4.4.1 (proposed model) and 4.5.2 (existing model).

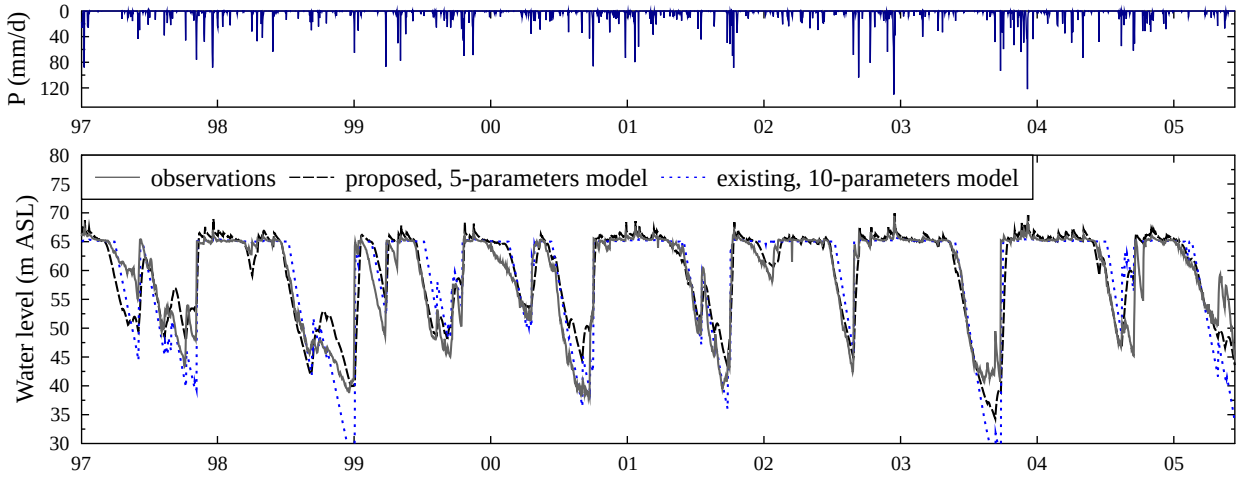

Figure 4.14: Existing model. Simulation results for the parameter set resulting from a calibration against water level data alone: top) daily rainfall, bottom) observed and simulated water levels. See discussion in Sections 4.4.1 (proposed model) and 4.5.2 (existing model).

Symbol	Meaning	Q-set	P-set	PQ-set
k_{ER}	partition coefficient from E to R	$8.0\,10^{-2}$	$1.0\,10^{-2}$	$3.9\,10^{-2}$
k_{ES}	partition coefficient from E to S	$3.1\,10^{-1}$	$5.0\,10^{-2}$	$5.6\,10^{-2}$
k_{EC}	partition coefficient from E to C	$6.1\,10^{-1}$	$9.4\,10^{-1}$	$9.0\,10^{-1}$
k_{R}	specific discharge coefficient from R	$3.0, 10^{-1}$/d	$7.6\,10^{-0}$/d	$4.6\,10^{-1}$/d
k_{S}	specific discharge coefficient from S	$2.9\,10^{-2}$/d	$2.0\,10^{-1}$/d	$3.8\,10^{-2}$/d
k_{C}	specific discharge coefficient from C	$6.0\,10^{-2}$/d	$3.1\,10^{-2}$/d	$1.9\,10^{-1}$/d
E_{inf}	minimum water level admissible in E	-108 mm	-29 mm	-36 mm
C_{ext}	threshold level for the secondary springs	70 mm	185 mm	122 mm
X	partition coefficient to the secondary springs	0 60	0 51	0 81
ω_H	effective porosity for high water periods	–	$4.3\,10^{-1}$	$5.1\,10^{-1}$
ω_L	effective porosity for low water periods	–	$2.3\,10^{-3}$	$2.1\,10^{-2}$

Table 4.5: Existing model. Parameter set obtained by calibration to discharge data alone (Q-set), water level data alone (P-set), and joint discharge and water level data (PQ-set). Note that the partition coefficients from the reservoir E are bound together by the relation $k_{\mathrm{ER}} + k_{\mathrm{ES}} + k_{\mathrm{EC}} = 1$.

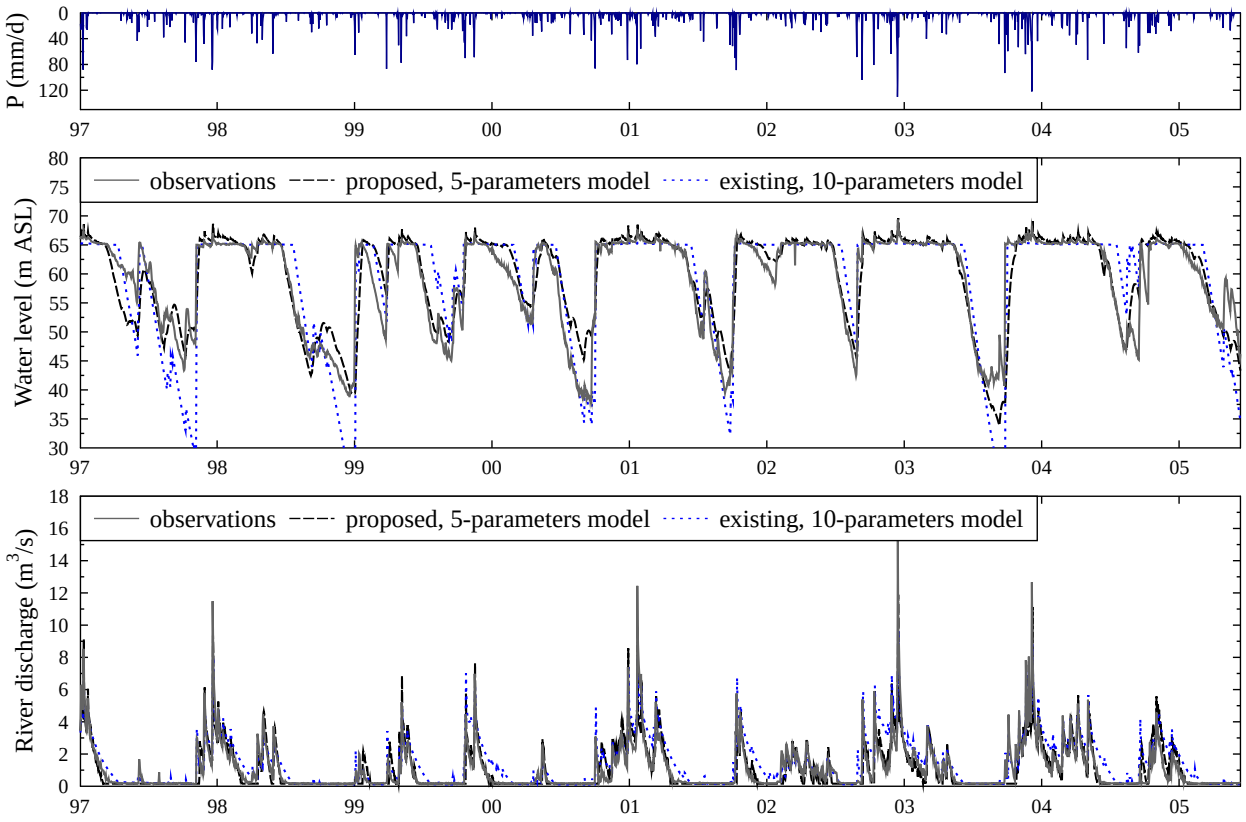

Figure 4.15: Existing model. Simulation results for the parameter set resulting from a calibration against discharge and water level data: top) daily rainfall, middle) observed and simulated water levels, bottom) observed and simulated spring discharge. See discussion in Sections 4.4.1 (proposed model) and 4.5.2 (existing model).

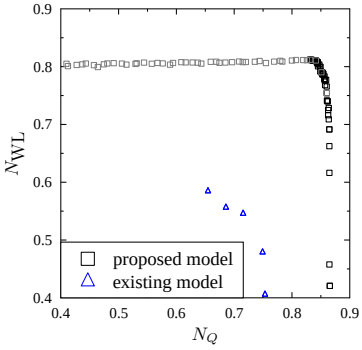

Figure 4.16: Existing model. Pareto-optimal solutions with respect to the Nash efficiencies for the spring discharge (x-axis) and the water level (y-axis) data. See discussion in Sections 4.4.1 (proposed model) and 4.5.2 (existing model).

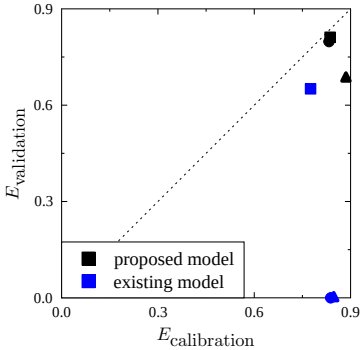

Figure 4.17: Existing model. Split sample test results. Model performance for the calibration (x-axis) and validation (y-axis) periods. Calibration on the P_1, P_2 and P_3 period are denoted by square, triangle and circle markers respectively. See discussion in Sections 4.4.3 (proposed model) and 4.5.2 (existing model).

4.6 Model evaluation against alternative parsimonious model structures

4.6.1 Model evaluation against a slightly modified version of the proposed model

The present section aims at assessing the contribution of the matrix-conduit transfer function Q_{MC} proposed in Section 4.2 to the performances of the proposed model. To that purpose, we investigate the calibration performance of a slightly modified version of the proposed model. This modified model is identical to the proposed model except that the transfer function Q_{MC} only allows flow from the matrix to the karst conduit: $Q_{MC} = k_{MC}M$.

The calibration of the modified model over the 1997-2005 spring discharge data yields a Nash efficiency similar to that of the proposed model (0.84). The calibration of the modified model over the 1997-2005 spring water level data yields a Nash efficiency of 0.76, which is significantly less than the calibration performance of the proposed model (0.81). The pareto front for the two-objective calibration is plotted in Figure 4.18. Its shape is very different from that of the pareto front of the proposed model. Indeed, there is significant trade-off between the performance indicator associated with water level and spring discharge simulation. The simulated time series for the parameter set resulting from the calibration against both discharge and water level data are shown in Figure 4.20 ($N_Q = 0.80$, $N_P = 0.73$) .

Figure 4.21 shows the dotty plots resulting from the modified model realisations, with the agregated performance indicator E on the y-axis and the parameter values on the x-axis. Compared to the proposed model (Figure 4.8c), the identifiability of the k_{MC} parameter is deteriorated, which indicates lower model consistency. The predictive capability of the modified version is also impaired compared to that of the proposed model (see split-sample test results in Figure 4.19).

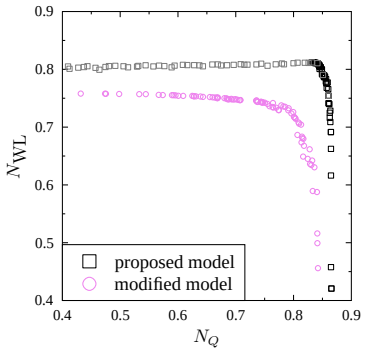

Figure 4.18: Modified version of the proposed model. Pareto-optimal solutions with respect to the Nash efficiencies for the spring discharge (x-axis) and the water level (y-axis) data. See discussion in Sections 4.4.1 (proposed model) and 4.5.2 (modified version of the proposed model).

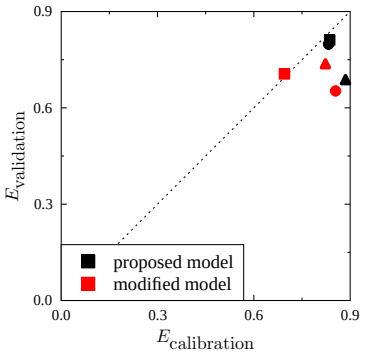

Figure 4.19: Modified version of the proposed model. Split sample test results. Model performance for the calibration (x-axis) and validation (y-axis) periods. Calibration on the P_1, P_2 and P_3 periods are denoted by square, triangle and circle markers respectively. See discussion in Section 4.4.3 (proposed model) and 4.6.1 (modified version of the proposed model).

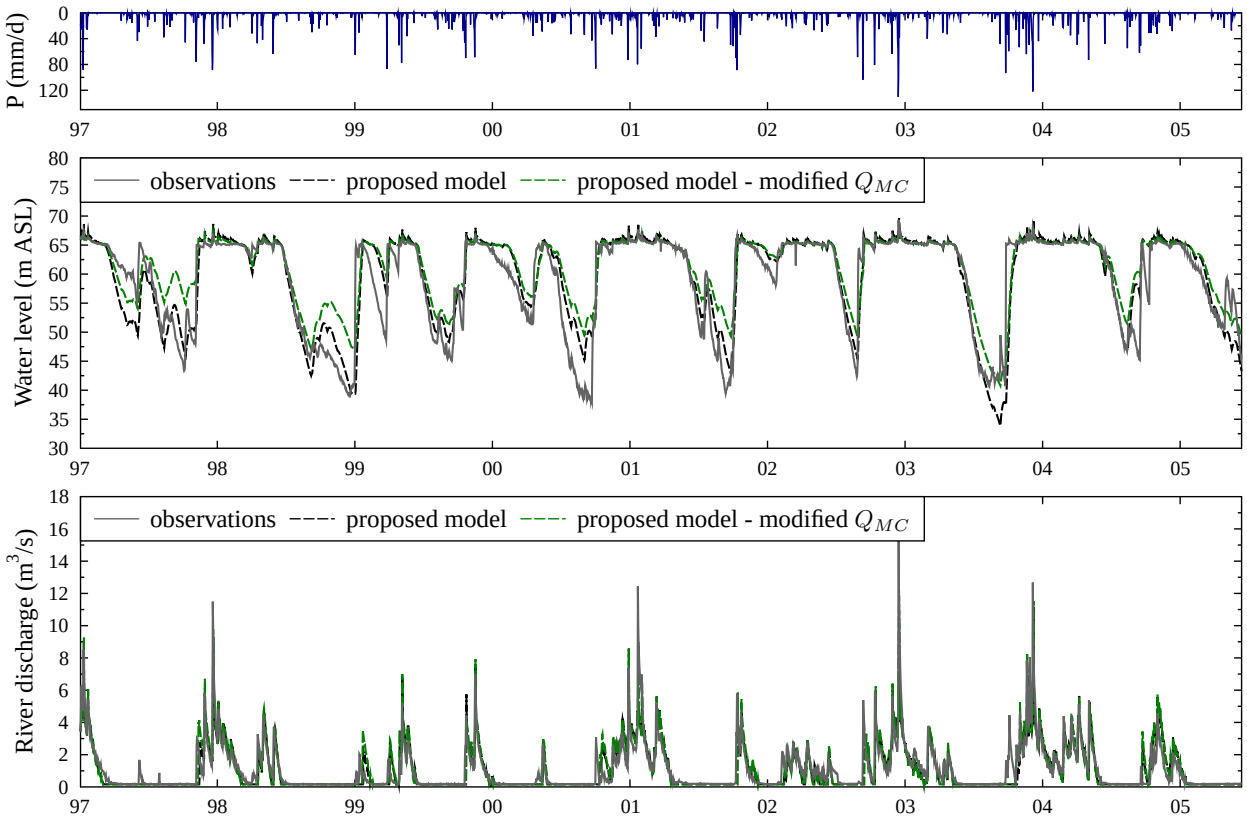

Figure 4.20: Modified version of the proposed model. Simulation results for the parameter set resulting from a calibration against discharge and water level data: top) daily rainfall, middle) observed and simulated water levels, bottom) observed and simulated spring discharge. See discussion in Sections 4.4.1 (proposed model) and 4.6.1 (modified version of the proposed model).

Symbol	Meaning	Q-set	P-set	PQ-set
E_{ext}	threshold level for the secondary springs	74 mm	147 mm	91 mm
k_{EC}	specific discharge coefficient from E to C	$3.4\,10^{-2}$/d	$5.5\,10^{-2}$/d	$4.0\,10^{-2}$ /d
k_{EM}	specific discharge coefficient from E to M	$2.5\,10^{-2}$/d	$1.4\,10^{-4}$/d	$4.0\,10^{-3}$ /d
k_{MC}	specific discharge coefficient from M to C	$1.3\,10^{-2}$/d	$1.7\,10^{-2}$/d	$6.2\,10^{-3}$ /d
ω	effective porosity	-	$3.1\,10^{-3}$	$2.7\,10^{-3}$

Table 4.6: Modified version of the proposed model. Parameter set obtained by calibration to discharge data alone (Q-set), water level data alone (P-set), and joint discharge and water level data (PQ-set).

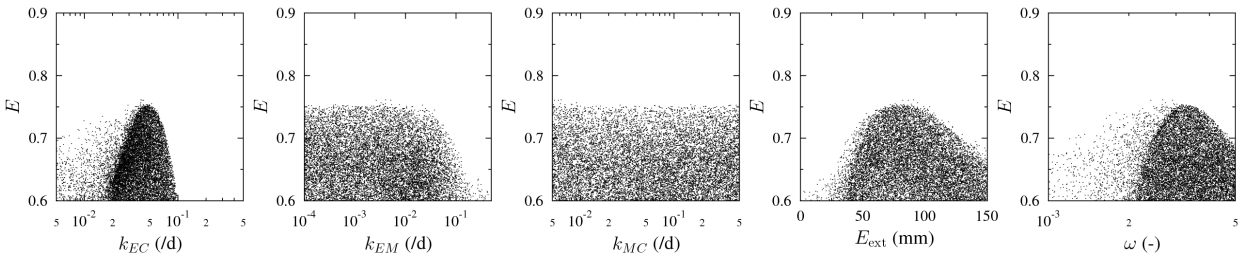

Figure 4.21: Modified version of the proposed model. Dotty plot resulting from model realisations, with the E indicator on the y-axis and the parameter values on the x-axis. Calibration against joint discharge and water level data.

4.6.2 Model evaluation against a 1-reservoir, 4-parameters model

A single-reservoir, 4-parameters model has been proposed by Fleury, 2011 (personal comm.). The model structure is meant to be the simplest possible, with no conceptualisation of the flow transfer processes in the karst aquifer. Note that this model has similar complexity (as measured by the degree of freedom) to the proposed, 3-reservoirs model.

Model structure and functioning. The proposed model is made of only one reservoir, and it comprises a total of four parameters (see model structure in Figure 4.22)

The model functioning may be summarized as follows:

1. the reservoir C receives the incoming precipitations and is affected by evapotranspiration,
2. part of the water is removed by pumping (rate Q_{pump}),
3. spring overflow occurs when the water level exceeds zero (discharge Q_{over}),
4. when C exceeds a given threshold C_{ext}, part of the water flows outside of the catchment (discharge Q_{ext}),
5. when the spring overflow rate is lower than a minimal value Q_{return}, part of the pumped water is released to the river so as to ensure a minimal flow rate $Q_{\text{spring}} = Q_{\text{return}}$.

The water level WL within the spring conduit is defined as

$$\text{WL} = z_0 + C/\omega \tag{4.21}$$

where z_0 is the pool overflow level (65 m ASL) and ω is an effective porosity coefficient.

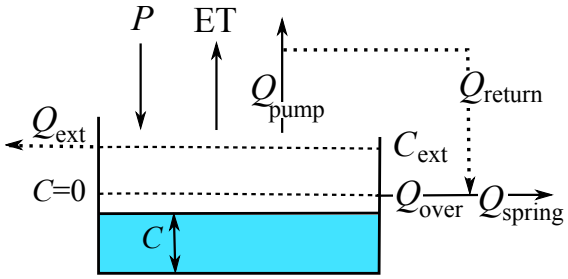

Figure 4.22: Structure and notation for the 1-reservoir, 4-parameters model proposed by Fleury, 2011 (personal comm.).

Governing equations. The model has one balance equation:

$$\frac{\mathrm{d}C}{dt} = P - \text{ET} - Q_{\text{pump}} - Q_{\text{over}} - Q_{\text{ext}} \tag{4.22}$$

where ET is the evapotranspiration rate, P is the precipitation rate, Q_{ext} is the discharge to secondary springs, Q_{pump} is the discharge pumped from the spring conduit and Q_{over} is the overflow discharge at the spring pool. Note that discharges are expressed as height of water per day. The actual evapotranspiration rate is assumed to be equal to the potential evapotranspiration rate. The discharges Q_{ext} and Q_{over} are defined as

$$Q_{\text{ext}} = \max(k_{\text{ext}}(C - C_{\text{ext}}), 0) \tag{4.23a}$$

$$Q_{\text{over}} = \max(k_{\text{spring}} C, 0) \tag{4.23b}$$

where k_{ext}, k_{spring} are specific discharge coefficients and C_{ext} is the threshold for the activation of the exterior losses. The spring discharge Q_{spring} is defined as the maximum of the overflow discharge Q_{over} and the return flow Q_{return}, multiplied by the total area of the catchment A.

$$Q_{\text{spring}} = A \max(Q_{\text{over}}, Q_{\text{return}}) \tag{4.24}$$

The water level WL within the spring conduit is defined as

$$\text{WL} = z_0 + C/\omega \tag{4.25}$$

where ω is an effective porosity coefficient and z_0 is the pool overflow level (65m ASL). The model equations are solved numerically using an explicit Euler scheme.

Calibration performance and predictive capability. The calibration of the 1-reservoir model over the 1997-2005 spring water level data yields a Nash efficiency similar to that of the proposed model (0.79). By contrast, the calibration over the spring discharge data yields a Nash efficiency of 0.80 which is significantly less than the calibration performance of the proposed model (0.84). The pareto front for the two-objective calibration of the 1-reservoir model is plotted in Figure 4.9. It has similar shape to the Pareto front of the proposed model but the maximum performance indicator for the water level simulation is lower than that of the proposed model. The simulated time series for the parameter set resulting from the calibration against both discharge and water level data are shown in Figure 4.23 ($N_Q = 0.80$, $N_{WL} = 0.79$). Compared to the proposed 3-reservoirs model, the 1-reservoir model has difficulties in adequately simulating piezometric rises (see e.g. winter 1999 and winter 2003 simulations), leading to missed flood events.

Figure 4.24 shows the dotty plots resulting from the 1-reservoir model realisations, with the agregated performance indicator E on the y-axis and the parameter values on the x-axis. The identifiability of all model parameters is good.

The predictive capability is assessed by a standard split-sample test (see test results in Figure 4.26). Calibration against the P_1 and P_2 periods yields increased performances during the validation period as compared to the calibration period. However when the calibration is performed against the P_3 data set the performance indicator over the validation period is greatly impaired.

4.6.3 Conclusion.

It may be concluded from Section 4.6 that the proposed model structure yields improved water level simulation and predictive capability as compared to alternative model structures of equivalent complexity.

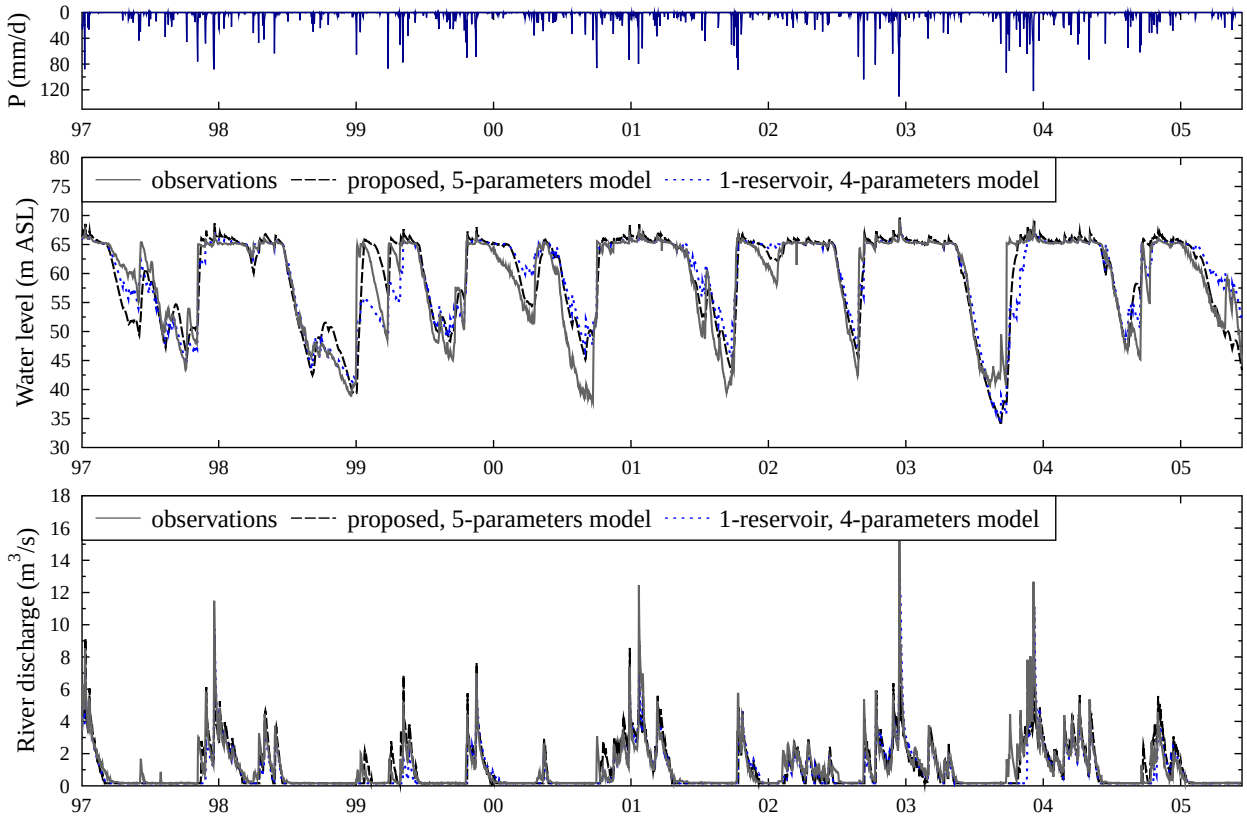

Figure 4.23: 1-reservoir model. Simulation results for the parameter set resulting from a calibration against discharge and water level data: top) daily rainfall, middle) observed and simulated water levels, bottom) observed and simulated river discharge. See discussion in Sections 4.4.1 (proposed 3-reservoirs model) and 4.6.2 (1-reservoir model).

Symbol	Meaning	Q-set	P-set	PQ-set
C_{ext}	threshold level for the secondary springs	63 mm	41 mm	79 mm
k_{ext}	specific discharge coeff. for the secondary springs	$9.9\,10^{-1}$/d	$2.0\,10^{-3}$/d	$1.6\,10^{-1}$/d
k_{over}	specific discharge coeff. for the spring overflow	$2.9\,10^{-2}$/d	$4.2\,10^{-2}$/d	$3.0\,10^{-2}$/d
ω	effective porosity	-	$9.3\,10^{-3}$	$9.1\,10^{-3}$

Table 4.7: 1-reservoir model. Parameter set obtained by calibration to discharge data alone (Q-set), water level data alone (P-set), and joint discharge and water level data (PQ-set).

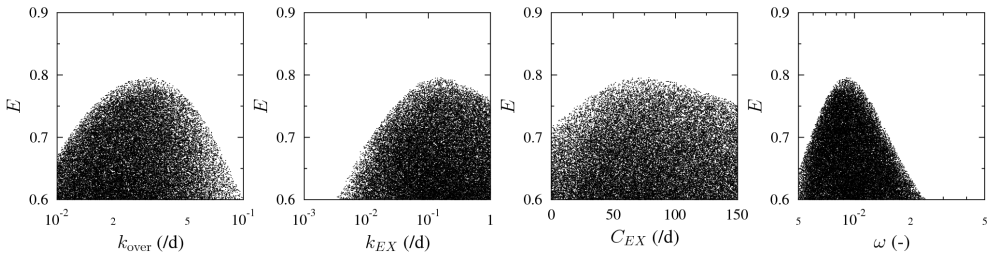

Figure 4.24: 1-reservoir model. Dotty plot resulting from model realisations, with the E measure on the y-axis and the parameter values on the x-axis. Calibration against joint discharge and water level data.

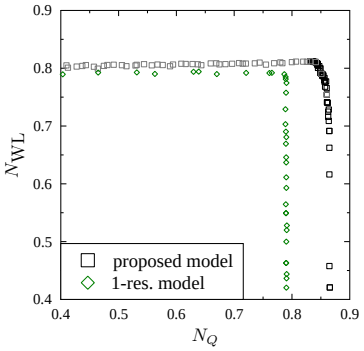

Figure 4.25: 1-reservoir model. Pareto-optimal solutions with respect to the Nash efficiencies for the river discharge (x-axis) and the water level (y-axis) data. See discussion in Sections 4.4.1 (proposed model) and 4.6.2 (1-reservoir model).

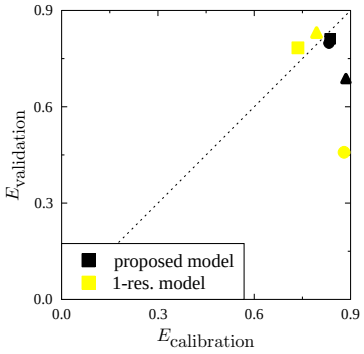

Figure 4.26: 1-reservoir model. Split sample test results. Model performance for the calibration (x-axis) and validation (y-axis) periods for the proposed and the existing models. Calibration on the P_1, P_2 and P_3 periods are denoted by square, triangle and circle markers respectively. See discussion in Section 4.4.3 (proposed model) and 4.6.2 (1-reservoir model).

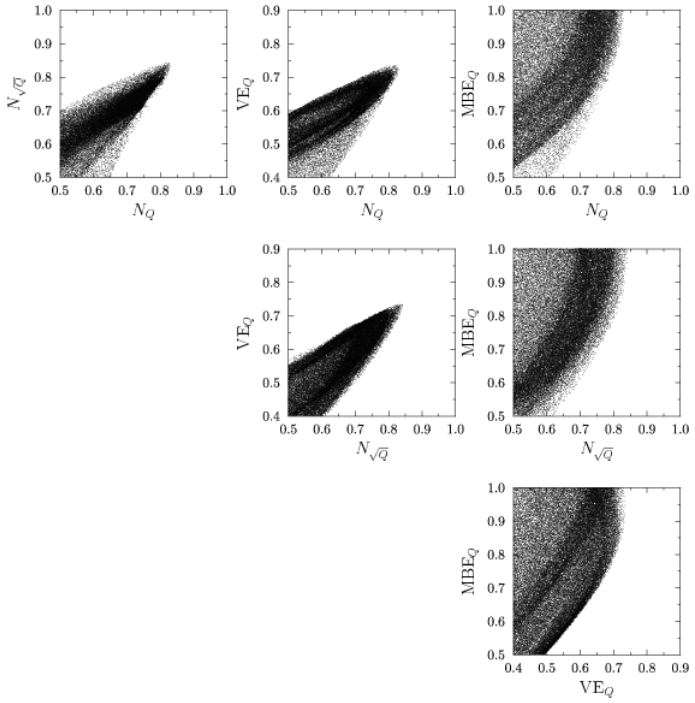

Figure 4.27: Proposed model. Calibration against discharge data alone. Dotty plot of N_Q, $N_{\sqrt{Q}}$, VE_Q and MBE_Q performance indicators resulting from Monte Carlo simulations.

4.7 Complementary discussion

4.7.1 Influence of the nature of the objective function on the calibration result

The nature of performance indicator used for the calibration procedure is likely to have an influence on the calibration result (calibrated parameter set and characteristics of the simulated spring water level and spring discharge time series). Several authors advocate a multi-objective calibration approach so as to force the model into reproducing different aspects of the system response [Madsen, 2000; Yapo et al., 1998]. This section aims at evaluating the influence of the performance indicator on the calibration results for the proposed model.

Performance indicator for the spring overflow discharge. An important aspect of the system response is the correct simulation of the succession between overflow and drying up periods. Calibration against objective functions that emphasize low flow periods are likely to yield a better simulation of that succession. In order to assess the influence of the objective function on that particular characteristics of the calibrated hydrographs, the calibration is carried out using the following objective functions

1. the Nash-Sutcliffe efficiency N_Q,
2. the Nash-Sutcliffe efficiency calculated against the square root of the discharge variable $N_{\sqrt{Q}}$,
3. the Volumetric Efficiency VE_Q,
4. the Modified Mass Balance error MBE_Q.

The definition of the different objective functions is given in Table 4.3. The Nash-Sutcliffe efficiency and the Volumetric Efficiency are distance-based functions whereas the Modified Balance Error is a weak-form based function [Guinot et al., 2011]. Compared to the Nash-Sutcliffe efficiency, the $\text{NSE}_{\sqrt{Q}}$ and the VE_Q emphasize low flow periods.

The complementarity of the different objective functions is investigated as follows. Monte-Carlo simulations of the proposed model are performed and the different performance indicators are calculated for each model run. Then each performance indicator is plotted against the others (see Figure 4.27). It is seen that the maximal performance in terms of NSE_Q, $\text{NSE}_{\sqrt{Q}}$ and VE_Q (all distance-based functions) is obtained for the same parameter sets. This means that multi-objective calibration based on these performance indicators would neither improve the simulation of the system response nor reduce the model parametric uncertainty, as compared to a calibration against the Nash efficiency only. Similarly, the maximal distance-based performance indicators are associated with the highest values of the MBE_Q.

Performance indicator for the water level within the conduit. In water resources management, the most important aspect of the system response consists in low water level simulation. This section aims to test whether excluding high water periods from the calibration data improves the simulation of low water level periods. The model is calibrated against water level data based on the Nash efficiency and high water periods are excluded from the Nash calculation. The high water periods are defined as the days when the observed spring water level is higher than a given threshold level. This threshold level is successively taken equal to 64, 60 and 55m ASL (arbitrary values). Figure 4.28 shows the simulated water level time series for the parameter sets resulting from the calibration. It is seen that the removal of high water periods from the calibration procedure does not improve the simulation of the low water level periods. Furthermore, the simulation of the alternation between the spring overflow and the non-overflow periods is impaired.

Conclusion. The parsimonious, 5-parameters structure of the proposed model is strongly constrained by the calibration data. The use of alternative performance indicators for the calibration procedures could not yield modified or more satisfying simulations of the system response.

4.7.2 Water level simulation results for the 1997-2010 period

Spring water level measurements are available for the 1997/2010 period. Figure 4.29 presents the simulation results for a calibration against spring water level data over the 1997/2010 period, for the proposed 3-reservoirs model and the 1-reservoir model. It is seen that compared to the single-reservoir model, the proposed model tends to better reproduce the succession between the spring overflow and non-overflow periods. However, large errors are found for the water level simulation during summer 2000, 2005 and 2006. Note that no systematic trend can be derived from Figure 4.29 for the modelling error during low flow period. Indeed, the simulated water level may be either higher (summer 2000) or lower (summer 2005, 2006) that the observed water level. The fact that the sign of the error (over-estimation or under-estimation of the system response) is the same for both models suggests that the meteorological input used for the simulation may be affected by local, non-systematic errors.

4.7.3 Conclusion

In this chapter we proposed a global reservoir model for the simulation of the rainfall - discharge - water level modelling of karst springs under active groundwater management. The main particularity of the proposed model is that it accounts for flow exchange between the spring conduit and the matrix compartment. The proposed model yields satisfying performances as regards the simulation of the water level and of the discharge time series for both the calibration and validation tests. Not allowing for flow exchange between the conduit and the matrix compartments greatly impairs the ability of the proposed model to reproduce the spring water level and discharge time series.

Compared to the existing four-reservoirs and 10-parameters model, the proposed three reservoirs, 5 parameters model yields improved simulations of both the spring water level and the spring discharge time series, and also enhanced predictive capability. Compared to a single-reservoir and 4-parameters model, the proposed model yields improved simulations of the spring water level and enhanced predictive capability. However, the relatively good performance of the single-reservoir model clearly demonstrates that the fact that a given model adequately fits the calibration data should not be considered as a proof that the corresponding flow conceptualisation is valid.

These results tends to indicate that the conceptualisation of the flow transfer proposed herein is well adapted to the system under consideration (Lez system). Further assessement of the proposed model structure on different test sites is needed.

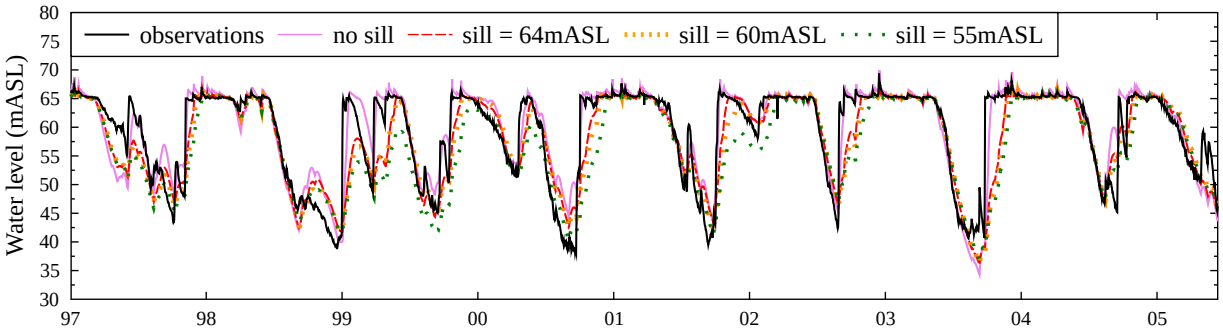

Figure 4.28: Proposed model. Calibration against water level data based on the Nash-Sutcliffe efficiency (1997 - 2005 data). High water level periods (observed water level greater that a given sill) are excluded from the calibration.

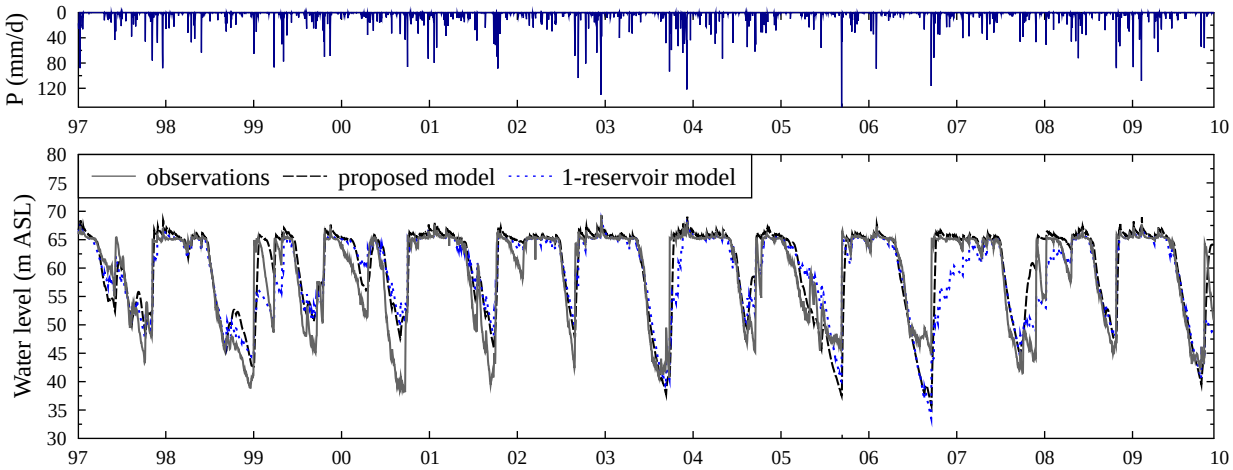

Figure 4.29: Simulation results for the parameter set resulting from a calibration against spring water level data: observed and simulated spring water level for the proposed model and for the 1-reservoir model. 1997/2010 data.

	N_Q	N_{WL}	E
proposed model	0.86	0.81	0.83
existing model	0.83	0.73	0.66
modified proposed model	0.84	0.76	0.76
1-reservoir model	0.80	0.79	0.80

Table 4.8: Summary of the calibration performances for the various models. Performance indicator for a calibration to discharge data alone (N_Q), water level data alone (N_P), and joint discharge and water level data (E).

	Calibration on P_1		Calibration on P_2		Calibration on P_3	
	$E_{\text{calibration}}$	$E_{\text{validation}}$	$E_{\text{calibration}}$	$E_{\text{validation}}$	$E_{\text{calibration}}$	$E_{\text{validation}}$
proposed model	0.84	0.81	0.89	0.68	0.83	0.80
existing model	0.78	0	0.65	0	0.85	0
modified proposed model	0.70	0.71	0.83	0.73	0.85	0.65
1-reservoir model	0.74	0.78	0.79	0.83	0.88	0.46

Table 4.9: Summary of the split-sample test results for the various models. Performance indicator for a calibration to discharge data alone (N_Q), water level data alone (N_P), and joint discharge and water level data (E).

4.8 References for Chapter 4

Avias, J. (1987). « Le cas de l'exsurgence karstique de la source du Lez alimentant en eau la ville de Montpellier ». In: *Pollution et Environnement des Eaux Souterraines : Protection et Problèmes d'Assainissement*. See p. 92.

— (1995). « Gestion active de l'exsurgence karstique de la source du Lez ». In: *Hydrogéologie* 1, pp. 113–127. See pp. v, ix, xvii, 90, 93, 134.

Bailly-Comte, V., J. B. Martin, H. Jourde, E. J. Screaton, S. Pistre and A. Langston (2010). « Water exchange and pressure transfer between conduits and matrix and their influence on hydrodynamics of two karst aquifers with sinking streams ». In: *Journal of Hydrology* 386.1-4, pp. 55–66. DOI: 10.1016/j.jhydrol.2010.03.005. See p. 91.

Butscher, C. and P. Huggenberger (2007). « Implications for karst hydrology from 3D geological modeling using the aquifer base gradient approach ». In: *Journal of Hydrology* 342.1-2, pp. 184–198. DOI: 10.1016/j.jhydrol.2007.05.025. See p. 91.

Efstratiadis, A. and D. Koutsoyiannis (2010). « One decade of multi-objective calibration approaches in hydrological modelling: A review ». In: *Hydrological Sciences Journal* 55.1, pp. 58–78. DOI: 10.1080/02626660903526292. See pp. 21, 96.

Fleury, P., B. Ladouche, Y. Conroux, H. Jourde and N. Dörfliger (2009). « Modelling the hydrologic functions of a karst aquifer under active water management - The Lez spring ». In: *Journal of Hydrology* 365.3-4, pp. 235–243. DOI: 10.1016/j.jhydrol.2008.11.037. See pp. ix, xviii, 7, 90, 93, 94, 102, 104.

Guinot, V., B. Cappelaere, C. Delenne and D. Ruelland (2011). « Objective functions for conceptual hydrological model calibration: Theoretical analysis of distance- and weak form-based functions ». In: *Journal of Hydrology* 401.1-2, pp. 1–13. DOI: 10.1016/j.jhydrol.2011.02.004. See pp. 21, 72, 114.

Gupta, H. V., S. Sorooshian and P. O. Yapo (1998). « Toward improved calibration of hydrologic models: Multiple and noncommensurable measures of information ». In: *Water Resources Research* 34.4, pp. 751–763. DOI: 10.1029/97WR03495. See pp. 18, 21, 96.

Hartmann, A., J. Lange and A. Rimmer (2009). « Applied dual porosity concept for large karst basins in the east Mediterranean ». In: *Geophysical Research Abstracts* 11. 6th EGU General Assembly, held in Vienna, Austria (April 19-24 , 2009), p. 682. URL: http://meetingorganizer.copernicus.org/EGU2009/EGU2009-682.pdf. See p. 91.

Jeannin, P.-Y. (1996). « Structure et comportement hydraulique des aquifères karstiques ». PhD thesis. Université de Neuchâtel. URL: http://91.121.162.160/THE/JEANNIN.pdf. See pp. 4, 9, 91.

Klemes, V. (1986). « Operational testing of hydrological simulation models ». In: *Hydrological Sciences Journal* 31.1, pp. 13–24. DOI: 10.1080/02626668609491024. See p. 97.

Madsen, H. (2000). « Automatic calibration of a conceptual rainfall-runoff model using multiple objectives ». In: *Journal of Hydrology* 235.3-4, pp. 276–288. DOI: 10.1016/S0022-1694(00)00279-1. See pp. 52, 96, 114.

Maillet, E. (1906). « La vidange des systèmes de réservoirs ». In: *Annales Ponts et Chaussées, Mém. et Doc* 21. See pp. 92, 103.

Marjolet, G. and J. Salado (1978). « Le système karstique de la source du Lez (Hérault) ». In: *Méditerranée* 1-2, pp. 71–83. See p. 93.

Maréchal, J.-C., B. Ladouche, N. Dörfliger and P. Lachassagne (2008). « Interpretation of pumping tests in a mixed flow karst system ». In: *Water Resources Research* 44, pp. –. DOI: 10.1029/2007WR006288. See pp. 4, 91.

Mazzilli, N., H. Jourde, V. Guinot, V. Bailly-Comte and P. Fleury (2011*a*). « Hydrological modelling of a karst aquifer under active groundwater management using a parsimonious conceptual

model ». In: *Proceedings of the H_2Karst Conference held in Besançon, France (Sept. 1-3, 2011)*. URL: http://sites.google.com/site/h2karst/. See p. 89.

Nash, J. and J. Sutcliffe (1970). « River flow forecasting through conceptual models. Part I - A discussion of principles ». In: *Journal of Hydrology* 10.3, pp. 282–290. DOI: 10.1016/0022-1694(70)90255-6. See pp. 77, 100.

Perrin, C., C. Michel and V. Andreassian (2001). « Does a large number of parameters enhance model performance? Comparative assessment of common catchment model structures on 429 catchments ». In: *Journal of Hydrology* 242.3-4, pp. 275–301. DOI: 10.1016/S0022-1694(00)00393-0. See pp. 6, 38, 77, 100.

Pinault, J. (2001). *Manuel utilisateur de TEMPO - Logiciel de traitement et de modélisation des séries temporelles en hydrogéologie et en hydrogéochimie*. Tech. rep. BRGM/RP-51459-FR. BRGM. URL: http://www.brgm.fr/Rapport?code=RP-51459-FR. See p. 102.

Roesch, A. and H. Jourde (2006). « Incidence d'une gestion active de la ressource en eau en milieu karstique sur le risque hydrologique. Exemple du fleuve Lez (Montpellier, France) ». In: *Proceedings of the 1st GIRE3D Conference held in Marrakech, Morocco (May 23-25, 2006)*. Comité Marocain de l'AIH. See pp. 96, 134, 136.

Thornthwaite, C. (1948). « An approach toward a rational classification of climate ». In: *Geographical Review* 38.1, pp. 55–94. URL: http://www.jstor.org/stable/210739. See pp. 39, 73, 77, 93.

Tritz, S., V. Guinot and H. Jourde (2011). « Modelling the behaviour of a karst system catchment using non linear hysteretic conceptual model ». In: *Journal of Hydrology* 397.3-4, pp. 250–262. DOI: 10.1016/j.jhydrol.2010.12.001. See pp. vi, xvii, 7, 38–41, 44, 46, 52, 59, 72, 73, 76, 77, 80, 93, 94.

Yapo, P. O., H. V. Gupta and S. Sorooshian (1998). « Multi-objective global optimization for hydrologic models ». In: *Journal of Hydrology* 204.1-4, pp. 83–97. DOI: 10.1016/S0022-1694(97)00107-8. See pp. 52, 114.

Part 2. Analysis of a distributed, hybrid flow model

Introduction to Part 2

This part is devoted to the analysis of the sensitivity properties for hybrid flow modelling approaches. Hybrid flow models are distributed models in which the karst drainage network is represented by one-dimensional discrete elements which are coupled to a three-dimensional matrix system representative of the fractured blocks. The main issues addressed are:

(i) do flow parameters, model geometry and boundary conditions influence model response in the same way ?

(ii) do confined and unconfined aquifers behave in the same way with respect to the sensitivity propagation ?

(iii) what is the impact of discrete karst conduit modelling on the sensitivity propagation ?

(iv) when a distributed model is shown to provide wrong simulation results, where should additional measurements be carried out in priority ?

(v) can general rules be defined for the optimal location of measurement points ?

These questions are addressed using both analytical and empirical sensitivity approaches.

In Chapters 5 and 6, an hybrid flow model is developed for the large karst hydrosystem located between the Hérault and Vidourle rivers, that includes the Lez karst hydrosystem (Hérault, France). In what follows, that large hydrosystem will be referred to as the "Lez karst hydrosystem". Chapter 5 presents the hydrogeologic and hydrodynamic settings of the study area. Chapter 6 describes the hybrid flow model setup and the simulation results.

The sensitivity properties are addressed in Chapter 7. As a preliminary step, Section 7.1 investigates the sensitivity propagation within the matrix system. More precisely, it analyses the sensitivity properties of the two-dimensional, steady-state groundwater flow equation to the flow parameters and to the boundary conditions based on an analytical perturbation approach. Section 7.2 investigates the influence of the discrete conduit network on the sensitivity propagation based on an empirical analysis of the Lez hydrosystem hybrid flow model.

Chapter 5

Study area

The Lez aquifer system has been presented briefly in chapter 4. The present chapter discusses its hydrodynamic functioning, in view of the hybrid flow modelling.

Contents

5.1 General situation

The Lez aquifer is located in the karst Garrigues area, which is encompassed between the Hercynian basement of the Cévennes to the north and the Mediterranean sea to the south (see situation map in Figure 5.1). The boundaries of Lez aquifer system can be roughly materialized by the Hérault and Vidourle rivers (western and eastern sides) and by the Cevennes fault and Montpellier faults (southern and northern sides).

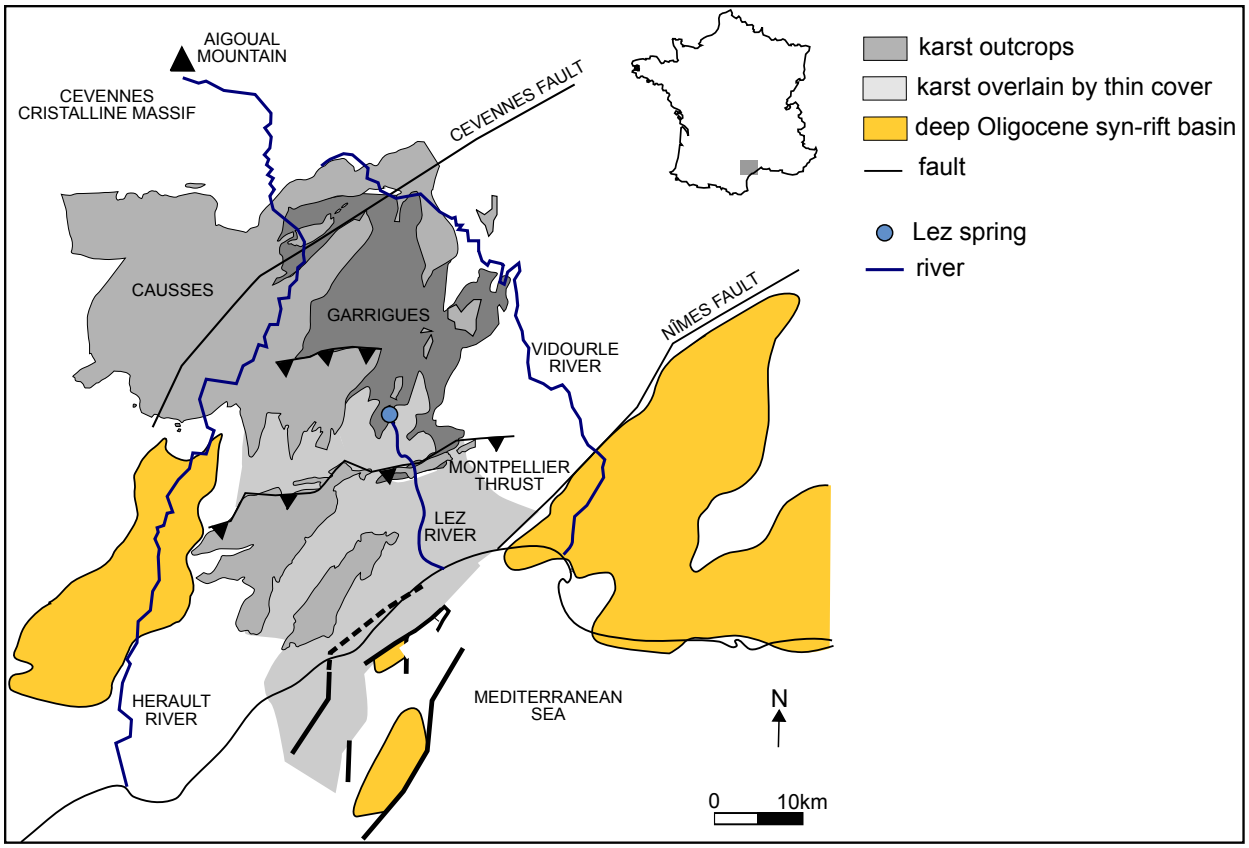

Figure 5.1: General situation of the Lez karst aquifer system. Simplified after Camus, 1999, 2003.

5.2 Hydrogeological setting

5.2.1 Hydrostratigraphy

This paragraph briefly presents the hydrostratigraphy of the study area. A summary of the formations is given in Table 5.3. A simplified geological map is presented in Figure 5.2.

The Lez aquifer is developed in Late Jurassic to Early Berriasian formations (see Figures 5.2 and 5.3). It is separated from the underlying Middle Jurassic aquifer by marly, Callovo-Oxfordian formations. The hydraulic properties of the Upper Callovian and Early Oxfordian units are contrasted. The facies of the Upper Callovian unit ranges from compact limestones with good hydraulic properties in the Hérault valley (west of the study area) to impervious marly limestones and lithographic marls in the eastern part of the study area [Drogue, 1969]. The Early Oxfordian unit is represented by a 20 to 50 m-thick, intensely faulted blue marl layer. An hydraulic connection between the Middle Jurassic aquifer and the Lez aquifer is likely to occur through leakage or along the faults [Drogue, 1969; Marjolet and Salado, 1976].

The Late Jurassic aquifer shows in average good aquifer properties. The Middle and Late Oxfordian units are made of marly limestones with relatively bad hydrodynamic properties. The Kimmeridgian and Portlandian units consist of sublithologic to corraligène massive limestones. The Early Berriasian unit consists in fossiliferous and marly limestones. The Kimmeridgian/Portlandian and then the Early Berriasian are the most conductive formations.

Late Berriasian and Early Valanginian marls and marly limestones make up the roof of the Lez aquifer unit. This unit is considered as impermeable at the regional scale. However, field evidence of local karstification have been reported (H. Jourde, personnal comm.). Local fracturation may also enable the circulation of water flowing from the underlying Jurassic aquifer (e.g. moulin de Vere

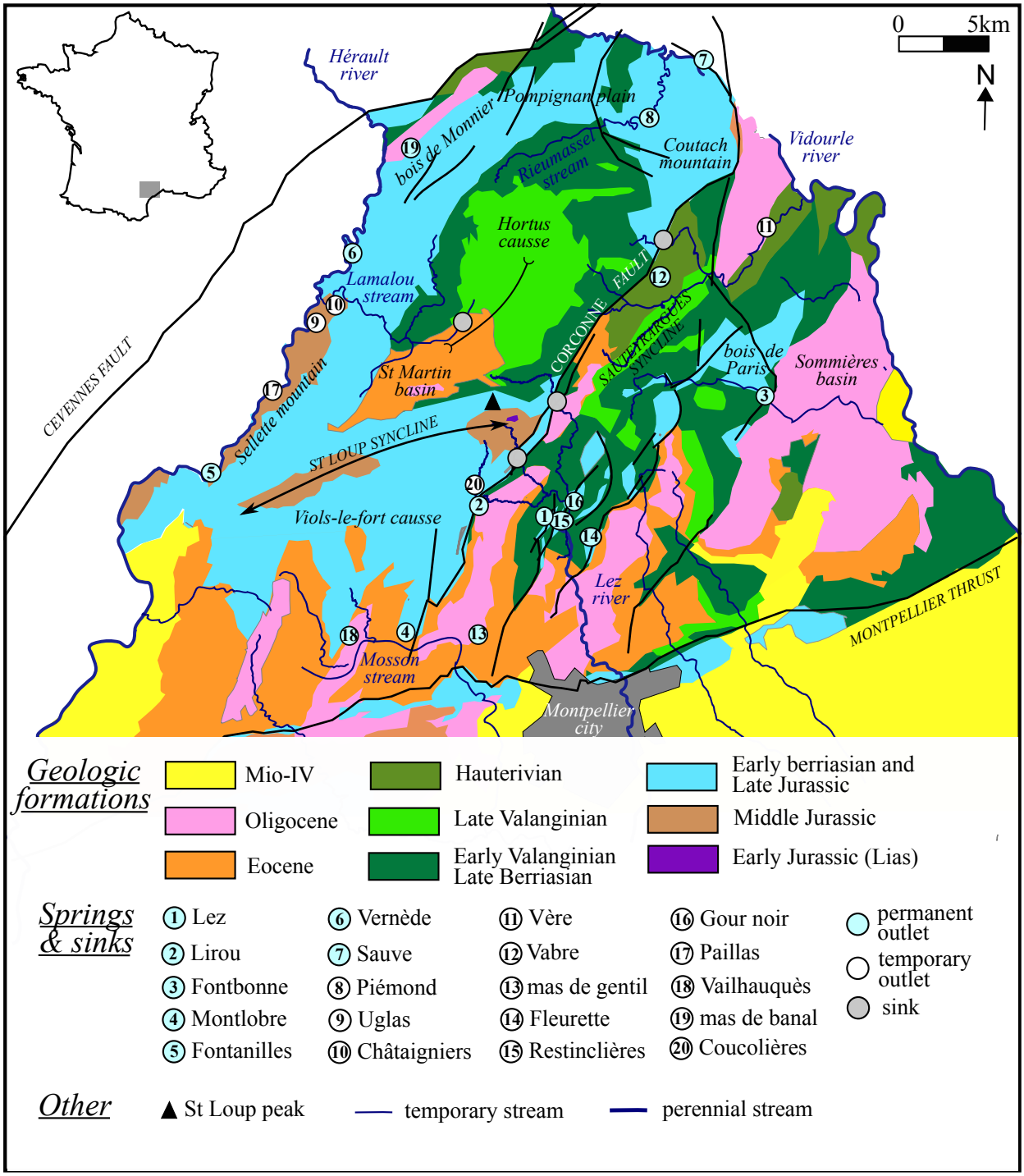

Figure 5.2: Schematic hydrogeological map of the Lez system.

springs). The facies of the Late Valanginian limestone ranges from miroitant limestones to marly limestones. The miroitant limestones are well karstified and show good hydraulic properties (south of the Hortus causse). The marly limestones have globally poor hydraulic properties. However, they may include locally massive, karstifiable mudstones layers as evidenced by the development of the Lauret and Lauzières caves (north of the Hortus causse, 9 and 3.5 km development respectively) [Boinet, 2002].

The roof of the aquifer is made of a 100 m-thick layer of Early Hauterivian marls. Most subsequent formations are impermeable. A few formations may have interesting aquifer properties, among which the Late Hauterivian limestones, the Lutetian limestones and some Oligocene formations (Castries-Sommières basin limestones in particular [Bel, 1963]).

The Early Cretaceous formations are missing west of the city of Montpellier (70 Myr depositional and erosional gap due to the uplift of the Durancian bulge [Combes, 1990; Séranne et al., 2002]).

5.2.2 Tectonic setting

This Section presents the main tectonic phases the study area has been submitted to, mainly based on the bibliographic review by Tissier, 2009 and Léonardi et al., 2011.

The Late Hercynian orogeny (Early Permian) is associated with a compression of direction NNE-SSW that sparked off major transcurrent tectonic features along the major conjugate directions NE-SW (e.g. Cévennes and Nimes faults) and NW-SE [Arthaud and Matte, 1975]. These tectonic features have conditioned the response of the sedimentary cover to the subsequent tectonic phases.

During the Permian, the extensive stress triggered by the breakdown of the Pangea causes the reactivation of the existing late Hercynian tectonic features (normal slip).

From the Lias to the Dogger, the opening of the Tethys is associated with an extensive stress of direction E-W then WSW-ENE that results in the initiation of normal faults with N-S then WNW-ESE direction [Durand et al., 2009; Guennoc et al., 2000; Guiot et al., 1991].

From the Late Jurassic to the Eocene, the area is influenced by the Pyrenean orogeny. During the Late Jurassic, the opening of the Biscay bay is responsible for the initiation of the Corconne fault [Benedicto, 1996; Olivet, 1996]. The Middle Cretaceous N-S compression in the Massif Central (surrection of the Durancian bulge) triggers a N-S extension of the Languedoc area and the initiation of N090 normal faults. During Eocene, the Pyrenean orogeny results in a N-S compressive stress that causes the initiation of major E-W folds (Montpellier thrust fold, Viols-le-fort and Saint-Loup peak anticline) [Arthaud and Seguret, 1981]. The existing E-W faults are reactivated as overlapping faults whereas the existing NE-SW faults act as oblic ramps with left-lateral strike-slip movement. The total shortening was estimated at 25 km [Arthaud and Laurent, 1995].

The opening of the Gulf of Lion during the Oligocene results in an extensive stress in the Languedoc area [Mauffret and Gennesseaux, 1989]. The existing NE-SW features (e.g. Corconne fault) are reactivated as listric extensional faults [Arthaud and Seguret, 1981; Dörfliger et al., 2008], whereas conjugated N170-N010 and N080-N100 faults are reactivated as right-lateral strike-slip faults [Tissier, 2009]. This extension is associated with synrift basin development near the major faults [Dörfliger et al., 2008]: half-graben structures with NE-SW axis of Saint Mathieu de Tréviers, Prades-Le-Lez and Assas basins as well as the Sommières basin. This tectonic phase results in the lowering of the compartment east of the Corconne fault.

The tectonic stress reverses at Miocene (NE-SW compression) [Bergerat, 1987].

5.2.3 Main geological structures

This paragraph briefly discusses the hydrogeological role of the main structures. These aspects will be more thoroughly addressed in Sections 5.5 and 5.6. The main structures are presented in Figure 5.2.

Period	Epoch	Stratigraphic unit	Main lithology	Thickness (m)	main hydrodynamic behaviour	modelled units
Neogene	Miocene	Burgdalian	molassic limestone, marls and molasse		aquitard	top aquitard
Paleogene	Oligocene	Chattian	conglomerates, marls and sandstones			
		Rupelian				
	Eocene	Ludian	lacustrine limestone		aquifer	superposed aquifer
		Bartonian	conglomerates and marls	0 to 300		
		Lutetian	lacustrine limestone	50 to 100		
	Paleocene	Selandian	sandstone and pink marls	0 to 50	aquitard	roof
Cretaceous	Late	Maastrichtian			aquifer	aquifer
	Early	Late Hauterivian	gravel limestone	100		
		Early Hauterivian	marls	100	aquitard	
		Late Valanginian	bioclastic limestone	50 to 200	aquifer	
		Early Valanginian	marly limestone	200 to 800	aquitard	
		Late Berrasian				
		Early Berrasian	pelletoid, fossiliferous and marly limestone	50 to 100	aquifer	
Jurassic	Late (Malm)	Portlandien	massive limestone	150 to 200		
		Kimmeridgian				
		Oxfordian	marly limestone (small beds)	60 to 100		
			marly limestone	300		
	Middle (Dogger)	Callovian	blue marls	20 to 50	aquitard	bedrock
			marly limestones and glauconic marls	80 to 100		
		Bathonian	limestone and dolomite	100 to 300	aquifer	
		Bajocian	cherty, marly and oolitic limstone	100 to 150		
		Late Aalenian				
	Early (Lias)	Early Aalenian	black marls	150	aquitard	
		Toarcian				

Figure 5.3: Litostratigraphy of the study area and main hydrogeological units.

The **Corconne fault** and the associated faults have a major impact on the circulations within the aquifer. The vertical displacement associated with the normal, Oligocene functioning of these faults is responsible for the division of the aquifer system into a raised north-western compartment, where the Jurassic aquifer outcrops and a lowered south-eastern compartiment where the Jurassic aquifer is mainly covered by impermeable formations. An important consequence is that the Jurassic aquifer is mainly unconfined west of the Corconne fault, whereas it is mainly confined east of the Corconne fault. Another consequence of the vertical displacement is the juxtaposition of aquifer and aquitard compartments, which is responsible for the settlement of numerous dammed-type karst springs (Lez, Lirou, Restinclières, Sauve, Fontbonne springs among others).

North of the area, the NE-SW **Cévennes fault** that separates the formations of the Montoulieu basin from the Jurassic limestones of the Lez system forms the northern boundary of the aquifer system. The **Sommieres basin** may be considered as the western hydraulic boundary of the study area. The large EW folds that result from the late Pyrenean orogeny behave as hydraulic barriers. The **Montpellier thrust fault** constitutes the southern boundary of the aquifer system. The **Viols-le-fort - Saint-Loup anticline** is an aerial-arch, assymetric, north-trending anticline. The core of the anticline outcrops in the Morties valley. The fold is associated with an EW inverse fault that caused the raising of the northern compartiment (Saint Martin basin and Hortus Causse). The Viols-le-fort - Saint-Loup anticline mainly acts as an hydraulic barrier for the fluid circulations [Bakalowicz et al., 1999].

5.2.4 Karstification of the carbonate units

The karstification is the result of chemical processes (that govern the dissolution of the carbonate rock) and power processes (that produce the energy for carrying and draining off the solution) [Bakalowicz, 1996; Ford and Williams, 2007]. It is governed by multiple factors with possible antagonistic effect: geographical and geological conditions of the exposure of the rock, climate, time available for the process evolution, direction and intensity of the hydraulic gradient, rock properties (and possible weaknesses), maturity of the karst system. Polycyclicity and polygenesis are typical features [Bosák, 2003]. Studying the genesis of a karst aquifer requires the combination of geomorphological, speleological, climatological and stratigraphical approaches [Abel et al., 2002]. The relationship between geodynamics and karstification in the Languedoc area is a subject of ongoing research at the Montpellier University (PhD of É. Husson (2010-2013), PhD of A. Dausse (2011-2014)). This Section aims to give some indications on the karst structuration.

Marine deposition prevails from the Trias to the Early Cretaceous time (0 to +200m ASL). Two main periods favourable for karstification are identified:

1. an emersion period between the Bajocian and Bathonian (Dogger) allows the karstification of the Lias and Late Aalenian limestones [Durand et al., 2009],
2. at the end of Barremian (Early Cretaceous), the emersion of the entire area sparks an intense karstification of the Late Jurassic and Early Cretaceous formations [Séranne et al., 2002] (N-S hydraulic gradient [Léonardi et al., 2011; Tissier, 2009]).

Continental deposition prevails from the Late Cretaceous on:

1. during the Late Cretaceous and Early Paleocene, high amplitude ($>$ 400m) successive drops of the base level [Combes et al., 2007; Husson, 2010; Séranne et al., 2009] may be related to the closure of a marine gulf. Opening and closure of the strait may be controlled by tectonic movements along the active orogenic axis of the Pyrenean Range and eustatic variations of the Paleocene World Ocean [Combes et al., 2007; Séranne et al., 2009],
2. during Eocene, a compressive stress is associated to a continuous drop of the sea level which results in an increase in the karstification [Dörfliger et al., 2008]. The hydraulic gradient

during that period is directed towards the South [Tissier, 2009],

3. during Messinian (-5Myr) the closing of the Mediterranean straits triggers the partial drying of the Mediterranea ("Messinian salinity crisis"). The crisis can be subdivided into two phases, with sea level drops of around 600m and 1500m respectively [Suc et al., 2007]. It caused the formation of deep karst systems and the reactivation of the existing karst systems [Audra et al., 2004; Mocochain et al., 2006], in particular the deep paleocene systems [Husson, 2010]. Geomorphological studies have evidenced the fact that "the Hérault Messinian paleovalley was perched during the Messinian Crisis. Due to this perched position, both the Hérault and Vidourle valleys were drained by streams, sinking while crossing limestone outcrops. The underground bypasses were connected at depth to the Lez karst aquifer that drained the whole area at this time" [Audra et al., 2004]. By that time the Lez aquifer discharged at the Mediterranean base level through a hydrogeologic watergap in the eastern part of the anticline of the Montpellier thrust (including limestones of the Gardiole massif) [Audra et al., 2004]. Subsequent flooding of the Mediterranean Basin (5.32 Myr) caused the adaptation of the Messinian karst systems to the raised base-level ("chemney-shafts" formation), and plugging of the Messinian outlets by sedimentary infilling [Mocochain et al., 2006],

4. the Quaternary time is characterized by eustatic-climatic oscillations of the sea level from -120m ASL (Würm glaciation, -15kyr) to 0m ASL during interglaciar periods.

5.3 Topography, climate and vegetation

The study area is flanked between the Cévennes cristalline massive at the north, and the littoral plain at the south. The topography rises gently from the south to the north of the area. The topographical heights range from 15m ASL (Vidourle's banks) to 658m ASL (Saint-Loup mountain) (see Figure 5.4a).

The region has typical mediterranean climate. The temperatures are hot in summer and mild in winter. Rainfall is characterized by both monthly and annual irregularity. Annual rainfall is bi-seasonal, occuring primarily from September to December and in a lesser extent from March to May. Precipitations may range from about 700mm (dry year) to 1200mm (wet year) (see Figure 5.5). At a more local scale, the geographic situation of the study area bears important consequences on the rainfall repartition. The mean annual cumulated precipitations increase from the south to the north of the study area due to the rising topography and the proximity of the Cevennes massive (see mean rainfall repartition in Figure 5.4b and see associate data in Table 5.1). The region is also prone to intense convective rain events during the autumn season, the so-called Cevenols episodes. The cumulated daily rainfall may reach several hundreds of mm (e.g. 473mm recorded at the Ceyrac raingauge the 08/09/2002, 272mm recorded at the Montpellier raingauge the 22/09/2003).

The northern part of the study area is little urbanized. Carbonate facies are predominant. Soils are either inexistant, or shallow and little developed. The residus of limestone dissolution may fill topographic lows and open fractures. This area is mostly covered by low scrublands and woods that are well suited to drought. The south-eastern part of the study area is characterized by vineyards and an increased urbanization.

The net rainfall (i.e., rainfall minus evapotranspiration) can be related on a yearly scale to the total rainfall by a simple relationship of the form $P_N = \alpha(P - P_0)$ where P_N is the net annual rainfall, P is the total annual rainfall, α is a dimensionless coefficient and P_0 is the minimal annual rainfall value below which no outflow is observed. Observations give values of α close to unity which means that the vegetation has a low capability to make use of excedentary precipitations, and P_0 values ranging from 450 to 550mm [Rambal et al., 2009].

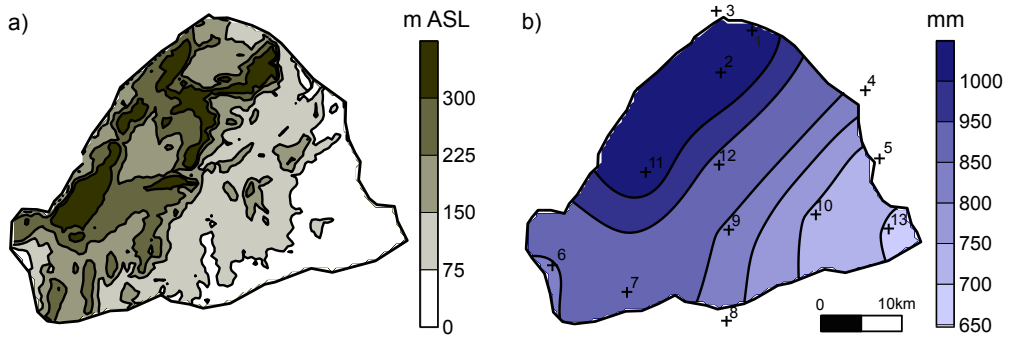

Figure 5.4: Study area: a) topographic map, b) mean cumulated annual rainfall over the 1998-2008 period. The crosses stand for rain-gauges. See details in Table 5.1.

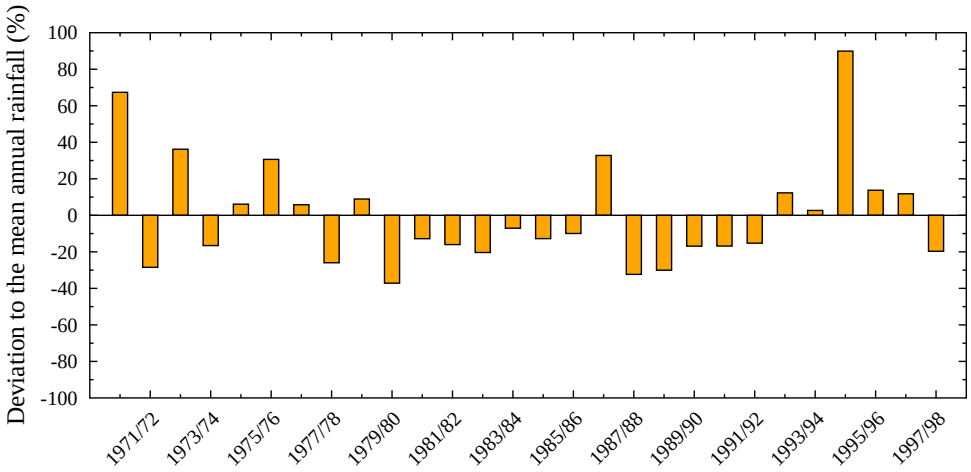

Figure 5.5: Percentage deviation from the mean annual rainfall at the Saint-Martin-de-Londres station (1969/2008 data).

Raingauge station	X (m)	Y (m)	Cumulated annual rainfall (mm)
1- Conqueyrac	725448	183511	1059
2- Pompignan	721748	178321	1045
3- Saint-Hippolyte-du-fort	721055	185813	990
4- Vic-le-Fesc	739423	176007	829
5- Villevieille	741112	167617	717
6- Aniane	700756	154270	829
7- Montarnaud	709841	150868	920
8- Montpellier	722120	147463	821
9- Prades-le-Lez	722529	158646	839
10- Saint-Drézéry	733316	160634	743
11- Saint-Martin-de-Londres	712349	165945	1039
12- Valflaunès	721338	166637	932
13- Verargues	742601	158727	699

Table 5.1: Raingauge stations: name, extended Lambert II coordinates and cumulated annual rainfall (1998-2008 data). See rainfall distribution in Figure 5.4c.

5.4 Surface hydrography

As a consequence of the large extent of karstified limestone outcrops, the drainage pattern of the study area comprises only a few perennial streams (Hérault, Vidourle and Lez rivers). The numerous springs and water losses testigate from the close interaction between surface water and groundwater over the karstified limestone outcrops.

The number of karst springs located within the **Hérault river** course (e.g. Vernède, Uglas, Fontanilles and Ressecs springs) suggests that the Hérault river constitutes the aquifer base level. Over the study area an average 40% of the Hérault discharge comes from karst contribution [Weng and Dörfliger, 2002]. The Hérault discharge has been reported to increase by up to $0.7\,m^3\,s^{-1}$ between the upstream and downstream ends of the study area during the summer low water period [Drogue, 1969].

Upstream of the study area, the **Vidourle river** drains a $35\,km^2$ non-karstic area. During low and medium water periods, the river leaks entirely within the karst system [Poty, 1998; Vaute et al., 1997]. The underground flow re-emerges at the Sauve spring. The underground Vidourle has been recognized over more than 3km by cave divers and its total estimated length is 8km based on tracing experiments [Vasseur, 2006]. Downstream of Sauve, the Vidourle is disconnected from the Lez aquifer as it flows over Cretaceous and Oligocene formations (Liouc and Sommières basins).

The **Lez river** rises at a contact between limestone and calcareous marls. Up to Montpellier city, its course undergoes little anthropic influence.

Temporary streams are numerous (see Figure 5.2). They have been and are still little monitored and there is a large uncertainty on their annual average outflow. These streams may be prone to dramatic flash floods. As an example, the Rieumassel stream (a tributary of the Vidourle river, drainage area of about $60\,km^2$) may drain off over $800\,m^3\,s^{-1}$ (september 1933 rainfall event) [Drogue and Puech, 1968]. The Lirou river is the main tributary of the Lez river. Its discharge rate may reach up to $15\,m^3\,s^{-1}$ [Drogue and Puech, 1968]. A few hundred of meters down the spring, after the confluence with the Deridière tributary discharges may reach $20\,m^3\,s^{-1}$ [Drogue and Puech, 1968].

South of the study area, the Mosson river drains off water from the Jurassic and Lutetian karstified limestones.

5.5 Hydrodynamics of the perched aquifer units

5.5.1 Late Valanginian aquifer from the Hortus karst plateau

The Hortus karst plateau (causse) is an individualized massif of Late Valanginian fractured and karstified limestone that is separated from the underlying Jurassic aquifer by Late Berriasian and Early Valanginian marls. At the South, the Hortus plateau sinks below the tertiary deposits of the St Martin de Londres basin (see cross-section in Figure 5.7). The drainage system is well characterized thanks to intense caving activity and numerous tracing experiments [Boinet, 2002]. Precipitations are quickly drained off through numerous temporary springs that are located mainly around the border of the causse, at the contact between the Valanginian limestones and the underlying marly formations. The karst plateau is drained towards the Hérault, the Vidourle and the Lez rivers. Part of the groundwater outflow from the Hortus causse may infiltrate into the Lez karst system through sinks localized in particular along the Corconne fault [Boinet, 2002; Drogue, 1969].

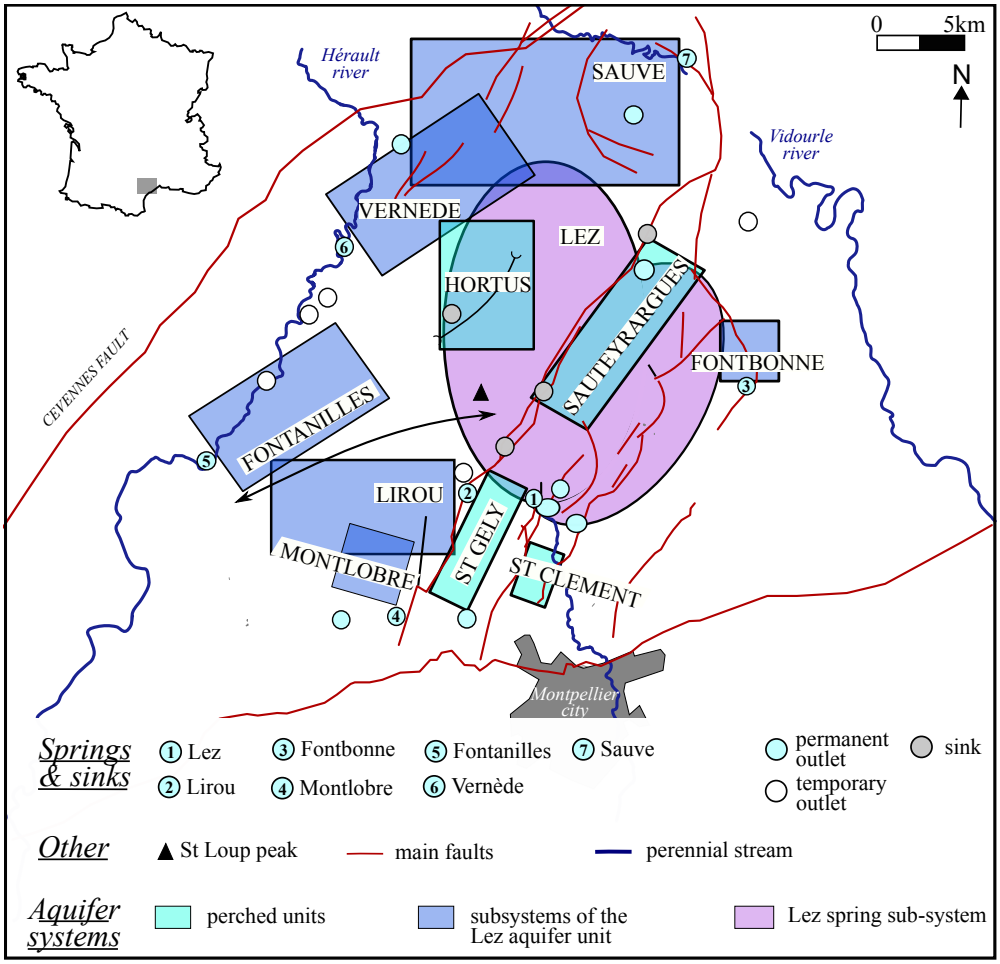

Figure 5.6: Schematic localisation of the aquifer sub-systems presented in Sections 5.5 and 5.6.

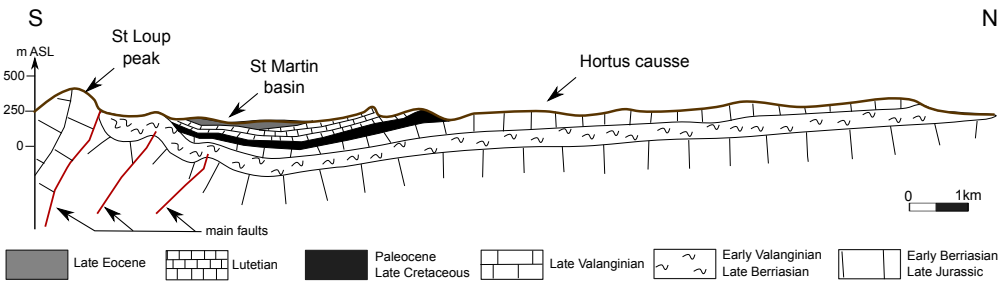

Figure 5.7: Schematic cross-section across the Hortus plateau. Adapted from Durand, 1992.

5.5.2 Late Valanginian and Late Hauterivian aquifers from the Sauteyrargues syncline

The Late Hauterivian and Late Valanginian series from the Sauteyrargues syncline have good aquifer characteristics. These aquifers are fed by concentrated or diffuse infiltration over the limestone outcrops (losses from the Brestalou river in particular). The main exsurgences of the Hauterivian aquifer are the Vabre temporary springs and the Viala temporary loss-emergence. As for the Late Valanginian, a number of temporary spring spark off within the Brestalou river (J. Grevellec, personnal comm.) and within the Brestalou tributaries (boulidou du moulin de Vère).

The Late Valanginian formation is separed from the underlying Jurassic formation by the low Valanginian marly roof, yet intense faulting of this area makes an indepth contact between the two formations possible. An hydraulic connection between the Late Hauterivian - Late Valanginian series and the Jurassic formations through the Corconne fault is probable (Figure 5.8). The hydraulic connection between the Late Hauterivian horizon and the Jurassic formations is suggested by tracing experiments ("boulidou B2 du mas de Vedel" tracing experiment, see Table 5.16). The hypothesis of a hydraulic connection between the Late Valanginian serie and the Jurassic formations through the Corconne fault is corroborated by the piezometric variations recorded at the Laudou well, which are closely correlated with those recorded at the Lez spring (see Figures 5.8, 5.10 and 5.15).

5.5.3 Lutetian aquifers

The Lutetian formations are dominated by marly facies but they may have locally good aquifer properties:

- within the Saint-Martin de Londres basin, the Lutetian limestones reservoir is fed in particular by the losses from the Lamalou river. In the south-eastern part of the basin, the Lutetian formation rests directly over the Jurassic limestones. Drainage of the Lutetian limestones by the Jurassic aquifer is likely, and may account for the low productivity of the wells drilled over the western border of the basin (J. Grevellec, personal comm.),
- the highly fractured Lutetian limestone from Saint Clément de Rivière shows good aquifer capability. There is no clear sign of a hydraulic connectivity with the Lez system,
- the Lutetian limestone serie of the Saint-Gély-du-Fesc syncline also has interesting hydrodynamic properties and it is used for the water supply of the city of Saint-Gély-du-Fesc. The Lutetian unit comprises three calcareous units that are separated by marly levels. The Lutetian aquifer is separated from the Jurassic karst aquifer by marly levels and fed principally by sinks from the Lirou river [Diluca, 1973]. The aquifer is drained towards the south of syncline (Mosson river base level). The main outlets are the perennial Grabels spring (approximate mean discharge rate of $50\,l\,s^{-1}$) which feeds the Mosson stream, and the Mas de Gentil spring which feeds a Mosson tributary [Diluca, 1973].

5.6 Hydrodynamics of the Lez aquifer system

The boundaries of the Lez spring catchment are only approximately known. Estimate of the spring catchment area range from 178 [Guilbot, 1975] to $200\,km^2$ [Chemin, 1974] based on conceptual modelling, $268\,km^2$ including the Lirou spring catchment based on hydrological balance [Drogue, 1969]. This Section offers an overview of the hydrodynamic circulations within the Lez karst system (see Figure 5.6 for an approximate localization).

5.6.1 The Lez subsystem

The Lez spring. The Lez spring is located at the contact zone between karstified Berriasian limestones and Late Valanginian impermeable marls [Drogue, 1969]. The spring conduit has been explored until the depth of 101 m below the pool level (−36 m ASL) by professional scuba divers (see simplified conduit topography in Figure 5.9).

The Lez spring has been used for the water supply of the city of Montpellier since 1854. The methods used for water withdrawal have evolved with the water demand. Gravity-driven water withdrawal was performed until 1965. Pumps were then installed some 6.5 m below the overflow level of the spring. This solution allowed the withdrawal of up to $800\,l\,s^{-1}$, even during low flow periods when the natural outflow of the spring was lower than $200\,l\,s^{-1}$ [Avias, 1995]. In 1981, to face an ever increasing water demand, four wells were drilled directly into the karst conduit at a depth of −48 m below the pool overflow level. Pumping into these wells allowed an increased withdrawal during low water periods, with no risk of dewatering for the pumps.

As long as the amount of groundwater pumped is smaller than the natural discharge in the conduit, pumping extracts only part of the flow and the residual water reaches the pool and feeds the Lez River. No residual water reaches the pool during low water periods due to the pumping. A minimal $160\,l\,s^{-1}$ return flow to the Lez river allows biotic organisms to survive. Only a few informations are available on the spring characteristics under natural conditions. Natural spring discharges range from $0.3\,m^3\,s^{-1}$ (lowest water period) to $17\,m^3\,s^{-1}$ during flood events [Botton, 1984; Durepaire, 1985]. Possible reasons for the limitations of the maximum discharge rate include limitations due to the karst conduit section. The average withdrawals are currently $1.1\,m^3\,s^{-1}$ in average. The maximal spring withdrawal allowed is $1.7\,m^3\,s^{-1}$.

The spring undergoes active management, i.e. the summer overexploitation of the aquifer's reserves is counterbalanced by the autumn floods, so that the permanent reserves of the aquifer are balanced over the year. The depletion of the aquifer that results from the summer pumping also has a mitigating impact on the first autumn floods. Indeed, the volume dewatered due to summer pumping is equivalent to that of a flood control dam [Avias and Legrand, 1989] of approximately 15 to $19 \times 10^6\,m^3$ in volume [Avias and Legrand, 1989; Jourde et al., 2011; Lafare, 2007; Roesch and Jourde, 2006].

Drainage along the Corconne fault. The Corconne fault determines the drainage of the Lez system to a large extent:

- rapid North-South transfers along the Corconne fault have been evidenced by tracing experiments (Brestalou de Claret, Brestalou de Lauret and Yorgues losses tracing experiments - see Figure 5.15 and Table 5.16),
- numerous losses and emergences-losses have been reported along the fault (e.g. Yorgues losses, Deridière losses, Brestalou losses, Vedel loss-emergence),
- water level fluctuations within wells drilled along the Corconne fault are closely correlated to water level fluctuations at the Lez spring, suggesting pressurized flow connection (see Figures 5.10, 5.11 and 5.15).

Deep water circulation. Positive temperature anomalies at the Lez spring and at the nearby Restinclières, Sourcette, Gour noir and Fleurette springs may be associated to deep circulations along the Corconne fault system [Marjolet and Salado, 1976]. The deep origin of part of the Lez spring water is corroborated by its chemical composition (Li/SO_4 and Cl/Br ratios in particular) which suggests contact with Triassic formations [Bicalho Caetano, 2010; Hébrard et al., 2006].

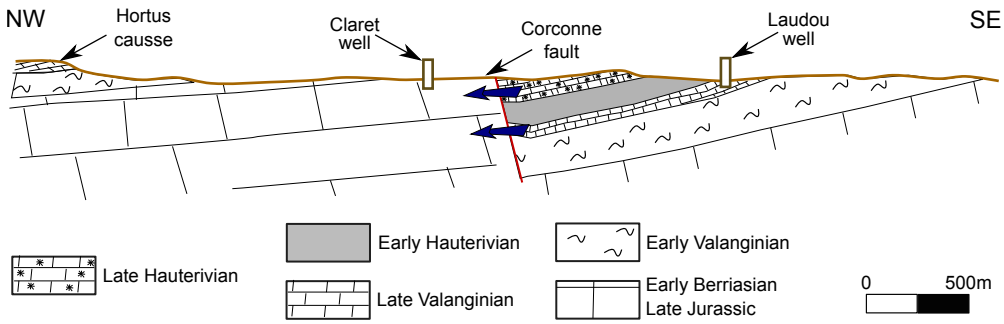

Figure 5.8: Hydraulic connectivity between the Late Hauterivian - Late Valanginian series and the Jurassic formations. Schematic cross-section across the Corconne fault and the Sauteyrargues syncline, in the Claret area. Adapted from Salado and Marjolet, 1975. The arrows indicate the probable drainage of the Late Hauterivian and Late Valanginian series by the Jurassic formations. Also see comparison of the hydraulic head fluctuations at the Lez spring and Laudou well in Figure 5.10. See wells location in Figure 5.15.

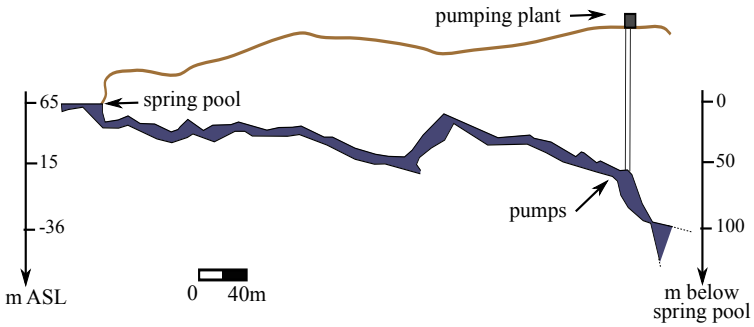

Figure 5.9: Lez spring: Simplified topography. Original topography by P. Rousset (G.E.P.S diving group, 1972).

Epikarst thickness. Geophysical surveys have been used to characterize the thickness of the epikarst at some locations within the Lez system:

- ground penetrating radar measurements indicate an average epikarst thickness of 8 to 12 m for the late Valanginian limestones of the Hortus causse [Alfares et al., 2002],
- electrical resistivity profiles performed along the Corconne fault suggest an average epikarst thickness of approx. 20 m (personal comm. J. Grevellec, see Figure 5.12).

Hydrodynamic behaviour during flood events. The use of natural tracers can help differentiate water flow from the different aquifer compartments [Bicalho Caetano, 2010; Lafare, 2007; Marjolet and Salado, 1976]. Water flowing from the Lez spring at the beginning of a high stage period is characterized by a high mineralisation and high temperature, which suggests piston-flow transfer (i.e., water with relatively high residence time is forced out of the aquifer by the increased pressure due to aquifer recharge). Piston-flow water is followed by rapid transfer water which is characterized by a low mineralization and high NO_3, high bacteria and high TOC (total organic carbon) concentrations [Bicalho Caetano, 2010; Bicalho Caetano et al., 2011; Lafare, 2007; Marjolet and Salado, 1976]. Rainfall occurring in the proximate area to the spring may be associated with the presence of rapid transfer water with relatively high turbidity due to karst conduit decolmation since the beginning of the flood event [Lafare, 2007].

Hydraulic connectivity within the Lez spring subsystem. Limestone outcrops located east of the Corconne fault near the Lez spring are drained by temporary springs (e.g. Restinclières spring), some of which are connected to the Lez spring system (e.g. Gour noir and Pouzets springs). The Fleurette spring is connected to the Lez system [Avias, 1992*b*] yet hydrogeochemical characterization indicates distinct groundwater flowpaths [Bicalho Caetano, 2010]. Theses springs have low mean annual discharge rates yet they may drain off high discharge rates during flood events (see Table 5.3).

Some 15 piezometers located mainly east of the Corconne fault are monitored continuously. Three typical hydrodynamic behaviours can be observed [Chaussard, 2005; Conroux, 2007; Perriquet, 2006; Roesch and Jourde, 2006] (see Figures 5.10, 5.11 and 5.15):

- "group 1" wells are characterized by water level variations closely correlated to that of the Lez spring, suggesting pressurized flow connection to the spring. Note that all "group 1" wells are drilled along the Corconne fault,
- "group 2" wells also display water level variations well correlated to that of the Lez spring. The response of "group 2" wells to the beginning of the recession period at the Lez spring is delayed by more than one day, which suggests that these wells are connected to "annex-to-drainage" systems,
- "group 3" wells show little or no correlation to water level variations at the Lez spring.

5.6.2 The Lirou subsystem

The Lirou spring. The Lirou spring is located west of the Viols causse. It is the outlet of a karst conduit network of over 2 km length (Lirou cave, grand boulidou des matelles, Baraque shaft, fausse-monnaie cave). The Lirou spring may drain off up to 15 $m^3 s^{-1}$ during flood events, 20 $m^3 s^{-1}$ including nearby springs [Chemin, 1974; Drogue, 1969]. Its mean annual discharge ranges from 0.4 to 1.8 $m^3 s^{-1}$ [Drogue, 1969]. The spring catchment area is around 65 km^2 (based on hydrologic balance) [Drogue, 1969]. The spring acts as an overflow outlet of the Viols-le-fort causse. Indeed:

- analysis of the spring water chemistry shows low mineralisation and high CO_2 content, which is the fingerprint of rapid infiltration water [Lafare, 2007; Marjolet and Salado, 1976],
- the characteristics of the spring hydrograph suggest overflow functioning [Drogue, 1969],

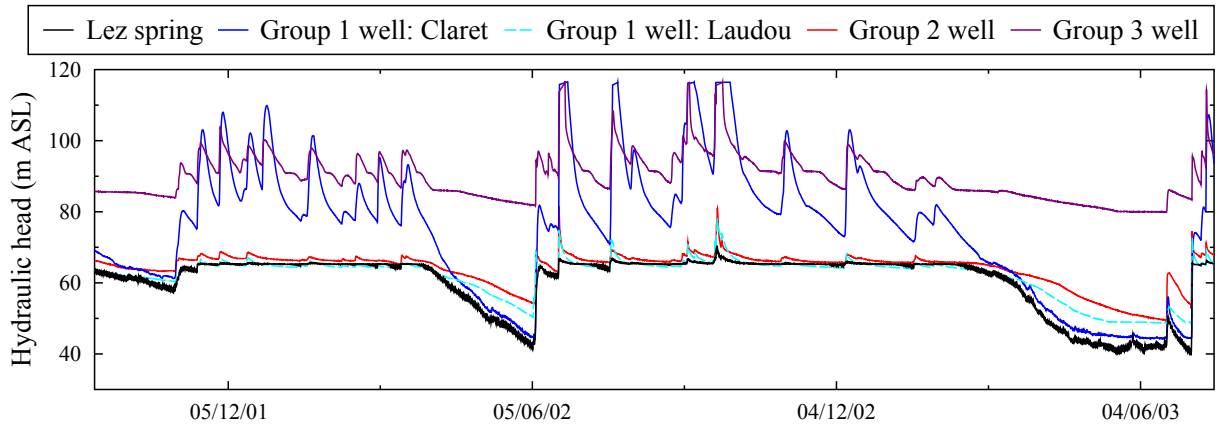

Figure 5.10: Typical hydrodynamic behaviours of group 1 (Claret and Laudou), group 2 (Bois Rosiers) and group 3 (Coutach) wells compared to the Lez spring hydrodynamic behaviour. Also see details of the Claret well behaviour in Figure 5.11. See wells location in Figure 5.15.

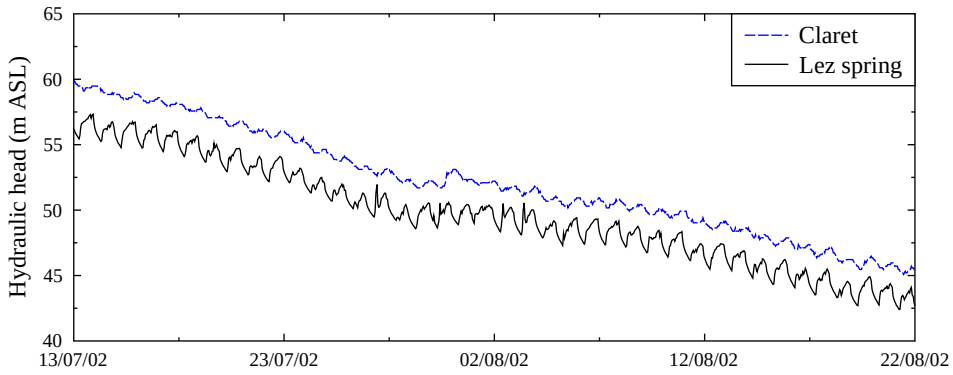

Figure 5.11: Hydraulic head variations at the Lez spring and Claret well. The pumping rate at the Lez supply plant alternates between unequal pulse and shut-in periods. The piezometric heads measured at the Claret well exhibits periods of drawdown and build up, which suggests pressurized flow connection. See wells location in Figure 5.15.

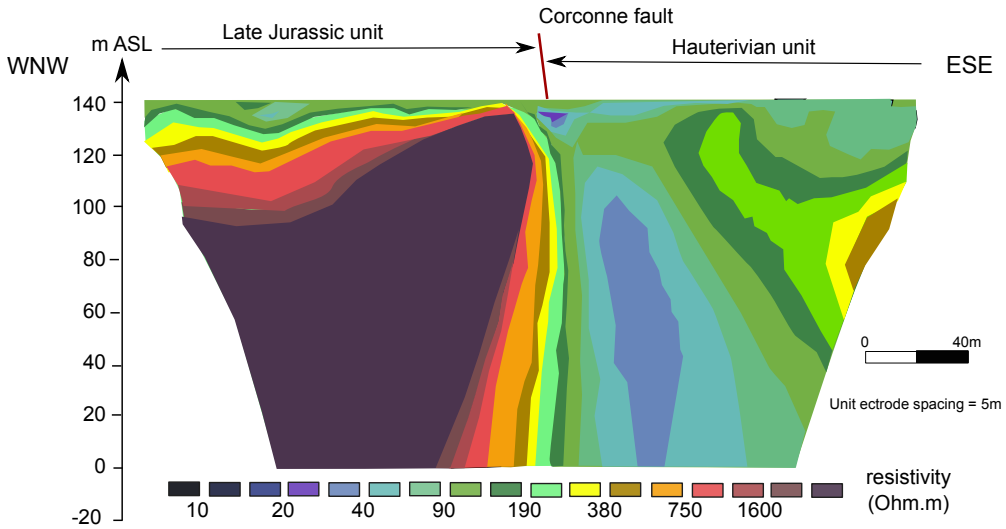

Figure 5.12: Resistivity profile across the Corconne fault. Profile performed by SAFEGE CETIIS, courtesy of J.Grevellec.

– monitoring of the water level within the spring conduit (Suquet well, grand boulidou des Matelles) and within a nearby well (Matelles well) indicates sharp reactivity of both wells to rainfall events (up to 30 m rises in the Matelles well and 40 m rises in the Suquet well).

Hydrodynamic connectivity with the Lez spring subsystem. Underground drainage of the Jurassic limestones of the Viols-le-fort causse towards the Lez spring may occur either through the Saint-Gély syncline, or along E-W accidents north of the Saint-Loup mountain until the Corconne drainage axis [Avias, 1988; Karam, 1989]. The structural continuity between the Jurassic limestones of the Viols-le-fort and those of the Lez spring has been established by structural analysis (see Figure 5.13) [Drogue, 1969]. Indications of an hydrodynamic continuity during high flow periods are the following

– correlation between the water level fluctuations monitored within wells drilled west of the Corconne fault within the karstified Jurassic limestones of the Lirou system (Suquet and Matelles wells) and the water level fluctuations within the Lez spring conduit (see Figures 5.14 and 5.15),
– tracing experiments ("Fausse monnaie" cave tracing test, see Figure 5.15 and see Table 5.16).

The hydrodynamic continuity is broken during low flow periods as evidenced by the complete stabilization of the water level within the Lirou karst conduit (see Figure 5.14).

5.6.3 The Sauve subsystem

The Sauve springs. The Sauve springs are located north of the system, at a contact zone between the Jurassic and Cretaceous formations on the Corconne fault. The mean and maximum discharges of the main, temporary outlet (94.5 m ASL) are approximately $1\,m^3\,s^{-1}$ and $13\,m^3\,s^{-1}$ respectively [Drogue, 1969; Vaute et al., 1997]. The maximum discharge of the whole group of secondary, perennial outlets is approximately $1\,m^3\,s^{-1}$ [Drogue, 1969]. The Sauve springs are the main outlets of the subterranean Vidourle river, as evidenced by tracing experiments, cave diving and field observations. The Vidourle losses do not constitute the only alimentation of the Sauve springs. Indeed:

– the flood rise at the Sauve springs may occur before that of the Vidourle river (measured at the Saint Hippolyte du Fort station) [Drogue, 1969],
– the low water periods discharge rate of the Sauve springs is higher than that of the Vidourle losses [Drogue, 1969].

Part of the alimentation of the Sauve springs comes from the Pompignan plain [Drogue, 1969]. Wells drilled in the Pompignan plain react sharply to rain events, with head loads up to 70m and rapid recessions [Avias et al., 1984]. The low water piezometric level within the Pompignan wells is close to the overflow level of the Sauve springs.

Hydrodynamic connectivity with the Lez spring subsystem. The lithological continuity between the Late Jurassic limestones of the Pompignan plain and those of the Lez is certain but the hydraulic connectivity is not obvious. The close correlation between the water levels in the piezometers of the pompignan plain as well as the quasi-stability of these water levels in low water periods exclude the hypothesis of a communication of the pompignan plain and the Lez spring during low water periods [Karam, 1989]. However a connection between the Pompignan plain and the Lez spring during high water periods may be possible. The only elements that supports this hypothesis is the result of a tracing test (Rieumassel loss tracing test) whose fiability is not established [Avias, 1992*b*].

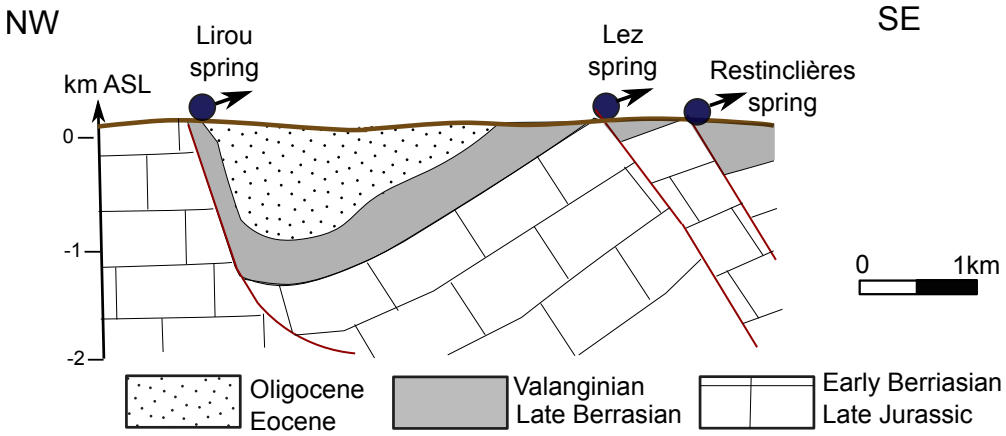

Figure 5.13: Schematic cross-section across the Saint-Gely syncline, after Benedicto et al., 1999.

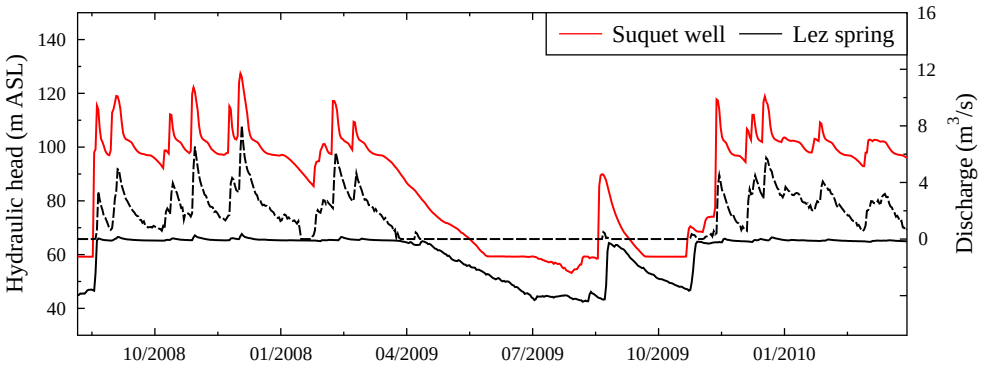

Figure 5.14: Hydrodynamic continuity between the Lez spring and the Lirou subsystem: water levels at the Suquet well and within the Lez karst conduit (solid lines, left y-axis) and Lez spring discharge (dotted line, right y-axis) as a function of time. The Suquet well is drilled directly within the Lirou karst conduit system. A pumping test is performed at the Suquet well during Sept. 2009. See wells location in Figure 5.15.

5.6.4 The Vernede subsystem

The Vernède spring (110 m ASL) is the major outlet of the "bois de Monnier" mountain (numerous tracing experiments, see Table 5.16). The draining direction of the Monnier mountain towards the Vernède spring is parallel to the major tectonic directions (NE-SW). The 171 m deep mas de banal cave (139 m ASL) is connected to the Vernède system. The maximal spring discharge is approximately $4\,m^3\,s^{-1}$ [Drogue, 1969]. Temporary outlets of the "bois de Monnier" drainage system include the Baoutes (127 m ASL) and the Cayla (122 m ASL) springs.

5.6.5 The Fontbonne subsystem

The Fontbonne spring. The Fontbonne spring (55 m ASL) flows from Oligocene marls, at the contact zone between karstified Berriasian and Jurassic limestones and the tertiary formations of the Sommières basin. The spring drainage area is constituted by the south-western part of a small mountain of karstified Jurassic limestones (bois de Paris mountain). The mean spring discharge is approximately $120\,m^3\,h^{-1}$ [Chemin, 1974]. The spring is used for water supply. The Fontbonne spring feeds the Benovie stream. The Benovie stream was perennial prior to the use of the Fontbonne spring for water supply. It is now temporary.

Hydrodynamic continuity with the Lez spring subsystem. The disconnection between the Fontbonne spring and the Lez system is evidenced by piezometric fluctuations within the nearby Bois des Rosier, mas Martin and Carnas Stade wells, by the "valat de Conques" tracing test and by pumping tests analysis. Pumping tests have established the hydraulic connection between the Fontbonne spring and the drainage area of the Saint-Clément spring which is located north of the "bois de Paris" mountain. The spring water temperature is abnormally high (constant 16.5 °C) which suggests semi-deep alimentation.

5.6.6 The Fontanilles subsystem

The Fontanilles springs are constituted by two perennial (90 m ASL) and several temporary outlets located at the western border of the system, at the level of or a few meters above the Hérault river. The mean annual dicharge is $315\,l\,s^{-1}$ with daily discharges ranging from $201\,s^{-1}$ up to $14.5\,m^3\,s^{-1}$ [Ladouche et al., 2002]. Pumping is performed within the karst conduit to supply the small city of Puéchabon with water. Average pumping rate range from 0.9 to $1.7\,l\,s^{-1}$. The karst conduit system has been explored and mapped by cave divers over 1.8 km.

The spring recharge area is approximately $18\,km^2$ [Ladouche et al., 2002; Schoen et al., 1999*a*]. Note that due to the spring configuration (numerous outlets) spring discharge measurements are difficult and underestimation of the actual discharge is likely, so that the hydrologic balance is only indicative. The recharge area includes the Saint Martin de Londres basin (losses from the Lamalou river) and the Selette mountain ("perte de Saint Martin de Londres" and "Baume Vidal" tracing tests - see Table 5.16). The Châtaigniers spring (120 m ASL, Lamalou gorges) is the main temporary high-water outflow spring of the Fontanilles system.

5.6.7 The Montlobre subsystem

The Montlobre spring (nine temporary and perennial outlets, approx. 80 m ASL) is located at a contact zone between Jurassic and Cretaceous formations, south of the Viols-le-Fort causse. Its discharge rate may reach $2\,m^3\,s^{-1}$ during flood events [Drogue, 1969]. The Mosson stream may dry out during low water periods but it is perennial at the level of the Montlobre spring, which indicates recharge of the river by the jurassic limestones of the Viols-le-fort causse. The hydraulic

connectivity between the Montlobre system and the Mosson river is supported by tracing tests ("perte du ruisseau d'Arnède" tracing test). The recharge of the Mosson river by the Jurassic limestones is supposed to be approximately $130\,l\,s^{-1}$ [Diluca, 1973].

5.6.8 Drainage through the Montpellier fold

The Montpellier fold is considered as an hydraulic barrier for the Lez system [Drogue, 1969], in particular due to its impermeable, Paleocene sole thrust. However, some indications exist for water transfers from the Lez aquifer system through the Montpellier fold

- West of the Montpellier fold. The low productivity of the Lutetian limestones near Montarnaud (south of the Viols-le-fort causse) suggests water transfer towards the south (J. Grevellec, personnal comm.). Conversely, the relatively high productivity of wells drilled within Lutetian limestones (Combe salinière wells near Gignac) and the relatively high flood discharge of a Jurassic limestone spring (Pradas spring near Saint-Bauzille-de-la-Sylve) compared to their supposed recharge area suggest a recharge from the northern karstified limestones,
- East of the Montpellier fold. The high productivity of the limestones series located South of the Montpellier fold ($400\,m^3\,h^{-1}$ pumping rate at the Crouzette well) indicates an exterior recharge. The positive temperature anomaly and high CO_2 pressure indicates deep or semi-deep water origin. Hydrochemistry and isotopic analysis suggest a connection with the Lez aquifer system [Joseph et al., 1987; Touet, 1987].

5.7 Conclusion

This chapter aimed at discussing the hydrodynamic functioning of the Lez karst hydrosystem, in view of the hybrid flow modelling. In the light of the elements presented, the main difficulties regarding the hybrid flow modelling of the Lez hydrosystem can be summarized as follows:

- partial knowledge of the boundary conditions of the system, in particular as regards flow through Montpellier fold,
- partial knowledge of the system recharge. Indeed, concentrated infiltration (in particular runoff infiltration through losses across the Corconne fault) is not quantified,
- lack of calibration data. Well head measurements can hardly be used as calibration variables. Indeed, both the absolute value and the variations of the hydraulic head are closely dependent on local settings (connectivity to the main drainage axis). These local connectivity variations do not match the scale of the hydrodynamic modelling of the system. On the other hand, discharge measurements are an adequate calibration variable but discharge monitoring data is available for only three of the main outlets of the system (Lez and Fontanilles springs).

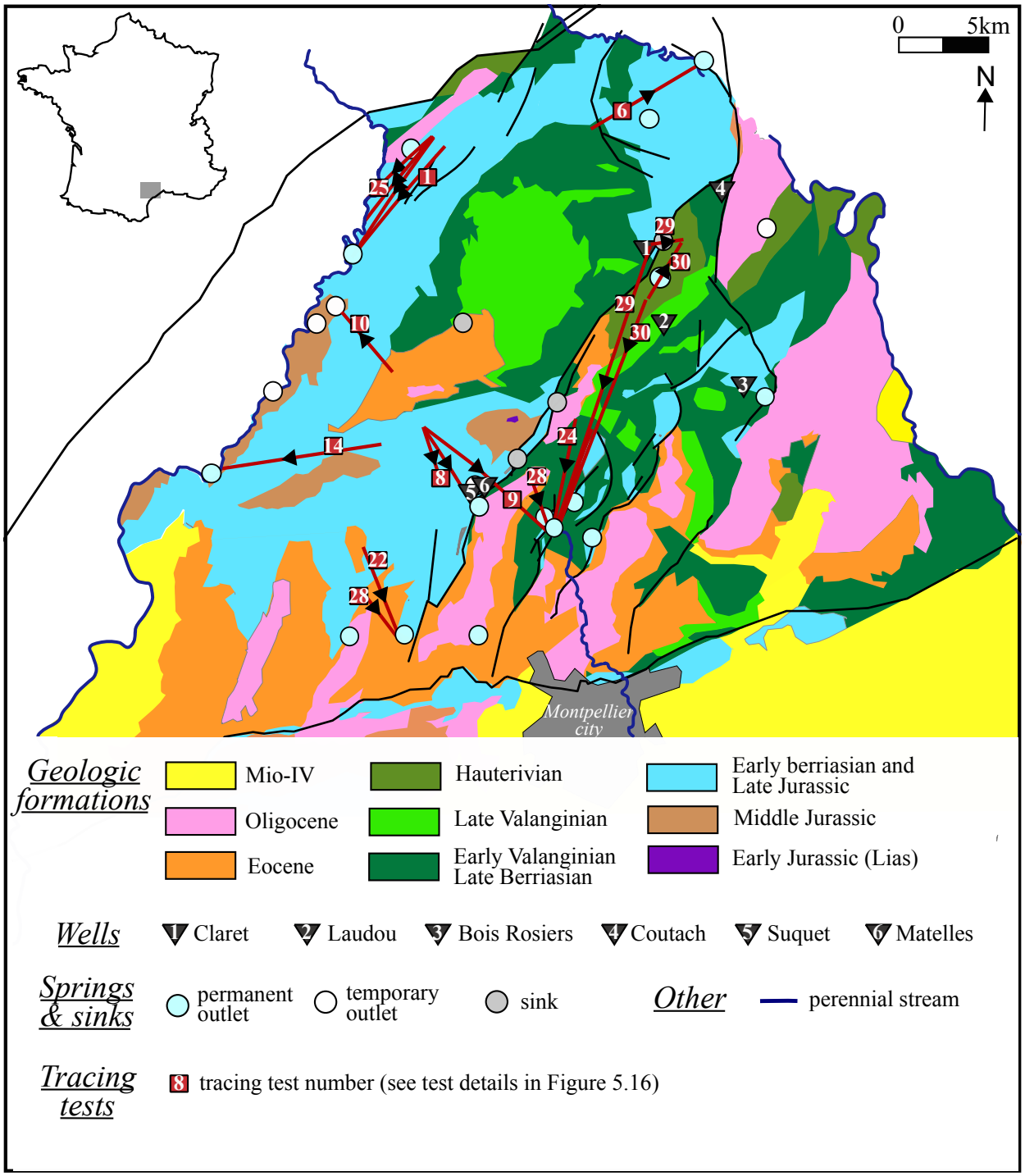

Figure 5.15: Schematic map of the Lez system: wells location and main dye tracing tests. See details of tracing tests in Figure 5.16.

		INJECTION SITE			POSITIVE SAMPLING POINT			NEGATIVE SAMPLING POINT
Reference	No	Date	Operator	Site	Site	Delay	Site	Delay	
[Schoen, 1999b; Durepaire, 1985]	1	03/04/71	Merle et Puig (CERH)	Montguilhem loss	Foux de Banal	21h			
[Paloc, 1966; Durepaire, 1985]	2	25/05/52	Bancal (GSG)	Trou de l'Olivier	Sourcettes spring	5d	Chataigners spring	13d	
					Triadou spring	105d	Vernede spring	537d	
[Durepaire, 1985]	3	29/08/54	Dubois (SCAL)	Trou de l'Olivier	Sourcettes spring	22d			
[Schoen, 1999b]	4	27/06/65	?	Hérault loss (Laroque)	Chataigners spring	216h			
[Paloc, 1966; Durepaire, 1985]	5	27/09/97	Martel	Tour de Molle cave	Sauve spring	1h20			
[Drogue, 1964; Durepaire, 1985]	6	14/10/62	Drogue (CERH)	Rieumassel loss	Sauve spring	12h			
[Durepaire, 1985]	7	15/04/68	SCAL	Fausse Monnaie cave	Source du Lez	27d			baraque shaft Lirou spring
[Durepaire, 1985]	8	14/09/69	Caumont / Gilles (CLPA)	Fausse Monnaie cave	baraque shaft	218h	Lez spring	10d	
							Lirou spring	10d	
[Selles, 2010]	9	20/04/10	HSM / CLPA	Fausse Monnaie cave	Source du Lez		Lirou spring	840h	
[Paloc, 1966; Durepaire, 1985]	10	08/11/64	Paloc (SCM)	Saint-Martin loss	Chataigniers spring	<140h	Fontanilles spring	<168h	
					Lez spring	648h			
[Schoen, 1999b; Durepaire, 1985]	14	23/03/69	Wienen	baume Vidal	Fontanilles spring				
[Paloc, 1966; Durepaire, 1985]	15	15/11/63	Paloc (SCM)	Lamalou loss	Fontanilles spring	28d	Lez spring		
[Durepaire, 1985]	16	09/05/77	Marjolet (CERH)		Lez spring	10,5d			
[Durepaire, 1985]	17	23/09/77	Marjolet (CERH)		Lez spring	5,2d			
[Durepaire, 1985]	18	18/04/62	Drogue (CERH)	Yorgues loss	Lez spring	58d			
[Paloc, 1966; Durepaire, 1985]	19	19/02/57	Guissart (SCM)	Brestalou de Claret loss	Viala spring	17h	Lez spring	312h (<15d)	
[Paloc, 1966; Durepaire, 1985]	20	07/03/59	Paloc	Brestalou de Claret loss	Viala spring	24h			
[Durepaire, 1985]	21	10/06/61	Dubois (SCAL)	Artigues stream loss n°1	Lez spring	2952h			
[Paloc, 1966; Durepaire, 1985]	22	15/01/63	Dorgue (CERH)	Saugras stream loss	Combaillaux spring (Montlobre)	10d			
[Durepaire, 1985]	23	02/02/64	Paloc (SCM)		Lez spring	14d	Fontanilles spring	14d	
[Fabris, 1970; Durepaire, 1985]	24	08/11/68	DROGUE - FABRIS	Terrieu loss	Lez spring	6d			
[Schoen, 1999b; Durepaire, 1985]	25	26/01/69	?	Triadou loss	Event 1 du Chemin	190h		740h	
					Mas de Banal spring	190h	Cayla spring	740h	
					Baoutes spring	740h			
[Durepaire, 1985]	26	09/03/72	Diluca / Salado (CERH)	Cantagrils loss	Montlobre spring	6d			
[Durepaire, 1985]	27	05/06/72	Marjolet (CERH)	Pouzet stream loss	Lez spring				
					Gour Noir spring		Fleurette spring		
[Schoen, 1999b]	28	26/01/73	?	Truc Peyrols	Montlobre spring		Lirou spring		
					Mosson river (Poujol)		Mas Gentil spring		
					Grabels spring		Siau spring = Aniane spring		
					Rieumassel spring				
					Puits de l'Aven				
[Durepaire, 1985]	29	10/04/76	Marjolet (CERH)	Brestalou de Claret loss	Lez spring	12d			
[Durepaire, 1985]	30	27/04/76	Marjolet (CERH)	Brestalou de Lauret loss	Lez spring	26d			

Figure 5.16: Dye tracing tests over the Lez karst system. In most cases, the procedure details (i.e., use of fluocaptors or spectral analysis) are unknown.

Name	Mean annual outtake
Lez spring	$1.1\,m^3\,s^{-1}$
Suquet well	$0.45\,m^3\,s^{-1}$
Fontbonne spring	$22\,l\,s^{-1}$

Table 5.2: Main outtakes from the Lez karst system.

Name	Q_{max}	Q_{mean}	Z (m ASL)	X (m)	Y (m)
Lez spring	$17\,m^3\,s^{-1}$	$2.2\,m^3\,s^{-1}$	65	721560	1858776
Lirou spring	$15\,m^3\,s^{-1}$	0 4 to $1.8\,m^3\,s^{-1}$	95	718493	1860111
Fontbonne spring	$3\,m^3\,s^{-1}$	$32\,l\,s^{-1}$	55	733669	1866205
Montlobre springs	$2\,m^3\,s^{-1}$		75 to 90	713692	1852687
Sauve spring*	$13\,m^3\,s^{-1}$	$1\,m^3\,s^{-1}$	94.5	729676	1883502
Vernède spring	$4\,m^3\,s^{-1}$		110	711563	1873153
Fleurette spring			64	723541	1857632
Fontanilles spring*	$12\,m^3\,s^{-1}$	$315\,l\,s^{-1}$	90	703766	1862096
Gour noir spring			64	723541	1858889
Restinclières spring		$501\,s^{-1}$	67	722119	1858322
Vabre spring			115	727415	1871375
Châtaigniers spring			120	710504	1870188
Cayla spring			133	709633	1869967
Vère spring			108	730132	1874786

Table 5.3: Characteristics of the main outlets of the Lez karst system: maximal (Q_{max}) and mean (Q_{mean}) discharge rate, altitude and extended Lambert II coordinates. *: main exsurgence.

5.8 References for Chapter 5

Abel, T., M. Hinderer and M. Sauter (2002). « Karst genesis of the Swabian Alb, south Germany, since the Pliocene ». In: *Acta Geologica Polonica* 52.1, pp. 43–54. See p. 128.

Alfares, W., M. Bakalowicz, R. Guerin and M. Dukhan (2002). « Analysis of the karst aquifer structure of the Lamalou area (Hérault, France) with ground penetrating radar ». In: *Journal of Applied Geophysics* 51, pp. 97–106. DOI: 10.1016/S0926-9851(02)00215-X. See pp. 5, 136.

Arthaud, F. and P. Laurent (1995). « Contraintes, déformation et déplacement dans l'avant-pays Nord pyrénéen du Languedoc méditerranéen ». In: *Geodinamica Acta* 8, pp. 142–157. See p. 126.

Arthaud, F. and M. Seguret (1981). « Les structures pyrénéennes du Languedoc et du Golfe du Lion (Sud de la France) ». In: *Bulletin de la Société Géologique de France* XXIII.7, pp. 51–63. See p. 126.

Arthaud, G. and P. Matte (1975). « Les décrochements tardi-hercyniens du Sud-Ouest de l'Europe. Géométrie et essai de reconstitution des conditions de la déformation ». In: *Tectonophysics* 25, pp. 139–171. DOI: 10.1016/0040-1951(75)90014-1. See p. 126.

Audra, P., L. Mocochain, H. Camus, E. Gilli, G. Clauzon and J. Bigot (2004). « The effect of the Messinian deep stage on karst development around the Mediterranean Sea. Examples from southern France ». In: *Geodinamica Acta* 17.6, pp. 389–400. DOI: 10.3166/ga.17.389-400. See p. 129.

Avias, J. (1988). *Rapport sur l'état des études entreprises sur la partie Est du causse de Viols-le-fort au 31 août 1988*. Tech. rep. CERGA. See p. 138.

— (1992*b*). *Suivi hydrogéologique de l'aquifère de la source du Lez - Rapport d'activité 1991*. Tech. rep. CERGA. See pp. 136, 138.

— (1995). « Gestion active de l'exsurgence karstique de la source du Lez ». In: *Hydrogéologie* 1, pp. 113–127. See pp. v, ix, xvii, 90, 93, 134.

Avias, J. and B. Legrand (1989). *Fonctionnement hydrogéologique, vulnérabilité et protection contre la pollution de l'aquifère de la source du Lez*. Rapport d'activité. CERGA. See p. 134.

Avias, J., B. Legrand, M Soulie and F. Touet (1984). *Fonctionnement hydrogéologique, vulnérabilité et protection contre la pollution de l'aquifère de la source du Lez*. Rapport d'activité. CERGA. See p. 138.

Bakalowicz, M. (1996). « Karst processes and the corresponding types of karst ». In: *Mémoires de la Société Géologique de France* 169, pp. 363–371. See p. 128.

Bakalowicz, M., R. Schoen, B. Ladouche, L. Aquilina and E. Petelet (1999). *Caractérisation du fonctionnement des systèmes karstiques nord-montpelliérains - Volume I - Contexte géologique et hydrogéologique*. Tech. rep. R40747. BRGM. URL: http://www.brgm.fr/Rapport?code=RR-40747-FR. See p. 128.

Bel, F. (1963). « Contribution à l'étude géologique et hydrogéologique de la région Sud-Ouest de Sommières ». PhD thesis. Université Montpellier II. See p. 126.

Benedicto, A., M. Séguret and P. Labaume (1999). « Tertiary Extension Within the Alpine Orogen ». In: ed. by B. Durand, L. Jolivet, F. Horvath and M. Séranne. Geological Society Special Publication. Chap. Interaction between faulting, drainage and sedimentation in extensional hanging-wall syncline basins: Example of the Oligocene Matelles Basin, Gulf of Lion margin (SE France), pp. 81–108. See pp. 139, 183.

Benedicto, E. A. (1996). « Modèles tectono-sédimentaires de bassins en extension et style structural de la marge passive du Golfe du Lion (partie Nord), Sud-Est France ». PhD thesis. Université Montpellier II. See p. 126.

Bergerat, F. (1987). « Stress field in the european platform at the time of Africa-Eurasia collision ». In: *Tectonics* 6.2, pp. 99–132. See p. 126.

Bicalho Caetano, C. (2010). « Hydrochemical characterization of transfers in karst aquifers by natural and anthropogenic tracers. Example of a Mediterranean karst system, the Lez karst aquifer (Southern France) ». PhD thesis. Agro Paris Tech. URL: http://pastel.archives-ouvertes.fr/pastel-00569544/fr/. See pp. 134, 136.

Bicalho Caetano, C., B.-G. Christelle, J.-L. Seidel, J.-D. Taupin, N. Patris, V. E. Sandra and H. Jourde (2011). « A conceptual model for groundwater circulation by using isotopic (δ^{18}O, δ^{2}H and ^{87}Sr/ ^{86}Sr) and geochemical tracers in a mediterranean karst system ». In: *Proceedings of the H_2Karst Conference held in Besançon, France (Sept. 1-3, 2011)*. URL: http://sites.google.com/site/h2karst/. See p. 136.

Boinet, N. (2002). *Inventaire spéléologique du Causse de l'Hortus. I. Le Causse de l'Hortus*. Ed. by CLPA. Bulletin Explokarst 4, p. 168. See pp. 126, 131.

Bosák, P. (2003). « Karst processes from the beginning to the end: How can they be dated ? » In: *Speleogenesis and Evolution of Karst Aquifers* 1.3, pp. 1–24. See pp. 2, 128.

Botton, R. (1984). « Étude de certaines modalités du fonctionnement de l'aquifère karstique (zone d'infiltration et zone saturée) sur deux champs de forages nord-montpelliérains ». PhD thesis. Université Montpellier II. See p. 134.

Camus, H. (1999). « L'organisation des réseaux de drainage à différents stades de l'évolution du paysage karstique de la bordure carbonatée sub-cévenole (de l'Aigoual à la basse vallée de l'Hérault) ». In: *Karst 99 - Livret guide des excursions Grands Causses - Vercors*. Ed. by Y. Perrette and J.-J. Delannoy. Cahiers savoisiens de Géographie, pp. 55–74. See p. 124.

— (2003). « Vallées et réseaux karstiques de la bordure carbonatée sud-cévenole : Relations avec la surrection, le volcanisme et les paléoclimats ». PhD thesis. Université Bordeaux III. See pp. 5, 124.

Chaussard, D. (2005). « L'aquifère karstique de la source du Lez ». MA thesis. Université de Paris-Sud XI. See p. 136.

Chemin, J. (1974). « Essai d'application d'un modèle mathématique conceptuel au calcul du bilan hydrique de l'aquifère karstique de la source du Lez ». PhD thesis. Université Montpellier II. See pp. 133, 136, 140.

Combes, P. J., B. Peybernes, M. J. Fondecave-Wallez, M. Seranne, J. L. Lesage and H. Camus (2007). « Latest-Cretaceous/Paleocene karsts with marine infillings from Languedoc (South of France): Paleogeographic, hydrogeologic and geodynamic implications ». In: *Geodinamica Acta* 20.5, pp. 301–326. DOI: 10.3166/ga.20.301-326. See p. 128.

Combes, P. (1990). « Typologie, cadre géodynamique et génèse des bauxites françaises ». In: *Geodynamica Acta* 4, pp. 91–109. See p. 126.

Conroux, Y. (2007). « Caractérisation du fonctionnement hydrodynamique de l'aquifère karstique du Lez (Hérault) à l'état naturel ». MA thesis. Université d'Avignon et des pays de Vaucluse. See p. 136.

Diluca, J. (1973). « Contribution à l'étude hydrogéologique de la région de Montarnaud-Grabels-les Matelles ». PhD thesis. Université Montpellier II. See pp. 133, 141.

Drogue, C. (1969). « Contribution à l'étude quantitative des systèmes hydrologiques karstiques d'après l'exemple de quelques karst périméditerranéens ». 482p. PhD thesis. Université Montpellier II. See pp. 124, 131, 133, 134, 136, 138, 140, 141, 182, 183.

Drogue, C. and J. Puech (1968). « Reconnaissances géologiques et hydrogéologiques pour la construction de barrages en terrains calcaires. Exemple des barrages écrêteurs de crues du Haut-Vidourle (Gard, France) ». In: *Terres et Eaux* 57, pp. 10–22. See p. 131.

Durand, V. (1992). « Structure d'un massif karstique. Relations entre déformations et facteurs hydro-météorologiques. Causse de l'Hortus ». PhD thesis. Université Montpellier II. See p. 132.

Durand, V., V. Léonardi, B. Deffontaines and J. Macquar (2009). « Fluid transfers in a carbonate-gaseous aquifer through the local tectonic and geodynamic history ». In: *Journal of the Geological Society* 166.4, pp. 643–654. DOI: 10.1144/0016-76492008-113. See pp. 126, 128.

Durepaire, P. (1985). *Inventaire et étude géologique, hydrologique et géomorphologique détaillés des cavités naturelles du bassin d'alimentation de la source du Lez (Hérault). I - Texte*. Mémoire XXV. CERH. See p. 134.

Dörfliger, N., P. Le Strat and P. Fleury (2008). *Caractérisation géologique et hydrogéologique des aquifères carbonatés karstiques sous couverture. Rapport d'avancement*. Tech. rep. BRGM/RP-56375-FR. BRGM. URL: http://www.brgm.fr/Rapport?code=RR-56375-FR. See pp. 126, 128.

Fabris, H. (1970). « Contribution à l'étude de la nappe karstique de la source du Lez ». PhD thesis. Université Montpellier II.

Ford, D. and P. Williams (2007). *Karst Geomorphology and Hydrology*. [Revised Edition]. Unwin Hyman (London and Boston), p. 601. ISBN: 0045511055. URL: http://eu.wiley.com/WileyCDA/WileyTitle/productCd-0470849967.html. See pp. v, vii, xvii, 128.

Guennoc, P., C. Gorini and A. Mauffret (2000). « Geological history of the Gulf of Lions: mapping the Oligocene-Aquitanian rift and Messinian surface ». In: *Géologie de la France* 3, pp. 67–97. See p. 126.

Guilbot (1975). « Modélisation des écoulements d'un aquifère karstique (liaisons pluie/débit). Applications aux bassins de Saugras et du Lez ». PhD thesis. Université Montpellier II. See p. 133.

Guiot, D., F. Roure, S. Elmi, D. Lajat and M. Steinberg (1991). « Découverte d'accidents distensifs majeurs d'âge Jurassique sur la marge continentale du bassin du sud-est, Ardèche, France ». In: *Compte Rendu de l'Académie des Sciences de Paris* 312, pp. 747–754. See p. 126.

Husson, E. (2010). « Remplissages karstiques et variations du niveau de base: Exemple des paléokarsts de la région de Ganges (34) ». MA thesis. Université Montpellier II. URL: http://www.gm.univ-montp2.fr/spip/IMG/pdf/Husson_memoire_2010.pdf. See pp. 128, 129.

Hébrard, O., S. Pistre, N. Cheynet, J. Dazy, C. Batiot-Guilhe and J.-L. Seidel (2006). « Origine des eaux des émergences karstiques chlorurées du Languedoc-Roussillon ». In: *Comptes Rendus Géoscience* 338, pp. 703–710. DOI: 10.1016/j.crte.2006.04.018. See p. 134.

Joseph, C., B Donville, M Soulie and F. Touet (1987). « Utilisation du traçage isotopique naturel de l'azote 15 pour la mise en évidence de mélanges dans les aquifères complexes ». In: *Symposium IAEA-Unesco*. Vienne. See p. 141.

Jourde, H., A. Lafare and N. Mazzilli (2011). « Flash flood mitigation in a karst catchment as a positive consequence of anthropogenic forcings on the groundwater resource ». In: *Proceedings of the H_2Karst Conference held in Besançon, France (Sept. 1-3, 2011)*. URL: http://sites.google.com/site/h2karst/. See p. 134.

Karam, Y. (1989). « Essais de modélisation des écoulements dans un aquifère karstique. Exemple de la source du Lez (Hérault - France) ». PhD thesis. Université Montpellier II. See p. 138.

Ladouche, B., N. Dörfliger, R. Pouget, V. Petit, D. Thiéry and C. Golaz (2002). *Caractérisation du fonctionnement des systèmes karstiques nord-montpelliérains - Rapport du programme 1999-2001-Buèges*. Tech. rep. BRGM/RP-51584-FR. BRGM. URL: http://www.brgm.fr/Rapport?code=RR-51584-FR. See p. 140.

Lafare, A. (2007). « Etude du comportement hydrodynamique de l'aquifère karstique de la source du Lez lors d'évènements de crue par une approche hydrologique, hydrogéologique et hydrochimique ». MA thesis. Université Montpellier II. See pp. 134, 136.

Léonardi, V., G. Tissier and H. Jourde (2011). « The relative importance of different karstogenesis phases on the flow path network organization in a Mediterranean karst system ». In: *Proceedings of the H_2Karst Conference held in Besançon, France (Sept. 1-3, 2011)*. URL: http://sites.google.com/site/h2karst/. See pp. 126, 128.

Marjolet, G. and J. Salado (1976). « Étude des écoulements dans les calcaires karstifiés du site du futur captage des eaux de la source du Lez. I. Aspect hydrochimique, II. Aspect hydrodynamique ». PhD thesis. Université Montpellier II. See pp. 124, 134, 136.

Mauffret, L. and M. Gennesseaux (1989). « Compression, décrochements et distension sur le pourtour méditerranéen Nord occidental ». In: *Comptes Rendus de l'Académie des Sciences - Série IIA* 308.10, pp. 961–967. See p. 126.

Mocochain, L., G. Clauzon, J.-Y. Bigot and P. Brunet (2006). « Geodynamic evolution of the peri-Mediterranean karst during the Messinian and the Pliocene: Evidence from the Ardèche and Rhône valley systems canyons, southern France ». In: *Sedimentary Geology* 188-189, pp. 219–233. DOI: 10.1016/j.sedgeo.2006.03.006. See p. 129.

Olivet, J. (1996). « La cinématique de la plaque Ibérie ». In: *Bulletin des Centres de Recherche Exploration-Production Elf-Aquitaine* 20, pp. 131–195. See p. 126.

Paloc, H. (1967). *Carte hydrogéologique de la France. Région karstique nord-montpelliéraine. Notice explicative*. BRGM. Paris.

Perriquet, M. (2006). « Caractérisation de la structure et du fonctionnement du système karstique du Lez en gestion active - Effet des pompages sur la source ». MA thesis. Université d'Avignon et des pays du Vaucluse. See p. 136.

Poty, F. (1998). « Contribution à la connaissance des populations bactériennes et de leur transfert dans les aquifères karstiques ». PhD thesis. Université Montpellier II. See p. 131.

Rambal, S., F. Mouillot and J.-P. Ratte (2009). « Entre Terre et Mer : Pour une Approche Intégrée de la Zone Côtière du Golfe du Lion ». In: ed. by Quae. Chap. Végétation méditerranéenne et cycle de l'eau. See p. 129.

Roesch, A. and H. Jourde (2006). « Incidence d'une gestion active de la ressource en eau en milieu karstique sur le risque hydrologique. Exemple du fleuve Lez (Montpellier, France) ». In: *Proceedings of the 1st GIRE3D Conference held in Marrakech, Morocco (May 23-25, 2006)*. Comité Marocain de l'AIH. See pp. 96, 134, 136.

Salado, J. and G. Marjolet (1975). *Contribution à l'étude de l'aquifère karstique de la source du Lez (Hérault): Étude du chimisme des eaux de la source du Lez et de son bassin*. Tech. rep. IX(II). CERGA. See p. 135.

Schoen, R., B. Ladouche, J. Cubizolles, L. Aquilina and M. Bakalowicz (1999*a*). *Caractérisation du fonctionnement des systèmes karstiques nord-montpelliérains - Volume II - Moyens mis en oeuvre*. Tech. rep. R40748. BRGM. URL: http://www.brgm.fr/Rapport?code=RR-40748-FR. See p. 140.

Schoen, R., M. Bakalowicz, B. Ladouche and L. Aquilina (1999*b*). *Caractérisation du fonctionnement des systèmes karstiques nord-montpelliérains - Volume III - Interprétation des données hydrologiques*. Tech. rep. R40939. BRGM. URL: http://www.brgm.fr/Rapport?code=RR-40939-FR.

Selles, A. (2010). « Caractérisation du transfert de masse en domaine karstique. Réalisation et interprétation d'un traçage artificiel au sein d'un aquifère karstique (Aumelas-Thau, France) ». MA thesis. Université Montpellier II.

Suc, J. P., J. M. Rouchy, M. Ferrandini and J. Ferrandim (2007). « The Messinian salinity crisis revisited ». In: *Geobios* 40.3, pp. 231–232. DOI: 10.1016/j.geobios.2007.03.001. See p. 129.

Séranne, M., H. Camus, F. Lucazeau, J. Barbarand and Y. Quinif (2002). « Polyphased uplift and erosion of the Cevennes (southern France). An example of slow morphogenesis ». In: *Bulletin de la Société Géologique de France* 173.2, pp. 97–112. See pp. 126, 128.

Séranne, M., H. Camus, P. Combes, B. Peybernès and M. Fondecave-Wallez (2009). « Géodynamique du bassin du Sud-Est et karstifications: Conséquences sur les réservoirs carbonatés ». In: *Conference Bassins sédimentaires français : Actualité de la connaissance, held in Rueil-Malmaison, France (March 03, 2009)*. Section Exploration-Gisements de l'AFTP. See p. 128.

Tissier, G. (2009). « Hiérarchisation des écoulements souterrains dans le bassin du Lez ». MA thesis. Université Montpellier II. See pp. 126, 128, 129.

Touet, F. (1987). « Détermination de l'origine des ressources en eau captées en bordure sud du pli de Montpellier entre Montpellier et Vendargues (Hérault) ». PhD thesis. Université de Paris XI. See p. 141.

Vasseur, F. (2006). « Plongées 1998 - 2005 dans le Vidourle souterrain ». In: *Le Fil - Bulletin de Liaison de la Commission Nationale de Plongée Souterraine* 16, pp. 25–31. URL: http://cnps.plongeesouterraine.org/uploads/FICHIERS/PUBLICATIONS/LE%20FIL/Fil_16.pdf. See p. 131.

Vaute, L., C. Drogue, L. Garrelly and M. Ghelfenstein (1997). « Relations between the structure of storage and the transport of chemical compounds in karstic aquifers ». In: *Journal of Hydrology* 199.3-4, pp. 221–238. DOI: 10.1016/S0022-1694(96)03245-3. See pp. 131, 138.

Weng, P. and N. Dörfliger (2002). *Projet PACTES. Module: Contribution des eaux souterraines aux crues et inondations; site de l'Hérault*. Tech. rep. BRGM/RP-51718-FR. BRGM. URL: http://www.brgm.fr/Rapport?code=RP-51326-FR. See p. 131.

Chapter 6

Model setup and calibration

This chapter presents the distributed, hybrid flow model setup and the calibration results for the steady and transient states. This hybrid model will be used as a basis for both the verification of the analytical results and the empirical approach in chapter 7.

Contents

6.1 Model setup

The model is developed using the proprietary code FEFLOW (Finite Element subsurface FLOW system) [Diersch, 1998*a*]. The karst drainage network is represented by one-dimensional discrete elements that are coupled to a three-dimensional matrix system representative of the fractured blocks, assuming continuous hydraulic heads. Only the main drainage networks (and drainage outlets) have been taken into account.

6.1.1 Model geometry

The model covers a 1110 km^2 area that extends between the Cevennes fault at the North, the Montpellier fold at the South and the Hérault and Vidourle rivers at the West and at the East respectively. The 3-D geological modelling was conducted using the GMS software [Owen et al., 1996]. The following geological units are represented in the 3-D geological model (from top to bottom) (see Table 5.3 and see model views in Figure 6.1):

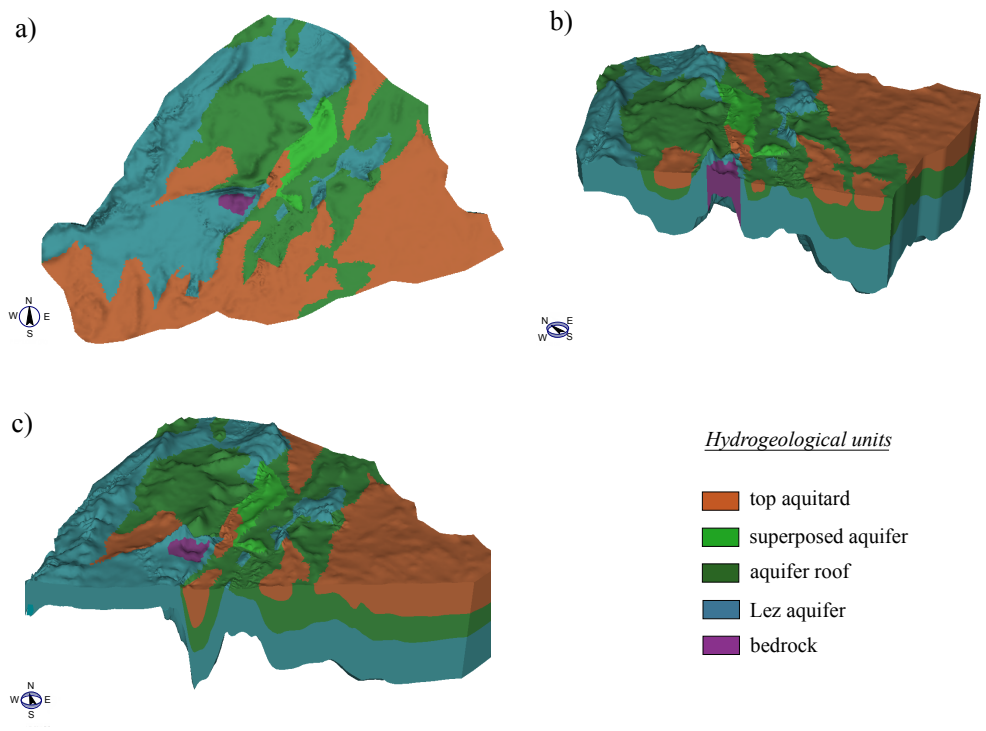

Figure 6.1: Model geometry: a) plan view, b-c) cross sections of the hydrogeological units..

- the "top aquitard" comprises the Hauterivian to Quaternary units. The aquifer properties of the Late Hauterivian and Lutetian units which are poorly connected to the Lez aquifer are neglected in this analysis,
- the "superposed aquifer" comprises the Late Valanginian to Late Hauterivian formations from the Sauteyrargues syncline. The aquifer properties of the Hortus causse and Liouc basin are not considered,
- the "aquifer roof" corresponds to the Early Valanginian marly unit,
- the "Lez aquifer" comprises the Late Jurassic and Early berriasian units. The lower, Middle Jurassic unit (partially separated from the Late Jurassic unit by the oxfordo-callovian serie) is neglected in this approach. Note that the Sauteyrargues syncline, "superposed aquifer formation" is connected to the "Lez aquifer" formation through the Corconne fault.

The "Lez aquifer" unit is divided into two units:

- an "epikarstic" unit with increased hydraulic conductivity,
- a "deep aquifer" unit.

6.1.2 Flow equations

Flow within the matrix. The flow within the fissured and porous matrix is modeled by the empirical[1] Darcy's law

$$\mathbf{v} = -\mathbf{K}\nabla H \tag{6.1}$$

where $\mathbf{v}$ [LT^{-1}] is the Darcy's velocity, $\mathbf{K}$ [LT^{-1}] is the tensor of hydraulic conductivity and H [L] is the hydraulic head.

1. the Darcy's law can also be derived based on the Navier-Stokes equation, assuming that the drag term of momentum exchange at the fluid/solid interface can be derived as a linear friction relationship, and provided that the inertial effects and the drag forces due to fluid viscosity be negligible [Neuman, 1977].

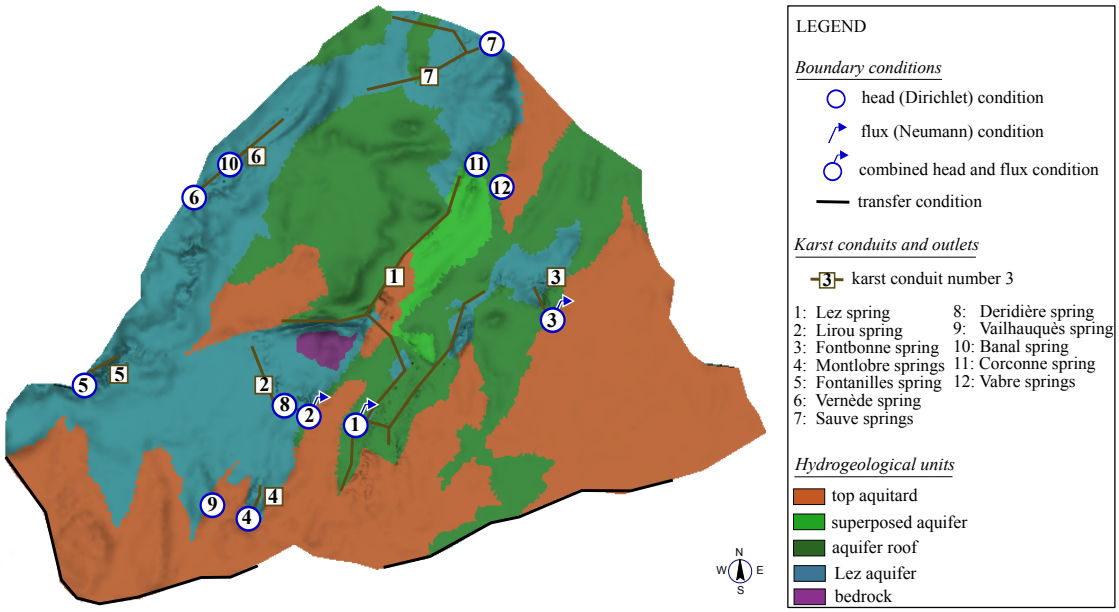

Figure 6.2: Model setup. Mesh, boundary conditions (also see Table 6.3) and modeled karst conduit network.

Flow within the conduits. The flow within the karst conduits is modeled using the diffusive wave approximation of the Saint-Venant equations. The Saint-Venant equations are partial differential equations based on the conservation of mass and momentum that are commonly used to describe the flow of water in open channels [Chow, 1959]. For low to moderate flow regimes, the inertial terms can be neglected compared with the gravitational terms, the friction and the pressure effects. Furthermore, the interior viscous effects and the shear effect at the fluid/air interface can be neglected over the shear stress effects at the fluid/rock interface. The 1-D diffusive wave approximation can be formulated as

$$\mathbf{v} = -K\nabla\mathbf{H} \tag{6.2}$$

where

$$K = \frac{Mr^{2/3}}{\sqrt{\|\nabla H\|}} \tag{6.3}$$

and M [$L^{-1/3}T$] is the Manning-Strickler friction factor, r [L] is the hydraulic radius, defined as the flow cross-sectional area divided by the wetted perimeter.

The 1-D discrete finite elements that represent the karst conduits are considered as fully saturated, and they are switched off as soon as one node becomes dry (hydraulic head lower than the node elevation).

Coupling between the matrix and the conduits. The coupling between the matrix and conduit systems is established assuming continuous heads [Diersch, 2005]. The 1-D conduits provide an alternative flow path to the matrix.

6.1.3 Modelled karst conduit network

The modelled karst conduits and karst outlets are presented in Figure 6.2. The karst conduits elements are located indepth within the Lez aquifer formation, at the interface between the "epikarst" and the "deep aquifer" units.

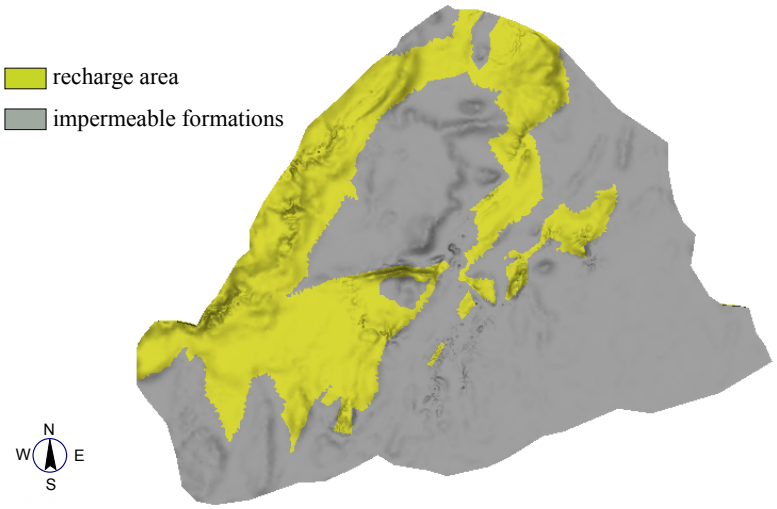

Figure 6.3: Model geometry: recharge (yellow) and impermeable (grey) areas.

6.1.4 Recharge and boundary conditions

The recharge is modelled as diffuse. The concentration of the infiltration is ensured by the high-conductivity "epikarst" unit as proposed by Kiraly, 1998. Rainfall over the impervious formations is taken equal to zero (see Figure 6.3). Concentrated infiltration from runoff over the impervious formations is neglected.

Karst outlets are modelled as a head boundary condition combined with a constraint condition of minimum flux. The hydraulic head is set equal to the spring outflow level as long as the associated calculated flux is positive (i.e., exiting the system). When the calculated flux is negative, the boundary condition switches to a zero-flux condition. The flux condition is turned again into a fixed head condition when the calculated hydraulic head reaches the spring outflow level. When the karst outlet is used for water supply, the minimum flux is taken equal to the spring pumping rate. The boundary conditions are summarized in Table 6.1.

Drainage through the Montpellier fold is modelled considering a transfer flow condition (see Figure 6.2). The parameters associated with the transfer boundary condition are calibrated during the steady-state simulations.

6.1.5 Numerical setting

A mesh of 550000 tetrahedral elements is generated automatically by means of the triangle [Shewchuk, 1996] algorithm. The mesh is refined around the discrete features elements (see Figure 6.4). Element sizes range from 30 to 300m. The resulting mesh is smoothed using a uniform laplacian operator.

The flow equations are solved based on a Galerkin finite element numerical approach (nodal basis function taken identical to the test function used in the weak formulation), with the algebraic multigrid SAMG solver [Stüben et al., 2003].

6.1.6 Short conclusion

The model proposed above is a simplified representation of the Lez aquifer. Major simplifications and their consequences are worth emphasizing here.

i) The fact that concentrated infiltration from runoff is not taken into account means that the recharge of the system during high water level periods may ben underestimated: as an example,

Outlet	Head condition	Flux constraint ($m^3 s^{-1}$)
1- Lez spring	65m ASL	1.10
2- Lirou spring	90m ASL	0.45
3- Fontbonne spring	55m ASL	0.03
4- Montlobre spring	85m ASL	0
5- Fontanilles spring	90m ASL	0
6- Vernède spring	110m ASL	0
7- Sauve spring	94.5m ASL	0
8- Deridière spring	132m ASL	0
9- Vailhauquès spring	167m ASL	0
10- Banal spring	140m ASL	0
11- Corconne spring	132m ASL	0
12- Vabre spring	108m ASL	0

Table 6.1: Boundary conditions and constraints associated with the karst outlets. The head condition is related to the spring overflow level. The flux constraint is related to pumpings performed within the karst conduit.

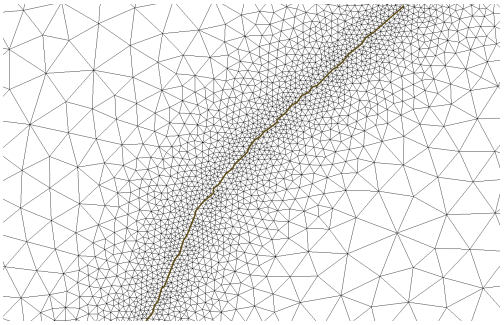

Figure 6.4: Mesh refinement around the conduit network. Element sizes range from 30m around the karst conduits to an average size of 300m.

the contribution of the water flowing out of the Hortus causse towards the recharge area of the Lez aquifer is neglected.

ii) The fact that the karst conduit network is represented by its main conduits and outlets only is expected to yield increased spring discharges at the different outlets of the aquifer compared to reality. This bias may be enhanced during flood events when a number of temporary outlets get active. As an example, the low number of modelled outlets along the Herault river is expected to be associated with an increased discharge of the outlets that are accounted for by the model (Vernède, Uglas, Fontanilles springs).

iii) The limited heterogeneity of the proposed model means that the well head measurements cannot be used for the model calibration. Indeed, both the water level absolute value and the water level variations are closely dependent on local settings (connectivity to the main drainage axis). As a consequence, calibration will be carried out against discharge measurements only.

Note that the effects described in items (i) and (ii) are antagonistic.

Compared to the global model proposed in Chapter 4, the proposed distributed, hybrid flow model is meant to:

- give insights into the distribution of the recharge between the different karst subsystems and the spatial distribution of the groundwater resource,
- test assumptions on the geometry of the system (geological structure and connectivity between the hydrogeological units),
- test assumptions on the boundary conditions of the Lez aquifer (water transfer through the Montpellier fold in particular).

6.2 Steady-state calibration

6.2.1 Aim of the steady-state calibration

The steady-state calibration is intended to yield first estimates of

1. the hydrodynamic properties of the various hydrogeological units (effective hydraulic conductivity),
2. the hydrodynamic properties of the karst conduits (effective cross-section area),
3. the order of magnitude of the transfer boundary condition associated with the Montpellier fold (boundary head and out transfer rate).

The roughness coefficient, length and location of the karst conduits are not taken as calibration parameters. The calibration is carried out against the mean annual discharges values of the main karst springs. Note that the lack of physical realism associated with steady-state calibration is especially critical for temporary, overflow springs. However, the steady-state calibration is only intended to yield a rough approximation of the hydrodynamic properties of the karst aquifer and of the boundary conditions.

6.2.2 Steady-state recharge and boundary conditions

Steady-state recharge. The steady-state recharge is determined using the mean rainfall rate over the october 1998 to october 2008 period. Thirteen rain gauges are used for the analysis (see raingauges location and rainfall distribution in Figure 5.4b and see mean annual rainfall rate in Table 5.1). A mean annual 450 mm evapotranspiration is substracted to the raw rainfall (see Section 5.3). The recharge is set to zero over the impermeable formations.

Steady-state boundary conditions. The boundary conditions associated with the karst outlets are summarized in Table 6.1 and Figure 6.2. The parameters of the transfer condition associated with the Montpellier fold are deduced from the calibration.

6.2.3 Steady-state calibration results

The field of simulated hydraulic heads within the Jurassic formations are shown in Figure 6.5 and the simulated discharge rates are given in Table 6.2. The parameters associated with the transfer boundary conditions are given in Table 6.3. The roughness coefficient of all conduits is set equal to $30 \mathrm{m}^{1/3}\mathrm{s}^{-1}$ as proposed by Jeannin and Maréchal, 1995. The calibrated karst conduits sections are presented in Table 6.5.

Outlet	Discharge ($\mathrm{m}^3\,\mathrm{s}^{-1}$)
Lez spring	2.03
Lirou spring	0.48
Fontbonne spring	0.20
Montlobre spring	0.15
Fontanille spring	0.50
Vernède spring	0.49
Sauve spring	0.66
West Montpellier fold	0.42
East Montpellier fold	0.07

Table 6.2: Steady-state calibration results: mean annual discharge rate.

Boundary	Head	Out transfer rate
West Montpellier fold	75m ASL	$43\,\mathrm{m\,s^{-1}}$
East Montpellier fold	60m ASL	$43\,\mathrm{m\,s^{-1}}$

Table 6.3: Steady-state calibration results. Parameters for the boundary conditions associated with the Montpellier fold.

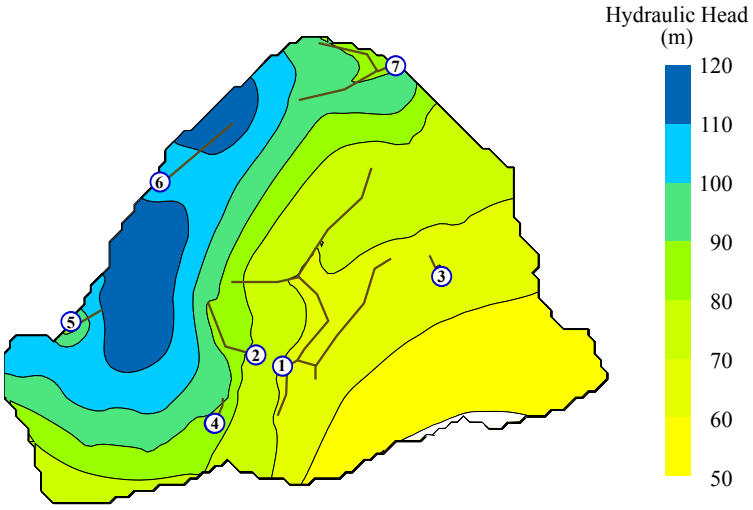

Figure 6.5: Steady-state calibration results. Hydraulic head within the Jurassic formations. Only the active outlets are featured on the map. See reference for conduit number in Figure 6.2.

Unit	Effective hydraulic conductivity ($\mathrm{m\,s^{-1}}$)
top aquitard	10^{-8}
superposed aquifer	10^{-5}
roof	10^{-8}
Lez aquifer "epikarstic" layer	5×10^{-5}
Lez aquifer	10^{-5}

Table 6.4: Steady-state calibration results: effective hydraulic conductivity.

Conduit number	Effective conduit section ($\mathrm{m^2}$)
1 - Lez system	4
2 - Lirou system	3
3 - Fontbonne system	0.5
4 - Montlobre system	1
5 - Fontanilles system	1
6 - Vernède system	1
7 - Sauve system	1

Table 6.5: Steady-state calibration results: effective conduit section. See reference for conduit number in Figure 6.2.

6.3 Transient-state simulation

6.3.1 Recharge estimation

Principle. Thirteen Météo-France raingauge stations are used for the calculation of the recharge (see coordinates in Table 5.1). The recharge is computed based on daily raingauge data as follows:

1. the gaps in the raingauge data are filled using a multi-linear regression method,
2. the daily potential evapotranspiration (PET) is estimated based on the Hargreaves formula [Hargreaves, 1994; Hargreaves and Samani, 1985],
3. the daily evapotranspiration ET is estimated as a fraction of the daily PET,
4. the recharge (effective rainfall) is computed for each raingauge station as the difference between rainfall and evapotranspiration,
5. the recharge is interpolated over the whole simulation area based on the effective rainfall calculated at the raingauge stations and it is set equal to zero over the area covered by impervious formations.

Steps 1 to 3 are detailed below.

Station name	gap length (d)	R^2 statistic	error variance	negative values before correction
Saint-Hippolyte-du-fort	339 d	0.88	15 mm^2	16
Montpellier	31 d	0.87	15 mm^2	9

Table 6.6: Reconstruction of the rainfall time series: number of missing data and characteristics of the regression. Total length of the time series: 3654 d (october 1998 to october 2008 data).

Gap-filling missing rainfall data. The gaps in the rainfall time series of the "Montpellier" and "Saint-Hippolyte-du-fort" stations are filled using a multi-linear regression technique (see gaps length in Table 6.6). The technique is based on the assumption that the rainfall $R_i(t)$ recorded at station i at time t may be expressed as the weighted sum of the rainfall recorded at the other stations :

$$R_i(t) = \sum_{\substack{j=1 \\ j \neq i}}^{n} \alpha_j R_j(t) \tag{6.4}$$

where n is the number of stations. The weights are determined by means of a multi-linear regression on the gap-free part of the data. Missing values are then estimated based on equation (6.4). All negative reconstructed rainfall values are set equal to zero. The quality of the data reconstruction may be estimated based on the characteristics of the regression over the gap-free part of the data (see Table 6.6 and see Figure 6.6).

Estimation of the reference evapotranspiration. The daily potential evapotranspiration (PET) is estimated based on the Hargreaves formula [Hargreaves, 1994; Hargreaves and Samani, 1985]

$$\mathrm{PET} = 0.0023(\overline{T} + 17.8)\sqrt{T_{\max} - T_{\min}} R_a \tag{6.5}$$

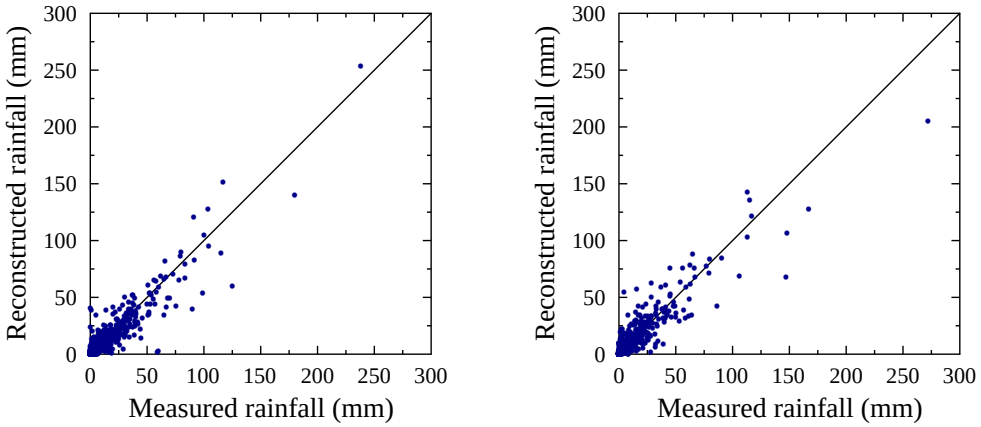

Figure 6.6: Patching of the rainfall data. Scatter plots of measured against regression-based rainfall at: a) Saint-Hippolyte-du-fort and, b) Montpellier.

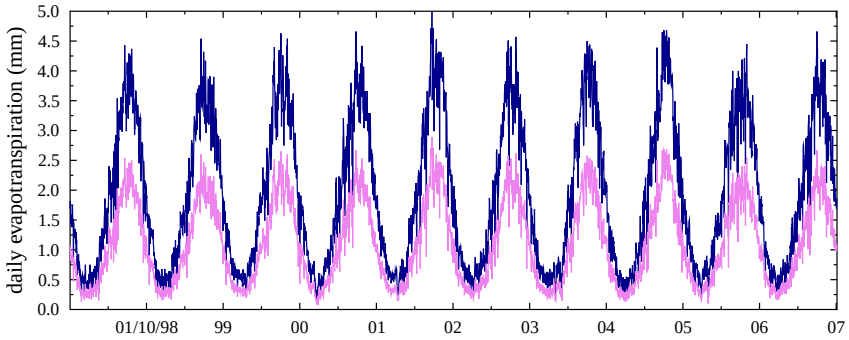

Figure 6.7: Reference (blue) and actual (purple) evapotranspiration based on Hargreaves calculation [Hargreaves, 1994]. The actual evapotranspiration is taken equal to a $\alpha = 57\%$ of the reference evapotranspiration.

where $\overline{T}$, $T_{\max}$ and $T_{\min}$ are the mean, maximal and minimal daily temperatures (°C) and R_a is the extraterrestrial radiation [1] (expressed here as equivalent evaporation: mm/d).

Estimation of the actual evapotranspiration. The actual evapotranspiration (ET) is assumed to be a fraction of the PET

$$\mathrm{ET} = \alpha \mathrm{PET} \tag{6.10}$$

where the coefficient α is assumed to be time-independant. The coefficient α is set so that the cumulative annual ET is approximately 450 mm. The reference and actual evapotranspiration time series are shown in Figure 6.7.

1. The extraterrestrial radiation is calculated based on [Allen et al., 1998]

$$R_a = 0.408 \frac{G_{sc} D}{\pi} [w \sin(\phi)\sin(\delta) + \cos(\phi)\cos(\delta)\sin(w)] \tag{6.6}$$

$$\delta = 0.4093 \sin\left(\frac{2\pi n}{365 - 1.405}\right) \tag{6.7}$$

$$w = \mathrm{acos}[-\tan(\phi)\tan(\delta)] \tag{6.8}$$

$$D = 1 + 0.033 \cos\left(\frac{2\pi n}{365}\right) \tag{6.9}$$

where G_{sc} is the solar constant ($G_{sc} = 118 MJ\,m^{-2}\,d^{-1}$), ϕ is the latitude (rad), δ is the solar declination (rad), D is the inverse of the relative Earth-Sun distance (/m), w is the sunset hour angle (rad) and n is the number of the day in the year. The factor 0.408 in equation (6.6) allows the conversion to equivalent evaporation units.

6.3.2 Initial conditions

The initial value of the hydraulic head field is derived as follows

1. a factor k is applied to the recharge distribution of the steady-state model. k is calibrated empirically so that the simulated water level of the Lez spring matches the water level measured at the beginning of the transient-state calibration,
2. the potential head distribution from the steady state model is used as input for the transient model.

6.3.3 Storage properties

The storage properties used for the transient state simulation are indicated in Table 6.7.

Variable	Unit	Value
Specific yield	aquitard units	2%
Specific yield	aquifer units	0.2%
Specific storage	aquitard units	10^{-5} m^{-1}
Specific storage	aquifer units	10^{-6} m^{-1}

Table 6.7: Transient-state simulation. Storage properties.

6.3.4 Transient-state simulation results

The simulation starts on January 28, 1999. Figure 6.8 and Figure 6.9 show the hydraulic head and the discharge simulated at the main outlets. Table 6.8 indicates the average discharge rate and the ratio of the outflow of the main sub-systems to the total model outflow (August 1999 - August 2000 period). Figure 6.10 compares the simulation results to the measured hydraulic head and discharge rate at the Lez spring. Note that the sensitivity of the model output to the initial hydraulic head condition and to the hydrodynamic parameters will be investigated in Chapter 7.2.2.a.

The main differences to the observed behaviour of the Lez aquifer are the following:

– underestimation of the peak flow discharge for the Lirou and Lez springs, and also probably at the Fontanilles and the Sauve springs (Figures 6.8 and 6.9),

System	Mean discharge (m^3/s)	Outflow ratio
Lez	2.03	39%
Lirou	0.57	11%
Fontbonne	0.21	4%
Montlobre	0.19	4%
Fontanilles	0.57	11%
Vernède	0.47	9%
Sauve	0.60	12%
West Montpellier fold	0.43	8%
East Montpellier fold	0.08	2%

Table 6.8: Simulation results for the transient state simulation. Simulated average discharge rate and ratio of the average discharge rate to the total model outflow, over the Aug. 99 - Aug. 00 period. Over that period the mean outflow measured at the Lez spring is 1.7m^3/s.

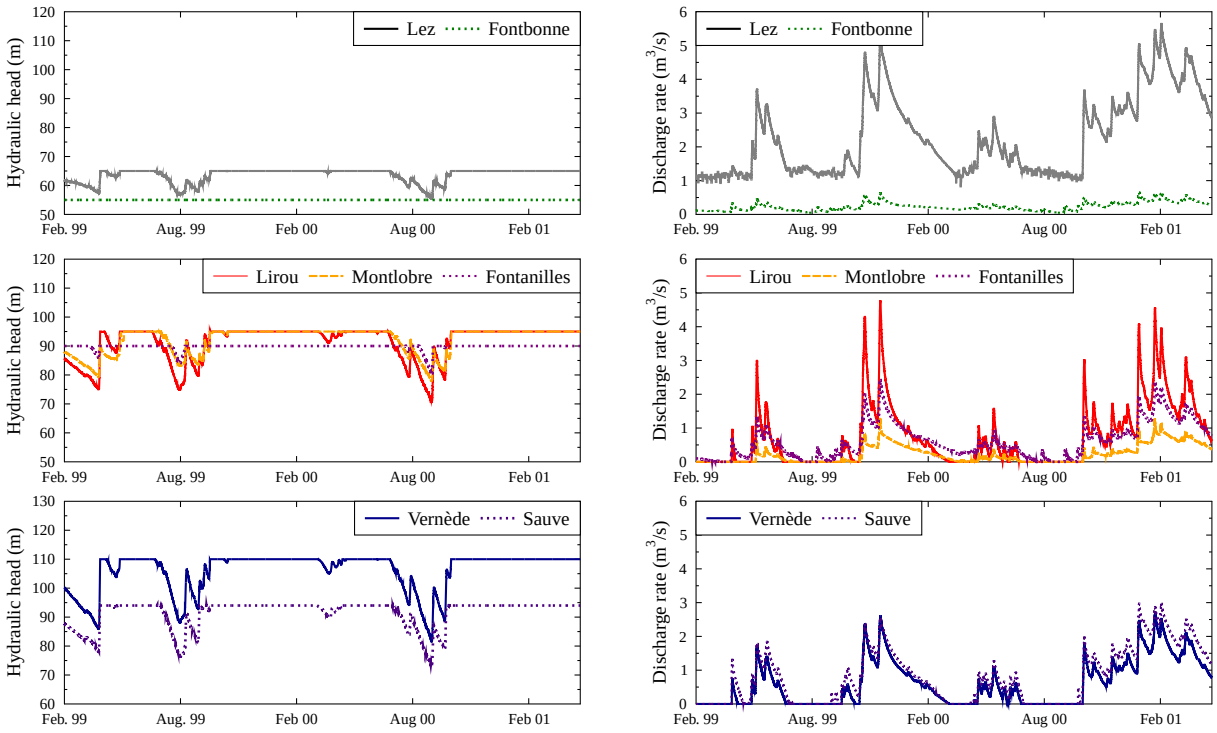

Figure 6.8: Simulation results for the transient state simulation. Hydraulic head and discharge at the main system outlets.

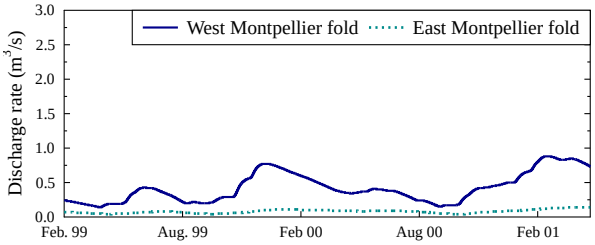

Figure 6.9: Simulation results for the transient state simulation. Discharge rate through the Montpellier fold.

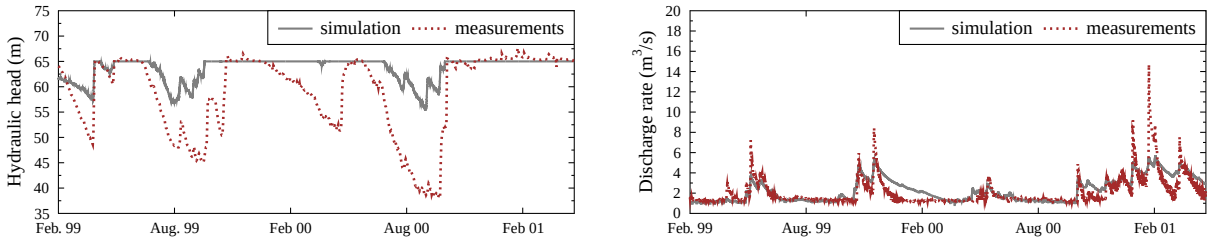

Figure 6.10: Simulation results for the transient state simulation. Hydraulic head and discharge rate at the Lez spring.

- bad simulation of the alternation between overflow and non-overflow periods for most springs: the overflow periods are too long (Figures 6.8 and 6.9) which causes a poor simulation of the hydraulic head during low flow periods,
- overestimation of the Lez spring discharge for the reference August 1999 - August 2000 period (see Table 6.8).

It may also be noted that:

- the Fontbonne spring behaviour is simulated satisfyingly, with a perennial behaviour and an acceptable magnitude of the average discharge rate,
- the relative outflow rates for the different outlets is also coherent with the observations.

These results yield the following remarks.

1. The fact that the model underestimates the peak spring discharge at the Lez, Lirou and probably also the Sauve and Fontanilles outlets suggests that
   - either the concentration of the recharge through the epikarst unit is not efficient enough,
   - or the drain sections may be too low.

   On the other hand, the consistent behaviour of the Fontbonne springs suggests that the drain section appropriately controls the flow towards the spring,
2. The fact that the overflow periods are too long and the overestimation of the average Lez spring discharge may be related to:
   - either the consequence of the inefficiency of flow concentration through the epikarst unit or the limitation of the peak flow due to the drain sections,
   - or an underestimation of the discharge rate through the Montpellier fold.

6.4 Conclusion

The proposed model is based on four hydrogeological units representing (from top to bottom):

- the Hauterivian to Quaternary units, which are assumed to have homogeneous, aquitard properties. The aquifer properties of the Late Hauterivian and Lutetian units which are poorly connected to the Lez aquifer are neglected in this analysis,
- the Late Valanginian to Late Hauterivian formations from the Sauteyrargues syncline, which form a superposed aquifer unit that is connected to the Lez aquifer unit through the Corconne fault,
- the Early Valanginian marly unit which constitutes the roof of the Lez aquifer,
- the Late Jurassic to Early Berriasian formations of the Lez aquifer which are divided into:
  - an "epikarst" unit,
  - a "deep aquifer" unit.

The recharge is modelled as diffuse. The concentration of the infiltration is ensured by the high-conductivity "epikarst" unit. Concentrated infiltration from runoff over the impervious formations is neglected.

The steady-state calibration of the model yields first estimates of the effective hydraulic conductivity of the different hydrogeological units, of the effective cross-section area of the karst conduits and of the properties of the transfer boundary condition associated with the Montpellier fold.

A transient simulation is run with first guess estimates of the storage properties. The main differences to the observed behaviour of the Lez aquifer are:

- the underestimation of the peak flow discharge for the Lirou and Lez springs, and also probably of the Fontanilles and the Sauve springs,
- the overestimation of the duration of the overflow periods, which causes a poor simulation of the hydraulic head during low flow periods,
- the overestimation of the overall Lez spring discharge.

Such differences to the observed behaviour of the Lez aquifer may be attributed to:

- inefficient concentration of the recharge through the epikarst unit,
- inadequate values of the drain sections,
- underestimation of the discharge rate through the Montpellier fold.

Chapter 7 investigates the relative controls of these different items on the behaviour of the Lez aquifer.

6.5 References for Chapter 6

Allen, R. G., L. S. Pereira, D. Raes and M. Smith (1998). « Crop evapotranspiration - Guidelines for computing crop water requirements ». In: *FAO Irrigation and Drainage Paper*. Ed. by FAO. Vol. 56. ISBN: 92-5-104219-5. DOI: 10.1007/s00271-007-0094-8. URL: http://www.fao.org/docrep/X0490E/x0490e00.HTM. See p. 160.

Chow, V. T. (1959). *Open-Channel Hydraulics*. Blackburn Press, p. 700. ISBN: 1932846182, 9781932846188. URL: http://www.blackburnpress.com/ophy.html. See p. 153.

Diersch, H. (1998*a*). *Feflow : Reference Manual*. Institute for Water Resources Planning and Systems Research, WASY. Berlin. URL: http://www.feflow.info/manuals.html. See pp. xii, 9, 151, 180.

— (2005). *Feflow : White Papers Vol. 1*. Institute for Water Resources Planning and Systems Research, WASY. Berlin. URL: http://www.feflow.info/manuals.html. See p. 153.

Hargreaves, G. (1994). « Defining and using reference evapotranspiration ». In: *Journal of Irrigation and Drainage Engineering* 120.6, pp. 1132–1139. DOI: 10.1061/(ASCE)0733-9437(1994)120:6(1132). See pp. 159, 160.

Hargreaves, G. H. and Z. A. Samani (1985). « Reference crop evapotranspiration from temperature ». In: *Applied Engineering in Agriculture* 1.2, pp. 96–99. URL: http://asae.frymulti.com/abstract.asp?aid=26773&t=1. See p. 159.

Jeannin, P.-Y. and J.-C. Maréchal (1995). « Lois de pertes de charge dans les conduits karstiques: Base théorique et observations ». In: *Bulletin du Centre d'Hydrogéologie de Neuchâtel* 14, pp. 149–176. See p. 157.

Kiraly, L. (1998). « Modeling karst aquifers by the combined discrete channel and continuum approach ». In: *Bulletin du Centre d'Hydrogéologie de Neuchâtel* 16, pp. 77–98. See pp. 4, 154.

Neuman, S. P. (1977). « Theoretical derivation of Darcy's law ». In: *Acta Mechanica* 25.3, pp. 153–170. DOI: 10.1007/BF01376989. See p. 152.

Owen, S., N. Jones and J. Holland (1996). « A comprehensive modeling environment for the simulation of groundwater flow and transport ». In: *Engineering with Computers* 12.3-4, pp. 235–242. URL: http://www.andrew.cmu.edu/user/sowen/papers/gms/gms.html. See p. 151.

Shewchuk, J. R. (1996). « Triangle: Engineering a 2D quality mesh generator and Delaunay triangulator ». In: *Selected Papers from the Applied Computational Geometry: Towards Geometric Engineering FCRC'96, WACG'96 workshop held in Philadelphia, USA (May 27-28, 1996)*. Ed. by M. C. Lin and D. Manocha. Vol. 1148. Lecture Notes in Computer Sciences. Springer-Verlag, pp. 203–222. DOI: 10.1007/BFb0014497. URL: http://www.cs.cmu.edu/~quake/tripaper/triangle0.html. See p. 154.

Stüben, K., P. Delaney and S. Chmakov (2003). « Algebraic multigrid (AMG) for ground water flow and oil reservoir simulation ». In: *Proceedings of the MODFLOW and More 2003 Conference held in Golden, Colorado, USA (September 16-19, 2003)*. Ed. by J. Dougherty and S. Seo. URL: http://www.scai.fraunhofer.de/fileadmin/download/samg/paper/Modflow_Paper.pdf. See p. 154.

Chapter 7

Sensitivity analysis of the hybrid groundwater flow model

This chapter investigates the sensitivity properties of hybrid groundwater flow models. The main issues addressed are:

(i) do flow parameters, model geometry and boundary conditions influence model response in the same way ?

(ii) do confined and unconfined aquifers behave in the same way with respect to the sensitivity propagation ?

(iii) what is the impact of discrete karst conduits modelling on the sensitivity propagation ?

(iv) when a distributed model is shown to provide wrong simulation results, where should additional measurements be carried out in priority ?

(v) can general rules be defined for the optimal location of measurement points ?

These questions are addressed using both analytical and empirical sensitivity approaches.

As a preliminary step for the sensitivity study of the hybrid model, Section 7.1 investigates the sensitivity propagation within the matrix system. Section 7.2 investigates the influence of the discrete conduit network on the sensitivity propagation based on an empirical analysis of the hybrid flow model of the Lez hydrosystem.

Contents

7.1 Preliminary study: analytical study of the steady-state sensitivity of the 2-D steady-state groundwater flow equation.

This Section investigates the sensitivity propagation within the matrix system. The sensitivity properties of the two-dimensional, steady-state groundwater flow equation to the flow parameters and to the boundary conditions are analysed using an analytical perturbation approach. The analytical findings derived from this analysis allow some general rules to be established for model design, model calibration and monitoring network design.

This work has been published in Advances in Water Resources [Mazzilli et al., 2010*b*]. It has also been presented at the SimHydro 2010 Conference held in Nice, France (June 2-4, 2010) [Mazzilli et al., 2010*a*].

7.1.1 Introduction

Sensitivity analysis is the study of a system response to disturbances [McElwee, 1978], and is now recognized as an integral part of the modelling process [Helton et al., 2006]. In the field of water resources, its range of application includes scenario analysis [Huysmans et al., 2006], optimization [Gunzburger, 1999; Ramarao et al., 1995], identification of the relevant parameters to model calibration [McKeown et al., 1999] and experimental network design [Graettinger et al., 2006; Meyer et al., 1994].

In this paper, sensitivity analysis is used to derive some general rules for two-dimensional groundwater flow model calibration and monitoring network design. Since the first step in the calibration process is a steady-state simulation, the analysis is carried out for steady-state, two-dimensional flow simulations. The analytical properties of the sensitivity of the steady-state two-dimensional groundwater flow equation to the flow parameters and to the boundary conditions are investigated, based on the perturbation approach. The main issues addressed are: (i) do flow parameters, model geometry and boundary conditions influence model response in the same way, (ii) do confined and unconfined aquifers behave in the same way with respect to the sensitivity propagation, (iii) when a two-dimensional model is shown to provide wrong simulation results, where should additional measurements be carried out in priority, and (iv) can general rules be defined for the optimal location of measurement points ? These issues have been previously addressed for the steady state, two-dimensional shallow water flow equations [Guinot and Cappelaere, 2009]. The present work follows the methodology described in this former study.

In most studies available from the litterature, the effects of a perturbation on the response of a groundwater flow system have been investigated with the concern of understanding the effects of the heterogeneity of the governing hydraulic parameters distribution on hydraulic tests [Copty et al., 2008; McElwee, 1978; Oliver, 1993; Tumlinson et al., 2006; Vela and McKinley, 1970; Willmann et al., 2007; Yukler, 1976, e.g.]. A review of papers on the actual meaning of the transmissivity estimates derived from drawdown data collected in pumping wells in heterogeneous aquifers can be found in Tumlinson et al., 2006. Analytical solutions for transient, pumping-induced drawdown sensitivity in non-uniform aquifers were derived by means of a first-order sensitivity formalism for simplified heterogeneity geometries by various authors [Butler and Liu, 1991; Butler and Liu, 1993; McElwee, 1978; Vela and McKinley, 1970; Willmann et al., 2007; Yukler, 1976] based on the Theis equation. McElwee [McElwee, 1978] investigated the difference in the drawdown sensitivity behaviour with respect to the nature of the perturbed parameter (transmissivity or storage), based on the Theis equation. Changes in the storage were shown to induce a perturbation in the simulated drawdown over a larger area than changes in the transmissivity. Sykes et al., 1985 developed the adjoint sensitivity equations for a two-dimensional steady state flow in a confined aquifer. Sensitivities of local hydraulic head and Darcy velocities (performance measure) with respect to elemental changes in the flow parameters and boundary conditions were computed for an aquifer with heterogeneous conductivity distribution. Butler and Liu, 1993 focused on the influence of an heterogeneity on the observed drawdown and rate of change in drawdown. Delay et al., 2007 developed an approach to the interpretation of interference pumping tests in fractal dual media. Analytical sensitivity calculations indicated that dual media have a sequential response in time to the pumping stress. On the basis of numerical simulations, Jiao and Zheng, 1997 concluded that the information on transmissivity is transferred mainly from upstream to downstream, while the information on storativity is transferred equally upstream and downstream. Conclusions were drawn as to pumping-tests design. The validity of these results is restricted to one-dimensional flow and specific boundary conditions. The spatial structure of the sensitivity of the hydraulic head with respect to the permeability field was investigated by means of a direct differentiation method by Khan et al., 2007. A method for high-sensitivity zones spotting was proposed, based on the observed

sensitivity patterns. A systematic pattern to the sign of the sensitivities was observed, as the sign of a sensitivity coefficient was noted to be a function of the relative location of the perturbation within the flow field with respect to the calibration point. Oliver, 1993 used a perturbation approach to evaluate the effects of two-dimensional areal variations in the aquifers transmissivity and storage on observation well drawdown, based on the Fréchet derivatives and kernels. This work suggested that the area influencing observation well drawdowns were bounded by an ellipse enclosing the pumping and the observation wells. A detailed analysis of the spatial distribution of the hydraulic head sensitivity with respect to transmissivity and storage perturbations was performed for classical pumping test configurations [Leven, 2002; Leven and Dietrich, 2006]. Sensitivity coefficients were derived by means of the adjoint-state method. Sensitivity distributions of hydraulic tests with spatially separated stimulation and observation locations were shown to be characterized by a division of the domain of interest into two regions of opposite sensitivities. Based on the Theis approximation, Knight and Kluitenberg, 2005 derived explicit expressions of the Fréchet kernels and the spatial sensitivity functions for variations in storativity and transmissivity during both pumping and slug test. For not-colocated pumped and observation wells, both wells were shown to have the same importance with respect to spatial sensitivity, which confirmed previous results obtained by Leven, 2002. The sensitivity of a groundwater flow system to the recharge boundary condition prescribed at the top boundary of a fully saturated groundwater flow model was investigated by Jyrkama and Sykes, 2006 by means of the adjoint method.

In most of the abovementioned studies, the sensitivity equation was solved using numerical methods. The analytical approach followed in this paper provides theoretical insights into the general behaviour of the two-dimensional, steady-state aquifer flow equations. The direct approach is used for the sensitivity computation. The direct sensitivity analysis is well suited to the computation of the sensitivity of several variables with respect to a given parameter. However, the computation of the sensitivity of a single variable with respect to multiple input parameters is best handled by an adjoint sensitivity analysis. The adjoint equation models similar physical processes as the direct equation, with a reversed flow of information. This means the direct and adjoint steady state sensitivity equations are the same, except that their velocity fields have opposite signs [Neupauer and Wilson, 2002; Neupauer and Wilson, 2003]. The analytical properties of the sensitivity derived in the present paper thus apply to both the direct and adjoint frameworks.

The present work is structured in the following way. Section 7.1.2 presents the derivation of the two-dimensional steady-state groundwater sensitivity equations, based on the perturbation method. The solutions of the sensitivity equations and their analytical properties are investigated next. Sections 7.1.3 and 7.1.4 deal with perturbations in the flow parameters for confined and unconfined aquifers respectively. Section 7.1.5 handles the case of a perturbation in the boundary condition. Computational examples are presented in Section 7.1.6. Section 7.1.7 is devoted to conclusions.

7.1.2 Sensitivity equations for 2-D aquifer flow

7.1.2.a The groundwater flow equations

Under Dupuit's hypothesis of negligible vertical flow, the steady state hydraulic head field satisfies the following equations [Bear, 1972]

$$-\nabla[Ke\nabla H] = R \quad \text{(confined flow)} \tag{7.1a}$$

$$-\nabla[K(H-z)\nabla H] = R \quad \text{(unconfined flow)} \tag{7.1b}$$

where H (m) is the hydraulic head, K (m/s) is the hydraulic conductivity (assumed independent from H), z (m) is the elevation of the aquifer bedrock, R (m/s) is the recharge rate and e (m) is the aquifer thickness (independent from H in the confined case).

7.1.2.b Sensitivity equations for confined aquifer flow

The sensivity equations are derived by carrying out a perturbation analysis of the steady state groundwater flow equation. The reader interested in a more thorough discussion on sensitivity calculation can refer to [Sun, 1994; Sun and Yeh, 1985; Yeh, 1986, e.g.]. Let ϕ be the parameter with respect to which the sensitivity analysis is carried out. Assume that ϕ is modified by a small quantity $\phi_o\varepsilon(x,y)$ over a region Ω, where ϕ_o is an infinitesimal constant and $\varepsilon(x,y)$ is the support function of the perturbation. Since ϕ may be any of the parameters of the flow equation, we denote the parameters of the perturbed equation $e+e'$, $K+K'$ and $R+R'$ where e', K' and R' are the perturbations in the initial parameters e, K and R respectively. The solution of the perturbed diffusivity equation is the hydraulic head $H+H'$. The perturbed flow equation thus becomes

$$-\nabla[(K+K')(e+e')\nabla(H+H')] = R+R' \tag{7.2}$$

Subtracting equation (7.1a) from equation (7.2) and eliminating the second-order terms leads to

$$-\nabla[(Ke'+K'e)\nabla H + Ke\nabla H')] = R' \tag{7.3}$$

Dividing equation (7.3) by ϕ_o and defining the sensitivity of the hydraulic head to the parameter ϕ as $\eta_\phi \equiv \lim_{\phi_o\to 0}\frac{H'}{\phi_o}$ leads to

$$-\nabla[(K\varepsilon_e + e\varepsilon_K)\nabla H + Ke\nabla\eta_\phi)] = \varepsilon_R \tag{7.4}$$

where

$$\varepsilon_K = \frac{\partial K}{\partial\phi_o}\varepsilon(x,y) \tag{7.5a}$$

$$\varepsilon_e = \frac{\partial e}{\partial\phi_o}\varepsilon(x,y) \tag{7.5b}$$

$$\varepsilon_R = \frac{\partial R}{\partial\phi_o}\varepsilon(x,y) \tag{7.5c}$$

Note that

$$\varepsilon_\phi = \begin{cases} \varepsilon(x,y) & \text{if } \phi \text{ is the perturbed parameter} \\ 0 & \text{otherwise} \end{cases} \tag{7.6}$$

The sensitivity equations may be rewritten in a more general manner

$$-\nabla(Ke\nabla\eta_\phi) = \rho \tag{7.7}$$

with

$$\rho = \begin{cases} \nabla(e\varepsilon\nabla H) & \text{if } \phi = K \\ \nabla(K\varepsilon\nabla H) & \text{if } \phi = e \\ \varepsilon & \text{if } \phi = R \end{cases} \tag{7.8}$$

Equation (7.7) is a transport equation with a source term and diffusive effects. The source term is zero outside the perturbed area. Note that H does not appear in equation (7.7) outside the perturbed area for the parameters K and e. H is not involved either in equation (7.7) inside or outside the perturbed area for the parameter R. Diffusivity is induced by $\nabla(Ke\nabla\eta_\phi)$. Diffusive effects mean that a perturbation influences the value of H over the whole domain.

The sensitivity of the velocity components to the parameter ϕ can be derived from the sensitivity of the hydraulic head to the same parameter using Darcy's law. The expression of the Darcy's velocity is identical for confined and unconfined aquifers

$$v = -K\nabla H \tag{7.9}$$

where v is Darcy's velocity. Differentiating equation (7.9) with respect to the parameter ϕ gives

$$\frac{\partial v}{\partial \phi} = -K\frac{\partial}{\partial \phi}(\nabla H) - \nabla H\frac{\partial K}{\partial \phi} \tag{7.10}$$

Remember that

$$\frac{\partial K}{\partial \phi} = \lim_{\phi_o \to 0} \frac{K'}{\phi_o} \tag{7.11}$$

If $\phi = K$ then $\phi_o = k_o$ and $K' = k_o\varepsilon$, which leads to

$$\frac{\partial K}{\partial \phi} = \varepsilon \tag{7.12}$$

Denoting by ω_ϕ the sensitivity of the flow velocity to the value of the parameter ϕ leads to

$$\omega_\phi = \begin{cases} -K\nabla\eta_\phi & \text{if } \phi \neq K \\ -K\nabla\eta_\phi - \varepsilon\nabla H & \text{if } \phi = K \end{cases} \tag{7.13}$$

Outside the perturbed area, $\varepsilon = 0$ regardless of the parameter considered. Equation (7.13) thus simplifies into

$$\omega_\phi = -K\nabla\eta_\phi \tag{7.14}$$

7.1.2.c Sensitivity equations for unconfined aquifer flow

Applying the perturbation approach used in Section 7.1.2.b to equation (7.1b) for an unconfined aquifer leads to

$$\begin{aligned} -\nabla\left[K\eta_\phi\nabla H + K(H-z)\nabla\eta_\phi\right] = \\ \nabla[(-K\varepsilon_z + (H-z)\varepsilon_K)\nabla H] + \varepsilon_R \end{aligned} \tag{7.15a}$$

Equation (7.15a) may be rewritten as

$$\nabla(v\eta_\phi) - \nabla[K(H-z)\nabla\eta_\phi] = \rho \tag{7.16}$$

with

$$\rho = \begin{cases} \nabla[(H-z)\varepsilon\nabla H] & \text{if } \phi = K \\ -\nabla(K\varepsilon\nabla H) & \text{if } \phi = z \\ \varepsilon & \text{if } \phi = R \end{cases} \tag{7.17}$$

Equation (7.16) is a transport equation with a source term and diffusive effects. Remember that second-order terms have been neglected. The main difference with the confined case lies in the advective component $\nabla(v\eta_\phi)$, which means that the sensitivity is advected at the Darcy velocity. Assuming that the aquifer bedrock elevation is constant, equation (7.16) can be simplified into

$$-\nabla[K\nabla((H-z)\eta_\phi)] = \rho \tag{7.18}$$

When the perturbed parameter is the bedrock elevation or the recharge, the variable $(H-z)\eta_\phi$ obeys the same equation under unconfined conditions as does η_ϕ under confined conditions. In this case, sensitivity patterns under unconfined conditions are identical to those obtained for confined conditions, but distorted by a factor $1/(H-z)$.

7.1.3 Sensitivity properties for confined aquifers

The theoretical developments are carried out for a homogeneous aquifer with a uniform, parallel flow directed in the negative y-direction (Figure 7.1). Anisotropic problems can be recast in the form of isotropic problems using a coordinate change. Whatever the parameter investigated, the support function of the perturbation $\varepsilon(x, y)$ is taken equal to zero everywhere except over a square zone Ω of size $2L \times 2L$ centred around (0,0), where it varies linearly from 0 at the edges of the zone to 1 at its centre (see Figure 7.1). Note that any continuous support function could be decomposed with first-order accuracy into a sum of elementary support function such as ε. Such an approach is customary in e.g. finite element modelling.

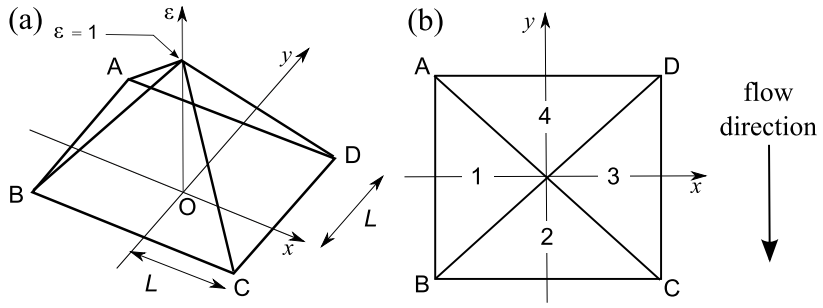

Figure 7.1: Definition sketch for ε : (a) Perspective view, (b) Plan view

7.1.3.a Influence of a perturbation in the hydraulic conductivity for parallel flow

Consider the case of a perturbation in the hydraulic conductivity. The source term in equation (7.7) is non-zero over the pertubed area only. At a distance r from the perturbation such that $r >> L$ (far field), the integral of the source term over the perturbed area can be approximated by a doublet of sources made of a sink with intensity $-eL\,\partial H/\partial y$ (point source 1) located at (0,$2L/3$) and a source with intensity $+eL\,\partial H/\partial y$ (point source 2) located at (0,$-2L/3$) (see demonstration in 7.1.8.a and see source configuration in Figure 7.2). The field generated by this equivalent source configuration is known from the theory of potential flow [Garabedian, 1964] to be

$$\eta_K = \frac{L}{2\pi K}\frac{\partial H}{\partial y}\ln\left(\frac{r_1}{r_2}\right) \tag{7.19}$$

where r_1 and r_2 are the distances to the equivalent point sources 1 and 2 respectively. The sign of η_K is negative upstream of the perturbed area, and positive downstream. This result is in agreement with the expected flow behaviour. Indeed, assume that the hydraulic conductivity decreases over the area Ω. Then head losses increase, and the hydraulic head increases upstream of the perturbed area and decreases downstream. The contour lines of η_K are defined by a constant r_1/r_2 ratio. The sensitivity contour lines are thus circles, the centre of which lies on the y-axis and is converging at the source 1 or at the source 2 for disminishing radius (see Figure 7.4a). Note that the sensitivity propagates mainly in the flow direction. The sensitivity propagates upstream and downstream with the same intensity, consequently the sensitivity pattern of the hydraulic head is symmetric with respect to the x-axis.

The sensitivities ν_K and ϖ_K of the longitudinal and transverse velocities can be derived using

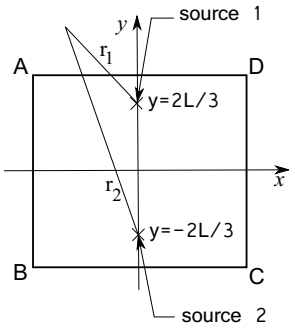

Figure 7.2: Equivalent source configuration for ε_K in the confined case.

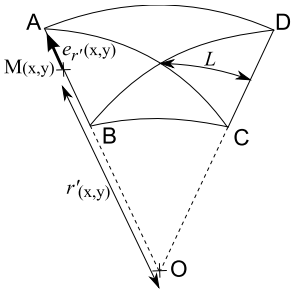

Figure 7.3: Definition sketch for for ε, non parallel flow case (plan view). The point O is the convergence point of the flow path lines, the point M has coordinate (x,y) in the cartesian frame, r' is the distance from M to O and $e_{r'}$ is the radial unit vector at M.

the results of Section 7.1.2.b

$$\nu_K = \frac{2L^2}{3\pi}\frac{\partial H}{\partial y}\frac{x^2+(2L/3)^2-y^2}{r_1^2 r_2^2} \tag{7.20a}$$

$$\varpi_K = -\frac{4L^2}{3\pi}\frac{\partial H}{\partial y}\frac{xy}{r_1^2 r_2^2} \tag{7.20b}$$

Unlike the sensitivity of the hydraulic head, the sensitivities of the transverse and longitudinal velocities propagate in the transverse direction. Figures 7.4b and 7.4c show typical contour lines for ν_K and ϖ_K respectively. The contour lines of the sensitivity of the longitudinal flow velocity have the shape of a cross, directed along the flow. The sensitivity of the transverse component of the flow velocity is also cross-shaped, but its branches are diagonal to the flow. This can be interpreted physically as follows. Assume that the hydraulic conductivity of the area Ω is lower than that of the remainder of the model. Then the flow path lines tend to pass round the low-conductivity area, leading to diverging flow pattern upstream from the perturbed area, and converging flow pattern downstream. A small, positive x-velocity appears to the upstream left and downstream right from the perturbed area, while a small, negative x-velocity appears to the upstream right and downstream left (Figure 7.4c). Besides, the flow is slowed down upstream and downstream from the low-conductivity area, while it is speeded up in the transverse direction to the flow (Figure 7.4b).

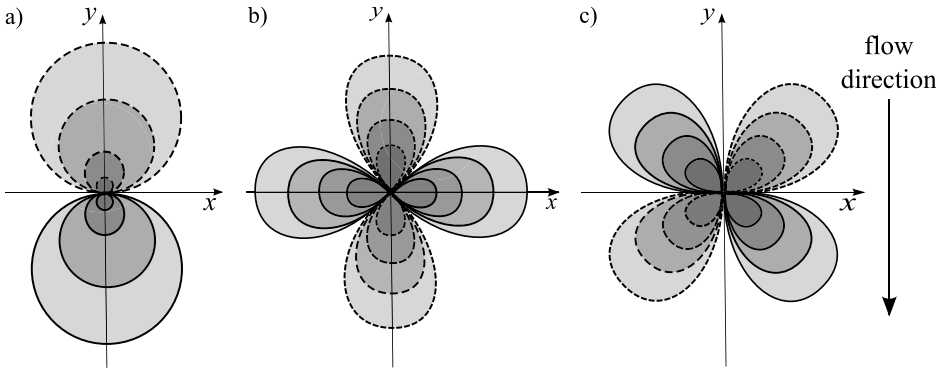

Figure 7.4: Parallel, steady-state confined flow : case of a perturbation in the hydraulic conductivity. Typical far field behaviour for the contour lines of : a) the hydraulic head sensitivity, b) the longitudinal velocity sensitivity, c) the transverse velocity sensitivity. Darker zones indicate higher absolute value. Dashed and solid lines indicate negative and positive values respectively.

7.1.3.b Influence of a perturbation in the aquifer thickness for parallel flow

For confined aquifers, a modification of the aquifer thickness amounts to a modification of the aquifer bedrock elevation. The sensitivity source term generated by a perturbation in the aquifer thickness is equal to that generated by a perturbation in the hydraulic conductivity, multiplied by a factor K/e. The sensitivity field generated by a perturbation in the aquifer thickness can thus be derived by analogy with the results of Section 7.1.3.a

$$\eta_e = \frac{L}{2\pi e}\frac{\partial H}{\partial y}\ln\left(\frac{r_1}{r_2}\right) \tag{7.21a}$$

$$\nu_e = \frac{\partial H}{\partial y}\frac{2L^2K}{3\pi e}\frac{x^2+(2L/3)^2-y^2}{r_1^2 r_2^2} \tag{7.21b}$$

$$\varpi_e = -\frac{4L^2K}{3\pi e}\frac{\partial H}{\partial y}\frac{xy}{r_1^2 r_2^2} \tag{7.21c}$$

The sensitivity patterns induced by a perturbation in the aquifer thickness are the same as previously seen for a perturbation of the hydraulic conductivity. Note that

$$K\eta_K = e\eta_e \tag{7.22}$$

Equation (7.22) means that a given relative variation in K has the same effect on the hydraulic head and the flow velocities as the same relative variation in e.

7.1.3.c Influence of a perturbation in the recharge for parallel flow

It stems from equation (7.5c) that the source term generated by a perturbation in the recharge reduces to $\varepsilon(x,y)$. Its integral over the perturbed area is $4L^2/3$. For far-field behaviour, this source configuration is equivalent to a point source of value $4L^2/3$ located at (0,0). The field generated by a point source is known from the theory of potential flow [Garabedian, 1964] to be

$$\eta_R = -\frac{2L^2}{3\pi Ke}\ln\left(\frac{r}{d}\right) \tag{7.23}$$

where d is the distance for which the sensitivity is zero. For an infinite domain, d must be fixed arbitrarily. In real-world applications, d depends on the boundary conditions. The contour lines of the sensitivity are circles centred on the perturbation. Figure 7.5 shows typical sensitivity patterns for η_R. Note that the value of the sensitivity is proportional to the inverse of the aquifer thickness and hydraulic conductivity, which means that the estimate of the aquifer recharge is all the more important as the aquifer is thin or little conductive. Denoting by δ the value below which η is considered negligible, equation (7.23) leads to

$$r_{(\eta=\delta)} = d\ \exp\left(-\frac{3\pi\delta}{2L^2}Ke\right) \tag{7.24}$$

Equation (7.24) shows that for a given d and L, the distance beyond which the sensitivity can be considered negligible decreases exponentially with the aquifer transmissivity Ke.

The sensitivities ρ_R and θ_R of the radial and tangential flow velocities are

$$\rho_R = \frac{2L^2}{3\pi e}\frac{1}{r} \tag{7.25a}$$

$$\theta_R = 0 \tag{7.25b}$$

The sensitivity propagates radially.

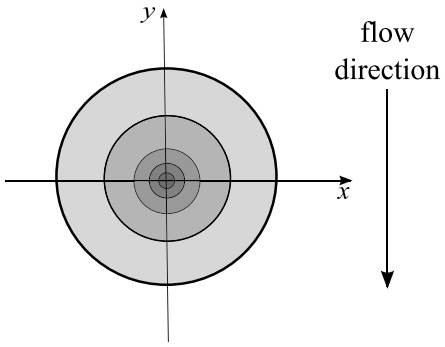

Figure 7.5: Parallel, steady-state confined flow : case of a perturbation in the recharge rate. Typical far field behaviour of the hydraulic head sensitivity contour lines. Darker zones indicate higher absolute value. Solid lines indicate positive values.

7.1.3.d Influence of a perturbation in the flow parameters for non-parallel flow

The sensitivity to the recharge is independent from the hydraulic head field, therefore non-parallel flow yields no change in the sensitivity patterns obtained in Section 7.1.3.c. The case of a perturbation in the hydraulic conductivity or in the aquifer thickness is different. Since the gradient of the hydraulic head gradient cannot be considered constant over the perturbed area, the source term changes.

Consider the case of a perturbation in the hydraulic conductivity. Assume that the flow can be approximated as radial over the perturbed area. The flow velocity may thus be expressed as $v = -Q/(2\pi e r')e_{r'}$, where r' is the distance to the convergence point of the flow path lines , $e_{r'}$ is the radial unit vector and Q is positive for converging flow and negative for diverging flow (see definition sketch in Figure 7.3). Assuming that K is a constant over Ω, the source term may be expressed as

$$\rho_K = \frac{Q}{2\pi K}\left[\rho_1 + \rho_2\right] \tag{7.26}$$

where

$$\rho_1 = -\frac{\varepsilon}{r'^2} \tag{7.27a}$$

$$\rho_2 = \frac{1}{r'}\frac{\partial \varepsilon}{\partial r'} \tag{7.27b}$$

When $L \ll r'$, ρ_1 is negligible compared to ρ_2 and the variations of r' over Ω can be neglected. The source term then reduces to $\rho_K = [Q/(2\pi K r'_o)]\partial\varepsilon/\partial r'$, where r'_o is the distance between the perturbation and the convergence point of the flow path lines. This source configuration is equivalent for far-field behaviour to a doublet of sources, as in the parallel flow case. It yields a symmetric hydraulic head sensitivity pattern with respect to the x-axis, with negative sign upstream of the perturbed area, and positive sign downstream. The second-order terms yields an increase of the absolute sensitivity values in the converging flow path lines direction (see demonstration in 7.1.8.b). Indeed, the perturbation in the hydraulic heads is expected to be more important as the flow section decreases.

The case of a perturbation in the aquifer thickness is similar to that of a perturbation in the hydraulic conductivity.

7.1.4 Sensitivity properties for unconfined aquifers

The theoretical developments are carried out using the same assumptions as in Section 7.1.3 and assuming that the aquifer bedrock elevation is constant. The values of the hydraulic head and bedrock elevation at the centre of the perturbed area are denoted by H_o and z_o.

7.1.4.a Influence of a perturbation in the hydraulic conductivity for parallel flow

The detailed derivation of the source term is provided in 7.1.8.c. The far field sensitivity source configuration is equivalent to the superposition of a doublet of sources of intensity $-L(H-z)_o\left(\partial H/\partial y\right)_o$ (point source 1) and $+L(H-z)_o\left(\partial H/\partial y\right)_o$ (point source 2) located at respectively (0, $2L/3$) and (0, $-2L/3$) (see Figure 7.2). The field generated by this equivalent source configuration is known from the theory of potential flow [Garabedian, 1964] to be

$$\eta_K = \frac{L}{2\pi K}\left(\frac{\partial H}{\partial y}\right)_o \ln\left(\frac{r_1}{r_2}\right)\frac{H_o - z_o}{H - z} \tag{7.28}$$

where r_1 and r_2 are the distances to the equivalent sources 1 and 2 respectively. The term $(H_o - z_o)/(H - z)$ is an advection term. As its absolute value is larger dowstream than upstream for a given distance to the perturbation, the contour lines are shifted downstream. The resulting sensitivity pattern is shown in Figure 7.6a.

The sensitivities ν_K and ϖ_K of the longitudinal and transverse flow velocities are

$$\nu_K = -\frac{L}{\pi}\left(\frac{\partial H}{\partial y}\right)_o \left[\frac{4L}{3}\frac{x^2 + 4L^2/9 - y^2}{r_1^2 r_2^2} - \frac{1}{2(H-z)}\frac{\partial H}{\partial y}\ln\left(\frac{r_1}{r_2}\right)\right]\frac{H_o - z_o}{H - z} \tag{7.29a}$$

$$\varpi_K = -\frac{2L^2}{3\pi}\left(\frac{\partial H}{\partial y}\right)_o \frac{xy}{r_1^2 r_2^2}\frac{H_o - z_o}{H - z} \tag{7.29b}$$

As an effect of advection, the contour lines of the sensitivity of the flow transverse velocity are shifted downstream. The sensitivity of the longitudinal flow velocity is made of two terms with opposite effects. The first term on the right-hand side of equation (7.29a) yields sensitivity patterns similar to those obtained in the confined case, but shifted downstream. The second term on the right-hand side of equation (7.29a) has negative sign upstream from the perturbation, and positive sign downstream. Its effect is a decrease of the algebraic sensitivity value upstream from the perturbed area, and an increase downstream. The resulting sensitivity patterns are shown in Figures 7.6b and 7.6c.

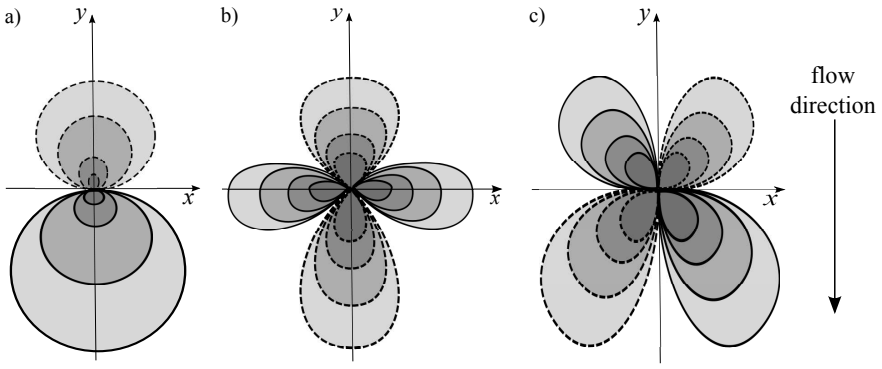

Figure 7.6: Parallel, steady-state unconfined flow : case of a perturbation in the hydraulic conductivity. Typical far field behaviour for the contour lines of : a) the hydraulic head sensitivity, b) the longitudinal velocity sensitivity, c) the transverse velocity sensitivity. Darker zones indicate higher absolute value. Dashed and solid lines indicate negative and positive values respectively. The contour lines deformation has been exaggerated for a better understanding.

7.1.4.b Influence of a perturbation in the bedrock elevation for parallel flow

Assume that the flow is parallel, directed along the y-axis over the perturbed area. Also assume that the hydraulic head gradient is constant over the perturbed area. Then the calculation of the

source term generated by a perturbation in the bedrock elevation is similar to that of the source term generated by a perturbation in the hydraulic conductivity. The sensitivity field generated by a perturbation in the bedrock elevation can thus be derived by analogy with the results of Section 7.1.4.a

$$\eta_z = -\frac{L}{2\pi}\left(\frac{\partial H}{\partial y}\right)_o \ln\left(\frac{r_1}{r_2}\right)\frac{1}{H-z} \tag{7.30}$$

The sensitivities ν_z and ϖ_z of the longitudinal and transverse flow velocities are

$$\nu_z = -\frac{LK}{\pi}\left(\frac{\partial H}{\partial y}\right)_o \left[\frac{4L}{3}\frac{x^2+4L^2/9-y^2}{r_1^2 r_2^2} - \frac{1}{2(H-z)}\frac{\partial H}{\partial y}\ln\left(\frac{r_1}{r_2}\right)\right]\frac{1}{H-z} \tag{7.31a}$$

$$\varpi_z = -\frac{2L^2K}{3\pi}\left(\frac{\partial H}{\partial y}\right)_o \frac{xy}{r_1^2 r_2^2}\frac{1}{H-z} \tag{7.31b}$$

7.1.4.c Influence of a perturbation in the recharge for parallel flow

The sensitivity of the hydraulic head to the recharge can be obtained directly by analogy with the confined case

$$\eta_R = -\frac{2L^2}{3\pi K}\ln\left(\frac{r}{d}\right)\frac{1}{H-z} \tag{7.32}$$

Compared to the confined case, the sensitivity contour lines are advected downstream (see Figure 7.7b).

The sensitivities ρ_R and θ_R of the radial and tangent flow velocities are

$$\rho_R = \frac{2L^2}{3\pi}\frac{1}{H-z}\left[\frac{1}{r} + \ln\left(\frac{r}{d}\right)\frac{\partial(H-z)}{\partial y}\frac{\cos\theta}{H-z}\right] \tag{7.33a}$$

$$\theta_R = -\frac{2L^2}{3\pi}\ln\left(\frac{r}{d}\right)\frac{\partial(H-z)}{\partial y}\frac{\sin\theta}{(H-z)^2} \tag{7.33b}$$

where θ is the angle coordinate with respect to the y-axis. The sensitivity of the radial flow velocity is made of two terms. The first term $2L^2/[3\pi r(H-z)]$ is independent from the angular coordinate θ. It is equal to the sensitivity of the radial flow velocity derived in the confined case, multiplied by a factor $1/(H-z)$. The effect of the $1/(H-z)$ factor is to advect the sensitivity of the radial flow velocity downstream. The second term of the sensitivity of the radial flow velocity and the sensitivity of the tangential flow velocity θ_R are better understood using Cartesian coordinates. Using Cartesian coordinates, the sensitivities ν_R and ϖ_R of the longitudinal and transverse flow velocities are (see 7.1.8.d for details)

$$\nu_R = \frac{2L^2}{3\pi}\frac{y}{(H-z)r^2} + \frac{2L^2}{3\pi(H-z)^2}\frac{\partial(H-z)}{\partial y}\ln\left(\frac{r}{d}\right) \tag{7.34a}$$

$$\varpi_R = \frac{2L^2}{3\pi}\frac{x}{(H-z)r^2} \tag{7.34b}$$

The first term on the right-hand side of each equation corresponds to $2L^2/[3\pi r(H-z)]$ in radial coordinates. The effect of the term $[(2L^2)/(3\pi(H-z)^2)]\ln(r/d)\ \partial(H-z)/\partial y$ is to decrease the longitudinal velocity sensitivity upstream of the perturbation, and to increase it downstream (see details in 7.1.8.d). This can be explained physically by the fact that an increase in the recharge causes the water level to increase upstream of the perturbed area (and to decrease downstream). This leads to an increase of the algebraic value of the hydraulic head gradient upstream of the perturbed area (and to a decrease downstream), which in turns causes the flow velocity to decrease upstream of the perturbed area (and to increase downstream) (see Figure 7.7a).

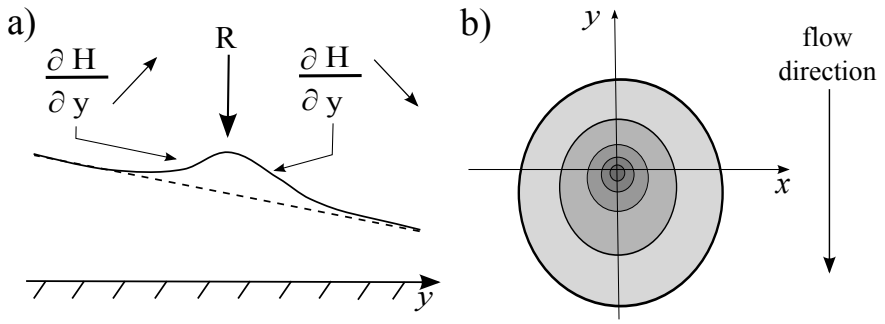

Figure 7.7: Parallel, steady-state unconfined flow : case of a perturbation in the recharge rate. a) Longitudinal head profile crossing the perturbed area. Dashed line : unperturbed head profile, solid line : perturbed head profile. An increase in the recharge causes the algebraic value of the hydraulic head gradient to increase upstream of the perturbed area, and to decrease downstream, b) Typical far field behaviour of the hydraulic head sensitivity contour lines. Solid lines indicate positive values. The contour lines deformation has been exaggerated in order to ease the understanding.

7.1.4.d Influence of a perturbation in the flow parameters for non-parallel flow

Non-parallel flow modifies the sensitivities established in the previous sections in two different ways. The sensitivity to all parameters is proportional to the inverse of the hydraulic head, which accounts for the advection of the perturbation in the flow direction. The variation in the hydraulic head gradient over the perturbed area also influences the source term of the sensitivities to the hydraulic conductivity and to the aquifer bottom level elevation, as in the confined case.

Consider the case of a perturbation in the hydraulic conductivity, and assume that the flow can be approximated locally with a radial flow field. The flow velocity may thus be expressed as $v = -Q/(2\pi r'(H-z))\ e_{r'}$. The source term of the sensitivity to the hydraulic conductivity becomes $\rho_K = \nabla[Q\varepsilon/(2\pi K r')\ e_{r'}]$. This expression is very close to that of the confined case, so that the results of Section 7.1.3.d can be adapted directly. The sensitivity patterns are the same as in the parallel flow case, but multiplied by a factor $1/(H-z)$. The effects of the distortion by the hydraulic head field and of the variation of the intensity of the source term over the perturbed area may be opposed.

Consider now the case of a perturbation in the aquifer bedrock elevation. Under a radial flow approximation, the source term of the sensitivity can be written as

$$\rho_z = -\nabla\left[\frac{Q\varepsilon}{2\pi(H-z)r'}\ e_{r'}\right] \tag{7.35}$$

The difference with the previous case lies in the coefficient $1/(H-z)$, that contributes to increase the sensitivity downstream of the perturbation.

7.1.5 Boundary conditions

7.1.5.a Sensitivity to boundary conditions

Boundary conditions along a boundary b may be written in general form as

$$f(x_b, y_b, \phi_b, H_b) = 0 \tag{7.36}$$

where the function f is known and the subscript b refers either to the value of the parameter or to the variable along the boundary. Differentiating equation (7.36) with respect to the parameter ϕ leads to the following equation

$$\frac{\partial f}{\partial H}\frac{dH}{d\phi_b} + \frac{\partial f}{\partial \phi_b} = 0 \tag{7.37}$$

which in turn leads to the sensitivity boundary condition

$$\frac{\partial f}{\partial H}\eta_{\phi_b} + \frac{\partial f}{\partial \phi_b} = 0 \tag{7.38}$$

where the term $\partial f/\partial \phi_b$ is known from the expression of the boundary conditions.

The case of the most commonly employed boundary conditions is detailed hereafter. Prescribed head conditions may be written as

$$H - H_b = 0 \tag{7.39}$$

where H_b is the value of the hydraulic head along the boundary. Note that equation (7.39) is only valid along the boundary. In this writing, f is defined as

$$f(H, H_b) = H - H_b \tag{7.40}$$

and the perturbed parameter is H_b

$$\phi_b = H_b \tag{7.41a}$$
$$\partial f/\partial H_b = -\varepsilon \tag{7.41b}$$
$$\partial f/\partial H = 1 \tag{7.41c}$$

Equation (7.38) thus becomes

$$\eta_{H_b} = \varepsilon \tag{7.42}$$

Similarly, flux conditions and head-flux relationships may be written as

$$-Ke\nabla H = F_b \quad \text{(prescribed flux, confined flow)} \tag{7.43a}$$
$$-KH\nabla H = F_b \quad \text{(prescribed flux, unconfined flow)} \tag{7.43b}$$
$$-Ke\nabla H = \lambda H \quad \text{(head-flux relationship, confined flow)} \tag{7.43c}$$
$$-KH\nabla H = \lambda H \quad \text{(head-flux relationship, unconfined flow)} \tag{7.43d}$$

where F_b is the flux prescribed along the boundary and λ is the fluid transfer coefficient (leakage parameter). Differentiating equations (7.43a) to (7.43d) with respect to F_b and λ respectively leads to

$$-Ke\nabla\eta_{F_b} = \varepsilon \quad \text{(prescribed flux, confined flow)} \tag{7.44a}$$
$$-K\eta_{F_b}\nabla H - KH\nabla\eta_{F_b} = \varepsilon \quad \text{(prescribed flux, unconfined flow)} \tag{7.44b}$$
$$-Ke\nabla\eta_\lambda = \varepsilon H + \lambda\eta_\lambda \quad \text{(head-flux relationship, confined flow)} \tag{7.44c}$$
$$-K\eta_\lambda\nabla H - KH\nabla\eta_\lambda = \varepsilon H + \lambda\eta_\lambda \quad \text{(head-flux relationship, unconfined flow)} \tag{7.44d}$$

Prescribing boundary conditions thus amounts to prescribing the boundary value of the sensitivity or sensitivity gradient, or a relationship between the sensitivity and the sensitivity gradient, depending on the nature of the boundary condition.

Inside the model, the sensitivity obeys equation (7.7) (confined aquifer) or (7.16) (unconfined aquifer)

$$\nabla(Ke\nabla\eta_\phi) = 0 \quad \text{(confined flow)} \tag{7.45a}$$
$$\nabla(K(H-z)\nabla\eta_\phi) = 0 \quad \text{(unconfined flow)} \tag{7.45b}$$

The solution of this equation depends on the boundary conditions fixed by equation (7.38). There is no analytical solution in the two-dimensional general case.

7.1.5.b One-dimensional case

Assume that the problem is one-dimensional. Denote by T the transmissivity Ke (confined case) or $K(H-z)$ (unconfined case). Then equations (7.45a) and (7.45b) imply that

$$T\frac{\partial \eta_\phi}{\partial n} = A \tag{7.46}$$

where A is a constant that depends on the boundary conditions. The hydraulic head sensitivity gradient $\partial\eta_\phi/\partial n$ is proportional to the inverse of the transmissivity.

If the transmissivity is uniform, then the hydraulic head sensitivity decreases linearly inside the model. Assume that the aquifer transmissivity is not homogeneous. Equation (7.46) implies that the hydraulic head sensitivity gradient in a given region is proportional to the inverse of the transmissivity.

Consider the case of a fixed head boundary condition. The value of the hydraulic head sensitivity at the perturbed boundary is equal to 1, regardless of the transmissivity value (see Section 7.1.5.a). The normal gradient of the hydraulic head sensitivity across the model depends on the transmissivity value based on equation (7.46). The value of the hydraulic head sensitivity at a given distance from the perturbed boundary thus depends on the average transmissivity value between the perturbed boundary and the location at which the sensitivity is investigated. The error stemming from wrongly specified head boundary condition will thus be minimized if the boundary lies in a low transmissivity area.

The case of flux boundary conditions and head-flux relationships is different. As for hydraulic head boundary conditions, a change in the transmissivity leads to a change in the hydraulic head sensitivity gradient. Yet the change in the hydraulic head sensitivity gradient is counterbalanced by a change in the hydraulic head sensitivity value at the perturbed boundary (see 7.1.8.e). As a consequence, the error or the uncertainty stemming from wrongly specified or uncertain boundary condition is not minimized if the boundary lies in a region with low transmissivity. In contrast, the uncertainty in the simulated hydraulic head is minimized for low average transmissivity between the area over which the hydraulic head is investigated and a well-known prescribed head condition.

The sensitivity of the flow velocity is related to the hydraulic head sensitivity based on equation (7.14). Equation (7.46) can thus be recast as

$$\omega_\phi = -A/e \qquad \text{(confined flow)} \tag{7.47a}$$

$$\omega_\phi = -A/(H-z) \qquad \text{(unconfined flow)} \tag{7.47b}$$

which means that the sensitivity of the flow velocity is proportional to the inverse of the aquifer thickness.

7.1.6 Computational examples

7.1.6.a Parallel flow in a confined aquifer : sensitivity to K and R

The present test case aims at checking that the theoretical results of Section 7.1.3 match the experimental sensitivities computed under confined parallel flow conditions. Note that as the analytical expressions established in Section 7.1.3 and 7.1.4 are approximate solutions of the sensitivity equation, the difference between the numerical results and the approximate far-field sensitivity is not expected to necessarily converge to zero. Two simulations are carried out. In the first simulation, the investigated parameter ϕ is uniform while in the second simulation, it is perturbed by a small amount ϕ_o over a square region of size L. The empirical sensitivity of the flow variable is computed as the ratio of the difference between the two simulation results to the perturbation ϕ_o. The two-dimensional groundwater flow equations are solved over a square domain of size D using

the finite element FEFLOW numerical code [Diersch, 1998*a*,*b*]. The lateral boundaries ($x = \pm D/2$) are no flow boundaries. A constant hydraulic head is prescribed at the upstream ($y = D/2$) and downstream ($y = -D/2$) boundaries of the domain, so as to allow steady state parallel flow. Note that in the following simulations, the flow is directed in the negative y direction. The resulting sensitivity patterns are drawn over a square domain of size $d \ll D$ in order to eliminate artefacts due to the boundaries (see definition sketch in Figure 7.8). The model characteristics are summarized in Table 7.1.

Figures 7.9a to 7.9c show typical sensitivity patterns generated by a perturbation in the hydraulic conductivity (see test case parameters in Table 7.2). The resulting sensitivity patterns match the results of Section 7.1.3.a (Figure 7.4).

Figure 7.10 shows the hydraulic head sensitivity pattern generated by a perturbation in the recharge (see test case parameters in Table 7.2). The experimental sensitivity pattern is in agreement with the results of Section 7.1.3.c (Figure 7.5).

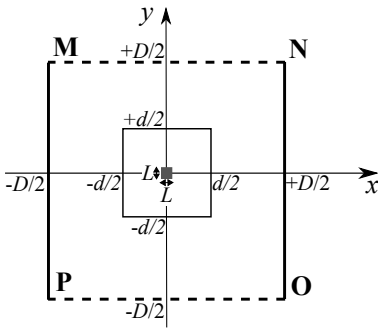

Figure 7.8: Definition sketch for the model used in application examples 7.1.6.a (parallel flow in a confined aquifer) and 7.1.6.b (parallel flow in an unconfined aquifer). The simulations are run in a square domain of size D. The hydraulic head is fixed along the borders (MN) and (OP). No-flux boundary conditions are prescribed along the borders (NO) and (PM). The parameters are perturbed over a square area of length L at the centre of the domain (grayed area). The resulting sensitivity patterns are drawn over a square domain of size d centred on the perturbed area.

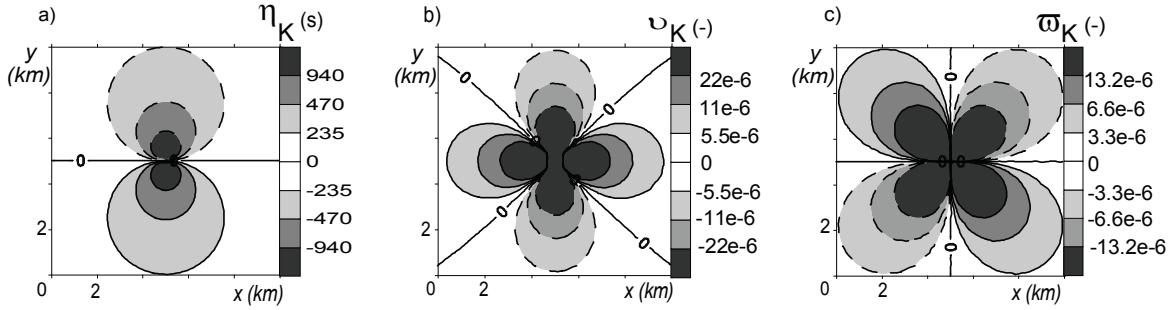

Figure 7.9: Parallel, steady-state confined flow. Case of a perturbation in the hydraulic conductivity : a) sensitivity of the hydraulic head, b) sensitivity of the longitudinal flow velocity, c) sensitivity of the transverse flow velocity. Dashed and solid lines indicate negative and positive values respectively. The simulation parameters are given in Table 7.1 and Table 7.2.

7.1.6.b Parallel flow in an unconfined aquifer : sensitivity to K and R

The present test case aims at checking that the theoretical results of Section 7.1.4 match the experimental sensitivities computed under unconfined parallel flow conditions. The methodology is the same as in Section 7.1.6.a. The test case parameters are given in Table 7.3 and 7.4.

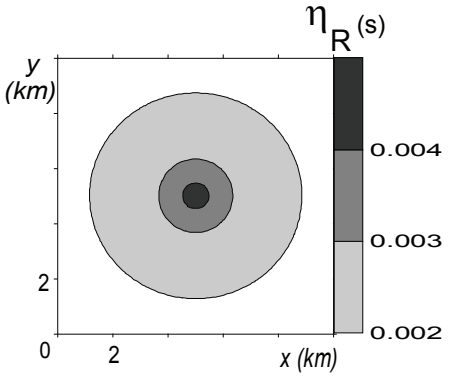

Figure 7.10: Parallel, steady-state confined flow. Case of a perturbation in the recharge rate: hydraulic head sensitivity. The simulation parameters are given in Table 7.1 and Table 7.2.

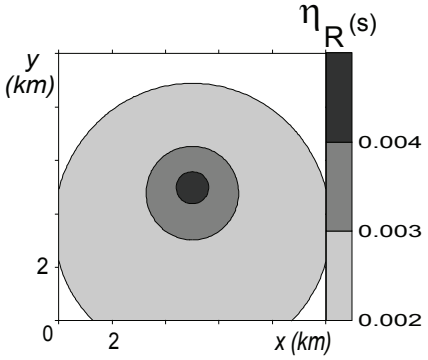

Figure 7.11: Parallel, steady-state unconfined flow. Case of a perturbation in the recharge rate: hydraulic head sensitivity. The simulation parameters are given in Table 7.3 and Table 7.4.

Symbol	Meaning	Value
D	Length of the simulation domain	40km
d	Length of the results visualization area	10km
L	Length of the perturbed area	600m
H_{MN}	Hydraulic head prescribed along the (MN) border	86.7m
H_{OP}	Hydraulic head prescribed along the (OP) border	10m

Table 7.1: Model characteristics for the application examples described in Section 7.1.6.a (steady-state confined parallel flow). (MP) and (NO) are no-flow boundaries.

Symbol	Meaning	Value
K	Hydraulic conductivity	10^{-4}m/s
R	Recharge rate	0m/s
e	Aquifer thickness	78.2m
k_o	Perturbation in the hydraulic conductivity	$-2.5\,10^{-5}$m/s
r_o	Perturbation in the recharge rate	$5.8\,10^{-9}$m/s

Table 7.2: Parallel, steady-state confined flow. Parameters for the application example described in Section 7.1.6.a : case of a perturbation in the hydraulic conductivity or in the recharge rate.

Figures 7.12a to 7.12c show typical sensitivity patterns generated by a perturbation of the hydraulic conductivity. Compared to the confined case, the sensitivity patterns are advected in the direction of the flow, as predicted in Section 7.1.4.a (Figure 7.6). Remember that contour lines deformation on Figure 7.6 has been exaggerated for comprehension purpose. Figure 7.11 shows the hydraulic head sensitivity pattern generated by a perturbation in the recharge. The deformation due to the advection is clearly visible. The experimental sensitivity pattern matches the results of Section 7.1.4.c (Figure 7.7).

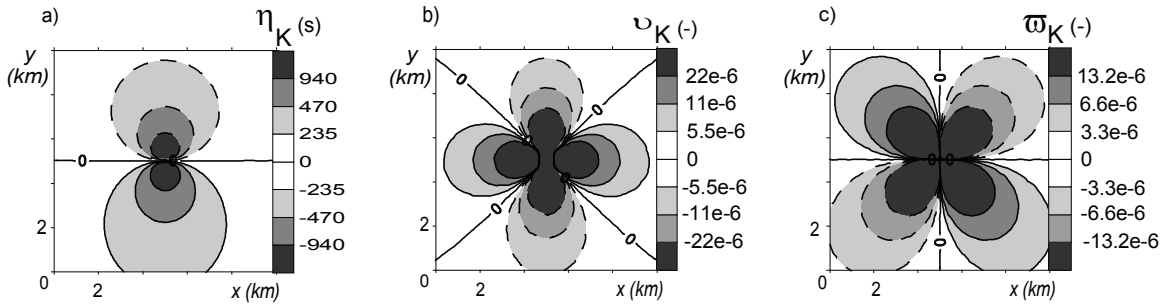

Figure 7.12: Parallel, steady-state unconfined flow. Case of a perturbation in the hydraulic conductivity : a) sensitivity of the hydraulic head, b) sensitivity of the longitudinal flow velocity, c) sensitivity of the transverse flow velocity. Dashed and solid lines indicate negative and positive values respectively. The simulation parameters are given in Table 7.3 and Table 7.4.

7.1.6.c Non-parallel flow in a mixed confined-unconfined aquifer : sensitivity to K and R

The present test case aims at checking the validity of the theoretical sensitivity patterns derived in Section 7.1.4 in a real-site geometry. With this purpose, the sensitivity patterns generated by a perturbation in the hydraulic conductivity or in the recharge are investigated under non parallel flow conditions over a schematic representation of the Lez karst aquifer system (Hérault, France).

The Lez aquifer system is developed mainly in karstified Jurassic to late Cretaceous limestones, with a thickness ranging from 650 to 1100m [Avias, 1992*a*]. Its main outlet is the Lez spring, that supplies the city of Montpellier with water. The aquifer system is bounded by the Hérault and Vidourle rivers at its western and eastern sides, and by impervious structural boundaries at its northern and southern sides [Drogue, 1969] (see Figure 7.13). The aquifer limestones outcrops over half of the aquifer surface. In the following, no account is taken of the karst conduit network. A flux boundary condition is set at the location of the pumping station (Lez spring). The pumping rate Q is taken equal to the mean of the annual discharge under natural regime. No-flow boundaries are used to represent the northern and southern borders. At the eastern and western borders, the hydraulic head is prescribed and taken equal to the average annual stream stage. The recharge R is

Symbol	Meaning	Value
D	Length of the simulation domain	40km
d	Length of the results visualization area	10km
L	Length of the perturbed area	600m
H_{MN}	Hydraulic head prescribed along the (MN) border	110m
H_{OP}	Hydraulic head prescribed valong the (OP) border	10m

Table 7.3: Model characteristics for the application examples described in Section 7.1.6.b (steady-state unconfined parallel flow). (MP) and (NO) are no-flow boundaries.

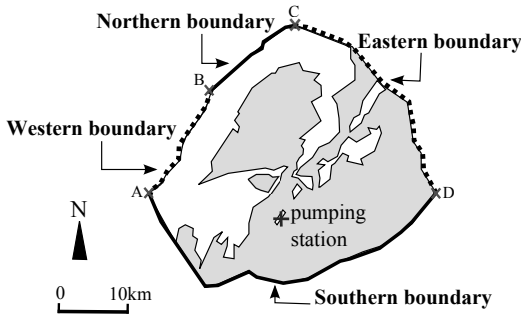

Figure 7.13: Definition sketch for the Lez model. The confined portion of the aquifer is grayed out.

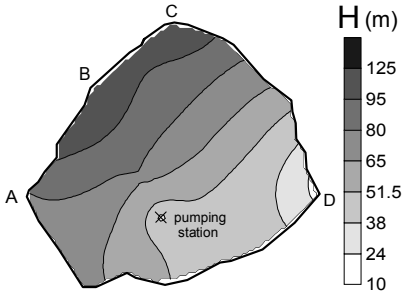

Figure 7.14: Steady state piezometric map of the Lez model.

assumed uniform. A 3-D geological model of the aquifer has been constructed based on lithological descriptions [Drogue, 1969], regional geological maps [Berger et al., 2001], available cross-sections [Benedicto et al., 1999; Séranne et al., 1995] and available stratigraphic logs, nine of which intersect the whole stratigraphic serie. The aquifer hydraulic conductivity K is assumed uniform, yet the perturbed aquifer bedrock geometry yields non-uniform aquifer transmissivity.

Experimental sensitivities are computed using the same methodology as in Section 7.1.6.a. The parameters are given in Table 7.5. The steady-state piezometry and transmissivity maps are presented in Figures 7.14 and 7.15.

Figures 7.17a to 7.17c show the sensitivity patterns generated by a perturbation in the hydraulic conductivity. Compared to the parallel flow case, the absolute value of the sensitivity is greater in the converging flow path direction. Figure 7.16 shows the hydraulic head sensitivity pattern generated by a perturbation in the recharge. The sensitivity contour lines are not fully circular due to the influence of the boundaries.

7.1.6.d Non-parallel flow in a mixed confined-unconfined aquifer : sensitivity to K under transient conditions

The present test case aims at checking the validity under transient flow conditions of the theoretical sensitivity patterns derived in Section 7.1.4. With this purpose, the sensitivity pattern generated by a perturbation in the hydraulic conductivity is investigated under transient conditions over a schematic representation of the Lez karst aquifer system. Experimental sensitivities are computed using the same methodology as in Section 7.1.6.a. Test case parameters are given in Table 7.6. The initial hydraulic heads are obtained from the steady-state simulation in Section 7.1.6.c. The recharge rate is interpolated from daily rainfall data recorded at 13 raingauge stations

Symbol	Meaning	Value
K	Hydraulic conductivity	10^{-4}m/s
R	Recharge rate	0m/s
z	Aquifer bedrock elevation	0m
k_o	Perturbation in the hydraulic conductivity	$-2.5\,10^{-5}$m/s
r_o	Perturbation in the recharge rate	$5.8\,10^{-9}$m/s
$H(0,0)$	Hydraulic head at the centre of the perturbed area	78.2m
$\nabla H(0,0)$	Hydraulic head gradient at the centre of the perturbed area	1.9mm/m

Table 7.4: Parallel, steady-state unconfined flow. Parameters for the application example described in Section 7.1.6.b : case of a perturbation in the hydraulic conductivity or in the recharge rate.

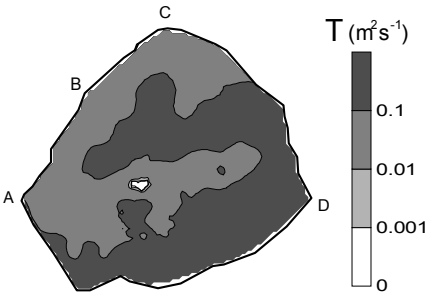

Figure 7.15: Steady state transmissivity map of the Lez model. The zero transmissivity at the centre of the model is due to a zero aquifer thickness.

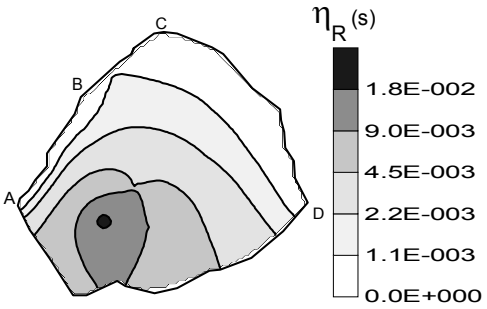

Figure 7.16: Non-parallel, steady-state mixed confined-unconfined flow. Case of a perturbation in the recharge rate : sensitivity of the hydraulic head. The simulation parameters are given in Table 7.5.

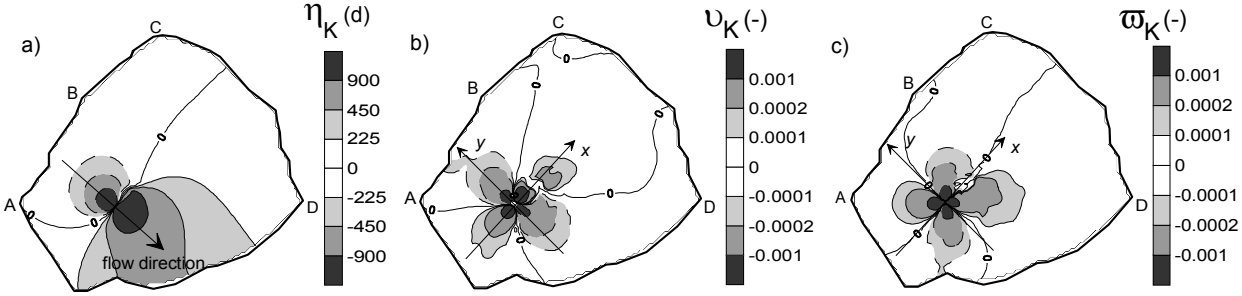

Figure 7.17: Non-parallel, steady-state mixed confined-unconfined flow. Case of a perturbation in the hydraulic conductivity : a) sensitivity of the hydraulic head, b) sensitivity of the longitudinal flow velocity, c) sensitivity of the transverse flow velocity. Dashed and solid lines indicate negative and positive values respectively. The simulation parameters are given in Table 7.5.

Symbol	Meaning	Value
K	Hydraulic conductivity	10^{-4}m/s
R	Recharge rate	$9.3\,10^{-9}$m/s
Q	Lez spring pumping rate	$2.2\text{m}^3/\text{s}$
k_o	Perturbation in the hydraulic conductivity	$-2.5\,10^{-5}$m/s
r_o	Perturbation in the recharge rate	$2.3\,10^{-10}$m/s
∇H	Hydraulic head gradient at the centre of the perturbed area	2.5mm/m
H_A	Prescribed hydraulic head at point A	70m
H_B	Prescribed hydraulic head at point B	126m
H_C	Prescribed hydraulic head at point C	115m
H_D	Prescribed hydraulic head at point D	15m

Table 7.5: Non-parallel, steady-state mixed confined-unconfined flow. Parameters for the application example described in Section 7.1.6.c : case of a perturbation in the hydraulic conductivity or in the recharge rate. The hydraulic head prescribed along the borders (AB) and (CD) is interpolated linearly between H_A and H_B along the border (AB), and between H_C and H_D along the border (CD). (BC) and (AD) are no-flux boundaries.

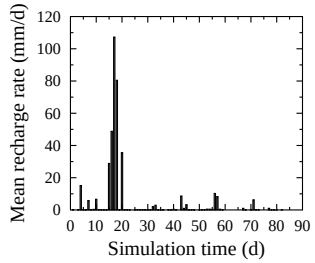

Figure 7.18: Non-parallel, transient mixed confined-unconfined flow. Case of a perturbation in the hydraulic conductivity. Mean daily recharge rate over the Lez aquifer during the simulation period.

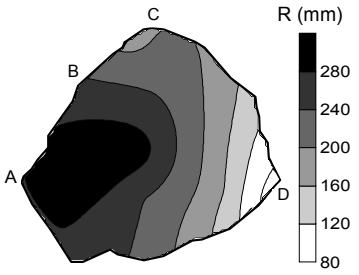

Figure 7.19: Non-parallel, transient mixed confined-unconfined flow. Case of a perturbation in the hydraulic conductivity. Cumulated rainfall over the Lez aquifer from day 15 to day 17.

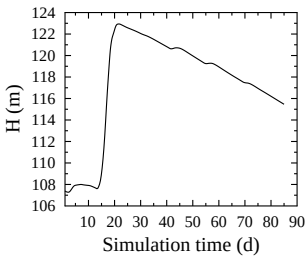

Figure 7.20: Non-parallel, transient mixed confined-unconfined flow. Case of a perturbation in the hydraulic conductivity. Hydraulic head at the centre of perturbed area, from day 1 to day 85 (application example 7.1.6.d).

distributed over the Lez basin from the 26th of november 2002 (day 1) to the 18th of february 2003 (day 85) (see Figure 7.18). The rainfall event from day 15 to day 17 is centred over the western part of the Lez basin (see cumulated rainfall distribution in Figure 7.19). Figure 7.20 shows the variations of the hydraulic head at the centre of the perturbed area during the simulation. Figure 7.21 shows the hydraulic head sensitivity pattern generated by a perturbation in the hydraulic conductivity at day 21 and day 60. The experimental transient sensitivity pattern matches the theoretical patterns established in Section 7.1.4.a for uniform properties and steady-state flow.

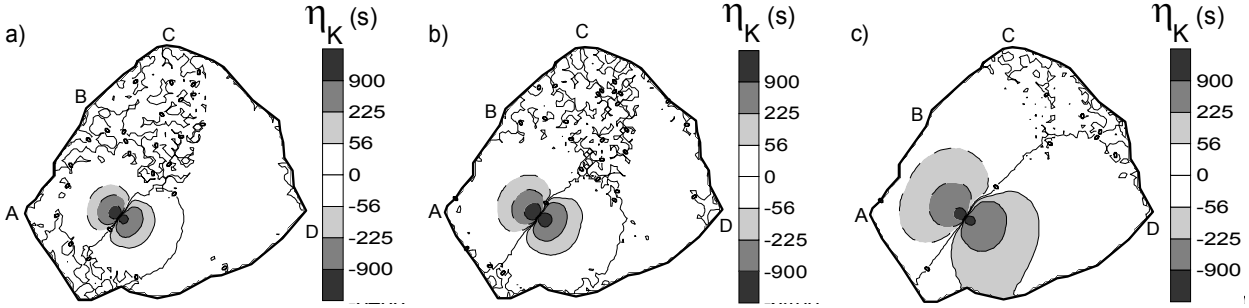

Figure 7.21: Non-parallel, transient mixed confined-unconfined flow. Case of a perturbation in the hydraulic conductivity. Sensitivity of the hydraulic head : a) at day 10, b) at day 21, c) at day 80. The simulation parameters are given in Table 7.6

7.1.6.e Sensitivity to boundary conditions

The hydraulic head sensitivity patterns generated by a perturbation in the boundary conditions are investigated over a schematic representation of the Lez karst aquifer system. Experimental sensitivities are computed using the same methodology as in Section 7.1.6.a. The parameters are given in Table 7.7.

Figure 7.22a shows the hydraulic head sensitivity pattern generated by a perturbation H_o in the hydraulic head prescribed along the western boundary. The perturbation yields a unit sensitivity value along the boundary, as seen in Section 7.1.5.a, while the hydraulic head prescribed along the eastern boundary yields a sensitivity value of zero along this boundary. The decrease of the sensitivity inside the model is quasi-linear, which is in agreement whith the results of Section 7.1.5.b. Indeed, the geometry of the sensitivity boundary conditions is quasi one-dimensional. Assume now

that a flux condition is prescribed along the western boundary. The flux values are chosen so that the hydraulic head pattern remains on the whole the same. The resulting sensitivity pattern is similar to the former one, as the sensitivity decreases linearly from the perturbed boundary to the eastern prescribed head boundary (Figure 7.22b). On the other hand, the sensitivity pattern generated by a perturbation in the flux condition prescribed along the northern border differs from the previous ones (see Figure 7.22c). This confirms that the boundary condition sensitivity pattern only depends on the geometry of the problem, as established in Section 7.1.5.a.

The next simulations investigate the effect of the transmissivity heterogeneity in the quasi 1-D geometry. The transmissivity in the area close to the perturbed boundary is 1% of the transmissivity value in the rest of the model (see Figure 7.23a). The hydraulic head sensitivity pattern generated by a perturbation in the hydraulic head prescribed along the western border is shown in Figure 7.23b. Compared to the case of an homogeneous transmissivity field (Figure 7.22a), the sensitivity to the head boundary condition is strongly attenuated by the low transmissive area, as predicted in Section 7.1.5.b. Assume now that the condition prescribed along the western boundary is a prescribed flux condition. Figure 7.23c shows the hydraulic head sensitivity pattern generated by a perturbation in this flux boundary condition. The comparison with the homogeneous case (Figure 7.22b) shows that the change in the transmissivity value in the area close to the boundary has no effect on the sensitivity value in the rest of the model, as established in Section 7.1.5.b.

The case of a 2-D geometry is investigated in the next simulations. Figure 7.24a shows the transmissivity distribution. Figures 7.24b and 7.24c show the sensitivity patterns generated by a perturbation in the hydraulic head or in the flux prescribed along the northern border. The resulting sensitivity patterns match the 1-D case, which confirms the validity of these results in the 2-D case.

7.1.7 Conclusions

The theoretical developments presented in Sections 7.1.2 to 7.1.5 indicate that the shape and extent of the sensitivity pattern depend on the nature of both the perturbed parameter (K, z, e or R) and the variable of interest (hydraulic head or Darcy velocity). Although derived for simple, homogeneous systems and steady-state parallel flow, these results have been validated for complex real-world systems under both non-parallel and transient flow conditions (Section 7.1.6), which allows some guidelines to be proposed for the calibration of groundwater flow models and for observation well network design. Items 1 to 5 focus on the sensitivity to the flow parameters.

Symbol	Meaning	Value
K	Hydraulic conductivity	10^{-4}m/s
R	Recharge rate	$9.3\,10^{-9}$m/s
S	Specific yield	$1.4\,10^{-2}$
Q	Lez spring pumping rate	$2.2\text{m}^3/\text{s}$
k_o	Perturbation in the hydraulic conductivity	$-2.5\,10^{-5}$m/s
H_A	Prescribed hydraulic head at point A	70m
H_B	Prescribed hydraulic head at point B	126m
H_C	Prescribed hydraulic head at point C	115m
H_D	Prescribed hydraulic head at point D	15m

Table 7.6: Non-parallel, transient mixed confined-unconfined flow. Parameters for the application example described in Section 7.1.6.d : case of a perturbation in the hydraulic conductivity. The hydraulic head prescribed along the borders (AB) and (CD) is interpolated linearly between H_A and H_B along the border (AB), and between H_C and H_D along the border (CD). (BC) and (AD) are no-flux boundaries.

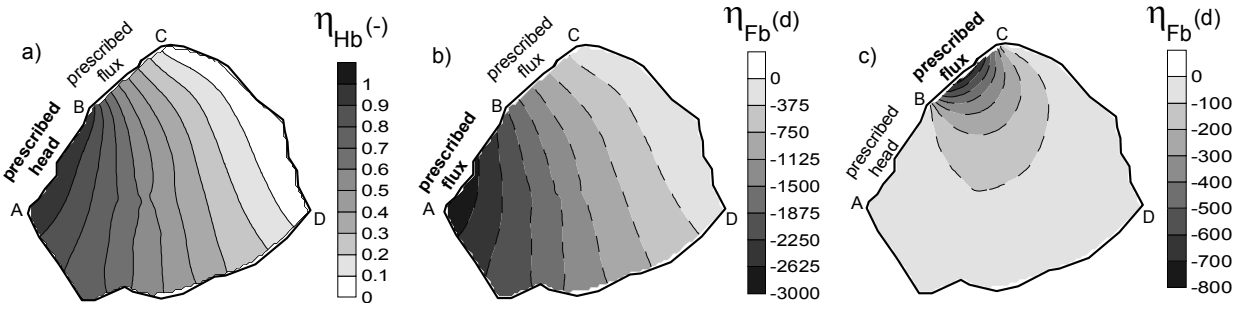

Figure 7.22: Steady-state, mixed confined-unconfined non-parallel flow. Case of a perturbation in the boundary conditions. Sensitivity of the hydraulic head to a perturbation : a) in the western border prescribed head boundary condition, b) in the western border prescribed flux condition, c) in the northern border prescribed flux condition. A zero flux is prescribed along the boundary (AD). The hydraulic head is fixed along the boundary (CD). The nature of the boundary condition prescribed along (AB) and (BC) depends on the simulation and is indicated on the corresponding figure (bold characters are used for the perturbed condition). Dashed and solid lines indicate negative and positive values respectively.

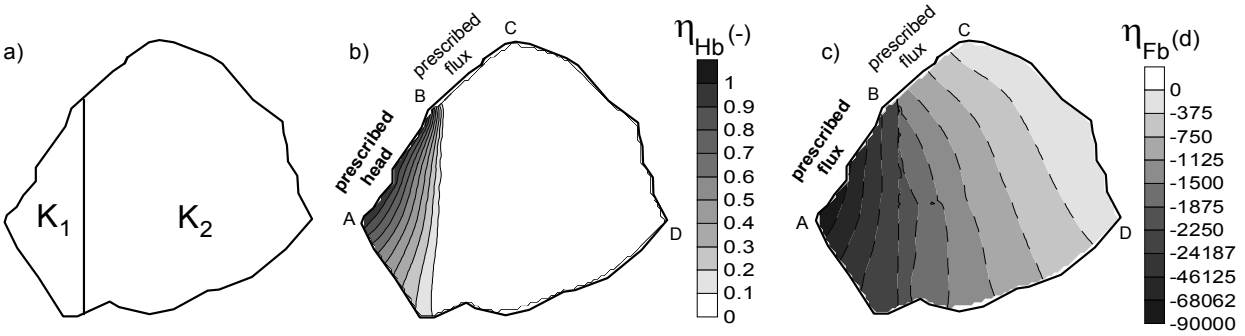

Figure 7.23: Steady-state, mixed confined-unconfined non-parallel flow. Case of a perturbation in the boundary conditions. Sensitivity of the hydraulic head to a perturbation in the western boundary condition, for a non homogeneous transmissivity distribution : a) definition sketch for the transmissivity distribution ($K_1 \ll K_2$), b) sensitivity pattern generated by a perturbation in the hydraulic head prescribed along the western boundary, c) sensitivity pattern generated by a perturbation in the flux prescribed along the western boundary. A zero flux is prescribed along the boundary (AD). The hydraulic head is fixed along the boundary (CD). The nature of the boundary condition prescribed along (AB) and (BC) depends on the simulation and is indicated on the corresponding figure (bold characters are used for the perturbed condition). Dashed and solid lines indicate negative and positive values respectively.

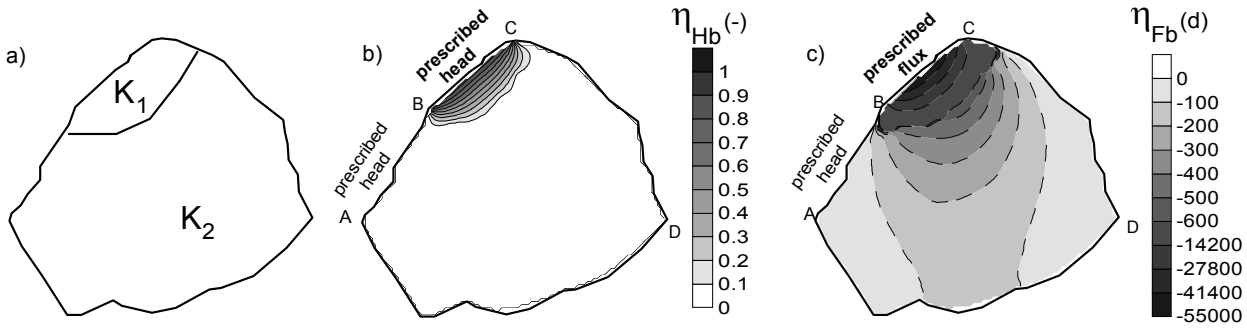

Figure 7.24: Steady-state, mixed confined-unconfined non-parallel flow. Case of a perturbation in the boundary conditions. Sensitivity of the hydraulic head to a perturbation in the northern boundary condition, for a non homogeneous transmissivity distribution : a) definition sketch for the transmissivity distribution ($K_1 \ll K_2$), b) sensitivity pattern generated by a perturbation in the hydraulic head prescribed along the northern boundary, c) sensitivity pattern generated by a perturbation in the flux prescribed along the northern boundary. A zero flux is prescribed along the boundary (AD). The hydraulic head is fixed along the boundary (CD). The nature of the boundary condition prescribed along (AB) and (BC) depends on the simulation and is indicated on the corresponding figure (bold characters are used for the perturbed condition). Dashed and solid lines indicate negative and positive values respectively.

Symbol	Meaning	Value
K	Hydraulic conductivity (homogeneous case)	10^{-4}m/s
K_1	Hydraulic conductivity (heterogeneous case)	10^{-4}m/s
K_2	Hydraulic conductivity (heterogeneous case)	10^{-6}m/s
R	Recharge rate	$9.3\,10^{-9}$m/s
Q	Lez spring pumping rate	$2.2\text{m}^3/\text{s}$
H_o	Perturbation in the hydraulic head	4m
F_o	Perturbation in the flux	$2.3\,10^{-8}$m/s
H_A	Hydraulic head prescribed at point A	70m
H_B	Hydraulic head prescribed at point B	126m
H_C	Hydraulic head prescribed at point C	115m
H_D	Hydraulic head prescribed at point D	15m
F_A	Flux prescribed at point A	$1.2\,10^{-7}$m/s
F_B	Flux prescribed at point B	$2.7\,10^{-7}$m/s
F_{BC}	Flux prescribed along the (BC) border	0m/s

Table 7.7: Steady-state, mixed confined-unconfined non-parallel flow. Parameters for the application examples described in Section 7.1.6.e : case of a perturbation in the boundary conditions. The hydraulic head prescribed along the border (CD) is interpolated linearly between H_C and H_D. A zero flux is prescribed along the (AD) border. Depending on the simulation, either the hydraulic head or the flux may prescribed along the borders (AB) and (BC). In any case, the hydraulic head H or the flux F prescribed along the borders (AB) and (BC) are interpolated linearly between their extremities.

Item 6 deals with the sensitivity to the boundary conditions. Item 7 concludes on the possibility to discriminate between the potential sources of model error.

1. The informations conveyed by hydraulic head and flow velocity measurements are complementary. As an example, consider the case when the model hydraulic conductivity is calibrated against piezometric level measurements. Regions with wrong K estimation located in the transverse and diagonal directions from the measurement point with respect to the flow direction may remain unnoticed, unless tracing experiments are performed.
2. For the case where model results do not coincide with the measurements, the region where the modelled hydraulic conductivity, aquifer thickness or bedrock elevation may be wrongly estimated must be sought downstream and upstream of the measurement point for a discrepancy in the hydraulic head. Besides, the origin of a discrepancy in the longitudinal flow velocity must be sought in both longitudinal and transverse directions to the flow, whereas the origin of a discrepancy in the transverse flow velocity must be sought in diagonal directions to the flow. Furthermore, if the discrepancy stems from bad recharge estimation, the region with wrong recharge estimation may be located anywhere in the model. The possibility to discriminate between the different sources of error is discussed in item 7.
3. Confined and unconfined aquifers behave differently with respect to sensitivity propagation. While the sensitivity to a perturbation in K (or z, or e) of both the hydraulic head and the flow velocities propagates with the same intensity upstream and downstream of the perturbed area in confined aquifers, it extends further downstream than upstream in unconfined aquifers. Consequently, the area in which the wrongly estimated parameter ought to be sought extends farther downstream than upstream for unconfined aquifers, while it extends equally in both directions in confined aquifers.
4. Model calibration should take into account the existence of dead zones in the sensitivity patterns of K, z and e. Indeed, suppose that the model is to be tuned so as to fit the hydraulic head at a given location (target point). Then calibrating K (or z, or e) in the transverse direction to the flow with respect to the target point would be meaningless, as the sensitivity of the hydraulic head to these parameters is zero. Moreover, doing so could lead to assign physically unrealistic values to the parameter in order to make model results fit the measurements.
5. Sampling network design should be adapted to the nature of the problem addressed. For instance, water resource assessment requires an accurate estimation of the hydraulic heads. In this case, the parameters K, z, and e have to be estimated upstream and downstream of the target point principally. Besides, the key variable in solute transport problems is the velocity field. Then the parameters K, z, and e must be evaluated principally in the longitudinal and transverse directions to the flow. The confined or unconfined character of the aquifer should also be taken into account, as the magnitude of the sensitivity is larger downstream than upstream of the target point for unconfined aquifers.
6. As far as the sensitivity to the boundary conditions is concerned, no general sensitivity pattern can be established in the two-dimensional case. Indeed, the sensitivity equation cannot be solved without specifying the boundary conditions, i.e. the model geometry. The uncertainty in the simulated hydraulic head stemming from an uncertain head boundary is minimized if the boundary lies in a region with low transmissivity. On the other hand, the uncertainty in the simulated hydraulic head stemming from an uncertain flux boundary is minimized for low average transmissivity between the target point and a known head condition. The consequences for model design are that : (i) whenever possible, uncertain head boundaries should be located in low transmissivity regions, so that the error on the hydraulic heads will

not propagate to higher transmissivity regions, (ii) although the influence of uncertain flux boundaries on hydraulic heads cannot be minimized, such boundaries should also be located in low transmissivity regions, if possible. Indeed, the uncertainty on the boundary condition will be more easily reduced if hydraulic head measurements are performed in a low transmissivity, high sensitivity gradient and high sensitivity value region.

7. The fact that the sensitivity pattern depends on the nature of the perturbed parameter may be used to discriminate between wrong hydraulic conductivity (or z, or e) estimation, wrong recharge and wrong boundary condition estimation, based on measurements of the flow variable at different locations. Indeed, the propagation of the error along the flow (if the observed variable is the hydraulic head) or in directions transverse to the flow (if the observed variable is the flow velocity) is typical of a wrongly estimated hydraulic conductivity (or z, or e), while an isotropic propagation of the error is typical of wrong recharge estimation. Classical nine-spot well pattern (see spatial setting in Figure 7.25) could allow for the observation of the error pattern, therefore enabling the identification of the error source. The error pattern stemming from wrong boundary condition estimation depends on the problem geometry, which makes it more difficult to identify. Yet wrong boundary condition estimation may influence a wider area than wrong flow parameter estimation. Nested observation networks could therefore help resolve the ambiguity between wrong boundary condition and wrong parameter estimation. Such networks were primarily designed by the petroleum industry to maximize the oil recovery by water flooding [Muskat, 1949; Muskat et al., 1933]. They are also used for the characterisation of the spatial variability of transmissivity fields by means of geostatistical moment analysis. Indeed, performing small-scale pumping tests at various locations across an aquifer and analyzing them by means of geostatistical moment analysis requires the availability of numerous transmissivity data spread more or less evenly across the site of interest [Riva et al., 2009]. The present work shows that existing nested well networks could offer insights on the nature and location of the aquifer heterogeneities even when used for passive monitoring.

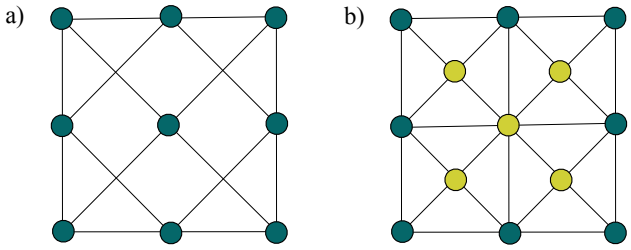

Figure 7.25: Observation wells network patterns : a) nine-spot pattern, b) five-spot pattern (light dots) and nested five-spot pattern (light and dark dots).

7.1.8 Appendix: Sensitivity source term

7.1.8.a Source term derivation for a perturbation in the hydraulic conductivity under confined, parallel flow conditions

The source term q generated by a perturbation in the hydraulic conductivity under confined conditions is

$$q = \nabla[e\varepsilon\nabla H] \tag{7.48}$$

Assume that the aquifer thickness is homogeneous over the perturbed area. Also assume that the flow is parallel and directed along the y-axis over the perturbed area. Then the hydraulic head

gradient is constant and the source term reduces to

$$q = e\frac{\partial H}{\partial y}\frac{\partial \varepsilon}{\partial y} \tag{7.49}$$

The value of the derivative of ε in the y direction is $+1/L$ over face 2, and $-1/L$ over face 4, which leads to

$$q = \begin{cases} -\dfrac{e}{L}\dfrac{\partial H}{\partial y} & \text{(face 4)} \\ \\ +\dfrac{e}{L}\dfrac{\partial H}{\partial y} & \text{(face 2)} \end{cases} \tag{7.50}$$

Consequently, the source term integral over each face Q is

$$Q = \begin{cases} -eL\dfrac{\partial H}{\partial y} & \text{(face 4)} \\ \\ +eL\dfrac{\partial H}{\partial y} & \text{(face 2)} \end{cases} \tag{7.51}$$

An equivalent source term pattern may be obtained by lumping the source term into source terms located at the gravity centres of the faces. The equivalent source term pattern is made of two point sources of intensity $-eL\,\partial H/\partial y$ and $+eL\,\partial H/\partial y$ located at (0,$-2L/3$) and (0,$2L/3$) respectively.

7.1.8.b Source term derivation for a perturbation in the hydraulic conductivity under confined, radial flow conditions

The second-order terms may be expressed as

$$\rho_1 = -\frac{\varepsilon}{r'^2} \tag{7.52a}$$

$$\rho_{22} = \frac{1}{r'}\frac{\partial \varepsilon}{\partial r'} - \frac{1}{r'_o}\frac{\partial \varepsilon}{\partial r'} \tag{7.52b}$$

Over face 4 the source term ρ_1 may be approximated as

$$\rho_1 \approx -\frac{\varepsilon}{r'^2_o} \tag{7.53a}$$

$$\rho_1 \approx -\frac{1}{r'^2_o}\left(1 - \frac{y}{L}\right) \tag{7.53b}$$

The integral of ρ_1 over face 4 may be expressed as

$$\rho_1 \approx -\frac{1}{r'^2_o}\int_0^L \left(1 - \frac{y}{L}\right) 2y\,dy \tag{7.54a}$$

$$\rho_1 \approx -\frac{1}{3}\frac{L^2}{r'^2_o} \tag{7.54b}$$

Over face 4 the source term ρ_{22} may be approximated as

$$\rho_{22} \approx -\frac{1}{r'_o L}\left(1 - \frac{y}{r'_o}\right) + \frac{1}{r'_o L} \tag{7.55a}$$

$$\rho_{22} \approx +\frac{y}{r'^2_o L} \tag{7.55b}$$

The integral of ρ_{22} over face 4 may be expressed as

$$\rho_{22} \approx + \frac{1}{r_o'^2 L} \int_0^L 2y^2 \, dy \tag{7.56a}$$

$$\rho_{22} \approx + \frac{2}{3} \frac{L^2}{r_o'^2} \tag{7.56b}$$

Similarly, the integrals of ρ_1 and ρ_{22} over face 2 may be may be expressed as

$$\rho_1 \approx - \frac{1}{3} \frac{L^2}{r_o'^2} \tag{7.57a}$$

$$\rho_{22} \approx + \frac{2}{3} \frac{L^2}{r_o'^2} \tag{7.57b}$$

The overall effect of the second-order source terms is to increase the algebraic value of the first-order sensitivity source terms. This leads to an increase of the absolute value of the sensitivity in the direction of the converging flow path lines, and a decrease in the direction of the diverging flow path lines.

7.1.8.c Source term derivation for a perturbation in the hydraulic conductivity under unconfined conditions

The source term q generated by a perturbation in the hydraulic conductivity under unconfined conditions is

$$q = \nabla[(H - z)\varepsilon \nabla H] \tag{7.58}$$

Assume that the flow is parallel and directed along the y-axis over the perturbed area. Then $(H - z)\nabla H$ is a constant and the source term is equal to zero over the faces 1 and 3. Over the faces 2 and 4, the source term may be written as :

$$q = (H - z)_o \left(\frac{\partial H}{\partial y} \right)_o \frac{\partial \varepsilon}{\partial y} \tag{7.59}$$

where $(H - z)_o$ is the aquifer thickness at the centre of the perturbed area and $(\partial H/\partial y)_o$ is the value of the hydraulic head gradient at the centre of the perturbed area. The value of the derivative of ε in the y direction is $+1/L$ over face 2, and $-1/L$ over face 4, which leads to

$$q = \begin{cases} -\dfrac{(H - z)_o}{L} \left(\dfrac{\partial H}{\partial y} \right)_o & \text{(face 4)} \\ \\ +\dfrac{(H - z)_o}{L} \left(\dfrac{\partial H}{\partial y} \right)_o & \text{(face 2)} \end{cases} \tag{7.60}$$

Consequently, the source term integral over each face Q is

$$Q = \begin{cases} -L(H - z)_o \left(\dfrac{\partial H}{\partial y} \right)_o & \text{(face 4)} \\ \\ +L(H - z)_o \left(\dfrac{\partial H}{\partial y} \right)_o & \text{(face 2)} \end{cases} \tag{7.61}$$

The equivalent source term pattern is made of two point sources of intensity $-L(H - z)_o \, (\partial H/\partial y)_o$ and $-L(H - z)_o \, (\partial H/\partial y)_o$ located at (0,$-2L/3$) and (0,$2L/3$) respectively.

7.1.8.d Sensitivity derivation for a perturbation in the recharge under unconfined, parallel flow conditions

In this paragraph we convert the sensitivity of the flow velocities in the Cartesian coordinate system. The Cartesian coordinates of the unitary radial and tangential vectors are

$$e_\rho = \begin{bmatrix} -\sin\theta \\ \cos\theta \end{bmatrix} \tag{7.62a}$$

$$e_\theta = \begin{bmatrix} -\cos\theta \\ -\sin\theta \end{bmatrix} \tag{7.62b}$$

The sensitivities of the radial and tangential flow velocities may thus be expressed in the Cartesian coordinate system as

$$\rho_R = \frac{2L^2}{3\pi(H-z)}\left(\frac{1}{r} + \ln\left(\frac{r}{d}\right)\frac{\partial(H-z)}{\partial y}\frac{\cos\theta}{H-z}\right)\begin{bmatrix} -\sin\theta \\ \cos\theta \end{bmatrix} \tag{7.63a}$$

$$\theta_R = -\frac{2L^2}{3\pi}\ln\left(\frac{r}{d}\right)\frac{\partial(H-z)}{\partial y}\frac{\sin\theta}{(H-z)^2}\begin{bmatrix} -\cos\theta \\ -\sin\theta \end{bmatrix} \tag{7.63b}$$

As $\sin\theta = -x/r$ and $\cos\theta = y/r$, equations (7.63a) and (7.63b) lead to

$$\nu_R = \frac{2L^2}{3\pi}\frac{y}{(H-z)r^2} + \frac{2L^2}{3\pi(H-z)^2}\frac{\partial(H-z)}{\partial y}\ln\left(\frac{r}{d}\right) \tag{7.64a}$$

$$\varpi_R = \frac{2L^2}{3\pi}\frac{x}{(H-z)r^2} \tag{7.64b}$$

7.1.8.e Sensitivity to boundary conditions

The following section investigates the effect of the transmissivity heterogeneity over the sensitivity of the hydraulic head to boundary flux conditions and to head-flux relationships, for a one-dimensional problem. The origin of the n-axis is taken at the crossing with the perturbed boundary.

Consider the case of a flux boundary condition, under confined conditions. As the problem is one-dimensional, a head condition must be prescribed at the other edge of the model in order to get a well-posed problem. Denote by Γ_F the flux boundary, and by Γ_H the prescribed head boundary. The sensitivity value at Γ_F is not fixed by the sensitivity boundary condition, while the sensitivity value along Γ_H is equal to zero (see Section 7.1.5.a). Assume that the model transmissivity is not uniform. Denote by $T_{(0)}$ the transmissivity value along Γ_F, and by $T_{(n)}$ the transmissivity value inside the model at the abscissa n. Under confined conditions, equation (7.44a) gives

$$T_{(0)}(\nabla\eta)_{(0)} = -1 \tag{7.65}$$

According to equation (7.46) :

$$T_{(n)}(\nabla\eta)_{(n)} = T_{(0)}(\nabla\eta)_{(0)} \quad \forall n \tag{7.66}$$

which leads to

$$T_{(n)}(\nabla\eta)_{(n)} = -1 \tag{7.67}$$

The value of the sensitivity gradient at a given abscissa n inside the model only depends on the transmissivity value at the abscissa n. The sensitivity value at the perturbed boundary is not fixed by the boundary conditions. The value of the sensitivity inside the model thus only depends on the

average transmissivity value between the unperturbed head boundary and the location at which the sensitivity is investigated.

Consider the case of a flux boundary condition, under unconfined conditions. Equation (7.66) is still valid, but the unconfined conditions yields a new sensitivity boundary condition

$$T_{(0)}(\nabla\eta)_{(0)} + K_{(0)}(\nabla H)_{(0)}\eta_{(0)} = -1 \tag{7.68}$$

The sensitivity value at the perturbed boundary can be expressed as

$$\eta_{(0)} = -\int_{\Gamma_F}^{\Gamma_H} (\nabla\eta)_{(n)}\, dn \tag{7.69}$$

Combining equations (7.69) and (7.66) leads to

$$\eta_{(0)} = -\int_{\Gamma_F}^{\Gamma_H} \frac{T_{(0)}}{T_{(n)}}(\nabla\eta)_{(0)}\, dn \tag{7.70a}$$

$$= -T_{(0)}(\nabla\eta)_{(0)} \int_{\Gamma_F}^{\Gamma_H} \frac{1}{T_{(n)}}\, dn \tag{7.70b}$$

Combining equations (7.68) and (7.70b) leads to

$$\eta_{(0)} = \int_{\Gamma_F}^{\Gamma_H} \frac{1}{T_{(n)}}\, dn \left(1 - K_{(0)}\nabla H_{(0)} \int_{\Gamma_F}^{\Gamma_H} \frac{1}{T_{(n)}}\, dn\right)^{-1} \tag{7.71}$$

The sensitivity value at the perturbed boundary thus depends on the average transmissivity, as in the confined case. The sensitivity value inside the model thus depends on the average transmissivity between the unperturbed head boundary and the location where the sensitivity is investigated.

The case of a head-flux relationship under confined or unconfined conditions can be handled following the same reasoning as above, and yields the same conclusion.

7.1.9 Complementary discussion: boundary condition versus hydrodynamic parameters

Sections 7.1.3 and 7.1.4 indicate that the sensitivity η_{HP} of the hydraulic head to a perturbation in the hydrodynamic parameters e or K

$$\eta_{\mathrm{HP}} \propto \ln\left(\frac{r_1}{r_2}\right) \tag{7.72}$$

Consider the sensitivity in the flow direction (maximum sensitivity values). Far from the perturbation ($r \gg L$) a first-order Taylor expansion of equation (7.72) gives

$$\eta_{\mathrm{HP}} \propto \frac{1}{r} \tag{7.73}$$

Equation (7.73) means that the decrease of the sensitivity of the hydraulic head to the hydrodynamic parameters is proportional to the inverse of the distance to the perturbation.

On the other hand, Section 7.1.5 indicates that for the one-dimensional case and with uniform transmissivity the sensitivity of the hydraulic head to the hydrodynamic parameters decreases linearly.

This short analysis highlights the fact that the influence of the boundary conditions may propagate farther than that of the hydrodynamic properties of the porous medium. The consequences for distributed hydrodynamic modelling are the following:

- special attention should be paid to the determination of the boundary conditions,
- calibration of the boundary conditions should be considered as an efficient option, as a complementary tool to hydrodynamic properties calibration.

7.2 Empirical study of the sensitivity of the hybrid model

This Section aims to assess the impact of discrete karst conduits modelling on the sensitivity propagation. To that purpose, the sensitivity of the hybrid flow model set up in Chapter 6 is investigated empirically for both steady and transient state simulations.

7.2.1 Steady-state analysis

7.2.1.a Impact of discrete karst conduits modelling on the propagation of the sensitivity to a perturbation in the hydrodynamic properties of the matrix

The analytical pattern for the sensitivity to a local perturbation in the hydrodynamic properties has been established in Section 7.1 for a porous medium. The modification of this analytical pattern in presence of karst conduits is illustrated in Figure 7.26 for different boundary conditions and karst conduit sections.

- Consider the case when a constant head boundary condition is set at the karst outlet. Suppose that the karst conduit section is not the limiting factor for fluid flow towards the karst outlet. Then the constant head condition propagates along the karst conduit. This results in a zero sensitivity along the karst conduit, which in turn results in a deformation of the analytical sensitivity pattern (strongly asymmetric sensitivity pattern, see Figure 7.26c). Now, suppose that the karst conduit section is limiting for fluid flow towards the karst outlet. Then the propagation of the boundary condition along the karst conduit is impaired. This results in a weaker deformation of the analytical sensitivity pattern (see Figure 7.26b).
- Consider the case when a flux boundary condition is set at the karst outlet. Then a constant head gradient condition propagates along the karst conduit. This means that the hydraulic head sensitivity tends to be constant along the karst conduit. This results in an advection of the analytical sensitivity pattern towards the karst conduit (Figure 7.26a).

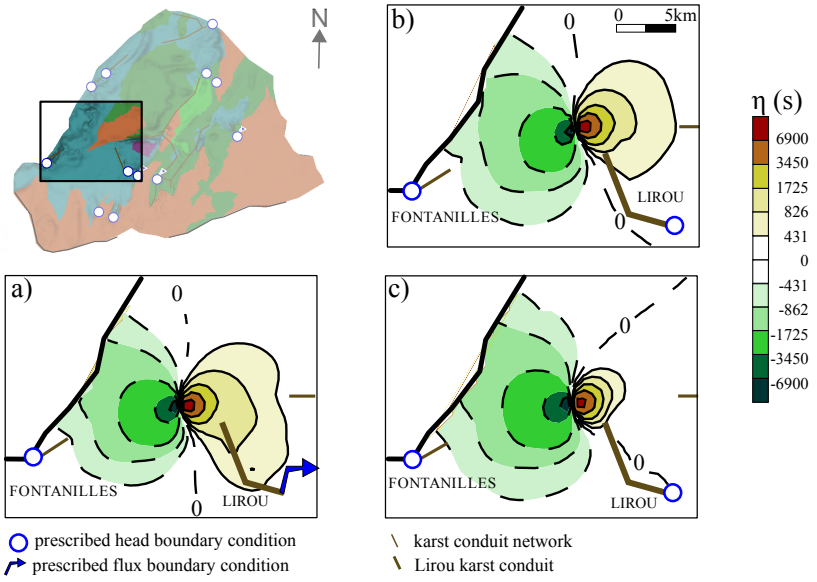

Figure 7.26: Steady-state sensitivity of the Lez model: Hydraulic head sensitivity near the Lirou karst conduit for a local perturbation of the hydraulic conductivity. a) prescribed flux boundary condition and $S_{\text{Lirou}} = 10\text{m}^2$, b) prescribed hydraulic head boundary condition and $S_{\text{Lirou}} = 1\text{m}^2$, c) prescribed hydraulic head boundary at the Lirou spring and Lirou conduit diameter (S_{Lirou}) equal to $10\,\text{m}^2$. Head boundary conditions are prescribed to the other karst conduit outlets. Dashed and solid lines indicate negative and positive sensitivity values respectively. See discussion in Section 7.2.1.a.

7.2.1.b Modification of the karst conduit properties

Consider the sensitivity of the spring discharge to the section of the karst conduit that feeds this spring. Figure 7.27 shows the discharge rate at two spring outlets as a function of the karst spring conduit section, for two different recharge distributions.

The sensitivity is maximal for the smallest drain sections and it tends to zero for larger drain sections. This may be explained by the fact that when the drain section increases, the resistance to the flow through the karst conduit becomes negigibles as compared to the resistance to the flow towards the karst conduit through the porous medium.

Also note that the drain section which is critical for flow control depends on the recharge distribution.

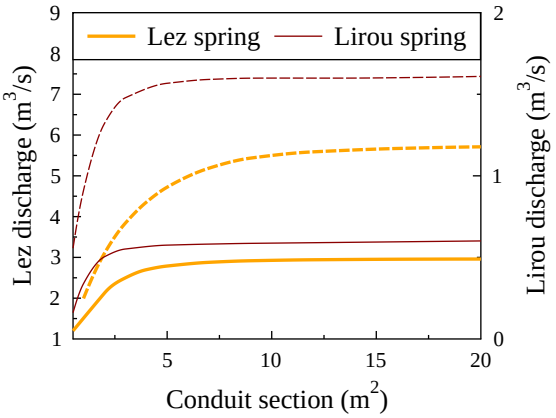

Figure 7.27: Steady-state sensitivity of the Lez model to a modification of karst conduit properties. Steady-state discharge at the Lez (bold, orange line) and Lirou (red line) springs as a function of the karst conduit section, for two different recharge fields (solid and dotted lines). See discussion in Section 7.2.1.b.

7.2.1.c Consequences for the transient-state behaviour of the sensitivity

The observations on the steady-state sensitivity behaviour stated above may be extended to transient-state sensitivity behaviour. Consider the case of a karst spring whith water withdrawal within the karst conduit (e.g. Lirou or Lez spring).

- During very low flow periods, the spring dries up and the water level at the outlet of the karst conduit is controlled by the water withdrawal rate (flux boundary condition). The karst conduit section is not the limiting factor for the flow towards the karst outlet. The sensitivity pattern for a local perturbation in the hydrodynamic properties of the matrix is therefore similar to the one presented in Figure 7.26a (Figure 7.28a).
- During flood events, the spring overflows (head boundary condition) and the karst conduit section is likely to limit the flow towards the karst outlet. The sensitivity pattern for a local perturbation in the hydrodynamic properties of the matrix is similar to the one presented in Figure 7.26b (Figure 7.28b).
- During the recession phase, the spring still overflows (head boundary condition) but the karst conduit section is not limiting the flow towards the karst outlet. The sensitivity pattern for a local perturbation in the hydrodynamic properties of the matrix is similar to the one presented in Figure 7.26c (Figure 7.28c).

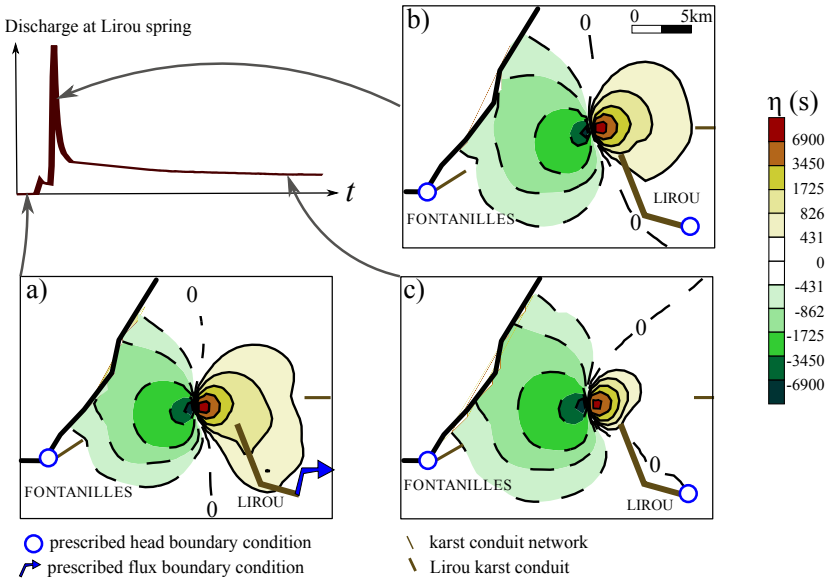

Figure 7.28: Predicted transient-state sensitivity of the Lez model: Hydraulic head sensitivity near the Lirou karst conduit for a local perturbation of the hydraulic conductivity. a) during very low flow periods (no spring overflow), b) during flood events (spring overflow), c) prescribed hydraulic head boundary at the Lirou spring and Lirou conduit diameter (S_{Lirou}) equal to $10\,\text{m}^2$. Head boundary conditions are prescribed to the other karst conduit outlets. Dashed and solid lines indicate negative and positive sensitivity values respectively. See discussion in Section 7.2.1.c.

7.2.1.d Conclusion

The impact of discrete karst conduits modelling on the propagation of a local perturbation of the hydrodynamic properties of the matrix can be summarized as follows:

(i) when a head boundary condition is set at the karst outlet, the head boundary condition propagates along the karst conduit. In that case the karst conduit tends to limit the propagation of the perturbation.

(ii) when a flux boundary condition is set at the karst outlet then it tends to extend the propagation of the perturbation farther towards the karst outlet.

(iii) when the conveyance of the karst conduit limits the fluid flow towards the karst outlet, then the propagation of the boundary condition is impaired. The impact of the discrete karst conduit on the sensitivity propagation tends to disappear.

(iv) it is important to note that the conveyance value which is critical for flow control depends on the recharge distribution.

Note that the boundary condition at the outlet of the karst conduit and the limiting character of the conveyance of the karst conduit with respect to the flow through the conduit are expected to change during a transient-state simulation. Similarly, the sensitivity of the discharge at the outlet of the karst conduit to the hydrodynamic properties of the karst conduit also depends on the limiting or non-limiting character of the conveyance.

The fact that the sensitivity pattern undergoes abrupt changes during a transient-state simulation means that the size and the extent of the area whose hydrodynamic properties are to be calibrated also change abruptly. This behaviour is expected to makes the calibration exercise difficult. It also suggests that only little help can be expected from a steady-state calibration exercise.

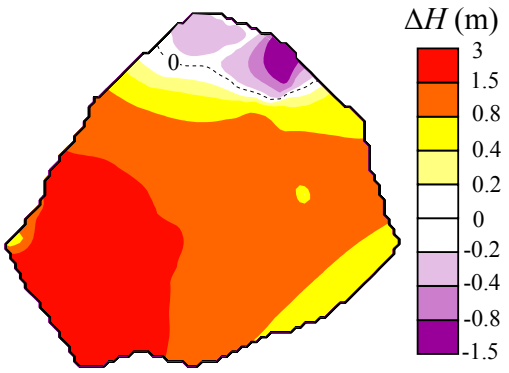

Figure 7.29: Sensitivity to the initial condition: difference in the initial hydraulic head of the modified and the benchmark simulations (epikarst unit).

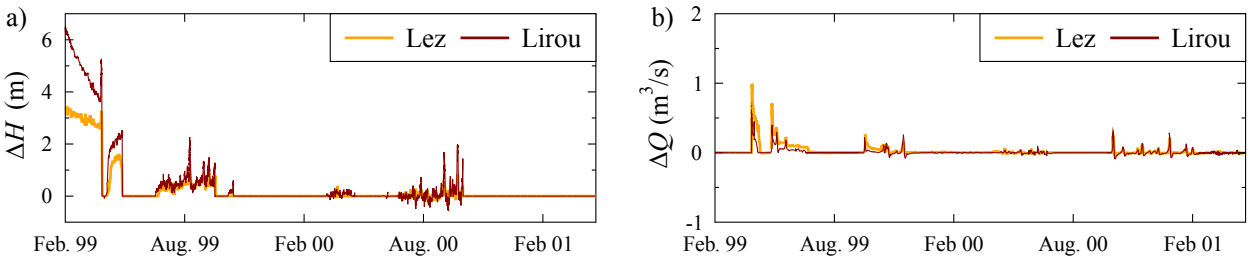

Figure 7.30: Sensitivity to the initial condition. Difference in: a) the hydraulic head, b) the overflow discharge of the two simulation runs. See discussion in Section 7.2.2.a.

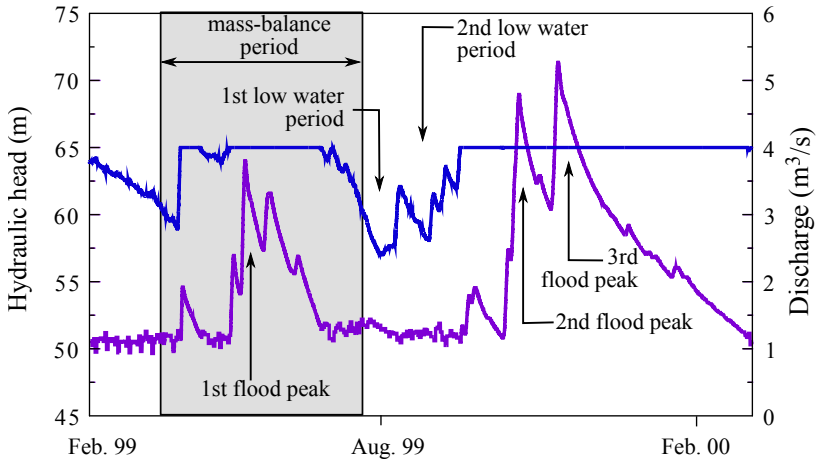

Figure 7.31: Lez spring. Simulated hydraulic head and spring discharge for the reference simulation used in Section 7.2.2. The flood peaks and the low water periods considered in Section 7.2.2.b are indicated by arrows. The mass balance period is greyed out.

7.2.2 Transient-state analysis

7.2.2.a Sensitivity to the initial condition

The sensitivity to the initial hydraulic head is investigated based on the following procedure.

1. The transient simulation presented in Section 6.3 is used as a benchmark for comparing the changes in the simulation results to the variations in the initial state.
2. A simulation is run with a slightly different initial state to that of the benchmark.
3. The difference in the hydraulic heads and in the discharge rate between the two simulation runs is presented in Figure 7.30 for the main outlets of the model.

The initial state for the modified simulation is computed following the procedure described in Section 6.3.1, with the only difference that only the years 2002 to 2008 are used for the computation. The difference between the two initial head fields is shown in Figure 7.29.

Figure 7.30 yields the following comments.

- Up to 90 days after the start of the simulation, the decrease of the sensitivity in the hydraulic head is quasi-linear for both outlets.
- 90 days after the start of the simulation, a rainfall event causes the overflow of both springs. The delay in the overflow time between the two simulations causes a sensitivity peak for both the hydraulic head and the spring discharge variables.
- Up to August 2000, the overall amplitude of the sensitivity of both variables decreases (although not monotonically). However, the overall sensitivity of both variables is seen to increase after August 2000. Such a behaviour may be related to an acceleration of the propagation of the sensitivity due to rainfall events of increased magnitude compared to the Feb. 2000 - Aug. 2000 period. The fact that the relatively high amplitude rainfall event that occur after Feb. 2001 is associated with no increase in the discharge sensitivity may mean that all the sensitivity has been drained off the model.

A more thorough assessment of the sensitivity propagation should include the analysis of the hydraulic head sensitivity at the inner nodes of the model.

7.2.2.b Sensitivity to the hydrodynamic properties

The hydrodynamic properties of the hybrid model are varied one at a time. The transient simulation presented in Section 6.3 is used as a benchmark for comparing the changes in the simulation results to the variations in the hydrodynamic properties. The indicators used for the analysis are the following:

- maximum flood peak discharge at the Lez spring,
- mean discharge at the Lez spring for a given mass-balance period,
- ratio of the mean discharge at the Lez spring to the mean total model outflow for a given mass-balance period,
- minimal hydraulic head reached during low water periods at the Lez spring.

The flood peaks, the low water periods and the mass balance period considered are indicated in Figure 7.31. The results are presented in Figure 7.32. Note that the average computational time steps (15 mn) allows an accurate estimation of the flood peak discharge rate. Also note that the reference period for the mass balance estimation is short (100 days) so that the ratio of the mean discharge at the Lez spring to the mean total model outflow during the mass-balance period may only be considered as indicative.

Storage properties

Specific yield (unconfined units). A decrease in the specific yield causes an increase in the drawdown at the Lez spring (Figure 7.32.1a) and increase in the flood peak discharge (Figure 7.32.1b). The decrease in the specific yield is also associated with a slight increase in the mean discharge at the Lez spring, and with a decrease in the ratio between the Lez discharge and the mean total model outflow (Figure 7.32.1c). This latter result may be related to the fact that the decrease in the specific yield causes overall higher water levels during flood events, which results in an extension of the overflow period of the temporary springs.

Specific storage (confined units). The impact of a decrease in the specific storage on the water level and on the discharge time series at the Lez spring is similar to that of a decrease in the specific yield. It causes an increase in the drawdown at the Lez spring (Figure 7.32.2a) and an increase in the flood peak discharge (Figure 7.32.2b). Moreover, the decrease in the specific storage is associated with an increase in the mean discharge at the Lez spring, and with a decrease in the ratio between the Lez discharge and the total model outflow (Figure 7.32.2c).

Transfer properties

Hydraulic conductivity of the "epikarst" unit. An increase in the hydraulic conductivity of the epikarst unit yields no change in the drawdown at the Lez spring (Figure 7.32.3a). It results in a slight increase in the flood peak discharge at the Lez spring (Figure 7.32.3b) due to a better concentration of the flow towards the conduits. The increase in the mean discharge at the Lez spring (Figure 7.32.3c) is associated with a decrease in the ratio between the Lez discharge and the total model outflow (for a low amplitude change in the hydraulic conductivity) and to an increase in the relative contribution of the Lez discharge as compared to the total model outflow (for a higher amplitude change in the hydraulic conductivity). This can be related to the fact that in a first time, the increase in the epikarst hydraulic conductivity fastens the drainage towards the temporary outlets that are located in the unconfined area of the aquifer. In a second time, the further increase in the epikarst hydraulic conductivity eases the drainage towards the Lez conduit and then the Lez spring.

Hydraulic conductivity of the "deep aquifer" unit. An increase in the hydraulic conductivity of the "deep aquifer" unit causes a decrease in the drawdown at the Lez spring (Figure 7.32.4a) and an increase in the flood peak discharge at the Lez spring (Figure 7.32.4b). Note that the increase in the hydraulic head is bounded because the hydraulic head at the spring can not exceed the spring overflow level. The overall increase in the mean total model outflow is mainly due to an increase in the Lez spring discharge (Figure 7.32.4c).

7.2.2.c Sensitivity to the drain properties

Figure 7.32.5 shows the absolute error on the hydraulic head and on the simulated discharge at the Lez spring, as a function of the percentage variation in the section of the karst conduit feeding the spring.

An increase in the conduit section yields an increase in the hydraulic head at the spring, and an increase in the flood peak discharge (Figures 7.32.5a and 7.32.5b). Note that the sensitivity to the conduit section is maximum for the smallest drain sections, whereas it tends to zero for the largest drain sections. This behaviour appears clearly on Figure 7.32.5a and it can also been noted on Figure 7.32.5b. This confirms the findings of Section 7.2.1.b: for larger drain sections the limiting factor for the flow turns to be the hydraulic head gradient towards the karst conduit rather than the karst conduit section. The value of the drain section above which the limiting factor for the

flow is the hydraulic head gradient towards the conduit depends on the value of the discharge that is drained off by the conduit. Last, an increase in the conduit section results in an increase in the mean total model outflow which is mainly related to an increase in the Lez spring discharge (Figure 7.32.5c).

7.2.2.d Complementary remarks on the sensitivity properties

The empirical sensitivity to the hydrodynamic properties confirms well-known results:

- a decrease in the storage properties (specific storage for the confined units or specific yield for the unconfined units) results in overall higher water levels, in particular during high-intensity rainfall. This in turn causes an extension of the overflow period of the temporary springs,
- an increase in the hydraulic conductivity of the epikarst fastens the drainage towards the temporary outlets that are located in the unconfined units (epikarst and superposed aquifer). A further increase in the hydraulic conductivity of the "epikarst" eases the drainage towards the spring,
- an increase in the hydraulic conductivity of the "deep aquifer" unit principally increases the drainage towards the Lez spring.

The empirical sensitivity of the spring discharge to the conduit section confirms the findings of Section 7.2.1.b. Indeed, for larger drain sections the limiting factor for the flow turns to be the hydraulic head gradient towards the karst conduit rather than the karst conduit section. The hydrodynamic properties of the "epikarst" unit were identified in Chapter 6 as a possible cause of limitation of the flood peak discharge at the main outlets. Our results suggest that their influence on the simulated spring discharges is significantly weaker than that of the drain sections.

Also note that the empirical sensitivity graphs presented in Figure 7.32 show identical sensitivity behaviour for the different flood events investigated. However, these graphs also reveal non-negligible variations in the absolue value of the sensitivity between different periods (up to a factor two), which suggests that the use of the model on an event-by-event basis may not be possible.

7.2.2.e Complementary remarks on the transient-state calibration

The empirical sensitivity analysis suggests that the differences between the transient simulation run and the observed behaviour of the Lez aquifer may be prioritarily attributed to:

(i) inadequate values of the drain sections,

(ii) underestimation of the discharge rate through the Montpellier fold. Empirical assessment of the sensitivity to the transfer boundary associated with the Montpellier fold is therefore needed,

(iii) inadequate values of the storage properties.

A complementary transient-state simulation is run as a preliminary check on the validity of hypotheses (i) and (ii). Compared to the initial transient-state simulation presented in Section 6.3, the complementary simulation has the following characteristics (see Tables 7.8 and 7.9):

- increased effective section for the Lez, Lirou, Fontanilles, Montlobre, Sauve and Vernède springs,
- increased transfer rate through the Montpellier fold.

The simulation results are presented in Figure 7.33 and Tables 7.10 and 7.11. Compared to the initial transient-state simulation, the main changes are the following:

- a decrease in the average discharge at the Lez and Fontbonne springs,
- an increase in the average discharge at the Fontanilles, Lirou, Sauve and Vernède springs,

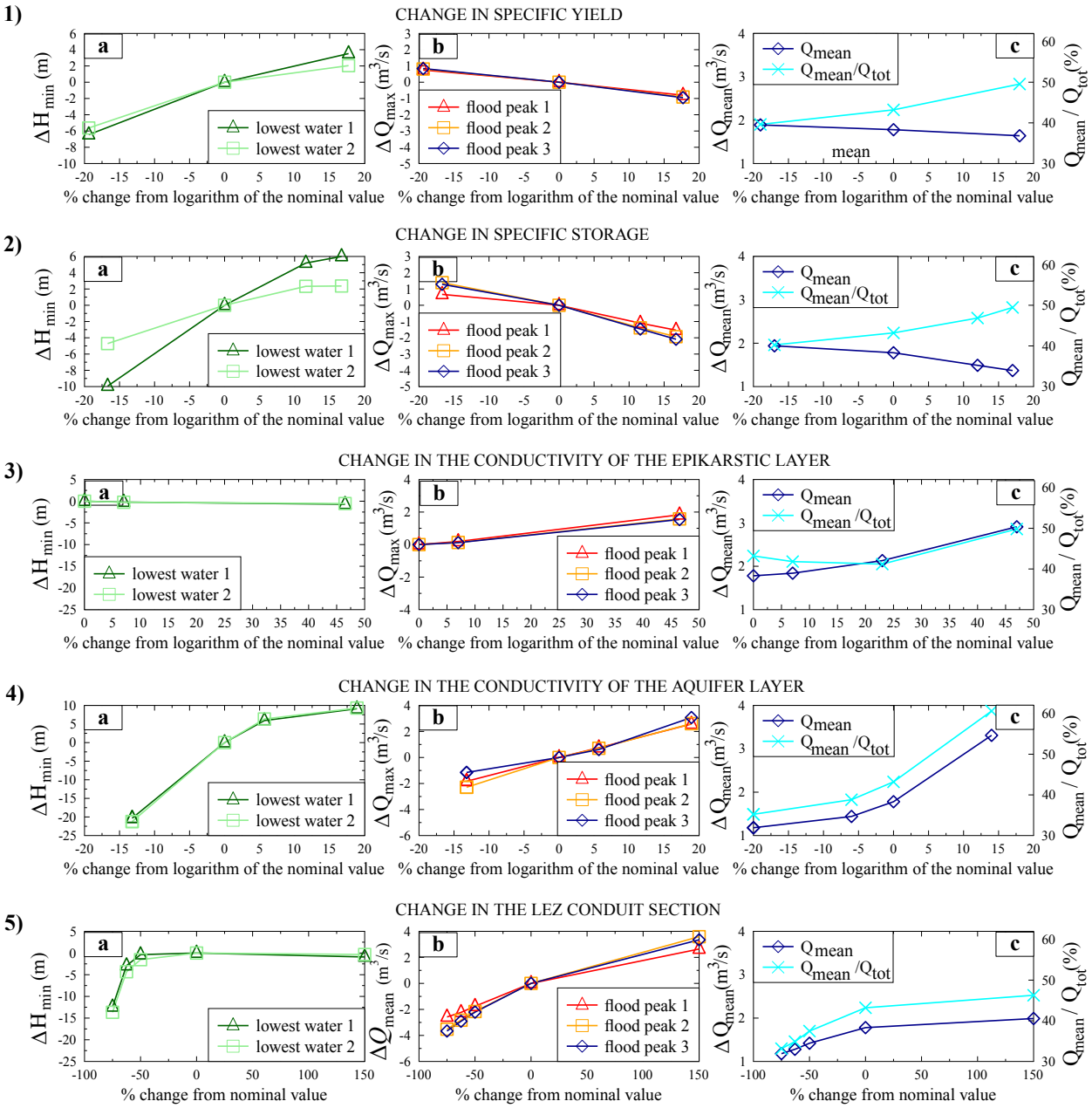

Figure 7.32: Lez spring. Left (graphs a): absolute error on the hydraulic head ($\Delta H_{\min}$). Middle (graphs b): absolute error on the discharge ($\Delta Q_{\max}$). Right (graphs c): average Lez outflow and ratio between the Lez outflow and the total model outflow over the reference period, as a function of the percentage variation in the hydrodynamic properties. The properties varied are: Graphs 1: specific yield, Graphs 2: specific storage, Graphs 3: hydraulic conductivity of the epikarst, Graphs 4: hydraulic conductivity of the deep aquifer, Graphs 5: Lez karst conduit section.

– no significant change in the average discharge at the Montlobre spring and through the Montpellier fold.

As regards the Lez spring hydrograph, Figure 7.33 shows an increased drawdown and a modification of the shape of the flood peaks. The complementary simulation has increased peak discharges and sharper recession curves compared to the initial simulation. The modification in the shape of the Lez spring hydrograph may be related to the increase in the drain section. The decrease in the average discharge at the Lez and Fontbonne springs may seem paradoxical, given the increase in the effective section of the conduits that feed these springs. That decrease may be related to the increase in the effective section of the conduits that feed the Fontanilles, Lirou, Sauve and Vernède springs and therefore to an increase in the drainage towards these springs. The increase in the drawdown at the Lez spring may also be attributed to the increase in the drainage towards the Fontanilles, Lirou, Sauve and Vernède springs.

The results of the complementary simulation confirm the fact that the effective drain section is a key factor for the shape of the Lez spring hydrograph. The modification performed in the transfer properties through the Montpellier fold is not sufficient to yield a modification in the average discharge rate through the fold. The complementary transient-state simulation matches better the observed records than the initial transient-state simulation but large differences remain, in particular:

– the underestimation of the drawdown at the Lez spring,
– the overestimation of the discharge rate at the Montlobre, Vernède and Fontanille springs.

These differences may be prioritarily attributed to:

(i) the underestimation of the discharge rate through the Montpellier fold,
(ii) inadequate values of the drain sections assigned to the Montlobre, Vernède and Fontanille springs,
(iii) inadequate values of the storage properties.

7.2.3 Conclusion

The empirical sensitivity analysis together with the complementary transient-state simulation stress the key role played by the drain section on the resulting shape of the spring hydrograph.

Our results suggest hat the differences between the complementary transient simulation run and the observed behaviour of the Lez aquifer may be prioritarily attributed to:

– the underestimation of the discharge rate through the Montpellier fold,
– inadequate values of the drain sections assigned to the Montlobre, Vernède and Fontanille springs,
– inadequate values of the storage properties.

Boundary	Head	Out transfer rate	
		complementary simulation	initial simulation
West Montpellier fold	75m ASL	$50\,m\,s^{-1}$	$43\,m\,s^{-1}$
East Montpellier fold	60m ASL	$250\,m\,s^{-1}$	$43\,m\,s^{-1}$

Table 7.8: Complementary transient-state simulation. Parameters for the boundary conditions associated with the Montpellier fold.

Conduit number	Effective conduit section (m^2)	
	complementary simulation	initial simulation
1 - Lez system	12	4
2 - Lirou system	9	3
3 - Fontbonne system	0.5	0.5
4 - Montlobre system	7	1
5 - Fontanilles system	7	1
6 - Vernède system	7	1
7 - Sauve system	7	1

Table 7.9: Complementary transient-state simulation. Effective conduit section. See reference for conduit number in Figure 6.2.

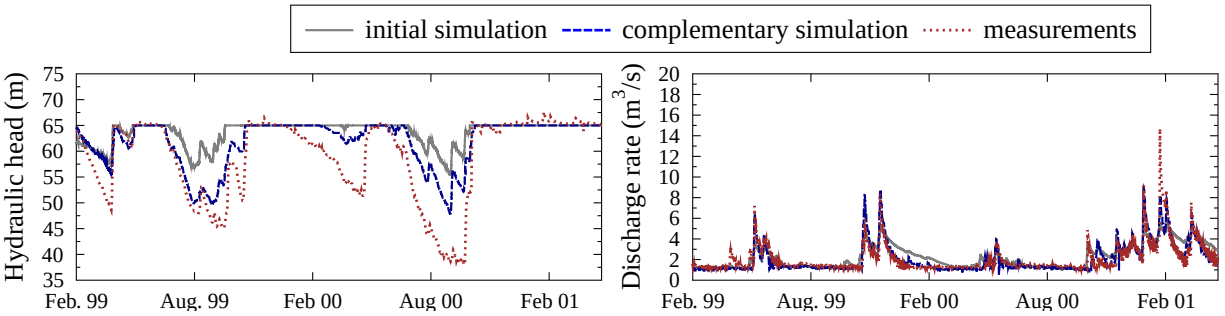

Figure 7.33: Simulation results for the complementary transient state simulation. Hydraulic head and discharge rate at the Lez spring.

Outlet	Discharge ratio	Outlet	Discharge ratio
Lez spring	0.90	Lirou spring	1.14
Fontbonne spring	0.75	Montlobre spring	0.95
Fontanille spring	1.13	Vernède spring	1.26
Sauve spring	1.32	West Montpellier fold	0.95
East Montpellier fold	0.94		

Table 7.10: Simulation results for the complementary transient state simulation. Average discharge ratio between the complementary and initial simulations for the Feb. 99 - Jun. 00 period.

Outlet	Discharge rate ($m^3\,s^{-1}$)	Outlet	Discharge rate ($m^3\,s^{-1}$)
Lez spring	2.04	Lirou spring	0.8
Fontbonne spring	0.17	Montlobre spring	0.21
Fontanille spring	0.68	Vernède spring	0.77
Sauve spring	1.07	West Montpellier fold	0.40
East Montpellier fold	0.08		

Table 7.11: Simulation results for the complementary transient state simulation. Average discharge rate for the Sept. 00 - Sept. 01 period.

7.3 References for Chapter 7

Avias, J. (1992*a*). « Karstic aquifers of mediterranean type, geological controls : "Lez spring" (North-Montpellieran karsts, France) example ». In: *Hydrogeology of Selected Karst Regions*. Ed. by W. Back, J. S. Herman and H. Paloc. Vol. 13. International Contributions to Hydrogeology. Hannover: IAH, pp. 89–113. See p. 182.

Bear, J. (1972). *Dynamics of Fluids in Porous Media*. New York: American Elsevier, p. 764. See pp. 6, 168.

Benedicto, A., M. Séguret and P. Labaume (1999). « Tertiary Extension Within the Alpine Orogen ». In: ed. by B. Durand, L. Jolivet, F. Horvath and M. Séranne. Geological Society Special Publication. Chap. Interaction between faulting, drainage and sedimentation in extensional hanging-wall syncline basins: Example of the Oligocene Matelles Basin, Gulf of Lion margin (SE France), pp. 81–108. See pp. 139, 183.

Berger, G., B. Alabouvette, J. Guérangé-Lozes, M. Demange and P. Ambert (2001). *Carte géologique de la France (1/250 000), feuille Montpellier (38)*. Orléans : BRGM. Notice explicative par B. Alabouvette, M. Demange, J.Guérangé-Lozes, P.Ambert (2003), 164p. See p. 183.

Butler, J. J. and W. Z. Liu (1991). « Pumping tests in non-uniform aquifers: The linear strip case ». In: *Journal of Hydrology* 128.1-4, pp. 69 –99. DOI: 10.1016/0022-1694(91)90132-2. See p. 167.

Butler, J. J. and W. Liu (1993). « Pumping tests in nonuniform aquifers: The radially asymmetric case ». In: *Water Resources Research* 29.2, pp. 259–269. DOI: 10.1029/92WR02128. See p. 167.

Copty, N. K., P. Trinchero, X. Sanchez-Vila, M. S. Sarioglu and A. N. Findikakis (2008). « Influence of heterogeneity on the interpretation of pumping test data in leaky aquifers ». In: *Water Resources Research* 44.11, W11419. DOI: 10.1029/2008WR007120. See p. 167.

Delay, F., A. Kaczmaryk and P. Ackerer (2007). « Inversion of interference hydraulic pumping tests in both homogeneous and fractal dual media ». In: *Advances in Water Resources* 30.3, pp. 314–334. DOI: 10.1016/j.advwatres.2006.06.008. See pp. 4, 167.

Diersch, H. (1998*a*). *Feflow : Reference Manual*. Institute for Water Resources Planning and Systems Research, WASY. Berlin. URL: http://www.feflow.info/manuals.html. See pp. xii, 9, 151, 180.

— (1998*b*). *Feflow : User's Manual*. Institute for Water Resources Planning and Systems Research, WASY. Berlin. URL: http://www.feflow.info/manuals.html. See p. 180.

Drogue, C. (1969). « Contribution à l'étude quantitative des systèmes hydrologiques karstiques d'après l'exemple de quelques karst périméditerranéens ». 482p. PhD thesis. Université Montpellier II. See pp. 124, 131, 133, 134, 136, 138, 140, 141, 182, 183.

Garabedian, P. (1964). *Partial Differential Equations*. John Wiley & Sons, 684pp. See pp. 171, 173, 175.

Graettinger, A., J. Lee, H. Reeves and D. Dethan (2006). « Quantitative methods to direct exploration based on hydrogeologic information ». In: *Journal of Hydroinformatics* 8.2, pp. 77–90. DOI: 10.2166/hydro.2006.006. See p. 167.

Guinot, V. and B. Cappelaere (2009). « Sensitivity analysis of 2D steady-state shallow water flow. Application to free surface flow model calibration ». In: *Advances in Water Resources* 32.4, pp. 540–560. DOI: 10.1016/j.advwatres.2009.01.005. See p. 167.

Gunzburger, M. D. (1999). « Sensitivities, adjoints and flow optimization ». In: *International Journal for Numerical Methods in Fluids* 31.1, pp. 53–78. DOI: 10.1002/(SICI)1097-0363(19990915)31:1<53::AID-FLD955>3.0.CO;2-Z. See p. 167.

Helton, J., R. Cooke, M. Mac Kay and A. Saltelli (2006). « Guest editorial - Sensitivity analysis of model output: SAMO 2004 ». In: *Reliability Engineering and System Safety* 91.10-11, pp. 1105–1108. DOI: 10.1016/j.ress.2005.11.013. See p. 167.

Huysmans, M, T Madarasz and A Dassargues (2006). « Risk assessment of groundwater pollution using sensitivity analysis and a worst-case scenario analysis ». In: *Environmental Geology* 50.2, pp. 180–193. DOI: 10.1007/s00254-006-0197-1. See p. 167.

Jiao, J. and C. Zheng (1997). « The different characteristics of aquifer parameters and their implications on pumping-test analysis ». In: *Ground Water* 35.1, pp. 25–29. DOI: 10.1111/j.1745-6584.1997.tb00056.x. See p. 167.

Jyrkama, M. and J. Sykes (2006). « Sensitivity and uncertainty analysis of the recharge boundary condition ». In: *Water Resources Research* 42.W01404, pp. 1–11. DOI: 10.1029/2005WR004408. See pp. 20, 168.

Khan, D., C. Deutsch, C. Mendoza and B. Rostron (2007). « Approximate sensitivity coefficients for integrating hydraulic head data into geological models ». In: *Journal of Hydrology* 347.3-4, pp. 460–473. DOI: 10.1016/j.jhydrol.2007.09.043. See p. 167.

Knight, J. and G. Kluitenberg (2005). « Some analytical solutions for sensitivity of well tests to variations in storativity and transmissivity ». In: *Advances in Water Resources* 28.10, pp. 1057–1075. DOI: 10.1016/j.advwatres.2004.08.018. See p. 168.

Leven, C. (2002). « Effects of heterogeneous parameter distributions on hydraulic tests - Analysis and assessment ». PhD thesis. Eberhard Kärls Universität Tübingen. URL: http://w210.ub.uni-tuebingen.de/dbt/volltexte/2003/710/index.html. See p. 168.

Leven, C. and P. Dietrich (2006). « What information can we get from pumping tests ? - Comparing pumping test configurations using sensitivity coefficients ». In: *Journal of Hydrology* 319.1-4, pp. 199–215. DOI: 10.1016/j.jhydrol.2005.06.030. See p. 168.

Mazzilli, N., V. Guinot and H. Jourde (2010*a*). « Sensitivity analysis of 2D steady-state aquifer flow equations. Implications for groundwater flow model calibration and monitoring network design: An overview. » In: *Proceedings of the SimHydro 2010 Conference held in Sophia-Antipolis, Nice, France (June 2-4, 2010)*. [CD-Rom]. See p. 166.

— (2010*b*). « Sensitivity analysis of two-dimensional steady-state aquifer flow equations. Implications for groundwater flow model calibration and validation ». In: *Advances in Water Resources* 33.8, pp. 905–922. DOI: 10.1016/j.advwatres.2010.04.014. See p. 166.

McElwee, C. D. (1978). « Sensitivity of groundwater models with respect to variations in transmissivity and storage ». In: *Water Resources Research* 14.3, pp. 451–459. DOI: 10.1029/WR014i003p00451. See p. 167.

McKeown, C., R. S. Haszeldine and G. D. Couples (1999). « Mathematical modelling of groundwater flow at Sellafield, UK ». In: *Engineering Geology* 52.3-4, pp. 231 –250. DOI: 10.1016/S0013-7952(99)00008-3. See p. 167.

Meyer, P. D., A. J. Valocchi and J. Wayland Eheart (1994). « Monitoring network design to provide initial detection of groundwater contamination ». In: *Water Resources Research.* 30.9, pp. 2647–2659. DOI: 10.1029/94WR00872. See pp. 20, 167.

Muskat, M. (1949). *Physical Principles of Oil production*. McGraw. Hill Book Company. See p. 190.

Muskat, M., R. Wuckoff and P. Pittsburgh (1933). « A theoretical analysis of water-flooding networks ». In: *AIME Technical publication* 507, pp. 62–77. See p. 190.

Neupauer, R. M. and J. L. Wilson (2002). « Backward probabilistic model of groundwater contamination in non-uniform and transient flow ». In: *Advances in Water Resources* 25.7, pp. 733–746. DOI: 10.1016/S0309-1708(02)00073-8. See p. 168.

Neupauer, R. M. and J. L. Wilson (2003). « Backward location and travel time probabilities for a decaying contaminant in an aquifer ». In: *Journal of Contaminant Hydrology* 66.1-2, pp. 39–58. DOI: 10.1016/S0169-7722(03)00024-X. See p. 168.

Oliver, D. S. (1993). « The influence of nonuniform transmissivity and storativity on drawdown ». In: *Water Resources Research* 29.1, pp. 169–178. DOI: 10.1029/92WR02061. See pp. 167, 168.

Ramarao, B. S., A. M. Lavenue, G. De Marsily and M. G. Marietta (1995). « Pilot point methodology for automated calibration of an ensemble of conditionally simulated transmissivity fields 1. Theory and computational experiments ». In: *Water Resources Research* 31.3, pp. 475–493. DOI: 10.1029/94WR02258. See p. 167.

Riva, M., A. Guadagnini, J. Bodin and F. Delay (2009). « Characterization of the Hydrogeological Experimental Site of Poitiers (France) by stochastic well testing analysis ». In: *Journal of Hydrology* 369.1-2, pp. 154–164. DOI: 10.1016/j.jhydrol.2009.02.040. See p. 190.

Sun, N.-Z. (1994). *Inverse Problems in Groundwater Modelling*. Vol. 6. Theories and applications of transport in porous media. Kluwer Academic Publishers, p. 337. ISBN: 978-0-7923-2987-9. See p. 169.

Sun, N.-Z. and W. W.-G. Yeh (1985). « Identification of parameter structure in groundwater inverse problem ». In: *Water Resources Research* 21.6, pp. 869–883. DOI: 10.1029/WR021i006p00869. See p. 169.

Sykes, J., J. Wilson and R. Andrews (1985). « Sensitivity analysis for steady state groundwater flow using adjoint operators ». In: *Water Resources Research* 21.3, pp. 359–371. DOI: 10.1029/WR021i003p00359. See pp. 15, 167.

Séranne, M., A. Benedicto, C. Truffert, G. Pascal and P. Labaume (1995). « Structural style and evolution of the Gulf of Lion Oligo-Miocene rifting : Role of the Pyrenean orogeny ». In: *Marine and Petroleum Geology* 12, pp. 809–820. DOI: 10.1016/0264-8172(95)98849-Z. See p. 183.

Tumlinson, L. G., J. L. Osiensky and J. P. Fairley (2006). « Numerical evaluation of pumping well transmissivity estimates in laterally heterogeneous formations ». In: *Hydrogeology Journal* 14.1-2, pp. 21–30. DOI: 10.1007/s10040-004-0386-5. See p. 167.

Vela, S. and R. McKinley (1970). « How areal heterogeneities affect pulse-test results ». In: *Society of Petroleum Engineers Journal* 10.2, pp. 181–191. DOI: 10.2118/2569-PA. See p. 167.

Willmann, M., J. Carrera, X. Sanchez-Vila and E. Vazquez-Suné (2007). « On the meaning of the transmissivity values obtained from recovery tests ». In: *Hydrogeology Journal* 15.5, pp. 833–842. DOI: 10.1007/s10040-006-0147-8. See p. 167.

Yeh, W. W.-G. (1986). « Review of parameter identification procedures in groundwater hydrology: The inverse problem ». In: *Water Resources Research* 22.2, pp. 95–108. DOI: 10.1029/WR022i002p00095. See p. 169.

Yukler, M. (1976). « Analysis of error in groundwater modelling ». PhD thesis. University of Kansas. See p. 167.

Conclusions

This dissertation aimed to provide improved understanding and insight into the general behaviour of numerical models of groundwater flow within karst systems, using sensitivity analysis as a primary tool.

Materials. In this work we used different approaches to sensitivity analysis. We also considered different flow models and application sites:

- the modelling approaches considered range from global reservoir flow modelling (Part 1) to distributed, hybrid flow modelling (Part 2),
- as far as global reservoir models are concerned, we investigated different model structures: an hysteresis-based model (Chapters 2 and 3), a non-linear reservoir model designed to account for the change in karst connectivity (Chapter 2) and two rainfall-discharge-hydraulic head models designed for the specific problem of flow modelling at springs under active groundwater management (Chapter 4),
- two application sites have been considered : the Durzon karst system (Chapters 2 and 3) and the Lez karst system (Chapters 4 and 7), that differ by their size, hydraulic functioning and complexity,
- we used both local and global sensitivity approaches. Local sensitivity analysis examines the model behaviour in the vicinity of a central value, based on an approximation of the model dynamics in the vicinity of this value. It allows to gain analytical insights into the model behaviour. This analysis is dominant in Chapters 2 and 7. Global approaches are based on the sampling of the parameter space and allows the investigation of order-of-magnitude parameter changes. Such approaches are used in Chapters 3 and 4.

Methods. As a systematic approach, sensitivity analysis has been used to answer the following questions:

(i) Is it possible to calibrate the model ? Is the calibration robust ?

As regards global models, Chapter 2 shows that the initialisation bias may be a concern. Indeed, threshold-based transfer functions generate Dirac sensitivity patterns. When associated with long-term memory reservoirs and fast discharge models, they may generate a substantial initialisation bias, even after very long periods of inactivity. As a consequence, the commonly-used one-year warm-up period may not ensure a proper elimination of the initialisation bias. Our work also provides general rules for the initialisation bias behaviour, depending on the model structure and the meteorological inputs. As a broad rule, the dissipation of the sensitivity is favoured by very low water level or very high water level periods. Furthermore, Chapter 2 evidences the fact that model structure may either fasten the dissipation of the initialisation bias or, on the contrary, favour its persistence.

As regards hybrid flow models, Chapter 7 shows that the influence of the boundary conditions may propagate farther than that of the hydrodynamic properties of the medium. Special attention should therefore be paid to the determination of the boundary conditions. However, the boundary condition at the outlet of the karst drainage network is subject to brutal changes due to the alternation between overflow and non-overflow periods. These changes in the nature of the boundary condition are associated with dramatic changes in the sensitivity pattern, which are likely to impair the calibration ability of the model.

Chapter 4 illustrates the fact that overparameterization may cause parametric equifinality and low predictive capability.

(ii) Is it possible to reduce equifinality, through multi-objective calibration ?
Multi-objective calibration aims at efficiently reproducing different characteristics of the calibration signal. Chapter 4 illustrates the complementarity between the high water level and low water level signals for the calibration of global models in the case of a spring under active groundwater management.
Chapter 4 also gives an example of unsuccessful multi-objective calibration, for a parsimonious model well-constrained by the calibration data. In that case, the redundancy of the different objectives functions highlights the fact that the model can not yield more satisfactory simulations of the hydrodynamic response of the karst aquifer.

(iii) Is it possible to reduce equifinality through multi-variable calibration ?
Chapter 3 discusses the use of ground-based gravity data for the calibration of a global rainfall-discharge reservoir model.
Chapter 7 shows that for distributed flow models, the hydraulic head and the hydraulic head gradient convey complementary informations. Indeed, the analytical study of the properties of the sensitivity of the groundwater flow equation to the flow parameters and to the boundary conditions indicates that the propagation of the sensitivity strongly depends on the variable considered.

(iv) Is it possible to determine which measurement network design will yield the highest information content ?
Chapter 7 shows that for distributed flow models, the design of the optimal monitoring network depends on the problem to be solved (water resource or solute transport assessment). The analysis carried out in Chapter 7 also gives general rules for the optimal network design when the regional flow directions are known.

Key results. The key points of our work are the following.

- Our contribution stresses the potentialities of local sensitivity approaches. Global sensitivity analysis has become preponderant in environmental systems modelling. This study shows that despite inherent limitations due to the local approximation and the one-at-a-time analysis, local sensitivity approaches may offer valuable complementary insights into the general behaviour of non-linear flow models.
- Our contribution also stresses the interest of multi-variable calibration as compared to multi-objective calibration, as regards equifinality reduction. Different objective functions correspond to differents manners of using the same information, with the emphasis put on different characteristics of the calibration signal. Multi-objective calibration therefore aims to use the available information in the most clever way. By contrast, different variables (e.g. the hydraulic head and the hydraulic head gradient) may carry complementary information, as illustrated by the findings of Chapters 2 and 7. Multi-variable calibration therefore amounts to a true increase in the information content.

Prospects. Future work may focus on:

- the assessment of the local sensitivity approach for uncertainty estimation by comparison to global, Monte-Carlo approaches,
- further investigation of the reduction of the equifinality through incorporation of geophysical measurements in the calibration process,
- the investigation of the reduction of the equifinality through incorporation of hydrochemical measurements in the calibration process.

Sensibilité et incertitude de modélisation sur les bassins versants à forte composante karstique

Résumé: L'objectif de cette thèse est de déterminer des caractéristiques générales du comportement de la sensibilité dans la modélisation hydrodynamique des écoulements en milieu karstique. Nous étudions l'influence des spécificités du milieu karstique (forte hétérogénéité de structure, dualité de l'écoulement, forte non-linéarité de fonctionnement) sur la propagation de la sensibilité en vue de déterminer des règles générales pour la calibration. En particulier, nous essayons de répondre aux questions suivantes: (i) la calibration est-elle possible ? (ii) la calibration est-elle robuste ? (iii) est-il possible de réduire l'équifinalité via une calibration multi-objectif ou multi-variable ? L'analyse est menée pour le cas d'une modélisation conceptuelle globale et pour celui d'une modélisation hybride distribuée.
Cette contribution met en évidence le potentiel des méthodes locales d'analyse de sensibilité. En dépit des limitations inhérentes à cette approche (approximation locale), l'analyse locale permet une compréhension fine du fonctionnement du modèle, pour un coût de calcul réduit. Par ailleurs, cet travail souligne l'intérêt d'une calibration multi-variable par rapport à une calibration multi-objectif, dans une optique de réduction de l'équifinalité.

Mots-clef: analyse de sensibilité, karst, modélisation hydrodynamique

Abstract: The present thesis aims to work out the general characteristics of the sensitivity of numerical models of flow within karst systems. A special attention is devoted to the study of the influence of karst specificities (high heterogeneity, duality of flow, highly non-linear behaviour) on the sensitivity propagation, with the final purpose of answering the following questions: (i) is it possible to calibrate the model ? (ii) is the calibration robust ? (iii) is it possible to reduce equifinality, through multi-objective calibration or through multi-variable calibration ? The analysis is performed for global reservoir models and distributed, hybrid flow models.
This contribution stresses the potentialities of local sensitivity analyses. Despite their inherent limitations (local approximation), local analyses have proved to bring valuable insights into the general behaviour of complex, non-linear flow models, at little computational cost. Besides, this contribution also stresses the interest of multi-variable calibration as compared to multi-objective calibration, as regards equifinality reduction.

Keywords: sensitivity analysis, karst, groundwater flow modelling

Laboratoire HydroSciences Montpellier, UMR 5569 (CNRS-IRD-UM1-UM2)
Université Montpellier II - HydroSciences Montpellier - CC MSE
Place E. Bataillon - 34095 MONTPELLIER CEDEX 5